Synthesis and Characterization of Nanoparticles Added CuTl-based Superconductors

By

ABDUL JABBAR

(1-FBAS/PHDPHY/S10)

Department of Physics

Faculty of Basic and Applied Sciences

International Islamic University, Islamabad

Synthesis and Characterization of Nanoparticles Added CuTl-based Superconductors

By

ABDUL JABBAR

(1-FBAS/PHDPHY/S10)

Supervisor

Dr. Muhammad Mumtaz

Co-Supervisor

Dr. Kashif Nadeem

A THESIS IS SUBMITTED
FOR THE DEGREE OF DOCTOR OF PHILOSOPHY
DEPARTMENT OF PHYSICS, FACULTY OF BASIC AND APPLIED SCIENCES, INTERNATIONAL ISLAMIC UNIVERSITY ISLAMABAD

Synthesis and Characterization of Nanoparticles Added CuTl-based Superconductors

By

ABDUL JABBAR

(1-FBAS/PHDPHY/S10)

A thesis is submitted to

Department of Physiscs

For the award of the degree of

Doctor of Philosophy in Physics

Signature.....

5-1-2016

(Chairman, Department of Physics)

CHAIRMAN
DEPT. OF PHYSICS
International Islamic University
Islamabad

Signature.....

(Dean FBAS, IIU Islamabad)

Department of Physics
Faculty of Basic and Applied Sciences
International Islamic University, Islamabad

International Islamic University, Islamabad
Faculty of Basic and Applied Sciences (FBAS)
Department of Physics

Dated: 23rd December, 2015

Final Approval

This is to certify that the work in this PhD dissertation entitled **"Synthesis and Characterization of Nanoparticles added CuTl-based Superconductors"** has been carried by **Mr. Abdul Jabbar** (Registration No. **01-FBAS/PHDPHY/S10**) and completed in Materials Research Laboratory, Department of Physics, Faculty of Basic and Applied Sciences (FBAS), International Islamic University Islamabad, Pakistan, is of sufficient standard in scope and quality for the award of **PhD** degree in **Physics.**

COMMITTEE

External Examiner 1
Dr. Pervaiz Akhtar
Ex. DG PICRET, Islamabad,
Pakistan.

External Examiner 2
Dr. Zafar Iqbal
Department of Physics
Ripah International University Islamabad,
Pakistan.

23-12-15

Internal Examiner
Dr. Naeem Ahmad
Department of Physics
Islamic International University Islamabad,
Pakistan.

Chairman
Dr. Waqar Adil Syed
Department of Physics
Islamic International University Islamabad,
Pakistan.

CHAIRMAN
DEPT. OF PHYSICS
International Islamic University
Islamabad

Supervisor
Dr. Muhammad Mumtaz
Department of Physics
Islamic International University Islamabad,
Pakistan.

A thesis submitted to

Department of Physics

International Islamic University Islamabad

As a partial fulfillment for the award of the degree of

Doctor of Philosophy


بسم الله الرحمن الرحيم

DEDICATED

to

My beloved

Mother

and

My

Respected teachers

DECLARATION

It is hereby declare that this thesis work neither as a whole nor a part of it has been copied out from any source. Further, work presented in this dissertation has not been submitted in support of any publication any other degree or qualification to any other university or institute and is considerable under the plagiarism rules of Higher Education Commission (HEC) Pakistan.

Abdul Jabbar

(1-FBAS/PHDPHY/S10)

CERTIFICATE

It is certified that Abdul Jabbar Registration No. 1-FBAS/PHDPHY/S10 has carried out the research work related to this thesis entitles, "Synthesis and Characterization of Nanoparticles Added CuTl-based Superconductors' under my supervision. This work fulfills all the requirements for the award of the degree of doctor of philosophy.

Dr. Muhammad Mumtaz

Assistant Professor (TTS)
Department of Physics,
International Islamic University,
Islamabad.

ACKNOWLEDGEMENTS

It gives me great pleasure and satisfaction to acknowledge the endowment of the creator of the universe, **Allah Almighty**, the most gracious, compassionate and beneficent to His creature, who enabled me to complete my research work successfully.

I would like to acknowledge the worth mentioning supervision of **Dr. Muhammad Mumtaz** and **Dr. Kashif Nadeem** and who guided me and supported me during my whole research work. Moreover, their supervision enabled me to develop an understanding of the field. Without their sincere efforts I was unable to complete this hard task of my life. **Almighty Allah** may bless them with long life, health, happiness and knowledge. I am also thankful and acknowledge to **Higher Education Commission (HEC) of Pakistan** for providing financial assistance in the form of indigenous scholarship. I want to specially thank **Dr. Nawazish Ali Khan** of Quaid-i-Azam University, for providing me the chance to work under the great environment of his materials science laboratory.

Moreover, I would like to express my sincere thanks to all the faculty members of Department of Physics IIU Islamabad especially to **Dr. Syed Salman Hussain**. I would also like to thank all other faculty members of my university for their sincere appreciation, comments and suggestions. I express my thanks to all staff of Physics Department, IIUI, for their various services. I shall express my heartiest thanks to all of my research colleagues **Faisal Zeb, Muhammad Kamran, Ghulam Hussain, Khalid Mehmood Khan,** especially **Irfan Qasim** and **Waqee Ur Rehman** for being very supportive and co-operative throughout my research work. I also pay special thanks to my lab fellows **Liaqat Ali, Waseem Sarwar, Munawar Zaman** and **Shahid Ahmed Khan** without their co-operation, it was not possible to complete this work.

Finally, I need to thank some individuals on the personal side of my life. To my loving parents, brothers and sisters, my sincerest gratitude for all they have done. I could not wish for a more supportive, loving family, and for them I am deeply thankful and blessed.

Abdul Jabbar

Synthesis and Characterization of Nanoparticles Added CuTl-based Superconductors

TABLE OF CONTENTS

List of Figures

List of Tables

List of Publications

1. **Abdul Jabbar**, Irfan Qasim, M. Mumtaz, and K. Nadeem "Synthesis and superconductivity of $(Ag)_x$/CuTl-1223 composites" Prog. Nat. Sci. Mater. Int. Issue 4, Vol. **25** (2015).
2. **Abdul Jabbar**, M. Mumtaz, and K. Nadeem "Noble metals (Ag, Au) nanoparticles addition effects on superconducting properties of CuTl-1223 phase", Eur. Phys. J. Appl. Phys. **69**, 30601 (2015).
3. **Abdul Jabbar**, Irfan Qasim, Khalid M. Khan, Zulqurnain Ali, K. Nadeem, and M. Mumtaz, "Synthesis and superconducting properties of $(Au)_x$/CuTl-1223 composites" J. Alloys Compd. **618**, 110 (2015).
4. **Abdul Jabbar**, Irfan Qasim, M. Waqee-ur-Rehman, Munawar Zaman, K. Nadeem, , M. Mumtaz, "Structural and Superconducting Properties of $(Al_2O_3)_y$/CuTl-1223 Composites" J. Elect. Mater. **44**, 1 (2015).
5. **Abdul Jabbar**, Irfan Qasim, M. Mumtaz, M. Zubair, K. Nadeem, and A. A. Khurram, "Suppression of activation energy and superconductivity by the addition of Al_2O_3 nanoparticles in CuTl-1223 matrix" J. Appl. Phys. **115**, 203904 (2014).
6. **Abdul Jabbar**, Irfan Qasim, Shahid A. Khan, K. Nadeem, M. Waqee-ur-Rehman, M. Mumtaz and F. Zeb "Highly coercive cobalt ferrite nanoparticles-CuTl-1223 superconductor composites" J. Magn. Magnetic Mater. **377**, 6 (2014).
7. Ghulam Hussain, **Abdul Jabbar**, Irfan Qasim, M. Mumtaz, K. Nadeem, M. Zubair, S. Qamar Abbas, and A. A. Khurram, "Activation energy and excess conductivity analysis of $(Ag)_x$/CuTl-1223 nanosuperconductor composites" J. Appl. Phys. **116**, 103911 (2014).
8. K. Nadeem, F. Naeem, M. Mumtaz, S. Naeem, **Abdul Jabbar**, Irfan Qasim and Nawazish A. Khan, "Synthesis and characterization of core-shell Ni/NiO nanoparticles/CuTl-1223 superconductor composites" Ceramics Int. **40**, 13819 (2014).
9. M. Mumtaz, S. Naeem, K. Nadeem, F. Naeem, **Abdul Jabbar**, Y.R. Zheng, Nawazish A. Khan and M. Imran "Study of nano-sized $(ZnFe_2O_4)_y$ particles/CuTl-1223 superconductor composites", Solid State Sciences **22**, 21 (2013).
10. M. Mumtaz, M. Kamran, K. Nadeem, **Abdul Jabbar**, Nawazish A. khan, Abida Saleem, S. Tajammul Hussain and M. Kamran "Dielectric Properties of (CuO, CaO_2 and $BaO)_y$/CuTl-1223 composites", Low Temperature Physics/Fizika Nizkikh Temperature **39**, 806 (2013).

LIST OF SYMBOLS AND ABBREVIATIONS

HTSCs	High-temperature superconductors
HTSC	High-temperature superconducting
LSCO	Lanthanum-based
YBCO	Yttrium-based
BSCCO	Bismuth-based
TBCCO	Thallium-based
CBSs	Cu-based superconductors
CRL	Charge reservoir layer
BCS	Bardeen Cooper Schrieffer theory
SC	Superconducting
J_c	Critical current density
T_c	Critical temperature
T_c^{mf}	Mean field critical temperature
H_c	Critical magnetic field
H_{irr}	Irreversibility field
SQUID	Superconducting quantum interference device
SEM	Scanning electron microscopy
XRD	X-ray diffraction
EDX	Energy dispersive X-ray spectroscopy
FTIR	Fourier transform infrared spectroscopy
FIC	Fluctuation-induced conductivity
FWHM	Full width at half maximum
GL	Ginzberg-Lindau
AL	Aslamazov-Larkin
LD	Lawrence-Doniach model
MT	Maki-Thompson
2D	Two dimensional
3D	Three dimensional
T*(K)	Pseudo gap temperature

T_o (K)	Crossover temperature
GB	Grain boundaries
NMI	Nonmagnetic impurity
APC's	Artificial pinning centers
BSEs	Back scattered electrons
F_L	Lorentz force
F_P	Pinning force
RCSJ	Resistively capacitively shunted junction
C_e	Electronic specific heat capacity
C_{es}	Electronic specific heat capacity in the superconducting state
C_{en}	Electronic specific heat capacity in normal state
SNS	Superconductor normal metal superconductor junction
SIS	Superconductor insulator superconductor junction

Abstract

Low anisotropic $(Cu_{0.5}Tl_{0.5})Ba_2Ca_2Cu_3O_{10-\delta}$ (CuTl-1223) phase of $Cu_{1-x}Tl_xBa_2Ca_2Cu_3O_{10-\delta}$ [CuTl-12(n-1)n]; n=1, 2, 3, ... high temperature superconducting (HTSC) family was synthesized by solid-state reaction method. Nanoparticles (NPs) were prepared separately by different techniques (i.e. co-precipitation, sol-gel, and colloidal solution methods). Different kinds and sizes of NPs such as non-magnetic metallic (Ag, Au), non-magnetic metallic oxide (Al_2O_3) and magnetic ferrite ($CoFe_2O_4$) were added with different wt.% during the final sintering process of CuTl-1223 superconducting matrix to get the required $(NPs)_x$/CuTl-1223 nanoparticles-superconducting composites. These composites were characterized by different experimental techniques such as x-ray diffraction (XRD), scanning electron microscopy (SEM), transmission electron microscopy (TEM), energy dispersive x-ray (EDX) spectroscopy, resistivity versus temperature measurements, critical current density (J_c) measurements, magnetic ac-susceptibility measurements, Fourier transform infrared (FTIR) spectroscopy etc. The experimental data were analyzed by different well established theoretical models such as Aslamazov-Larkin (AL), Lawerence-Doniach (LD) and Maki-Thompson (MT) models. It was observed that tetragonal structure and stoichiometry of the host CuTl-1223 superconducting phase remained unaltered after the addition of these NPs, which indicates about the occupancy of these NPs at the inter-granular spaces. Non-magnetic metallic NPs (Ag, Au) have improved the superconducting transport properties (T_c, J_c, etc) up to certain optimum concentration of these NPs in CuTl-1223 matrix. The improvement in the superconducting properties can be attributed to an increase in the inter-grains connectivity by healing up the inter-grains voids and pores after the addition of these NPs. The improved inter-grains connections can facilitate the carriers transport processes across the inter-crystallite sites due to their metallic nature. But the superconducting volume fraction starts to be decreased after certain optimum inclusion level of these non-magnetic non-superconducting metallic NPs, which causes the suppression of superconductivity parameters. The effects of highly coercive cobalt ferrite ($CoFe_2O_4$) nanoparticles addition on superconducting properties of CuTl-1223 matrix were also explored. The magnetic behavior of $CoFe_2O_4$ nanoparticles was determined by MH-loops with the help of superconducting quantum interference device (SQUID). The resistivity versus temperature measurements showed an increase in $T_c(0)$, which could be most probably due to improvement of weak-links by the addition of these nanoparticles. The increase of mass density with

increasing content of these NPs can also be an evidence of filling up the voids in the matrix. But the addition of these NPs beyond an optimum level caused the agglomeration and produced additional stresses in material and suppressed the superconductivity. We observed non-monotonic variation of superconducting properties after the inclusion of nano-Al_2O_3 particles, which can be associated with inhomogeneous distribution of these NPs at the grain-boundaries in CuTl-1223 matrix. But overall suppression of superconducting properties was attributed to a pair-breaking mechanism caused by reflection/scattering of carriers across these insulating nano-Al_2O_3 particles present at the grain-boundaries of the host CuTl-1223 matrix. The presence of Al_2O_3 nanoparticles at the grain-boundaries possibly reduced the number of flux pinning centers, which were present in the form of weak-links in pure CuTl-1223 superconducting matrix. The suppression of activation energy {U (eV)} may be due to weak flux pinning in the nano-Al_2O_3 particles added samples. The superconducting microscopic parameters (i.e. zero temperature coherence length along c-axis {ξc (0)}, inter-layer coupling (J), inter-grain coupling (α) etc.) deduced from fluctuation induced conductivity (FIC) analysis with the help of above mentioned theoretical models explained the experimental findings very well. For example, the increase in the values of inter-grain coupling (α) deduced from FIC analysis is a theoretical evidence of improved inter-grain coupling in the host CuTl-1223 matrix with the increased contents of these nanoparticles. We also calculated the activation energy {U (eV)} of $(NPs)_x$/CuTl-1223 nanoparticles-superconducting composites. The increase in $T_c(0)$, J_c, U (eV) etc and decrease in normal state resistivity {$\rho_{300\ K}$ (Ω-cm)} were observed after the addition Ag, Au and $CoFe_2O_4$ NPs in CuTl-1223 superconducting phase. The suppression of superconducting properties (i.e. $T_c(0)$, J_c, U (eV) etc) after the addition of Al_2O_3 nanoparticles in host CuTl-1233 superconducting matrix was observed.

Chapter 1

Introduction and Literature Review

1.1 Discovery and Historical Development of Superconductors

The phenomenon of superconductivity was discovered over 100 years ago by Heike Kamerlingh Onnes, in 1911[1]. He made the unexpected discovery that below a finite critical temperature (T_c) of $4.2K$, the electrical resistance of mercury falls to zero. Fig 1.1 shows the experimental results of mercury and platinum. To be noted, platinum does not exhibit superconducting behavior as designated by its finite resistivity as T_c approaches $0K$. In 1913 Kamerlingh Onnes was awarded the Nobel Prize in Physics, for the study of matter at low temperatures and the liquefaction of helium [2].

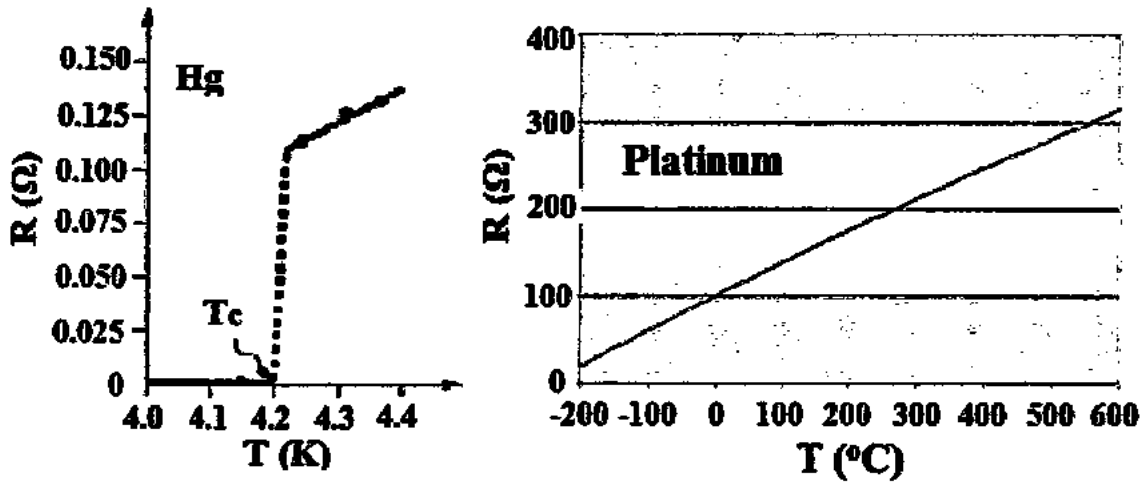

Fig. 1.1: Plots of resistance versus temperature for (a) mercury (b) platinum [2].

Discovery of superconductivity was announced in tantalum in 1928 with $T_c = 4.4K$, thorium in 1929 with $T_c = 1.4K$ and Nb in 1930 with $T_c = 9.2K$. The period of 1930 was an excruciating time of research on binary alloys. Various materials undergo a phase transition from the metallic state to the superconducting (SC) one at different values of T_c's. Conventional metals have relatively lower T_c's (i.e $T_c \leq 10$) as shown in Table 1.1. The highest value of $T_c \geq 23$ for conventional low temperature superconductors is observed in Nb_2Ge compound [3].

Table 1.1: The values of T_c's in some conventional low temperature superconductors [3].

Material	Al	Ti	Ga	Hg	In	Pb
T_c (K)	1.18	0.39	1.09	4.16	3.40	7.19
Material	V	Nb	W	V_3Si	Nb_3S_4	Nb_3Ge
T_c (K)	5.4	9.20	0.01	17.10	18.05	23.20

In1933, another property of superconductors was discovered, the Meissner effect, that is now considered a defining feature of superconductors. Meissner and Ochsenfeld [4] found that a superconductor in an applied field will exclude the magnetic flux from its interior, i.e. it becomes a perfect diamagnet. Soon after Meissner's effect, numerous other elements of the periodic table were added to the list.

Fritz and Heinz London developed a phenomenological theory of superconductivity in 1935 [5]. Although the discovery of superconductivity was made in1911, it took over 50 years to achieve a complete understanding of the microscopic mechanism. In1957, Bardeen, Cooper and Schrieffer presented a theory of superconductivity in which electrons form *Cooper pairs* through interactions of electrons and phonons usually known as the BCS theory. BCS theory explains well, the formation and flow of these pairs without scattering through the superconducting material. However, BCS theory validity is limited for the materials having T_c of $\sim 30-40K$ [6]. In 1962 Brain D. Josephson prognosticated that the supercurrent could tunnel between two superconductors dissevered by a thin ($<2nm$) insulating barrier [7]. Soon afterward, Josephson's prognostications were proved correct, and today there exist an entire field of contrivance physics predicated on the Josephson outcome. In early1986, J.G. Bednorz and K.A Muller in the IBM Zurich laboratory gives indication for the superconductivity in an oxide of lanthanum, barium, and copper at a temperature of about $30K$ and in the $La_{2-x}(Ba,Sr)_xCuO$ compounds at about $35K$ [8]. This was an important innovation in superconductivity, which marked the origination of incipient era of high temperature superconductivity and it established universal consideration in both the scientific community and the business world. Subsequently, it was found that the critical temperature was elevated to 93K with the discovery of $YBa_2Cu_3O_{7-\delta}$ ($YBCO$) by M. K. Wu and his research students in1987 [9]. It was a first discovered superconducting material above the boiling point of liquid nitrogen (i.e. 77 K). It was important

to know that liquid nitrogen was used as a refrigerant at that time. In 1988, Tl-based ($Tl_2Ca_2Ba_2Cu_3O_x$) was reported with maximum transition temperature of 125K. For this superconducting material T_c varies from 118K to 125K depending on the synthesis conditions [10]. Mercury (Hg)-based cuprate superconductor was discovered in1993 with $T_c$of 133K at atmosphere pressure [11]. In 2000, a marginal increase in the transition temperature was detected for fluorinated $HgBa_2Ca_2Cu_3O_{6+\delta}$ $(Hg-1223)$ sample $(i.e.\ T_c = 138\,\mathrm{K})$ [12]. After this revelation, further efforts were undertaken to find cuprates with higher values of T_c. A record T_c of 164K was acquired for *HgBaCaCuO* cuprates under 30 *GPa* pressure [13]. The history of the development in T_c of superconductors with year is shown in Fig. 1.2.

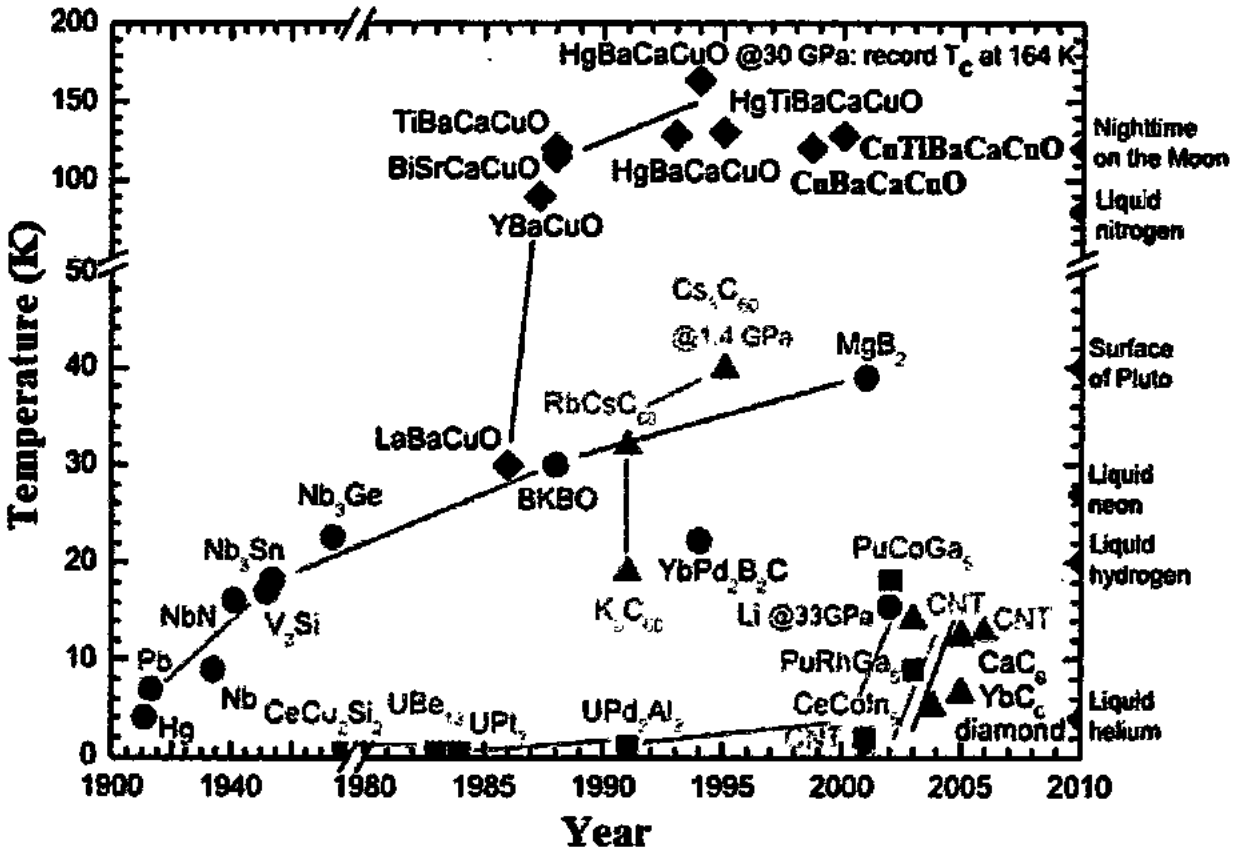

Fig. 1.2: History of superconductors with T_c versus year of discovery [14].

1.2 Types of Superconductors

It could not be said that a pure metal with zero impurities when cooled up to absolute zero will show zero resistance. However a superconducting material should show definite phase transition on reaching T_c. A real superconductor must show Meissner effect, i.e. convert from paramagnetic to diamagnetic form [15]. According to Alexei A. Abrikosv, there are two main types of superconductors named as Type-I and Type-II superconductors, respectively [16].

1.2.1 Type-I Superconductors

Type-I superconductor basically composed of metals and metalloids. The pure elements are contained in this type excluding Niobium, Vanadium and Technetium. These superconductors show a quick response to the external magnetic fields applied to them and as a result their superconducting state is suppressed at once just above H_c (critical magnetic field). Above H_c the magnetic flux penetrates the superconductor completely and the normal state is restored. This means that superconductivity can be destroyed (with a return to a normal state) not only by increasing the temperature but also by either a large enough electric current $I > I_c$ or a large enough magnetic field $H > H_c$. The critical field H_c, at which superconductivity disappears, is decreased with increasing temperature. Empirically it is established that the temperature dependence of H_c is well described by the formula [17];

$$H_c(T) = H_c(0)[1-(\frac{T}{T_c})^2] \qquad 1.1$$

The type-I superconductors are soft and display diamagnetic behavior. Their behavior is shown in the Fig. 1.3 (a).

1.2.2 Type-II Superconductors

In 1930, first time type-II group of superconductors was prepared with the alloy and metallic compounds. Their response to applied magnetic fields is quite different from type-I superconductors. These superconductors have two critical field values of applied field i.e H_{c1} and H_{c2}, which are named as lower critical field and upper critical field, respectively. However at H_{c1}, the magnetic flux abruptly penetrates into sample and above H_{c1}, the magnetization consistently increases up to H_{c2}. Above H_{c2}, the material behaves as normal superconductors and shows no diamagnetism anymore [19, 20]. Superconductors in which the mixed state exists

in the intermediate region $H_{c1} < H_c < H_{c2}$, was called by Abrikosov [16] as type II superconductors. In comparison, these are preferred over Type-I superconductors due to their over tolerance to applied magnetic field 'H'. Their behavior is also shown in the Fig. 1.3 (b).

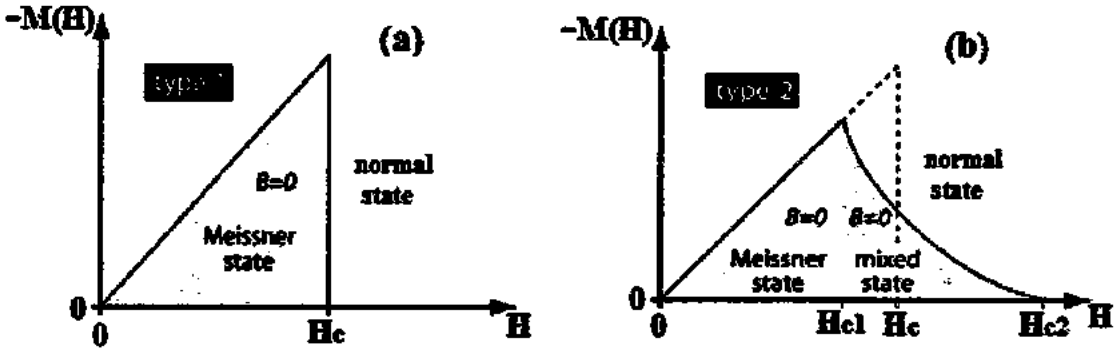

Fig. 1.3: Type-I and type-II superconductors in applied magnetic field [18].

According to the Meissner effect, far inside the superconductor, the magnetic induction '$\vec{B}$' is zero, while outside it $\vec{B} = \vec{H}$. The magnetic induction $\vec{B}$ and the magnetic field $\vec{H}$ are related to each other by the well-known expression $\vec{B} = \vec{H} + 4\pi\vec{M}$; where $\vec{M}$ is the magnetization of the superconductor. From electrodynamics, the change in the internal energy of a system arising from a small change in the magnetic induction at constant volume of the system is given by;

$$dU = TdS + \frac{\vec{H}}{4\pi}d\vec{B} \qquad 1.2$$

where 'S' is the entropy density, 'T' is temperature and '$\vec{H}$' is the magnetic field.

Since the Helmholtz free energy density 'F' is not continuous at the critical magnetic fields, while the Gibbs free energy density is continuous at critical magnetic fields. As we know that the Gibbs free energy of a gas is $G = U + PV - TS$, where P and V are the pressure and volume of the gas. Replacing P and V accordingly by $-\vec{H}/4\pi$ and $\vec{B}$ [21], we obtain the Gibbs free energy of the superconductor

$$G = U - TS - (1/4\pi)\vec{H}\vec{B} = F - (1/4\pi)\vec{H}\vec{B} \qquad 1.3$$

By using Eq. 1.2, the differential of the Gibbs free energy is obtained as;

$$dG = -SdT - B\frac{dH}{4\pi} \qquad 1.4$$

Type-I superconductors exhibit a complete Meissner effect up to the thermodynamic critical magnetic field H_c, above which they become normal metals. When the magnetic field penetrates

the surface layer of a type I superconductor, an induced current arises which, according to Lenz's law, generates a magnetic field in the direction opposite to that of the external field. At $H < H_c$, the magnetic flux lines are expelled completely from the interior of the superconductor. When taking into account that $B = 0$ at $H < H_c$ and $B = H$ at $H > H_c$, by taking the integration of Eq. 1.4 at constant T, expression becomes;

$$G(T) = G(T,0) - \frac{1}{4\pi}\int_{H_c}^{H} \vec{B}\, d\vec{H}$$

$$= G(T,0) - \frac{1}{8\pi}\left(H^2 - {H_c}^2\right) \quad for \quad H > H_c \qquad 1.5$$

and

$$G(T,H) = G(T,0) \quad for \quad H < H_c \qquad 1.6$$

From the above expression, it is clear that $G\,(T,H)$ is continuous at $H = H_c$. Initially type-II superconductors expel all the magnetic field lines out and demonstrate the Meissner effect (i.e., $\vec{B} = 0$ inside the superconductor). In the region $H_{c1} < H > H_{c2}$, the magnetic induction $\vec{B} < \vec{H}$, the normal and superconducting phases coexist. This region is known as the Abrikosov mixed state [16].

1.3 Different Properties of Superconductors

Superconductivity is one of most unique and intriguing phenomena in nature. This phenomenon was discovered first in simple metals and then in inter-metallic compounds. The SC behavior of these materials is closely tied to their electrical, magnetic, thermal and other properties, which are essentially different in the normal and SC states. A superconductor is a material which can carry an electrical current without any resistance. Conventional superconductors lose their resistivity at low enough temperatures and their normal state resistance is restored as the temperature exceeds critical value 'T_c'. The SC behavior of simple metals and alloys depends on other important parameters besides 'T_c', namely, the critical magnetic fields (H_c, H_{c1} and H_{c2}) and the critical current density '(J_c)'. Many of the properties of conventional superconductors can be understood by standard Bardeen-Cooper-Schrieffer (BCS) theory [6], which assumes that the electrons responsible for superconductivity are paired with antiparallel spins and the weak electron-phonon interaction binds electrons into the Cooper pairs. The SC state of conventional superconductors has several characteristic properties.

1.3.1 Electromagnetic Properties

The first characteristic feature of SC state is that the flow of the electronic current electrons below T_c is resistanceless, i.e superfluid. Another fundamental property of conventional superconductors is their ability to expel a magnetic field completely from their interior below T_c. The complete expulsion of the magnetic field lines from a superconductor is called "*Meissner effect*" as shown in Fig. 1.4 [4].

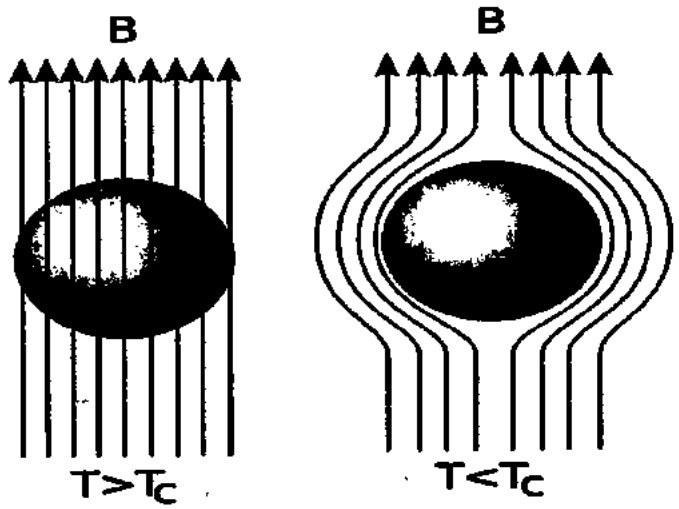

Fig. 1.4: Schematic diagram of Meissner effect [15].

It means that the superconductor exhibits perfect diamagnetism and the magnetic induction $\vec{B}$ inside the superconductor is zero.

The magnetic susceptibility for the superconducting material is given by

$$\chi = -\frac{1}{4\pi} \qquad 1.7$$

In the mixed state, the magnetic flux penetrates the superconductor in the form of a regular array of flux lines which behaves as magnetic flux tubes, each carrying a flux quantum "$\phi_o = -\frac{h}{2e}$".

The effect of magnetic flux quantization in units of 'ϕ_o' was predicted first by F. London [22] and observed then experimentally by Deaver and Fairbank [23] and by Doll and Näbauer [24]. The SC currents circulate around the core of the normal tubular lines and the circulating currents form Abrikosov's vortices inside these tubes. The vortices quantized in units of ϕ_o, form a

peculiar vortex lattice similar to a crystal lattice. According to the Silsbee's rule [25], the critical current creating the critical magnetic field 'H_c' around the SC wire is given by

$$I_c = 2\pi r_o H_c \qquad 1.8$$

where r_0 is the radius of the superconducting wire.

1.3.2 Thermal Properties

The most important and distinctive property of the SC state of conventional superconductors is the behavior of their electronic specific heat C_e below T_c as shown in Fig. 1.5. The total specific heat 'C_v' of the superconductor at constant volume is defined as the sum of the lattice and electronic specific heats. For the normal and SC states of simple metals, the specific heat C_v at $T \ll \theta_D$ may be expressed as

$$C_{vn} = C_{en} + \gamma_D T^3 \qquad 1.9$$

and

$$C_{vs} = C_{es} + \gamma_D T^3 \qquad 1.10$$

where C_{en} and C_{es} are the electronic specific heats of the superconductor in the normal and SC states, respectively.

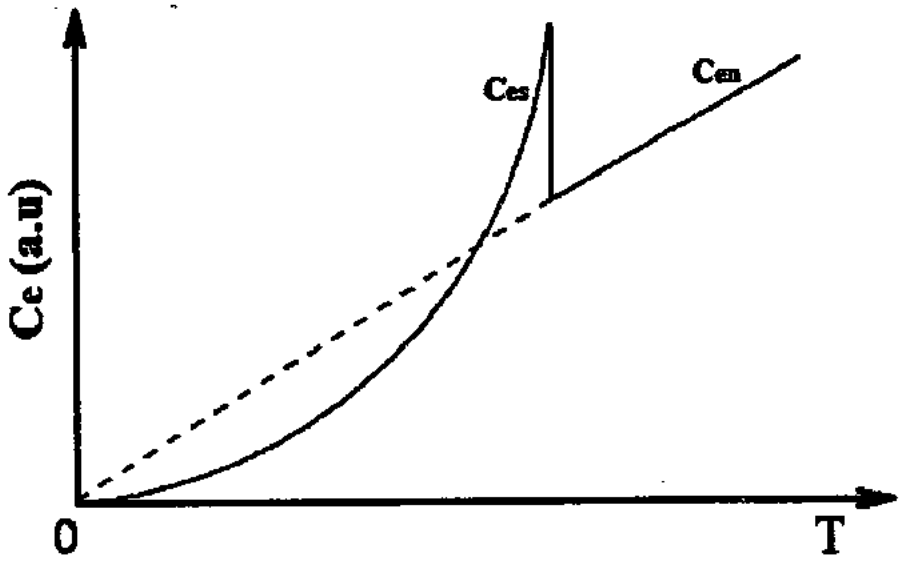

Fig. 1.5: Schematic diagram of the electronic specific heat capacity (C_e) on temperature dependence of conventional superconductors in the superconducting state (C_{es}) as well as in normal state (C_{en}) [3, 26].

The quantity of C_{es} can also be determined from the following relation

$$C_{es} - C_{en} = C_{vs} - C_{vn} \qquad 1.11$$

The observed electronic part of specific heat C_{es} for the SC state of some metals is approximately proportional to T^3 [26]. Whereas, the temperature dependence of C_{es} observed in other superconductors (below 'T_c') is well described by the exponential law

$$C_{es}(T) = \gamma_s \exp\left(-\Delta/k_B T\right) \quad 1.12$$

where γ_s is the factor of proportionality, 'Δ' is an energy gap in the excitation spectrum of superconductors. Note that the origin of the deviation of $C_{es}(T)$ from the simple exponential law still remains to be understood. This means that the ground and excited states of the superconductor is separated by 'Δ'. However, over many years (i.e., before the appearance of a new approach to superconductivity [27, 28]), the T^3 temperature dependence of C_{es} in some superconductors remained as rather poorly understood. Eliashberg supposed [29] that a small additional term proportional to T^3 enters into the expression for C_{es} and it is associated with the possible lattice contribution to the difference '$C_{vs} - C_{vn}$'. It is unlikely that such a small additional term in $C_{es}(T)$ can provide a quantitative explanation for the T^3-behavior of $C_{es}(T)$ observed in several conventional superconductors.

1.3.3 Thermodynamics of Superconductors

Metals in the normal and SC states have not only different electrical conductivities but also have different values of thermodynamic parameters. Since the normal and SC states of metals represent different thermodynamical phase of matter. To evaluate the thermodynamics of superconductors, we first of all consider the change of their magnetic properties at the transition from the normal to the SC state. The free energy of the system in the external magnetic field is given by

$$F = U' - TS \quad 1.13$$

where $U' = U - MH$, U is the internal energy of the superconductor at $H = 0$, S is the entropy.

A small change in energy U' arising from a small change in the magnetic field at constant volume of the system is given by,

$$dU' = TdS - MdH \quad 1.14$$

The differential of the free energy is given by,

$$dF = -SdT - \vec{M}dH \quad 1.15$$

At a fixed temperature, we have,

$$F(T,H) = F(T,0) - \int_0^H \vec{M} dH \qquad 1.16$$

In the normal state of the superconductor, the free energy F_n does not depend on H, so that $F_n(T,H) = F_n(T,0)$. In the SC phase, the magnetization is given by $M = -H/4\pi$.

Eq.1.16 transformed as;

$$F_s(T,H) = F_s(T,0) + \frac{H^2}{8\pi} \qquad 1.17$$

The thermodynamic equations (1.16) and (1.17) can also be applied to the type II superconductors, for which the value of H_c characterizes any auxiliary quantity or average critical magnetic field. Thus, this thermodynamical approach is very important to find relationship between the magnetic and thermal properties of superconductors [30].

1.3.4 Isotope Effect

Superconductivity after its discovery in simple metals remained obscure and mysterious phenomenon for a long time. Starting from the early 1950s, there have been great advances in understanding many key features of conventional superconductors. In particular, theoretical studies carried out by Fröhlich in 1950 [31] led to the prediction of the important role of the electron-phonon interaction in superconductivity. Fröhlich predicted important property of the superconductors, namely, the dependence of the SC transition temperature T_c on the isotope mass 'M' of the atomic nuclei of the superconductor. This so-called isotope effect was also discovered experimentally in 1950 by Maxwell [32] and Reynolds [33]. It was found that the mass of the isotopes is related with the SC transition temperature T_c as follows

$$M^{\alpha} T_c = constant \qquad 1.18$$

where α is the isotope effect exponent.

The isotope mass determines the frequency of lattice vibrations, $\omega \sim M^{-1/2}$. Experimentally, it was found that for most simple metals, $\alpha = 0.5$. Hence, it follows that superconductivity in metals is caused by the electron-phonon interaction. This discovery of the isotope effect allowed for the right starting point in developing a successful theory of superconductivity, commonly known as the BCS theory in which superconductivity results from the Cooper pairing mediated by the electron-phonon interaction. The BCS theory yields the excellent result for the isotope effect exponent $\alpha = 0.5$ in conventional metals. But the observed values of $\alpha = 0 - 0.1$ in transition metals (Ru, Os, Zr, U) are much smaller than the value of

$\alpha = 0.5$ or even negative $\alpha = -0.015$ (for Ir) [34] and $\alpha = -5$ (for U) [35]. These features of conventional superconductors cannot be understood in terms of the standard BCS theory.

1.3.5 Optical Properties

SC state of conventional superconductors is characterized by the existence of an energy gap in their electronic spectrum and superconductivity can be destroyed by long-wave irradiation. The presence of energy gap between the ground and excited states of superconductors was conjectured first theoretically by F. London [34, 36]. The determination for the possibility of the destruction threshold of superconductivity by using the electromagnetic radiation was already discussed in 1930s [34, 37]. At that time, the energy gap in the excitation spectrum of superconductors was not observed experimentally due to absence of the appropriate technique for absorption measurements of low frequency radiation. The possibility of absorption measurements of electromagnetic radiation by superconductors in the region of the frequency $h\upsilon \sim k_B T_c$ appeared only in the middle of the 1950s [38]. Glover and Tinkham [39] succeeded in reaching the far-infrared region of the electromagnetic spectrum (i.e., the threshold of the low-frequency electromagnetic radiation for destruction of superconductivity) and observed an energy gap in the electronic spectrum of the superconductor. At the same time, Bardeen, Cooper, and Schrieffer proposed a microscopic theory of superconductivity. The BCS theory accounted for many of the experimental observations; in particular, the existence of the energy gap $E_g = 2\Delta$ between the ground and excited states of electrons. According to this theory, the electron-phonon interaction binds electrons into Cooper pairs and the binding energy of these pairs is manifested as a gap in the excitation spectrum of superconductors. Later, many experiments confirmed the presence of such a BCS energy gap in conventional superconductors. For instance, the clear absorption edges were observed directly at frequencies corresponding to the width of the energy gap in superconductors [40, 41]. Nevertheless, in-gap states and precursor peaks beyond the absorption edges or above the gap structures [42] were also observed in conventional superconductors. Apparently, such unusual features of these conventional superconductors represent open questions waiting for an adequate physical explanation [28], by going beyond the scope of the standard BCS theory. Another more simple and informative method of experimental detection of gap like features in superconductors is the measurement of the tunnel current flowing across the superconductor-insulator-metal (or superconductor) contact (Fig. 1.6).

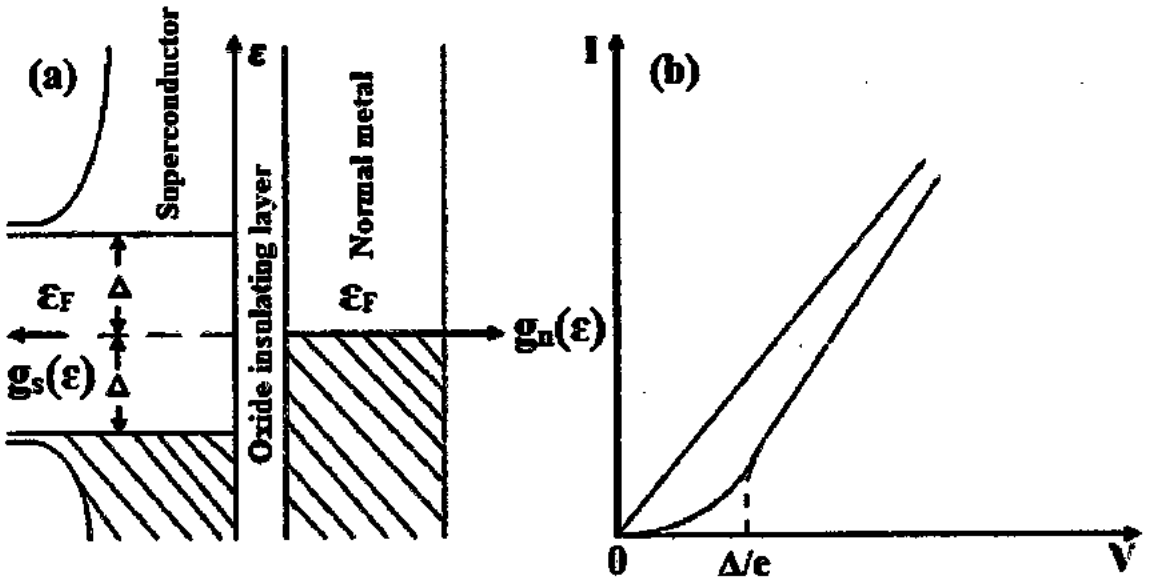

Fig. 1.6: The density of states as a function of energy (a) for current-voltage characteristics (b) for tunneling across superconductor-oxide insulator-normal metal junction at $T = 0$ [42].

In 1960, Giaeyer observed [43] that the current voltage characteristics of sandwiches consisting of a superconductor and either another superconductor or a normal metal, separated by a thin oxide insulating layer, were nonlinear, and that the nonlinearity is indicative of the existence of an energy gap in the excitation spectrum of the superconductor. At $T = 0$, the tunnel current is equal to zero up to a threshold voltage $V = {}^{E_g}/_{2e} = {}^{\Delta}/_{e}$. At $V \geq {}^{\Delta}/_{e}$, the tunnel current appears due to the destruction of Cooper pairs and grows quickly approaching to the Ohmic value with increasing voltage (Fig. 1.6b).

At $T > 0$, the weak tunnel current appears even at low voltage due to the thermal excitation of some electrons from the states below $\varepsilon_F - \Delta$ to the states above $\varepsilon_F + \Delta$. The tunneling across superconductor-oxide insulator-superconductor junction (Fig. 1.7) can be explained in analogous manner.

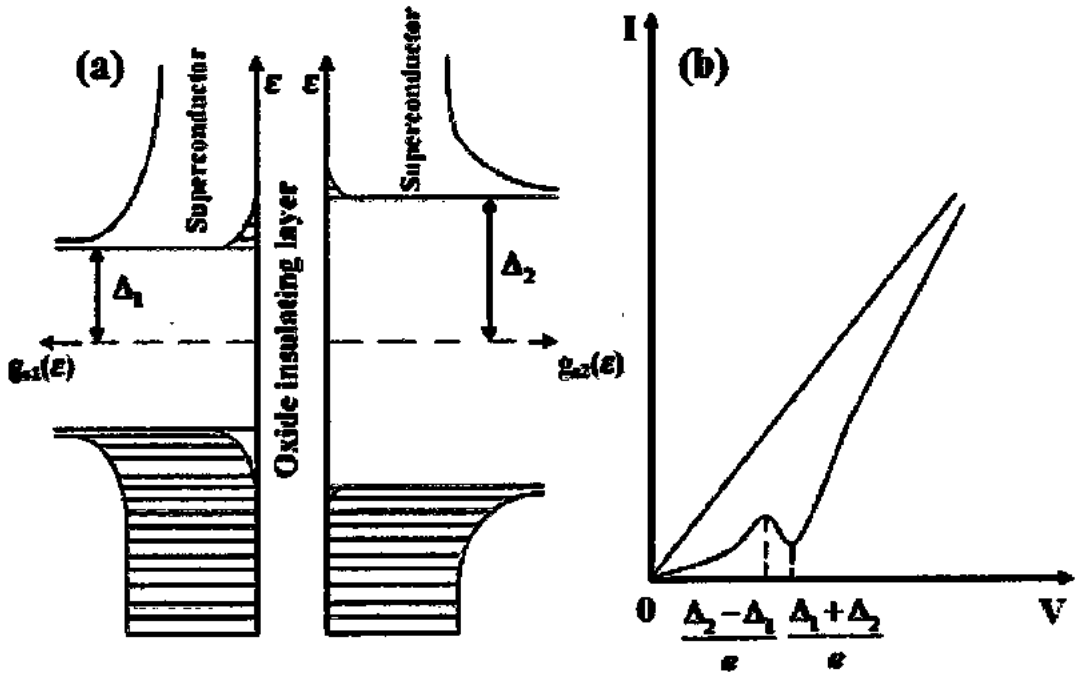

Fig. 1.7: The density of states as a function of energy (a) for the current-voltage characteristics (b) for tunneling across superconductor-oxide insulator-superconductor junction at $T \neq 0$ [43].

1.4 Phenomenological Theories of Superconductivity

Many properties of superconductors described in previously can be understood in terms of phenomenological theories of superfluidity and superconductivity, which are based on the fundamental works of Landau, Gorter and Casimir, two brothers F. London and H. London, Ginzburg and Landau, Pippard, Abrikosov, Saint-James and De Gennes and others [6, 44, 45]. Actually, the phenomenon of superconductivity discovered by Kamerlingh Onnes [1] is very similar to superfluidity in liquid helium (^{4}He), discovered by Kapitza [46]. These two remarkable phenomena have one characteristic feature in common; the superconductivity is a frictionless flow of charged electrons through the crystal lattice, whereas the superfluidity is a frictionless flow of helium atoms through thin capillaries. The successful phenomenological theory of superfluidity was formulated by Landau [47], who derived the criterion for superfluidity. Any quantum fluid including also electron fluid will be a superfluid when the fluid flow velocity does not exceed some critical value determined by the Landau criterion. Therefore, superconductivity can be explained as the superfluidity of the electron liquid in solids. In 1934, Gorter and Casimir [48] proposed 'two-fluid model' in which the electron gas within the superconductor is viewed as mixture of two fluids; one fluid behaves like a normal fluid and the second fluid is a

superfluid that carries the supercurrent. In 1935, F. London and H. London [49] derived their famous equations using the two-fluid model and Maxwell's equations. They gave an important phenomenological description of superconductivity. London's phenomenological theory was later generalized by Ginzburg and Landau (GL) [50] and by Pippard [51], who introduced independently the concept of a coherence length 'ξ', which is different from the London penetration depth 'λ_L' and characterizes the spatial change of the SC order parameter. The starting point of the GL theory was the idea of the Landau's theory of second order phase transitions (without latent heat) and the introduction of the concept of a complex order parameter 'ψ', which is allowed to vary in space. This theory provides a good phenomenological description of superconductivity near the SC transition temperature 'T_c'. Further, the GL theory was developed by Abrikosov [16] and by Saint-James and De Gennes [52], who predicted the existence of the mixed state (or vortex state in the type-II superconductors) and the phenomena of surface superconductivity, respectively. Abrikosov subdivided all superconductors into the two classes called as the type-I and type-II superconductors, using his own phenomenological theory and the concept of the surface energy of superconductors.

1.4.1 Two-Fluid Model

Long before the BCS theory [6], the most successful attempt to explain the known properties of superconductors was the Two-Fluid Model. This model was developed by Gorter and Casimir in 1934 [48]. In this model they assumed the conduction electrons were separated into a superfluid electron group with electron density n_s, and a normal electron group with an electron density n_n. The total electron density is $n = n_s + n_n$. For best explanation of the thermal properties of superconductors, the fraction of n_s/n_n should be chosen to have the form,

$$n_s/n_n = 1 - \left[T/T_c\right]^4 \qquad 1.19$$

where T_c is the critical temperature.

1.4.2 Landau Criterion for Superfluidity

A quantum fluid flowing with velocity $v < v_c$ (where v_c is the critical flow velocity of the fluid) becomes superfluid. Landau formulated [47] that under the condition $v < v_c$ the quantum fluid should flow as a superfluid without any friction and the superfluidity is destroyed at $v > v_c$. For the processes which may lead to the destruction of superfluidity (or superconductivity), consider an excitation-free superfluid flowing through a long tube (or crystal

lattice) with velocity v relative to the immobile tube (or laboratory system of coordinates) at $T = 0\ K$. To go over into the system of reference in which the superfluid is at rest, the walls of the tube are moving with respect to the superfluid with velocity $-v$. When the flow velocity of the fluid approaches to v_c the drag friction between the tube and the superfluid arises. Therefore, the viscosity of the fluid will appear and the creation of an excitation in the superfluid becomes possible. Suppose that a single excitation with energy $\varepsilon(p)$ and momentum p appeared in the superfluid. Because of the recoil, the velocity of the tube is then changed and become equal to $-v$. According to the principles of conservation of energy and momentum, one can write

$$\frac{Mv^2}{2} = \frac{Mv_1^2}{2} + \varepsilon(p) \tag{1.20}$$

and

$$-M\vec{v} = -M\vec{v_1} + \vec{p} \tag{1.21}$$

where M is the mass of the tube.

Combining (1.20) and (1.21), we obtain,

$$\varepsilon(p) + \vec{p}\vec{v} + \frac{p^2}{2M} = 0 \tag{1.22}$$

from which it follows that,

$$\varepsilon(p) + \vec{p}\vec{v} = \varepsilon(p) + pv\cos\theta < 0 \tag{1.23}$$

where θ is the angle between $\vec{p}$ and $\vec{v}$.

The condition for the appearance of an excitation in the superfluid is written as

$$v > \frac{\varepsilon(p)}{p} \tag{1.24}$$

The minimum value of v at which an excitation can appear in the superfluid is equal to

$$v_c = min\left[\frac{\varepsilon(p)}{p}\right] \tag{1.25}$$

If $v < v_c$, the excitation cannot be appeared in the superfluid, which will flow through a tube or a crystal lattice with any dissipation. Thus, the Landau criterion for superfluity is written as

$$v < v_c = min\left[\frac{\varepsilon(p)}{p}\right] \tag{1.26}$$

The most extreme possible value of the function $\varepsilon(p)/p$ can be determined as:

$$p\frac{d\varepsilon(p)}{dp} = \varepsilon(p) \tag{1.27}$$

These relations presented are also valid for $T \neq 0$. The Landau theory of superfluidity is based on the excitation spectrum of liquid ^{4}He and the Eq. 1.27 has two solutions corresponding to different regions of the spectrum. One solution corresponds to the origin and all points of the phonon region of the spectrum, whereas the second solution corresponds to the point near the minimum in the roton region.

1.4.3 London Equation and Penetration Depth

Gorter and Casimir put forward the idea of "two-fluid model" in 1934 [48] and developed the early phenomenological theory of superconductivity based on this model. Maxwell's equations cannot explain why the magnetic field **B** is zero inside the superconductor (Meissner's effect).

In order to understand the behavior of a superconductor in an external electromagnetic field (the Meissner's effect), F. London and H. London [49] using the Gorter-Casimir two-fluid model postulated their new well-known equation:

$$B + \frac{m}{n_s e^2} \nabla \times j_s = 0 \qquad 1.28$$

where m is the mass of an electron, n_s is the local density of superconducting carriers and j_s is the field-induced supercurrent density. This equation is referred to as the 'Second London equation'. This equation is commonly cited with the 'First London equation' as:

$$\frac{\partial}{\partial t} j_s = \frac{n_s e^2}{m} E \qquad 1.29$$

where E is the electric field.

The thermodynamic properties of superconductors can be described by the following equations;

$$j = j_n + j_s \text{ where } j_n = \sigma E$$

$$\frac{1}{\mu_0 \lambda_L^2} B + \nabla \times j_s = 0 \qquad 1.30$$

$$\frac{\partial}{\partial t} j_s = \frac{1}{\mu_0 \lambda_L^2} E$$

where σ is the conductance of the electron. The variable λ_L is called the London penetration depth (λ_L is in the order of 10 nm) and is given by:

$$\lambda_L = \sqrt{\frac{m}{\mu_0 n_s e^2}} \qquad 1.31$$

However, London's equations are only a phenomenological theory developed to explain some experimental results. The estimated λ_L is much lesser than the experimental results for certain conventional superconductors. To solve these discrepancies, in 1950 Pippard introduced non-

local effects into the London equations. He introduced a coherence length 'ξ_0' and the effective coherence length 'ξ', which limit the spatial extent of some quantities like n_s. From an uncertainty-principle, Pippard estimated the coherence length to be;

$$\xi_0 = a\frac{\hbar v_F}{2\pi k_B T_c} \quad 1.32$$

where a is a constant with a length scale of one, k_B is the Boltzmann constant, v_F is the Fermi velocity and T_c is the critical temperature. Another relation for ξ is:

$$\frac{1}{\xi} = \frac{1}{\xi_0} + \frac{1}{al} \quad 1.33$$

where a is a constant of the order of unity. For a pure superconductor, $\xi = \xi_0$.

In particular, Pippard's theory yields the penetration depth:

$$\lambda = \lambda_L \left[\frac{\xi_0}{\xi}\right]^{1/2} \quad \text{when } \xi \ll \lambda \quad 1.34$$

$$\lambda = \left[\frac{\sqrt{3}}{2\pi}\xi_0\lambda_L^2\right]^{1/2} \quad \text{when } \xi \gg \lambda \quad 1.35$$

Table 1.2: The values of superconducting carrier density (n_s) and London penetration depth (λ_L) for some superconducting materials [3].

Metal	Al	Ga	In	Zn	Cd	Pb	Sn
n_s 10^{22} cm^{-3}	1.542	0.267	0.298	0.460	0.209	0.521	0.525
λ_L (0), Å	521	785	1140	723	990	1034	824
λ_L^{exp}, Å	500	---	640	---	1300	390	510

1.4.4 Ginzburg-Landau (GL) Theory

The Ginzburg Landau theory basically correlated the superconductivity and mean field theory of thermodynamics state. The most vigorous appearance is that it can be used up to original mean field limit, so it introduced the effect of thermal fluctuation. This fluctuation is mostly negligible in case of conventional low T_c superconductor. This theory helps to describe type-I superconductors without going through microscopic details. The target of GL theory is superconducting electrons rather than the excitation process. The GL theory explain that the free energy of superconductors near superconducting transition can be determined in terms of complicated order parameter (Ψ). They further introduced that 'Ψ' can be asserted

with Gibbs free energy in the proximity of transition temperature. Equation that comparing all parameters can be expressed as;

$$F = F_n + \alpha|\Psi|^2 + \frac{\beta}{2}|\Psi|^4 + \left|\frac{1}{2m}(-i\hbar\nabla - 2eA)\Psi\right|^2 + \frac{|B|}{2\mu_0} \quad 1.36$$

where α and β treated as phenomenological parameters, F_n is Gibbs free energy in normal phase, e is charge of an electron, m is effective mass, A is magnetic vector potential and B is magnetic field. By taking derivative of free energy to find the solution, one can get GL equations as:

$$\alpha|\Psi| + \beta|\Psi|^2 + \frac{1}{2m}(-i\hbar\nabla - 2eA)^2\Psi = 0 \quad 1.37$$

$$j = \frac{2e}{m}Re\{\Psi^*(-i\hbar\nabla - 2eA)\Psi\} \quad 1.38$$

where j is the electrical current density without any dissipation and Re shows the real part, while Eq. 1.38 showed the relation for 'Ψ' in the range of applied magnetic field [50, 53].

In the absence of magnetic field, the value of equilibrium is represented by (Ψ_0), which tells that an external magnetic field penetrates the surface of superconductor [50].

The ratio $K = \frac{\lambda}{\xi}$ is called GL parameter,

where,

$$0 < K > {}^1/_{\sqrt{2}}, \quad \text{for type-I superconductors} \quad 1.39$$

and

$$K > {}^1/_{\sqrt{2}} \quad \text{for type-II superconductors} \quad 1.40$$

1.4.5 Brief Description of BCS Theory of Superconductors

The idea about the BCS theory was given by John Bardeen, Leon Cooper and Robert Schrieffer in 1957. This theory explains the electron pairing through electron-phonon interaction. It is intrinsically theoretical picture of type-I superconductors. When electron passes through the lattice, it distorts the structure. The second electron gets twist to pair with first electron to reduce the energy of system. This coupling of electrons take place in lattice and these pairing electrons are called Cooper pairs as shown in Fig. 1.8.

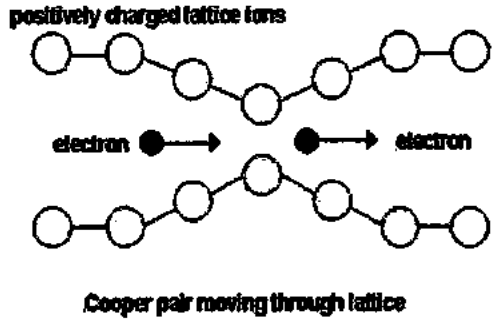

Fig. 1.8: Schematic picture is showing pairing of electrons in deformed lattice [54].

Furthermore, this theory also reveals that only electrons near Fermi level take part in Cooper pair formation. Here it is worth mentioning that pairs carry less energy than the band gap energy. But once Cooper pairs energy exceeds band gap energy, Cooper pairs cease to exist, which ultimately destroys superconducting state [6, 54, 55].

1.5 Josephson Effect

A Josephson junction is made up of two superconductors which are separated by a thin layer of a normal metal or insulating material. These coupling medium are known as SNS junction and SIS junction respectively.

In 1962, British Physicist Brain D. Josephson predicted that a zero-voltage supercurrent could flow between two superconducting materials separated by a thin tunnel barrier. The junction between two superconductors is weak enough to allow a slight overlap of the electron pair wave function of the two superconductors. Then the electron pairs can tunnel between the close superconductors even without any applied potential difference. This effect was firstly observed by Anderson and Rowell in 1964 [56, 57].

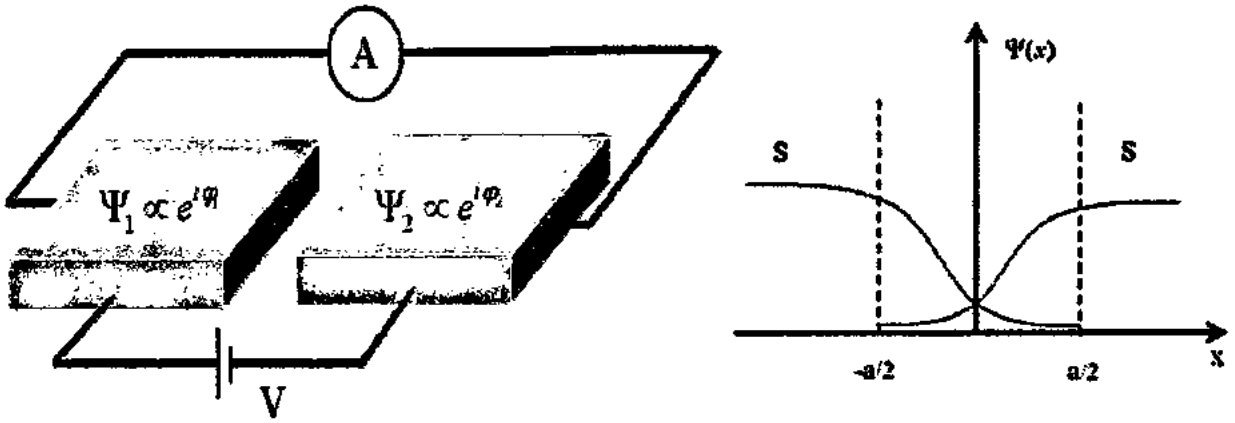

Fig. 1.9: Josephson Effect

The common behavior either in SIS or SNS junction can be expressed by Eq. 1.41 and Eq. 1.42 given below;

$$I_s = I_c \sin(\Delta\varphi) \tag{1.41}$$

where I_c is the critical current of the junction and '$\varphi = \varphi_2 - \varphi_1 - \frac{4\pi e}{h}\int_1^2 A.dl$' is gauge invariant phase, where 'A' is the vector potential while φ_1 and φ_2 are the phases of superconducting parameters. This is termed as the dc-Josephson effect. If across the junction, a potential difference 'V' is applied then φ (time-evolving phase difference) becomes:

$$d(\varphi)/_{dt} = 4\pi eV/_h \tag{1.42}$$

Between the two superconducting electrodes, flow of current will be kept constant without applying voltage, which is known as the ac-Josephson current. From above both equations (Eq. 1.41 and 1.42), if V (applied voltage) is constant, φ will linearly increase with time, which shows I_s will oscillate with frequency;

$$\nu = 2eV/_h \tag{1.43}$$

This is known as ac-Josephson effect.

By combining Eq. 1.41 and 1.42, the coupling energy stored in a Josephson junction can be integrated as;

$$E = \int IVdt = -\frac{hI_c}{4\pi e}\cos(\varphi) = E_J\cos(\varphi) \tag{1.44}$$

$$E_J = (h/_{4\pi e})I_c \tag{1.45}$$

Proximity effect and RSJ model

Cooper pairs in a SNS Josephson junction can diffuse into the normal metal from the adjacent superconductors [58]. Some superconducting properties are extended into the normal metal across the boundary, which is called the proximity effect. A Josephson junction whose coupling is established on the proximity effect is called a proximity-coupled junction.

The proximity effect enables the junction to have a larger gap distance between the superconductors. Generally compared to a SIS tunnel junction a proximity-coupled SNS junction has low resistance, nearly zero capacitance and a strongly temperature-dependent critical current. The temperature dependence of the critical current of a SNS junction was derived by DeGennes [59].

$$I_c = I_o(0)\left[1-\frac{T}{T_c}\right]^2 e^{-\frac{d}{\xi_n(T)}} \quad 1.46$$

where T_c is the superconductor transition temperature, d is the gap size and ξ_n is the temperature dependent normal metal coherence length, a key parameter characterizing a proximity coupled SNS junction. It describes the decay length scale of the order parameter in the normal metal. The behavior of the coherence length shows two different formats depending on limit chosen to describe the junction. If the junction is in the clean limit (mean free path $l \gg \xi_n$) then the 'ξ_n' is described as;

$$\xi_n = a\frac{\hbar v_F}{2\pi k_B T_c} \quad 1.47$$

In the dirty limit ($l \ll \xi_n$), ξ_n is given by DeGennes as;

$$\xi_n(T) = \left[\frac{\hbar v_F l}{12\pi^2 k_B T}\right]^{1/2} \quad 1.48$$

where v_F is the Fermi velocity for the normal metal.

The realistic description of the Josephson junction is called the Resistively and Capacitively Shunted Junction model, known as the RCSJ model [60]. RCSJ model may be the most successful and widely used one to describe the dynamics of a Josephson Junction. Most of the numerical simulation results have been verified by experiments. In addition to the supercurrent I_c, a real Josephson junction may also carry the normal current 'I_n' from the resistance and the displacement current Id due to the presence of junction capacitance. The equivalent circuit of this model is illustrated in Fig. 1.10.

The RCSJ circuit is composed of three elements.

1) An ideal Josephson junction.

2) A capacitor which takes into account the capacitance of the Josephson junction. This element is contributed by two metal surfaces of the junction, the effects of the barrier and any stray capacitor from the substrate.

3) A resistor with the normal resistance of the junction 'R'.

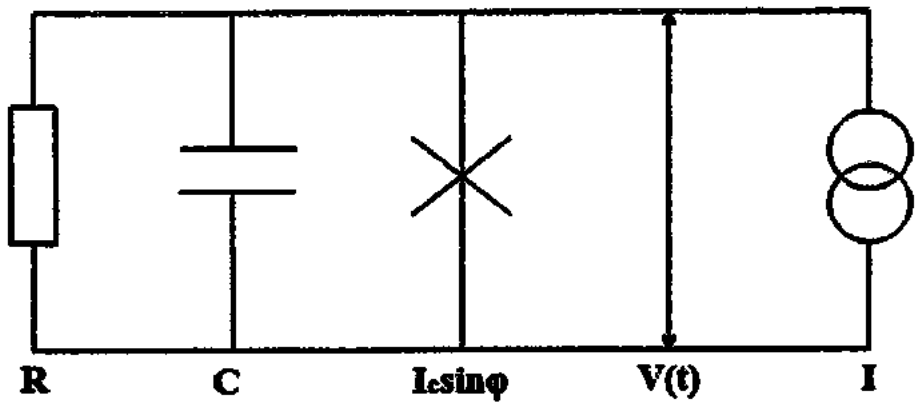

Fig. 1.10: Equivalent circuit of the Resistively and Capacitively Shunted Junction model (RCSJ model), the cross indicates the Josephson junction.

Since they are in parallel, according to Kirchhoff's law, the total current in this circuit is the sum of all the three;

$$I(t) = I_c \sin(\varphi) + C\frac{dV}{dt} + \frac{V}{R} \qquad 1.49$$

where the effect of thermal noise is neglected.

At finite temperatures, current from thermal noise also exists in the junction. However the result from the above equation is good enough to describe the junction, considering finite temperature effects only smear the results and do not alter any major results in qualitative way.

Using Eq. 1.42, the total current can be expressed in terms of the phase differences;

$$I(t) = I_c \sin(\varphi) + \frac{hC}{4\pi e}\frac{d^2(\varphi)}{dt^2} + \frac{h}{4\pi eR}\frac{d(\varphi)}{dt} \qquad 1.50$$

To obtain Eq. 1.50, there are two assumptions; R is independent of V & φ, while I_c is independent of V. By introducing the dimensionless parameters [61, 62] $\tau = \omega_p t$ and

$$\omega_p = \sqrt{\frac{4\pi e I_c}{hC}} \qquad 1.51$$

$$Q = \omega_p RC \qquad 1.52$$

Eq. 1.50 becomes as;

$$\frac{I(t)}{I_c} = \sin(\varphi) + \frac{d^2(\varphi)}{d\tau^2} + \frac{1}{Q}\frac{d(\varphi)}{d\tau} \qquad 1.53$$

where ω_p is called plasma frequency of the junction and Q is the qualify factor. Eq. 1.50 is also an equation of the motion for a 'particle' with mass $M_\varphi = (\hbar/2e)^2 C$ moving along φ axis in a potential;

$$V(\varphi) = -E_J Cos(\varphi) - [\hbar I/2e]\varphi \qquad 1.54$$

where E_J is coupling energy in Eq. 1.45. $V(\varphi)$ is also called the tilt washboard potential.

The motion of this "particle" can be classified as "underdamped" or "overdamped" depending on the value of C. When C is small and $Q \ll 1$ (overdamped), this equation is equivalent to the equation of motion for a forced pendulum if the capacitance is chosen to be zero. The RSJ model is best choice for overdamped junctions. In contrast, for a finite capacitance $Q \gg 1$ (C is large), the motion is underddamped, like the SIS junction. In simplest case, if the capacitance is neglected, the RCSJ model is reduced to RSJ model (Resistively Shunted Junction model).

1.5.1 DC Josephson Effect

Josephson effect is mainly divided into AC and DC Josephson effects based on the change in phase difference "φ", where the φ changes with respect to time. The Josephson effect in which phase difference φ remains constant and also voltage is zero across the junction is known as DC Josephson effect. In this effect the critical current density is always greater than the Josephson current density [63], such as;

$$V = 0,\ \varphi(t) = cons\tan t,\ I = I_s(\varphi),\ \text{and}\ I \le I_c \qquad 1.55$$

In DC Josephson effect, an extremely small current flows through the Josephson junction with no dissipation. When such a small current flows through a Josephson junction, voltage generated across the junction is zero that's why current remains sufficiently small and the self generated magnetic field is neglected. One of the important characteristic of Josephson junction includes phase gradient, the difference in phase across the junction is given by

$$\varphi = \varphi_2 - \varphi_1 \qquad 1.56$$

Where φ_1 is the wave function phase in the first and φ_2 is the wave function phase in the second superconductor. The relationship between I_s, I_c and phase difference φ is already given in the above Eq. 1.41.

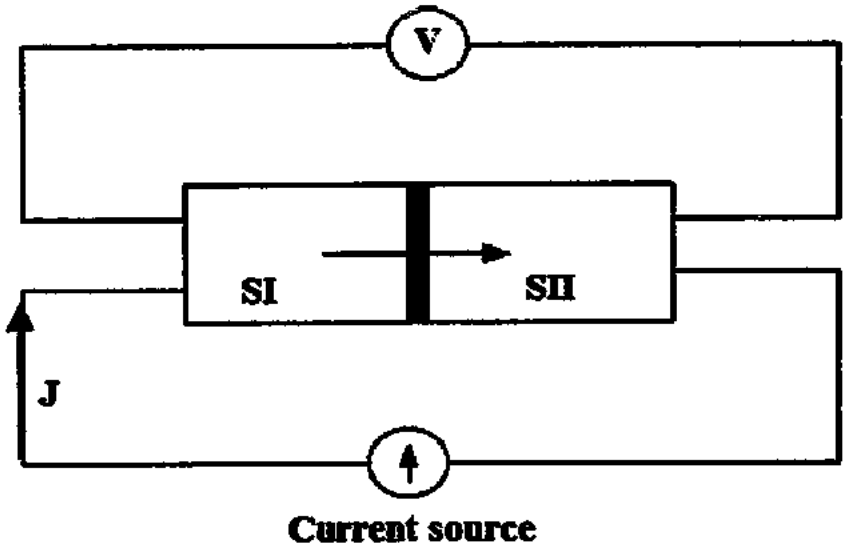

Fig. 1.11: DC Josephson circuit.

1.5.2 AC Josephson Effect

When there is change in the phase of wave function with respect to time, the Josephson effect is considered as the AC Josephson effect. Initially I is less than I_c through the junction. If the external current applied to the junction through an external source becomes greater than the critical value of current I_c, voltage is generated across the junction. This quantum mechanical behavior in the system is demonstrated by Schrödinger wave equation such as

$$i\hbar\frac{\partial\Psi}{\partial t}=\mathrm{H}\Psi \qquad 1.57$$

In the above equation H represents the Hamiltonian of quantum mechanical system, 'Ψ' is stationary state wave function, fulfill the equation;

$$\mathrm{H}\Psi=\mathrm{E}\Psi \qquad 1.58$$

where E represents the energy of the state, also $\Psi=\Psi e^{i\theta(t)}$, where Ψ is time dependent wave-function then we get;

$$-\hbar\frac{\partial\theta}{\partial t}=\mathrm{E} \qquad 1.59$$

In superconductor, energies of the Cooper pair on the both side of the junction due to the voltage 'V' present across the junction are E_1 and E_2 which related as;

$$\mathrm{E}_1-\mathrm{E}_2=2eV \qquad 1.60$$

where $2eV$ energy is due to charge of two electrons, while another fundamental equation of Josephson [64] is given as;

$$2eV = \hbar \frac{\partial \varphi}{\partial t} \qquad 1.61$$

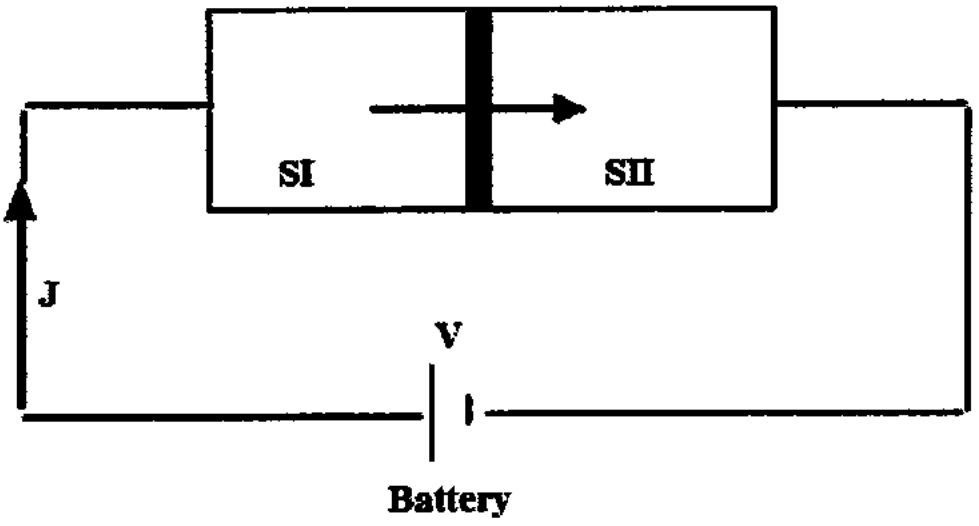

Fig. 1.12: AC Josephson effect

1.5.3 Some Examples of Josephson Junctions

A possible arrangement that yields a weakly coupled contact (Josephson junction) between two superconductors is shown in Fig. 1.13 (a-c).

Fig. 1.13(a) shows a junction, which consists of two superconducting thin films separated by an insulating oxide film. This insulating layer is an oxide of one of the superconductors and may be intentionally created or simply be the natural oxide film, which exists on the surface of most of the metals exposed to the atmosphere. In this type of junction, the two superconductors are coupled by tunnelling process (tunnelling of Cooper pairs).

Fig. 1.13(b) is essentially two pieces of superconductors connected by a very small bridge with dimensions of the order of a coherence length. It is usually an evaporated thin film, with the bridge formed by evaporating through an appropriate mask or by photo-etch techniques. The mechanism by which two superconductors are coupled is not simply Cooper-pair tunnelling.

Fig. 1.13(c) shows a point contact junction. It is simply a small area contact between a micro-size sharp point on one piece of superconductor and another piece of superconductor. It may be of particular interest, because it is extremely easy to fabricate. It can behave like a weak-link or tunnel junction, depending on the contact pressure and the nature of oxide films on the superconductors at the contact (critical current can be adjusted by varying applied pressure) [65].

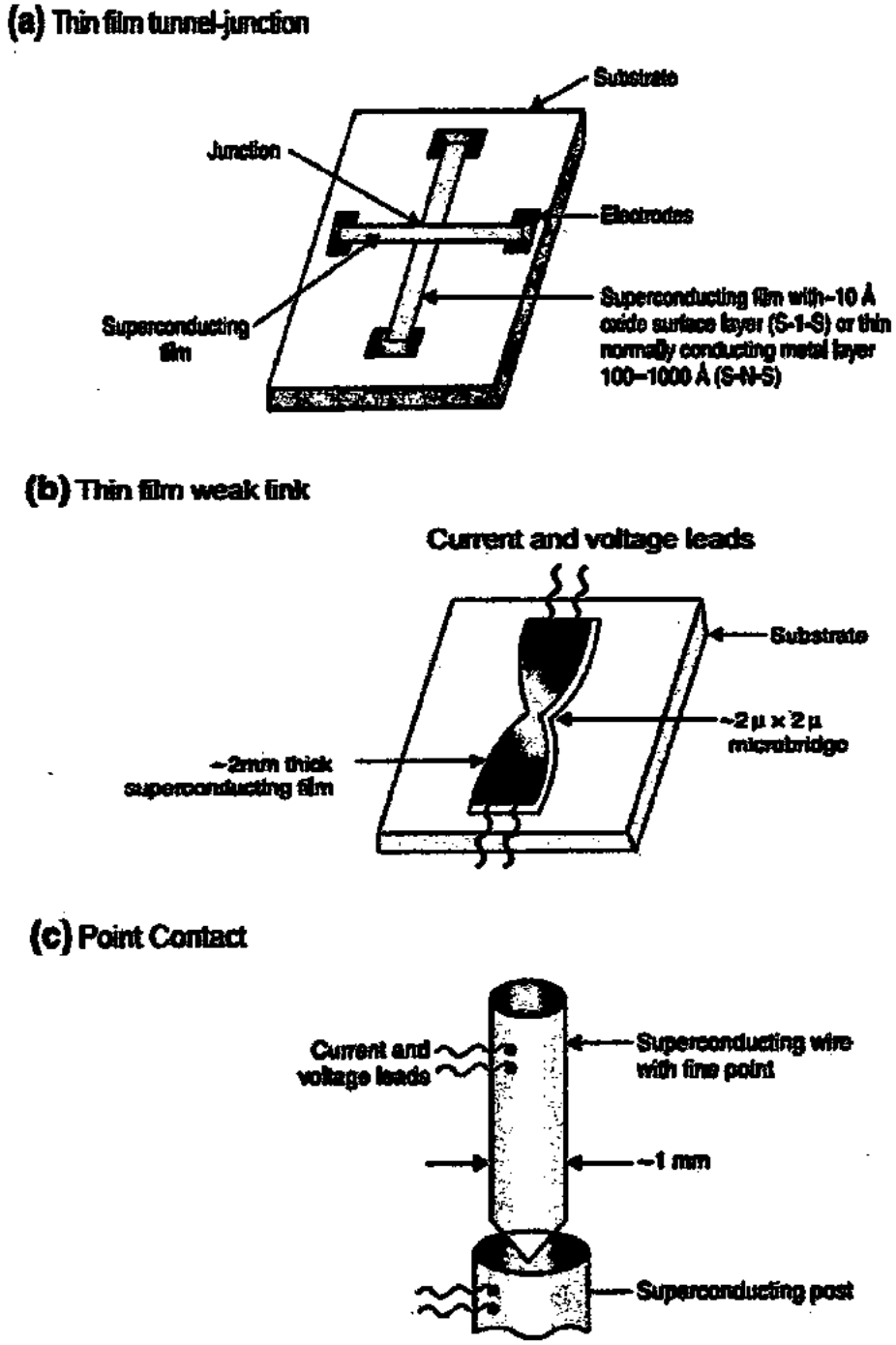

Fig. 1.13: Some Josephson junctions (a) thin film tunnel junction, (b) thin film weak-link, (c) a point contact [66].

1.6 Structures and Physical Properties of Cuprates Superconductors

The discovery of HTSCs gave paradigm shift to the study of the phenomenon of superconductivity. K. Alex Muller and George Bednorz shared noble prize for their important contribution of introducing ceramic materials [2]. Latest research showed that many compounds of copper and oxygen (cuprates) have $HTSC$ properties, and the expression of high-temperature superconductor is being used interchangeably with cuprate superconductor for compounds, like, yttrium barium copper oxide ($YBCO$) and bismuth strontium calcium copper oxide ($BSCCO$) [67]. Similarly, thallium-based, copper-based, copper-thallium-based and iron-based superconductors are well-known for high T_c.

High temperature superconductor has a chemical formula which is rather difficult and lengthy. A four-digit scheme was developed to shorten the chemical formula. It states that, the number of insulating layers among adjacent conducting blocks is represented by first digit. The number of spacing layers among similar CuO_2blocks is represented by second digit. The number of layers that split adjacent CuO_2 planes inside the conducting block is represented by third digit and the number of CuO_2 planes inside a conducting block is represented by fourth digit [68].

The structure of cuprate superconductors is normally associated to perovskite structure [69]. The morphological study shows that there are charge blocks and superconducting blocks in almost all $HTSCs$. The superconducting block is usually sandwiched between two charge blocks. This block gives path to conducting electrons while charge blocks act as a charge reservoir. The structure of $HTSC$ consists of $(n = 1,2,3,\ldots)CuO_2$layers. These layers are placed on each other with Ca layer in between them [70-72]. The increasing number of CuO_2 layers increases probability for the higher T_c. This arrangement is basically responsible for greater anisotropy. The Cu-based superconductors ($CBSs$) family contains CuO_2 plane as a common element, shown in Fig. 1.14 [73-75].

Microscopic study reveals that ceramic compounds are not uniform but a chain of linked grains, which disturbs the flow of current. In the development of crystal it is observed that all the impurities are collected at grain boundaries, which cause blockage to the current [76]. Additionally, the angle between grains also hinders the flow of super-current. The high-T_c superconductivity mechanism is probably the most crucial issue in the condensed-matter science during the last three decades. Even now, scientists are struggling for elucidating the mechanism [77, 78].

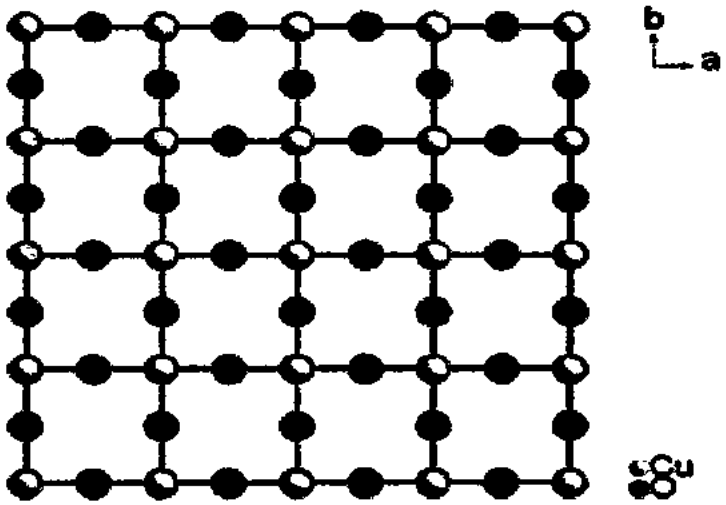

Fig. 1.14: Bonding structure of CuO layer in superconductors [73-75].

From an antiferromagnetic insulator La_2CuO_4, the first family of high-temperature superconductor was derived. When the material of this family was doped with holes (creating trivalent Cu species by the substitution of La^{+3} with divalent Sr^{+2} or by inserting excess oxygen) transformed to superconducting material. The structure of La_2CuO_4 at the temperature of 300 K is orthorhombic, which converts to tetragonal at the temperatures higher than 300 K. While the structure of $La_{2-x}Sr_xCuO_4(LSCO)$ is tetragonal at temperature of 300 K and converts to orthorhombic at 180 K, well above the transition temperature of superconductivity. The next homologue of $LSCO$ family under high oxygen pressure with two CuO_2 planes is $(La,Sr)CaCu_2O_6$having superconducting critical temperature (T_c) of 90 K.

$YBa_2Cu_3O_{7-\delta}$ and other 123 cuprates with orthorhombic structure exhibit superconductivity with critical temperature (T_c) of 90 K [79]. The structure and superconductivity of these materials are very sensitive to oxygen stoichiometry. Thermodynamically, $YBa_2Cu_3O_{7-\delta}$ is not stable but $YBa_2Cu_4O_8$ synthesized under high oxygen pressure having T_c of 80 K is more stable [80]. Also the superconducting phase $Y_2Ba_4Cu_7O_{15}(Y-247)$ was also prepared under 1 atm of oxygen pressure with T_c of 90 K [81-83].

The bismuth-based system has three superconducting phases $Bi-2201$, $Bi-2212$ and $Bi-2223$ with general formula $Bi_2Sr_2Ca_{n-1}Cu_nO_{4+2n+\delta}(n=1,2\ and\ 3)$. These numbering systems are showing number of atoms for $Bi, Sr, Ca\ and\ Cu$ respectively [84]. The unit cell of

these phases has double Bi–O planes, which are arranged in such a way that the Bi atom of one plane is placed below the oxygen atom of the successive planes. In between the CuO_2 layers, there is Ca atom layer, but Ca layer is missing in the $Bi-2201$ phase. Furthermore, these phases are different from one another in the strength of CuO_2 planes. Fig. 1.15 represents schematic diagram of the structure of three typical cuprates; $La_{2-x}Sr_xCuO_4(LSCO)$, $Bi_2Sr_2Ca_{n-1}Cu_nO_{4+2n+\delta}(BSCCO)$ and $YBa_2Cu_3O_{7-\delta}$ [73-75].

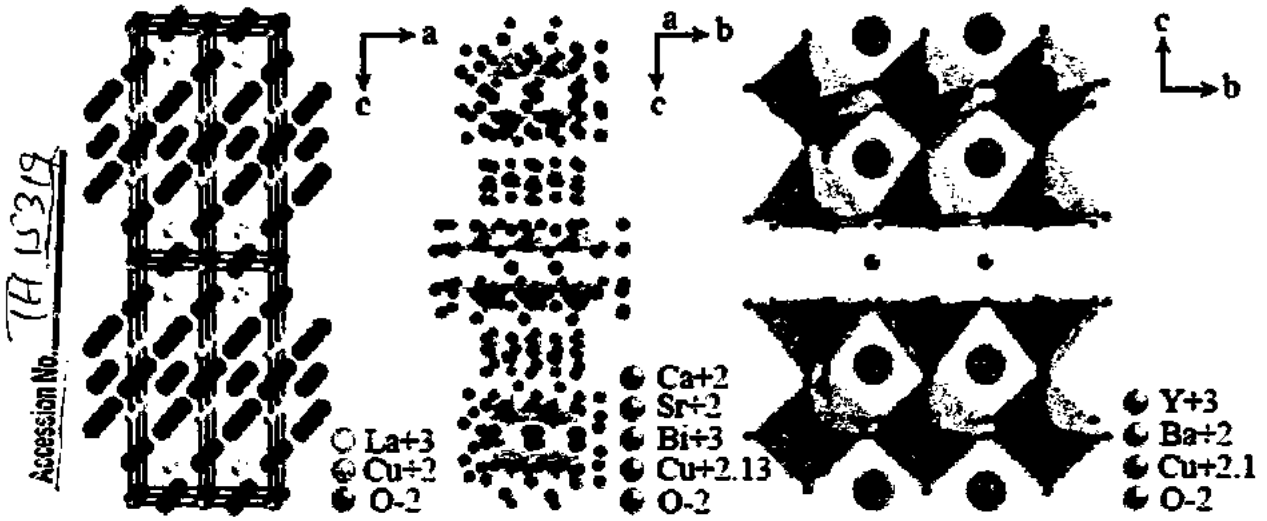

Fig. 1.15: Schematic diagram of typical superconductors; $La_{2-x}Sr_xCuO_4(LSCO)$[73], $Bi_2(Sr,Ca,Ln_3Cu_2O_8)(BSCCO)$ [74], and $YBa_2Cu_3O_{7-\delta}(YBCO)$ [75] (from left to right).

The $HgBa_2Ca_{n-1}Cu_nO_{2n+2+\delta}$ (Hg -based) family of HTSCs has been considered as to be the most interesting among high T_c superconductors [85-96]. The members of this family have tetragonal structure with space group P4/mmm and lattice parameters a = 3.88 Å and c = 9.5+3.2(n-1) Å [93-96]. Since the discovery of this (Hg-based) superconductor, its structural and physical properties have been investigated extensively. $HgBa_2Ca_2Cu_3O_{8+\delta}(Hg-1223)$ phase has gained much attention due to its highest T_c of 135.4 K under ambient pressure [98] and 164 K under high pressure of 30 GPa [95, 98, 99]. The pressure dependence of T_c was studied for each Hg-based compound. The values of T_c at high pressure (i.e 40 GP) are 118, 154 and 164 K for $Hg-1201$, $Hg-1212$ and $Hg-1223$, respectively [98]. Fig. 1.16 shows the crystal structure of Hg-1234 superconductor.

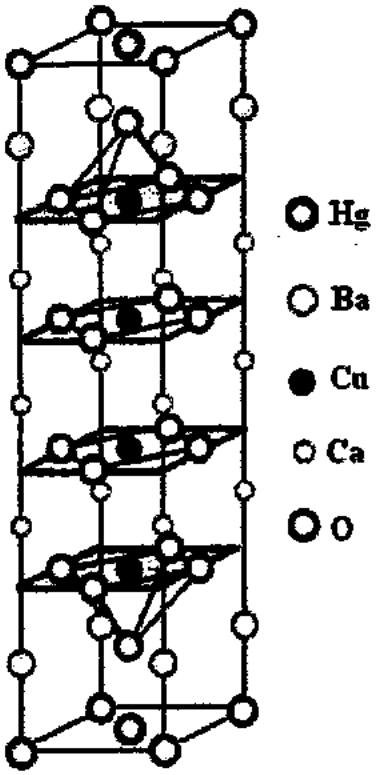

Fig. 1.16: Crystal structure of Hg-1234 [100].

In 1988, Sheng and Hermann discovered Tl-based $HTSCs$ family [101-103]. These cuprates $HTSCs$ are thought to be very promising due to their higher zero resistivity critical temperature $T_c(0)$, higher critical current density 'J_c' and lower superconducting anisotropy. After this discovery, many new phases of $Tl_mBa_2Ca_{n-1}Cu_nO_{2n+4}$ $(m = 1-2\ and\ n = 1-5)$ family have been discovered [104-108]. Different compounds of this family contain different number of CuO_2planes. The mono-layered Tl-based $HTSCs$ includes $TlBa_1Ca_1Cu_2O_7$, $TlBa_2Ca_2Cu_3O_9$, $TlBa_2Ca_3Cu_4O_{11}$, and $TlBa_2Ca_4Cu_5O_{13}$ phases, which can be denoted as $Tl-1212$, $Tl-1223$, $Tl-1234$ and $Tl-1245$ having T_c around $103, 123, 112$, and $107\ K$, respectively [109-114]. Unit cell structures of all mono-layered $HTSCs$ compounds are also tetragonal following $P4/mmm$ symmetry. These mono-layered superconducting compounds have got attraction due to their higher $T_c(0)$, higher J_c, higher irreversibility field (H_{irr}) and lower superconducting anisotropy ($\gamma = \xi_{ab}/\xi_c$) as compared to their counterpart in bi-layered compounds [112-114].

Also in mono layered Tl-based superconducting compounds critical temperature is linked with number of CuO_2 conducting planes. In $Tl_mBa_2Ca_{n-1}Cu_nO_{2n+2}$ for $n > 3$, T_c decreases,

which means $Tl-1223$ is most important because of higher superconducting and flux pinning properties [115-120]. Fig. 1.17 shows the crystal structure of mono-layered *Tl*-based *HTSCs*.

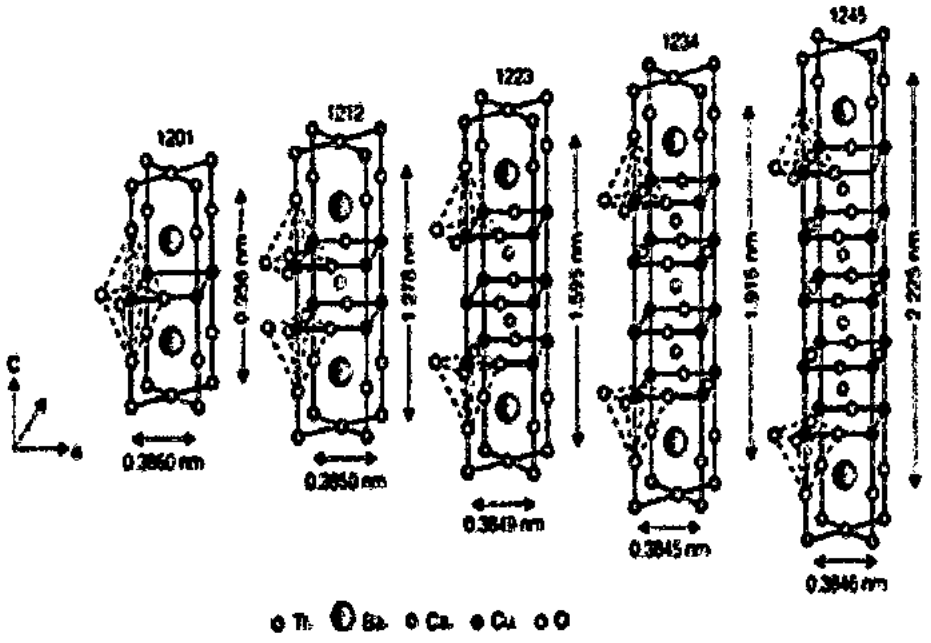

Fig. 1.17: Crystallographic cells of $Tl_mBa_2Ca_{n-1}Cu_nO_{2n+4}$ with ($m=1$ *and* $n=1-5$) [121, 122].

Some compounds in *Tl*-based high *HTSCs* have double TlO layers in which $Tl_2Ba_2Cu_1O_6$, $Tl_2Ba_2Ca_1Cu_2O_8$, $Tl_2Ba_2Ca_2Cu_3O_{10}$, $Tl_2Ba_2Ca_3Cu_4O_{12}$ and $Tl_2Ba_2Ca_4Cu_5O_{14}$ are important phases, which can be represented as $Tl-2202$, $Tl-2212$, $Tl-2223$, $Tl-2224$ and $Tl-2245$ having T_c about $95, 118, 127, 112,$ and $105\,K$ respectively. Unit cell structures of all above mentioned compounds are tetragonal following $P4/mmm$ symmetry. General expression to represent these compounds is $Tl-22(n-1)n$, where 'n' is representing the number of CuO_2 conducting planes.

Cu-based $CuBa_2Ca_{n-1}Cu_nO_{2n+4}$ $(n=1,2,3,\ldots)$ *HTSCs* family is more important due to its fascinating superconducting properties. General expression to represent compounds of this family is $Cu-12\,(n-1)n$, where n is representing the number of CuO_2 conducting planes. All the members of this family have the tetragonal structure following $P4/mmm$ symmetry, same as $Tl-12\,(n-1)n$, but superconducting properties of Cu-based *HTSCs* family is higher than Tl-based family [123-129]. Fig. 1.18 shows the crystal structure of $Cu-1223$ *and* $Cu-1234$ *HTSCs*.

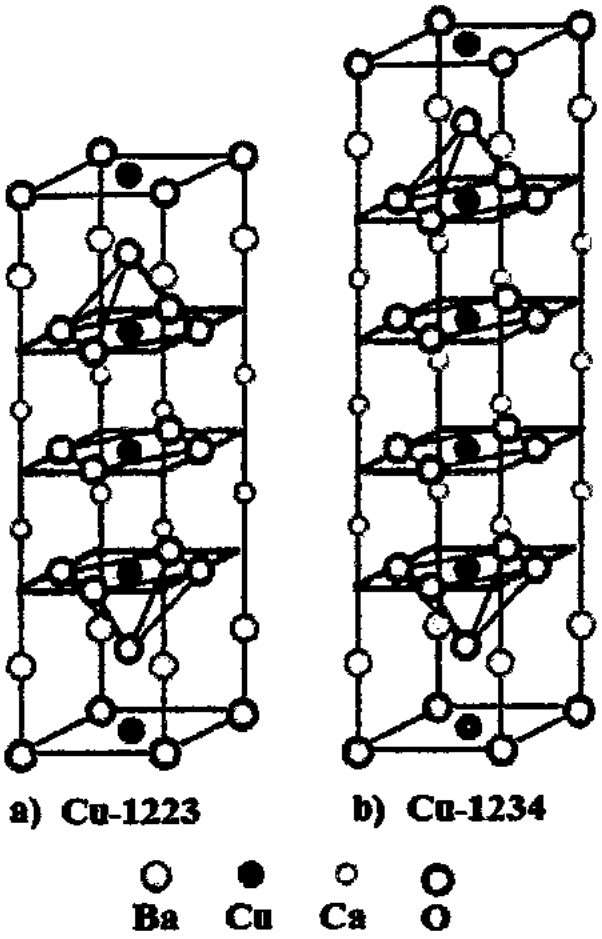

Fig. 1.18: Crystal structure of $Cu-1223$ and $Cu-1234$ [129].

Charge reservoir layer of Cu-based *HTSCs* family ($CuBa_2O_{4n+\delta}$) contain copper, which is a high quality conductor. Conducting charge reservoir layer of this family make it least anisotropic as compared to *Tl*-based *HTSCs* family. Among all the members of Cu-based *HTSCs* family, highest critical temperature was achieved for $Cu-1223$ having three CuO_2 conducting planes. As stronger inter-plane coupling between CuO_2 conducting planes decreases the anisotropy in *HTSCs* and improve their superconducting properties, so any *HTSC* material with strong inter-plane coupling will be very suitable from the applications point of view.

Higher transition temperature, low superconducting anisotropy and long coherence length along c- axis are the reasons for *CuTl* -based *HTSCs* family to be one of the most alluring family among the other *HTSCs* families [15, 130]. Amongst the *Cu* -based superconductor families, the $Cu-1223$ superconductor has the highest critical temperature $120K$ [109]. Anisotropy $\gamma=\frac{\xi_{ab}}{\xi_c}$

is defined as the ratio of ab-plane coherence length (ξ_{ab}) to c-axis coherence length (ξ_c). This compound has least anisotropy $(\gamma = 1.6)$ and long c-axis coherence length [131]. *CuTl*-based superconductors can be obtained by partial substitution of '*Tl*' in the charge reservoir layer of *Cu*-based '$CuBa_2Ca_{(n-1)}Cu_nO_{(2n+2)}$ $[Cu_{12(n-1)n}]$' superconductors where $n = 1,2,3.....$, [132]. It is not simple to synthesize this compound at ambient pressure. Superconducting phases can be synthesized effortlessly through fractional substitution of '*Tl*' in the charge reservoir layer of Cu-based superconductor [133]. In this process '*Tl*' acts as reaction accelerator and structure stabilizer. These compounds have superconducting characteristics very close to $Cu_{12(n-1)n}$ and could be equipped under low and high pressure [129]. By post-annealing and substitution of diverse cations, superconducting properties of these compounds can be improved. It is important to have the replacement of impurities in the *HTSC* material for different applications. Fig.1.19 shows the unit cell of $CuTl-1223$ superconductor in which $Cu_{1-x}Tl_xBa_2O_{4-\delta}$ is a charge reservoir layer and three CuO_2 planes, separated by two '*Ca*' atoms.

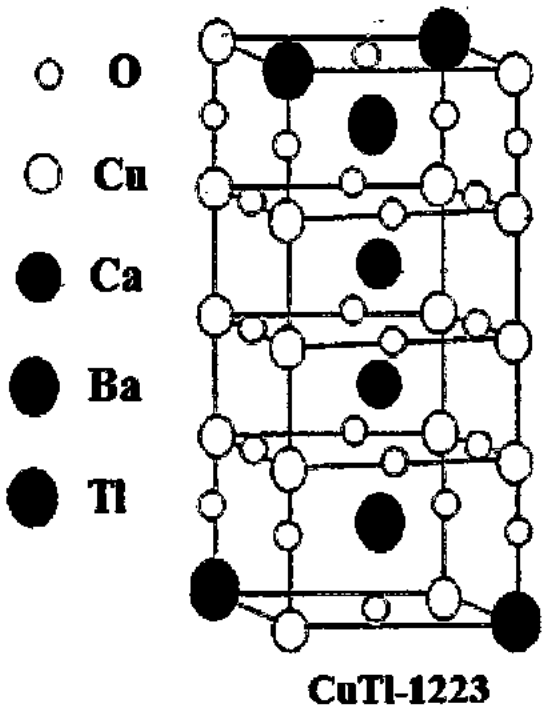

Fig. 1.19: Crystal structure of CuTl-1223 [129].

The CuO_2 planes in contact with $Cu_{1-x}Tl_xBa_2O_{4-\delta}$ charge reservoir layer is known as ' p ' planes. The central plane or s -plane is sandwiched between p -planes, which is connected by ' Ca ' atoms with the outer planes. Normally, s -planes are optimally doped whereas p - planes are over doped. The p -planes act as bridge to provide carriers from charge reservoir to s-plane [129, 133]. The O_3 atom or O_δ is the central oxygen of $Cu_{1-x}Tl_xBa_2O_{4-\delta}$ charge reservoir layer.

1.7 Role of Impurities in Superconductivity

In a superconducting material, the grain and grain boundaries, inhomogeneties in the structure and twinning planes scatter conducting carriers; hence order parameters are affected by these irregularities [134]. Here our focus is on one type of imperfection i.e., the impurity atom or the atomic defect.

The pair-breaking effects by magnetic and nonmagnetic impurities have been discussed in this section. The nonmagnetic impurity effects depend strongly on the gap symmetry while the magnetic impurities suppress superconductivity independent of the gap symmetry.

(i) Nonmagnetic Impurities

The nonmagnetic impurity (NMI) like Zn, suppresses 'T_c' according to the equation [135-137],

$$ln\frac{T_{c0}}{T_c} = \Omega[\varphi\left(\frac{1}{2}+\frac{\mu}{2}\right) - \varphi(\tfrac{1}{2})] \quad 1.62$$

where $\varphi(x)$ represents the digamma function. Mathematically, the digamma function can be given as the logarithmic derivative of the gamma function [136]

$$\varphi(x) = \frac{d}{dx} ln\Gamma(x) = \frac{\Gamma'(x)}{\Gamma(x)} \quad 1.63$$

Integral form can be represented as;

$$\varphi(x) = \int_0^\infty (\frac{e^{-x}}{t} - \frac{e^{-xt}}{1-e^{-t}})dt \quad 1.64$$

where μ is

$$\mu = \frac{\hbar}{2\pi k_B T_c \tau} \quad 1.65$$

and the gap anisotropy (Ω) can be defined as;

$$\Omega \equiv 1 - \frac{\langle\Delta(k)\rangle^2}{\langle\Delta(k)^2\rangle} \quad 1.66$$

For an isotropic SC gap, for s-wave, $\Omega = 0$, while for an anisotropic gap $\Omega = 1$ like d-wave and s-wave.

From Eq. 1.62, the nonmagnetic impurity effect vanishes for the isotropic s-wave superconductors, since $\Omega = 0$. This is known as the Anderson's theorem; the introduction of isoelectronic *NMI* does not break pairing of electrons for an isotropic SC gap but does for an anisotropic gap [138]. Thus, the *NMI* effect on SC is quite useful to judge the gap symmetry. According to the BCS theory, T_c is related to the Debye frequency 'ω_D' and density of states '$D(E_f)$' by the equation,

$$K_B T_c \approx 1.14\hbar\omega_D \exp\left(\frac{-1}{D(E_f)V}\right) \quad 1.67$$

Thus if the inclusion of NMI affects $D(E_f)$ (due to the carrier doping) or ω_D, T_c will change even in the isotropic s-wave superconductor. For anisotropic superconductors, since $\Omega \neq 0$, T_c will be suppressed by NMI. At a low impurity concentration with $\mu \ll 1$, the Eq. 1.62 will be transformed as;

$$T_c = T_{c0}\left[1 - \Omega\frac{\pi\hbar}{8k_B\tau}\right] \quad 1.68$$

It is clear from the above equation that the suppression of T_c is proportional to the impurity concentration. For higher concentration with $\mu \gg 1$, Eq. 1.62 will become as:

$$T_c = T_{c0}\left[\Delta(0)\frac{k_B\tau}{\hbar}\right]^{\frac{\Omega}{1-\Omega}} \quad 1.69$$

Thus, T_c will not be suppressed completely to zero unless $\Omega = 1$ [139].

(ii) Magnetic Impurities

The magnetic impurity like Ni, Co etc introduces additional exchange interaction causing scattering, so, T_c will be suppressed even in isotropic s-wave superconductors as;

$$ln\frac{T_{c0}}{T_c} = \varphi\left(\frac{1}{2} + \frac{\mu_m}{2}\right) - \varphi\left(\frac{1}{2}\right) \quad 1.70$$

Above equation (Eq. 1.70) has the same form as Eq. 1.62 for the anisotropic superconductors;

$$\mu_m = \frac{\hbar}{2\pi k_B T_c \tau} \quad 1.71$$

The T_c suppression is two times greater than the value in Eq. 1.64.

Eq. 1.70 can also be expressed as [137]:

$$ln\frac{T_{c0}}{T_c} = \varphi\left(\frac{1}{2} + 0.14\frac{\alpha T_{c0}}{\alpha_c T_c}\right) - \varphi\left(\frac{1}{2}\right) \quad 1.72$$

where, α is the pair-breaking parameter which is defined as $^1/_\tau$, and α_c is the pair-breaking parameter when superconductivity is completely suppressed. This 'α_c' is very important to judge the symmetry of the order parameter.

(iii) Pair-breaking Study in Cuprates Superconductors

The Zn substitution for Cu has been carried out for the cuprate superconductors such as $YBa_2Cu_3O_{7-\delta}$ [134,140-142], $(La,Sr)_2CuO_4$ [132,143-145], $(Nd,Ce)_2CuO_4$ [134], and $Bi_2Sr_2CaCu_2O_8$ [134,146-148]. The Zn atoms act as strong scattering centers and surprisingly suppress superconductivity due to the d-wave anisotropic gap symmetry of the cuprates [134,140-148]. Fig. 1.20 shows the impurity content dependence of T_c in the $YBa_2Cu_{3-x}M_xO_{7-\delta}$ superconductor [142], where M is Fe, Co, Ni, Al and Zn. The magnetic and nonmagnetic impurities have similar T_c suppression effects due to the anisotropic order parameter of $YBa_2Cu_3O_{7-\delta}$.

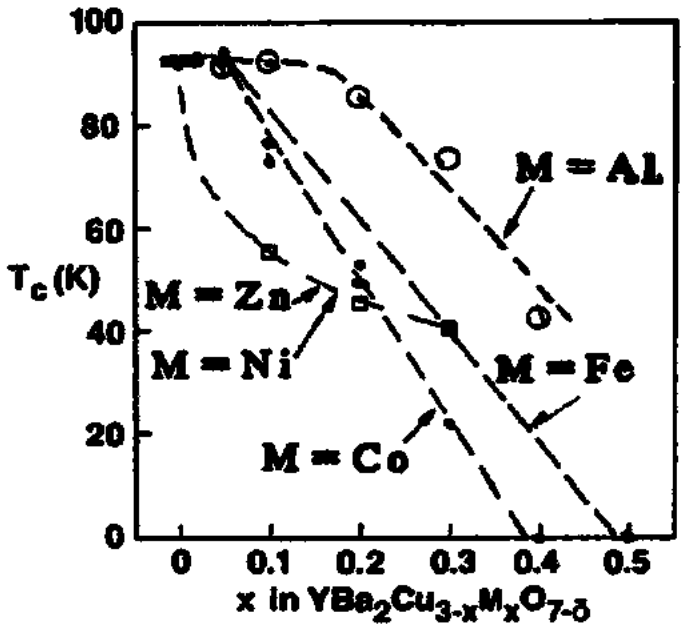

Fig. 1.20: The variation of T_c as a function of impurity content 'x' in $YBa_2Cu_{3-x}M_xO_{7-\delta}$ superconductor [142].

The substitution effects of $Co, Ni,$ and Zn on T_c in the $(La,Sr)_2CuO_4$ and $(Nd,Ce)_2CuO_4$systems are shown in Fig. 1.21 [144]. The substitution of Zn suppresses T_c more slowly in the Nd-system than in the La-system suggesting that the disorder produced by Zn is less pronounced in the Nd-system. In contrast, the magnetic impurities of Co *and* Ni depress T_c

more dramatically in the *Nd*-system than in the *La*-system, indicating that the magnetic pair-breaking effect is stronger in the *Nd*-system.

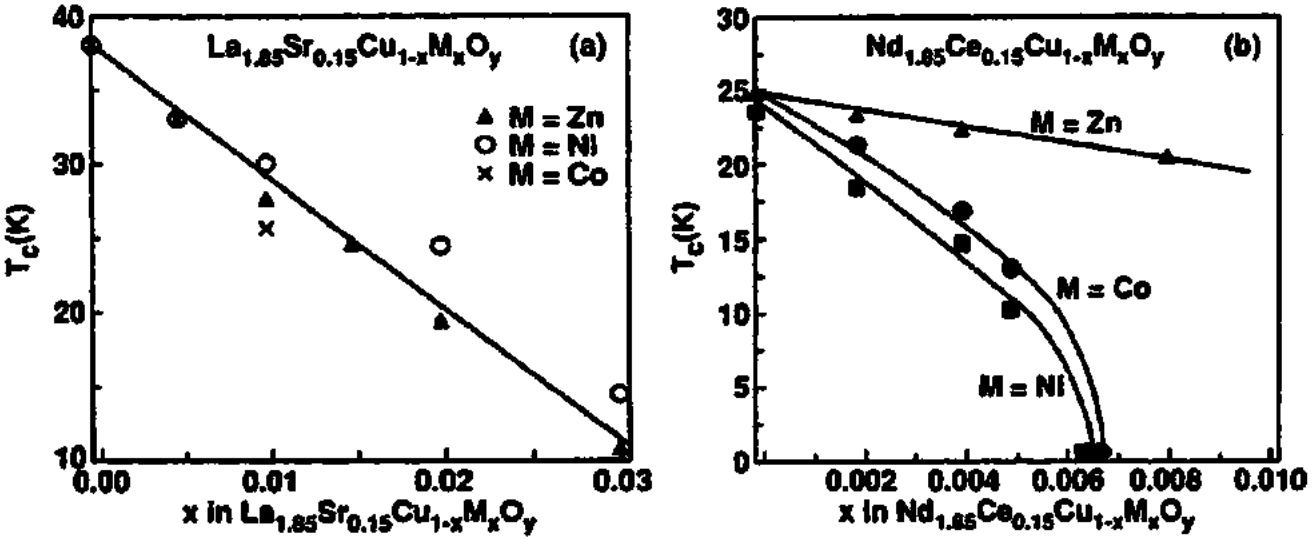

Fig. 1.21 The variation of T_c versus the impurity content x in (a) $(La,Sr)_2CuO_4$ and (b) $(Nd,Ce)_2CuO_4$series [144].

1.8 Grain Boundaries (GB) and Their Role in Superconductivity

There are numerous applications of HTSC materials, where the grain-boundaries (GBs) play an important role like electronic circuits, sensors, superconducting quantum interference devices (SQUIDs) and power cables. Especially, the critical current density J_c is influenced by the GBs in a complex manner. Polycrystalline HTS samples have typical *Jc* values of a few hundred A/cm^2 at 4.2 K, while single crystalline samples have values in the range of MA/cm^2. A GB introduces structural disorder that in the case of HTS materials strongly affects the order parameter in the region of the boundary. Considering the degree of connectivity, it can be distinguished between low-angle GBs having strong coupling between the grains, and high-angle GBs with a weak coupling. Transmission electron microscopy (TEM) investigations reveal that low-angle GBs consist of an array of uniformly spaced dislocations produced to accommodate the mismatch between adjacent grains [149, 150]. Fig. 1.22 shows schematically such a low-angle grain boundary. For small misorientation angles θ, the dislocations are separated by channels of a nearly undisturbed lattice.In the standard GB theory, the distance d between the dislocation cores is given by Frank's formula,

$$d = \left|\vec{b}\right| / \sin\theta$$

where $\left|\vec{b}\right|$ is the magnitude of the Burgers vector $\vec{b}$ [151].

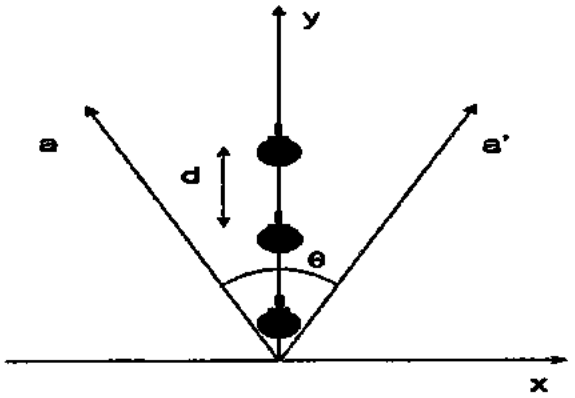

Fig. 1.22: Chain of edge dislocations which form a symmetric low-angle grain boundary in the $y-z$ plane [151].

The distance between dislocation cores reduces with increasing GB angle, with the result that for misorientation angles of approximately 10° the dislocation cores overlap leading to an area with high structural disorder and a reduced order parameter [150, 152]. These GBs are named high-angle GBs and present typical Josephson junction characteristics.

GBs are usually classified according to the misorientation and rotation of the adjacent grains. Fig. 1.23 presents the three different types of GB geometry. In the [001] tilt boundary Fig. 1.23 (a), the c-axis are perpendicular to the plane of the film so that the CuO_2 planes in the adjacent grains are parallel to each other. The angle θ between the principal in-plane directions defines the misorientation (tilt) angle. In Fig. 1.23 (b), the c-axis of the adjacent grains are misaligned by an angle 'φ' in a plane normal to the grain boundary plane; this misorientation produces a [100] tilt boundary.

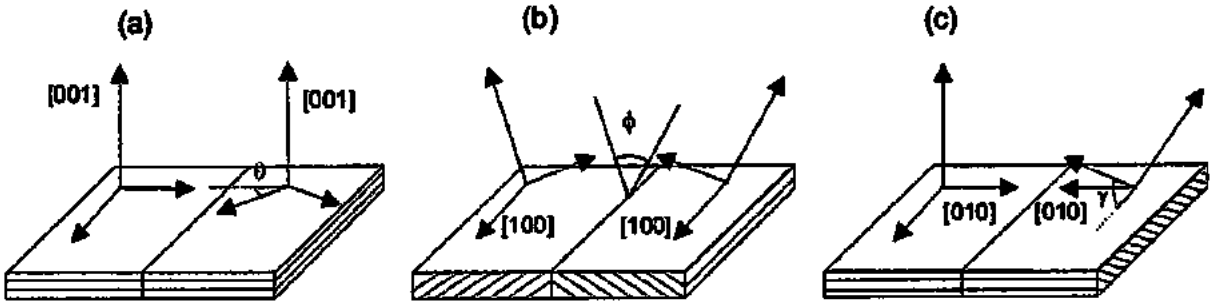

Fig. 1.23: Sketches showing the crystallography (a) [001] tilt boundary (b) [100] tilt boundary (c) [010] twist boundary [152].

In Fig. 1.23 (c), the misorientation angle γ between the c-axis is in a plane parallel to the boundary. In the latter case, the 'a' (or 'b') axes are normal to the boundary plane so that a [010] twist boundary is formed. GBs with identical misorientations of the grains with respect to the boundary are called symmetric, otherwise they are asymmetric. For a detailed investigation of GBs and their transport properties, they can be produced artificially by growing epitaxially HTS films on bicrystal substrates, which consist of two crystals with different crystallographic orientations that are fused together [152].

Josephson junctions are very sensitive devices to examine SC state, GB is of great interest among these junctions, because it exhibits reasonably phase sensitive behavior for the superconductors with anisotropic SC gap [153]. The general behavior of GB and recent development of GB in HTSCs are discussed below:

Since it is very difficult to fabricate a perfect single crystalline sample, GBs are usually present in a superconducting specimen, and they thus form a three-dimensional (3-D) network across which any long-range transport has to occur. As early discussed that both $HTSCs$ of cuprates and Fe-baesd superconductors ($FBSCs$) have two-dimensional (2-D) structures, in which superconductivity occurs primarily on specific atomic planes, namely, in the $Cu-O$ plane in the cuprates and the $Fe-As$ plane in $FBSCs$ [153-156]. The GBs engineering is a critical matter in developing practical superconducting tapes as well wires, because SC properties mainly depend on θ_{GB} (the misorientation angle) at GBs.

The low carrier densities, unconventional pairing symmetry, short coherence lengths and large screening lengths are common characteristics for cuprates and $FBSCs$, and they suppressed superconductivity at GBs effectively through different mechanisms. The most significant effects can be summarized as [153]:

1) Strains at GB dislocation cores, which can be converted into current-blocking regions.

2) Space charges created due to nonlinear elastic deformations or charged dislocation cores at the GB.

3) Impurity segregations induced by the electric field and strain at the GB.

4) Competing current-blocking AF phase induced at the GBs by charge, strain and impurity effects.

5) GB shows relatively phase sensitive behavior for the anisotropic SC gap.

Hu and his colleagues [157] have calculated the $J_c(T)$ of Josephson tunneling for *YBCO* superconductors, by applying different cases such as *s*-state, *d*-state, mixed $S + id$ state, as shown in Fig. 1.24. By comparing with the experimental data, the mixed $S + id$ state with a dominant *d*-wave component and a very small *s*-wave component seems more likely for the GB junction and also for the *YBCO* -based heterojunction.

Generally, to understand the behavior of a bulk polycrystalline sample, it is very important to get information about the interfaces among the grains [153]. However, it is rather challenging to elucidate the SC properties near the interfaces form the results of a polycrystalline sample, due to the complexity. The bicrystal technique is often used to unveil the basic properties of the interface. Bicrystal experiments readily yielded several intriguing results on various superconductors, especially for the cuprates [158]. GB can be an excellent Josephson junction, which is easy to be fabricated and sometimes successfully applied to devices. In particular, bicrystalline (or multi-crystalline) junctions have been found to be very useful for illuminating the basic nature of the superconductivity.

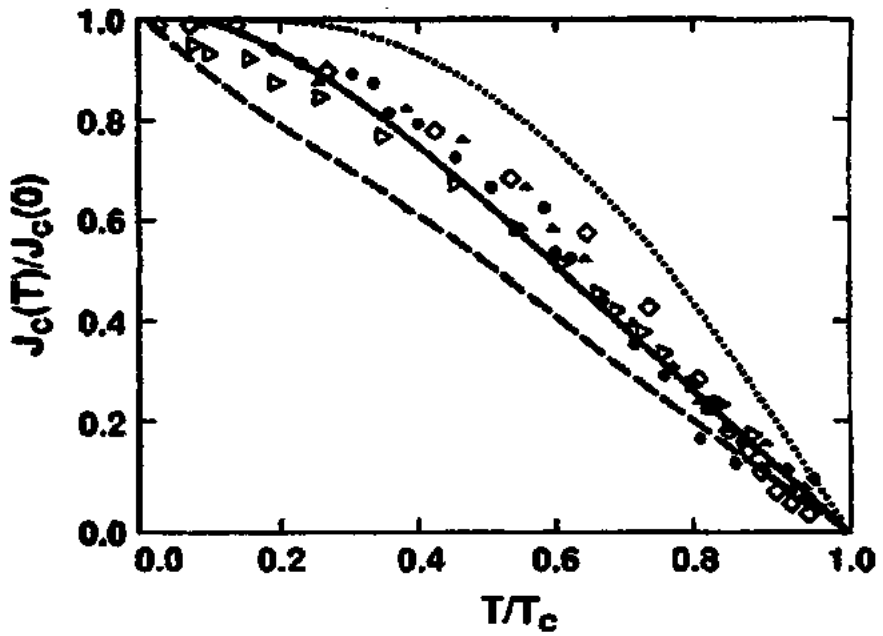

Fig. 1.24: Temperature dependence of Josephson critical current density $J_c(T)/J_c(0)$, for different symmetries of order-parameter such as *s*-wave (dotted line), *d*-wave (dashed line) and $\bar{s} + id$ (solid line) [157]. Experimental data collected in *YBCO* /metal/ *YBCO SNS* step junctions (open diamonds) [159] and (open triangles) [160], as well as on *YBCO GB* junction (filled dots) [161].

Fig. 1.25 represents an exploration of spontaneous generation of half-flux magnetic quanta, created by rings structured in tricrystalline and tetracrystalline epitaxial films by using scanning *SQUID* microscopy, provided clear evidence of dominating $dx^2 - y^2$ order-parameter symmetry in the cuprates. The inner diameter and width of the rings are $48\,mm$ and $10\,mm$, respectively. Lower half of the figure shows that middle ring is centered on the tricrystal point of the substrate. In this ring, a supercurrent producing half of a magnetic flux quantum $^{h}/_{4e}$, is generated. The sample was cooled in a field of $< 2mG$ and imaged at $4.2\,K$ [163].

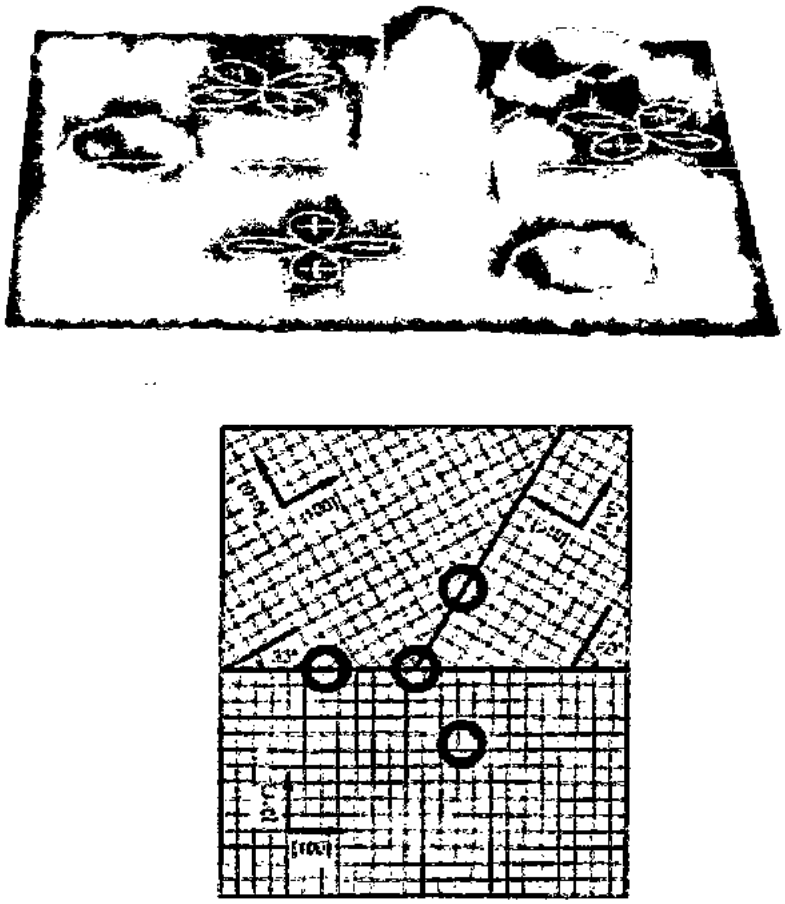

Fig. 1.25: Scanning *SQUID* microscopy image of four SC rings into a tricrystalline $YBa_2Cu_3O_{7-\delta}$ film [162].

On the thin-film fabrications of *FBSCs*, only few reports are presented [163-166], because, usually it is very tough to attain a well-defined single-crystalline film of *FBSC*. Recently, Hosono's group reported the GB junctions with various θ_{GB} for the cobalt-doped $BaFe_2As_2$ epitaxial film on a bicrystal substrate shown in Fig. 1.26 [163]. The transport

measurements for the junctions showed that the 'J_c' through the bicrystal GB (J_c^{BGB}) remained high ($> 1\ MA\ cm^{-1}$) and also remained unchanged up to a critical angle θ_c of ~9^o, which is greater than θ_c of ~5^o for $YBa_2Cu_3O_{7-\delta}$. For $\theta_{GB} > \theta_c$, the decay of J_c was slower than that of $YBa_2Cu_3O_{7-\delta}$. However, the current against voltage characteristics ($IVCs$) showed absence of hysteresis, which seems unreasonable, because $FBSCs$ have 2-D nature with the Stewart-McCumber Parameter β_c large enough for the occurrence of hysteresis [153].

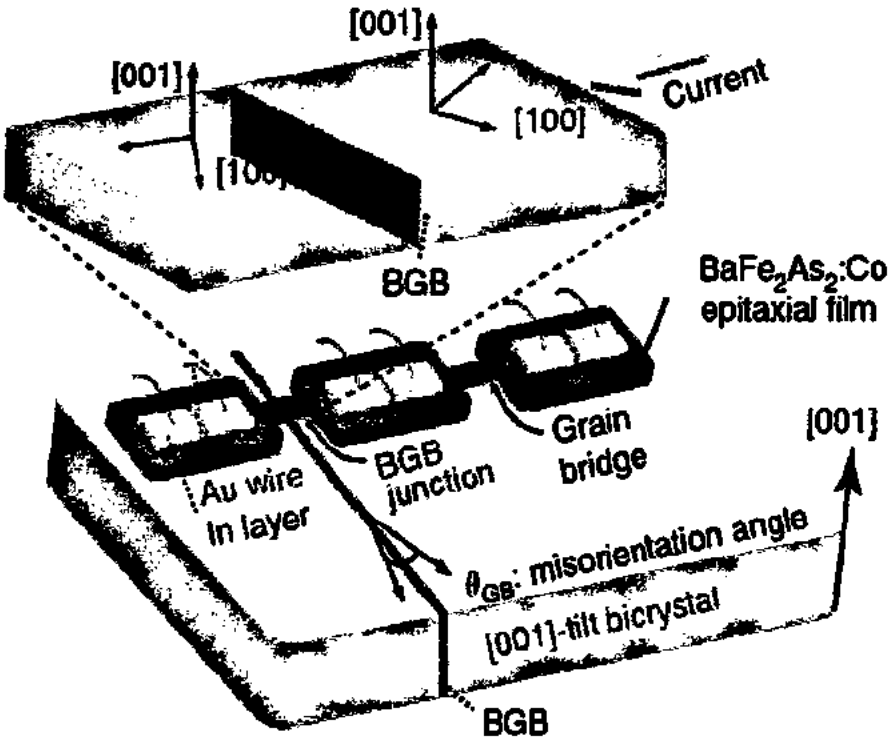

Fig. 1.26: Structure of the BGB junctions device and Grain bridges. The upper rectangular solid is a magnification at the BGB junction [163].

Although, the bicrystal technique had been widely used for many decades to conventional superconductors, cuprates, also for $FBSCs$ [162, 163], but still there is a serious technical problem. Since the thin films are usually fabricated in large area on the bicrystal, it is not typically single-crystalline with extra GBs, except for some fortunate cases like the $YBa_2Cu_3O_{7-\delta}$ film [158, 162]. Due to these extra GBs, serious affection on the junction properties may be arises. Although more advanced technique, molecular beam epitaxy (MBE),

has been applied to fabricate the thin films, it is effective only for the systems with simple structures, like $FeSe$, $K_{1-x}Fe_2Se_2$ [166], etc. So, still it is quite difficult to get good thin films for more complicated compounds like $Sr_3Sc_2O_5(Fe_2As_2)$, $Ca_{10}(Pt_4As_8)(Fe_2As_2)$, or even $LaO_{1-x}Fe_2As_2$.

1.9 Vortices and Flux Pinning

Type-II superconductors have an intermediate state where magnetic field enters into superconductor's normal region gradually. This mixed state exists between the regions H_{c1} and H_{c2}. Inhomogeneous Type-II superconductors own different types of defects. Vortices are pinned by the defects. Those paths along which applied magnetic field is trapped, are called pinning centres [167].

There are different ways in which vortices interact with defects; usually these interactions may be attractive. Therefore vortex is captured or "pinned" at the defect. Due to this fact, superconductor will carry transport current without any dissipation, until this pinning force is less than Lorentz force from this current. If current density is increased above its critical value then normal state will be restored implying that transition is dependent on limited dissipation of energy. Pinning of vortices on defects also depicts Type-II superconductor when exposed to magnetic field as represented by the Fig. 1.27.

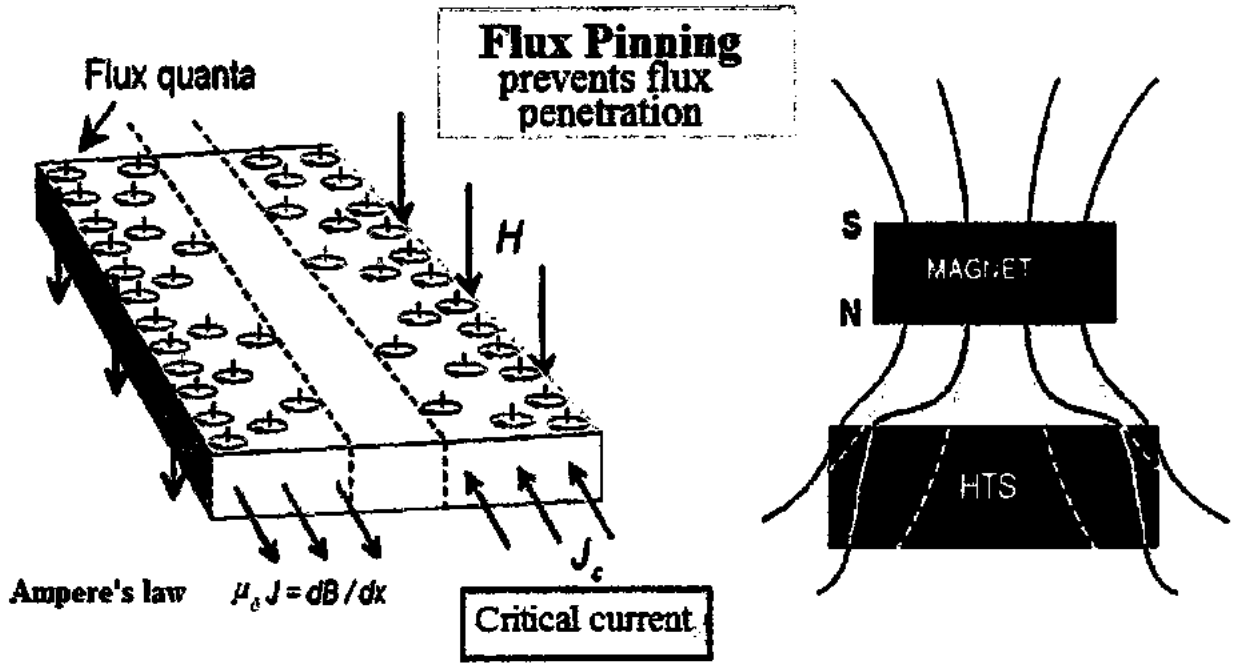

Fig. 1.27: Magnetic flux representation in the plane of high temperature superconductors [168].

Abrikosov predicted that the vortex state of the type-II superconductors allowed magnetic field lines to pass through the material in a regular array of quantum units of $\Phi_0 = {}^{hc}/_{2e} = 2.07 \times 10^{-7} Gcm^2$, which is known as flux quantum. In a thin film, a vortex is a current circulating around a normal core. Except the vortex lattice, the remaining material will be in the superconducting state. When upper critical field H_{c2} reached, the superconductivity will be completely suppressed. The expression for H_{c2} can be given by

$$H_{c2} = {}^{\emptyset_0}/_{2\pi\xi^2} = \sqrt{2}kH_c \qquad 1.73$$

Abrikosov's relation for H_{c1} is given by

$$H_{c1} = {}^{\emptyset_0}/_{2\pi\lambda^2} = \frac{H_c}{k}(lnk - 0.27) \qquad 1.74$$

where H_c is the thermodynamic critical field while $H_c^2/8\pi$ is the free-energy difference between normal and superconducting states of the metal.

A schematic description of the vortex phase diagram for HTSC is shown in Fig. 1.28. Vortices can form three distinct phases in HTSC: vortex lattice, glassy vortex state and vortex liquid. Vortex lattice represents almost perfect crystalline structure, vortex glass is strongly disordered vortex solid and vortex liquid in a disordered phase, where thermal fluctuations destroy the crystalline order. The vortex lattice may melt with increasing temperature and near B_{c2}, vortex liquid phase has been observed [169]. Generally, critical current density (J_c) decreases with increasing temperature and magnetic field reaches zero at the melting line, also called irreversibility line 'B_{irr}'. Above this line, the superconductor does not carry loss-free current, although, it is still in a superconducting state [170].

In the presence of a magnetic field perpendicular to the current direction, a Lorentz force $F_L = j \times \phi_o$, (where j is the current and ϕ_o is the magnetic flux quantum), acts on the vortices and as long as F_L is smaller than pinning force F_P, vortices do not move. If a current is applied, as shown in Fig. 1.29, vortices move according to F_L, dissipating energy, which can be observed as resistance. In a case of a defect free sample (Fig. 1.29a), vortices move according to F_L. In the presence of point defect pinning (Fig. 1.29b), vortices are partially pinned. If columnar defects parallel to the applied magnetic field are introduced (Fig. 1.29c), the entire sections of vortices are pinned and this is an example of strong pinning [169].

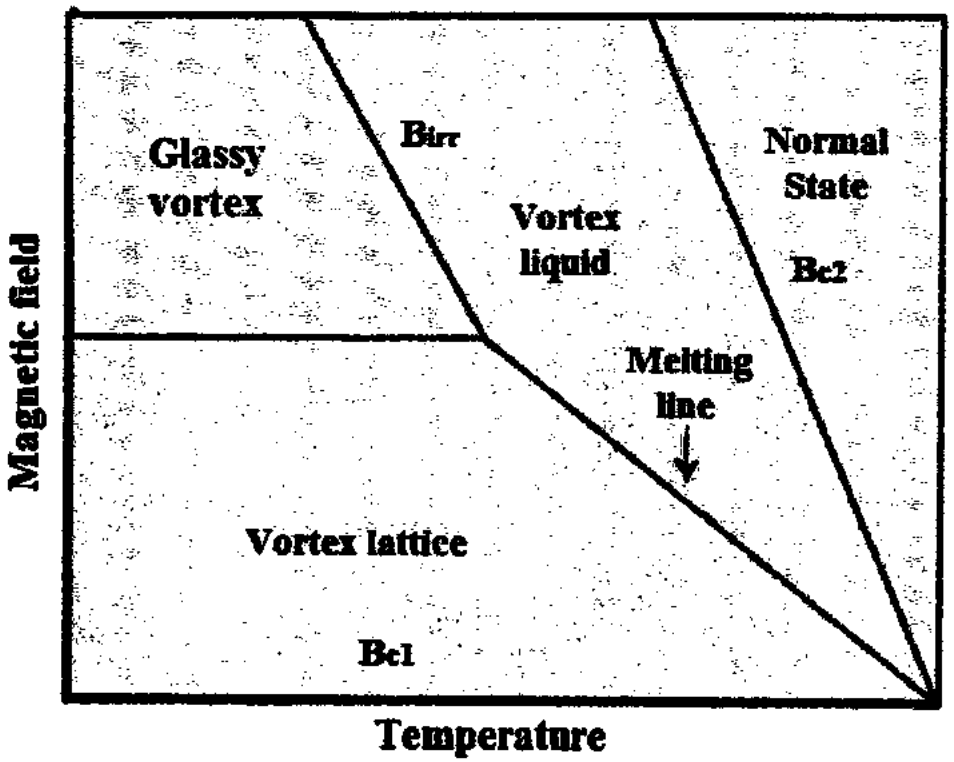

Fig. 1.28: Schematic vortex phase diagram for a HTSC [169, 170].

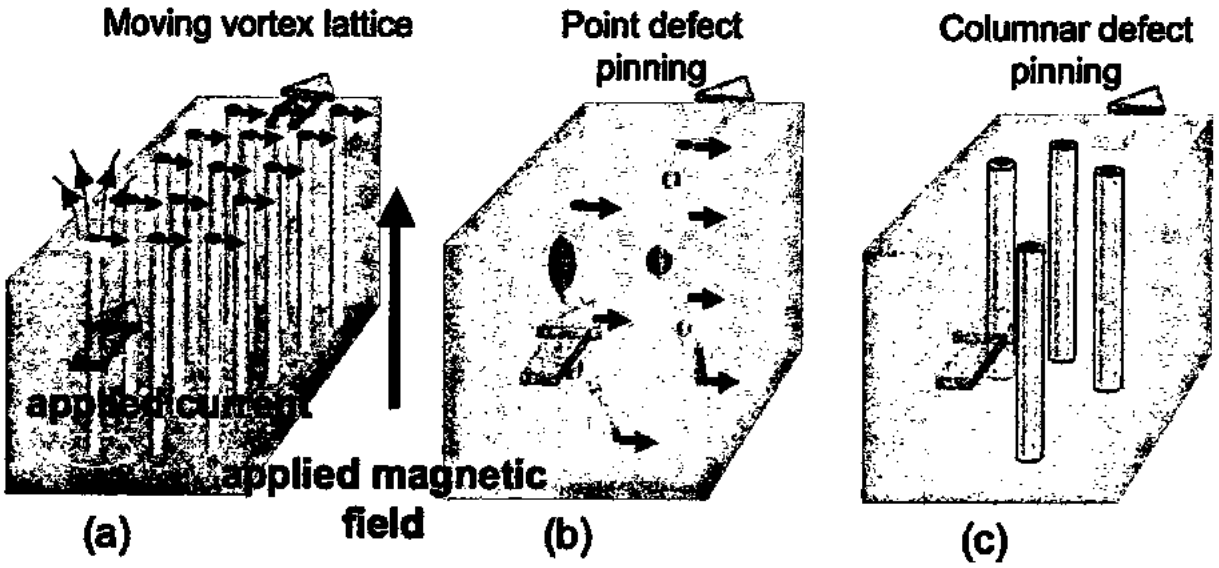

Fig. 1.29: A simplified illustration of vortices moving under the Lorentz force F_L (black arrows), induced by an applied current (green arrow) in the presence of an external magnetic field (red arrow) perpendicular to the film surface. a) A defect-free sample. b) Vortices are partially pinned by point defects. c) Entire sections of vortices are pinned by columnar defects [169, 170].

When the pinning forces F_P are not strong enough to prevent flux motion, the superconductor is called soft; otherwise it is termed as hard. As the transport current is present, F_L together with thermal fluctuations, acts to depin the vortices and induce a collective flux motion. This very slow flux motion, called a thermally activated flux creep when F_P dominates, and the faster motion is called a flux flow when F_L dominates [169].

If vortices are immobilized by a counteracting F_P, a superconductor can sustain high J_c. However, the higher the current density, the greater F_L will act on the vortices. J_c is essentially the point at which the F_L begins to exceed the maximum available F_P [171]. The F_P is generated from the presence of lattice defects, which create potential energy wells for vortices. Size, shape, composition, structural interaction between the lattice and the defect define F_P of a single defect. These pinning sites can be divided into natural pinning sites, e.g. intrinsic pinning of the CuO_2 planes in HTSC, lattice defects formed during the sample deposition process, and artificial pinning centres (APC's), which can be obtained e.g. by doping superconducting materials with various non-superconducting foreign materials [172-174], substrate decoration [175–178] or through heavy-ion radiation [179, 180].

The critical current density is one of the most crucial properties of high temperature superconductor (HTSC) for both physical understanding and applications [181]. A lot of work has been carried out on the question of how to enhance the critical current density of superconducting material. There are a number of defect types that can act as artificial pinning centres (APC) which can be described as one-dimensional (1D-APC); such as dislocations [182-184] and nanorods [185], two-dimensional (2DAPC); such as grain boundaries [186, 187], anti-phase boundaries [188-190], surface roughness [191], and three-dimensional (3D-APC); such as nanoparticles and second phases [192] of size 'ξ' (coherence length) or more. Fig. 1.30 illustrates the various types of film defect that can be acted effectively as pinning center.

The experimental route is another classification criterion that can lead to artificial pinning centres such as antidotes (holes) [193, 194], magnetic-dots [194- 197] and substrate decoration [198-200] followed by deposition of superconducting phase by pulsed laser deposition (PLD), chemical solution deposition (CSD), metal-organic chemical vapor deposition (MOCVD) etc.

Another route is the fabrication of alternate layer (multi layer) [201-206] of APC and superconductor.

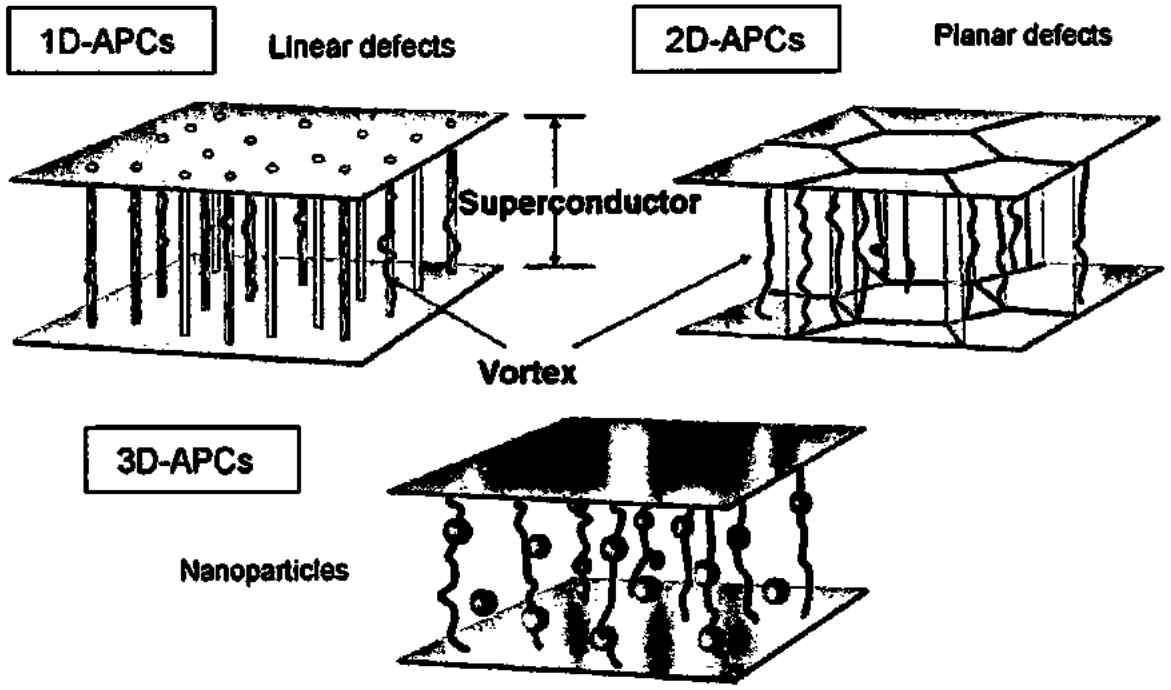

Fig. 1.30: An illustration of the dimensionality of artificial pinning centers (APC's): 1D-APC's, 2D-APC's, and 3DAPC's [192].

1.10 Nanostructures Inclusion in HTSCs

The superconducting properties of the compounds synthesized at ambient pressure are slightly lower than those prepared at high pressure. Relatively lower superconducting properties of different compounds of *HTSCs* family synthesized at ambient pressure in bulk form are mainly due to the presence of large density of inter-grains voids and pores in these compounds. There have been consistent efforts to overcome this problem and to enhance the superconducting properties of different compounds of *HTSCs* families by different techniques [207-209]. One of the most effective and easiest ways to address this issue is the inclusion of nanostructures at the grain-boundaries to heal up the inter-grains voids and pores to improve the inter-grains weak-links and superconducting properties of granular bulk superconductors. But the real challenge is to control the size, concentration and homogenous distribution of nanostructures at the grain-boundaries of the bulk *HTSCs* [210-213]. The improved inter-grains connections can facilitate the carriers transport across the inter-crystallite sites, but after certain optimum inclusion level of

nanostructure, the superconducting volume fraction start to decrease, which causes the suppression of superconductivity parameters. The nature of the material of nanostructure is also very crucial in this regards because nanostructure of different materials have different effects on the superconductor properties.

The addition of nanoparticles cause additional pinning centers, which help in increasing J_c in the polycrystalline structure [214, 215]. It was observed that low concentration of nano-ZnO particles addition in $(Cu_{0.5}Tl_{0.25}Pb_{0.25}) - 1223$ enhanced superconducting transition temperature, critical current density and melting point while high concentration of nano-ZnO particles enhanced the secondary phases and grain boundary resistance. This may be due to large agglomeration of nano-ZnO particles [216]. MgO nanoparticles dispersed in $Bi - 2212$ matrix retaining cubic morphology without disturbing the superconducting matrix structure results in improved J_c [217]. It was investigated that superconducting properties were improved by $nano - Fe_2O_3$ particles addition up to certain concentration level and then started to decrease with higher concentration of $nano - Fe_2O_3$ particles in $CuTl - 1223$ superconductor [218]. The study of the effects of Al_2O_3 nanoparticles addition on superconducting properties of $YBa_2Cu_3O_y$ revealed that there was no change in the structural symmetry, while the orthorhombicity slightly decreases with the increase of nano-Al_2O_3 particles content in the matrix. In applied magnetic field, J_c of the superconducting material was observed to be enhanced significantly by nano-Al_2O_3 addition, which can be rendered to the existence of the flux pinning centers [219]. Nano-Al_2O_3 particles in the polycrystalline $(Bi, Pb) - 2223$ superconductors illustrates greater transport properties. The volume pinning force density, onset temperature of dissipation, activation energy and J_c in applied magnetic field were found to be improved [220].

The addition of Ag nanoparticles in $Y - 123$ superconducting thin films reveals greater J_c values and improved structure in the form of higher crystallinity and ab alignment [221]. Multilayered nanostructures of metal-superconductor-semiconductor fabricated by electro-deposition technique show decrease in normal state resistance and offer improved properties than conventional materials [222]. Bulk superconductor $YBCO$ doped by Ag-nanoparticles of different size and concentrations showed monotonic increase in J_c and this is attributed to improvement of connectivity between crystallites and better crystallization [223]. Higher valued pinning centers may be created in superconducting MgB_2 by adding optimal SiC and Ag nano

powder of $30\ nm - 130\ nm$ size. The increase in amount above 16 wt.% of SiC and Ag nano powder, the supercurrent flow start decreasing [224]. In (nano-Ag)$_x$-CuTl-1223 composite volume fraction, T_c and J_c are improved up to $x = 1.5\ wt.\%$ and reverse trend is seen to be observed with further increase of nano-Ag particles [225]. ($Tl_{0.85}Cr_{0.15}$)$Sr_2Ca_2Cu_2O_7$-(Ag)$_x$ for x = 0.0 to 0.05) composites have shown decrease in T_c as compared to non added samples but XRD analysis confirm the dominancy of $Tl - 1212$ phase [226]. The addition of nanoparticles like Al_2O_3, ZrO_2, $NiFe_2O_4$ etc in suitable amount helps in generating the effective flux pinning centers, which can enhance the critical superconductivity parameters [227-229]. The addition of nanostructures of noble metals such as Ag and Au has shown significant improved superconducting parameters in many superconducting systems [230-233]. Increased nano-Ag content in $Bi - 2223$ improved the connectivity among the grains and enhanced J_c [234, 235].

1.11 References

[01] H. K. Onnes, Commun. Phys. Lab. Univ. Leiden **124** (1911).

[02] C. Kittel, "Introduction to Solid State Physics", John Wiley & Sons, 7th ed. (1996).

[03] Dzhumanov Safarali, "Theory of Conventional and Unconventional Superconductivity in the High-T_c Cuprates and Other Systems", Nova Science Publishers, Inc. New York (2013).

[04] W. H. Meissner and R. Ochsenfeld, Naturwissenschaften **21**, 787 (1933).

[05] F. London, and H. London, Proc. R. Soc. Lond. A **149**, 71 (1935).

[06] J. Bardeen, L. N. Cooper and J. R. Schrieffer, Phys. Rev. **108**, 1175 (1957).

[07] B. D. Josephson, Phys. Letters **1**, 251 (1962).

[08] I. G. Bednorz, and K. A. Mueller, Zeit. für Phys. **B 64**, 189 (1986).

[09] M. K. Wu, J. R. Ashburn, C. J. Torng, P. H. Hor, R. L. Meng, L. Gao, Z. J. Huang, Y. Q. Wang, and C. W. Chu, Phys. Rev. Lett. **58**, 908 (1987).

[10] S. S. P. Parkin, V. Y. Lee, E. M. Engler, A. E. Nazzal, T. C. Huang, G. Gorman, R. Savoy, and R. Beyers, Phys. Rev. Lett. **60**, 2539 (1988).

[11] A. Schilling, M. Cantoni, J. D. Guo, and H. R. Ott, Nature **56**, 363 (1993).

[12] S. N. Putilin, E. V. Antipov, A. M. Abakumov, M. G. Rozova, K. A Lokshin, D. A. Pavlov, A. M. Balagurov, D. V. Sheptyakov, M. Marezio, Physica C **52**, 338 (2000).

[13] S. N. Putilin, E. V. Antipov, O. Chmaissem, and M. Marezio, Nature **362**, 226 (1993).

[14] http://www.ccas-web.org/superconductivity

[15] J. F. Annett, "Superconductivity, Superfluids and Condensates", Oxford Univ. Press (2004).

[16] A. A. Abrikosove, Soviet Phys. JETP **5**, 1442 (1957).

[17] A. A. Abrikosov, "Fundamentals of the Theory of Metals" (Nauka, Moscow 1987).

[18] http:// web.ornl.gov

[19] J. B. Kettereson, and S. N. Song "Superconductivity", Cambridge Univ. Press (1999).

[20] V. V. Schmidt, "The Physics of Superconductors" P. Muller, and A. V. Ostinov (Eds), Springer (1997).

[21] Y. B. Rumer and M. S. Rivkin, Thermodynamics, Statistical Physics and Kinetics (Nauka, Moscow, 1977).

[22] F. London, "Superfluids" V. 1 JohnWiley, New York (1950).

[23] B. S. Deaver, and W. M. Faibank, Phys. Rev. Lett. **7**, 43 (1961).

[24] R. Doll, and M. Näbauer, Phys. Rev. Lett. **7**, 51 (1961).

[25] M. Tinkam, "Introduction to Superconductivity" (Atomizdat, Moscow, 1980).

[26] W. S. Corak, and C. B. Satterthwaite, Phys. Rev. **99**, 1660 (1954).

[27] S. Dzhumanov, and P. K. Khabibullaev, Pramana J. Phys. **45**, 385 (1995).

[28] S. Dzhumanov, Int. J. Mod. Phys. B **12**, 2151 (1998).

[29] G. M. Eliashber, Zh. Eksp. Theor. Fiz. **43**, 1105 (1962).

[30] B. B. Goodman, Phys. Rev. Lett. **6**, 597 (1961).

[31] H. Frohlich, Phys. Rev. **79**, 845 (1950).

[32] E. Maxwell, Phys. Rev. **78**, 477 (1950).

[33] C. A. Reynolds, B. Serin,W. H.Wright, and L. B. Nesbitt, Phys. Rev. **78**, 487 (1950).

[34] L. M. Falicow, IEEE Quantum Electronics. **25**, 2358 (1989).

[35] M. L. Cohen, G. Gladstone, M. A. Jensen, and J. R. Scrieffer, "Superconductivity in Semiconductors and Transition Metals" (Mir, Moscow 1972).

[36] V. L. Ginsburg, Zh. Eksp. Theor. Fiz. **14**, 134 (1944).

[37] A. S. Davidov, "High Temperature Superconductivity" (Naukova Dumka, Kiev, 1990).

[38] M. A. Bioni, M. P. Garfunkel, and A. O. McCoubrey, Phys. Rev. **101**, 1427 (1956).

[39] R. E. Glover, and M. Tinkham, Phys. Rev. **104**, 844 (1956).

[40] P. L. Richards and M. Tinkham, Phys. Rev. **119**, 575 (1960).

[41] G. Richaysen, Proc. Phys. Soc. **89**, 129 (1966).

[42] A. Vaknin, and Z. Ovadyahu, Z. Phys.: Condens. Matter **9**, L303 (1997).

[43] I. Giaever, Phys. Rev. Lett. **5**, 147 (1960).

[44] E. A. Lynton, "Superconductivity" (Mir, Moscow, 1971).

[45] D. R. Tilly, and J. Tilly, "Superfluidity and Superconductivity" (Adam Hilger, Bristol, 1990).

[46] P. L. Kapitza, Nature **141**, 74 (1938).

[47] L. D. Landau, J. Phys. (USSR) **11**, 91 (1947).

[48] C. J. Garter, and H. B. G. Casimir, Z. Techn. Phys. **15**, 539 (1939).

[49] F. London, and H. London, Physica **2**, 341 (1935).

[50] V. L. Ginzburg, and L. D. Landau, Zh. Eksp. Theor. Fiz. **20**, 1064 (1950).

[51] A. B. Pippard, Proc. Roy. Soc. **A203**, 210 (1950); **A216**, 547 (1953).

[52] D. Saint-James, and P. G. De Gennes, Phys. Lett. **7**, 306 (1963).

[53] C. P. Poole Jr., H. A. Farach, and R. J. Creswick, "Superconductivity", (Elsevier, *3rd ed.*, 2014).

[54] L. N. Cooper, Phys. Rev.**104,** 1189 (1956).

[55] R. A. Shukor, "High Temprature Superconductors: Materials, Mechanism and Applications", AkaedemiSains, Malaysia (2009).

[56] B. D. Josephson, Phys. Lett., **1,** 25 (1962).

[57] P. W. Anderson and J. M. Rowell, Phys. Rev. Lett., **10,** 230 (1963).

[58] L. N. Cooper, Phys. Rev. **104,** 1189 (1956)

[59] P. G. DeGennes, Rev. Mod. Phys. **36,** 225 (1964)

[60] M. Tinkham, Introduction to Superconductivity, McGraw-Hill, New York, 1996.

[61] W. C. Stewart, Appl. Phys. Lett., **12** ,277 (1968).

[62] D. E. McCumber, Jour. of Appl. Phys., **39,** 3113 (1968).

[63] C. Kaiser, High Quality Nb/Al-AlO_x/Nb Josephson Junctions, KIT Scientific Publishing (2011).

[64] J. C. Gallop, "SQUIDs, the Josephson Effect and Superconducting Electronics", Adam Hilger, Bristol (1991).

[65] A. K Saxena, "High Temperature Superconductors" Springer, New York (2010).

[66] A. K. Saxena, "Principles of Modern Physics" (Alpha Science International, Oxford, UK, 2007).

[67] A. J. Leggett, *Nature Physics* **2,** 134 (2006).

[68] A. Iyo, Y. Ishiura, Y. Tanaka, P. Badica, K. Tokiwa, T. Watanabe, and H. Ihara, Physica C **370,** 205 (2002).

[69] C. P. Poole, T. Datta, H. A. Farach, "Copper oxide superconductors" New York, NY; John Wiley and Sons Inc (1988).

[70] C. W. Chu, J. Superconductivity **12,** 85 (1999).

[71] C. W. Chu, IEEE Trans. Appl. Superconductivity **7,** 80 (1997).

[72] H. Yamauchi, M. Karppinen, and S. Tanaka, Physica C **263,** 146 (1996).

[73] X. Zhang, C. R. A. Catlow, S. C. Parker, A. Wall, Journal of Physics and Chemistry of Solids **53,** 761 (1992).

[74] P. Millet, O. Seeger, R. Enjalbert, J. Galy, Journal of Solid State Chemistry **90,** 344 (1991).

[75] S. Sato, I. Nakada, T. Kohara, and Y. Oda, Acta Cryst. **C44,** 11 (1988).

[76] M. Okada, Supercond. Sci. Technol. **13**, 29 (2000).

[77] N. P. Armitage, P. Fournier, and R. L. Greene, Rev. Mod. Phys. **82**, 2421 (2010).

[78] C. C. Tsuei and J. R. Kirtley, Rev. Mod. Phys. **72**, 969 (2000).

[79] C. N. R. Rao, Phil. Trans. R. Soc. Lond. **336**, 595 (1991).

[80] J. Karpinski, E. Kaldis, E. Jilek, and B. Bucher, Nature, Lond. **336**, 660 (1988).

[81] R. J. Cava, J. J. Krajewski, W. F. Jr. Peck, B. Betlogg, L. W. Rupp, R. M. Fleming, A. C. W. P. James, and P. Marsh, Nature, Lond. **338**, 328 (1989).

[82] R. S. Liu, R. Janes, M. J. Benett, and P. P. Edwards, App. Phys. Lett. **57**, 290 (1990).

[83] C. N. R. Rao, G. R. Rao, M. K. Rajumon, and D. D. Sarma, Phys. Rev. B **42**, 1026 (1990).

[84] R. M. Hazen, C. T. Prewitt, R. J. Angel, N. L. Ross, L. W. Finger, C. G. Hadidiacos, D. R. Veblen, P. J. Heaney, P. H. Hor, R. L. Meng, Y. Y. Sun, Y .Q. Yang, Y. Y. Xue, Z .J. Huang, L. Gao, J. Bechtold, and C. W. Chu, *Phys. Rev. Lett.* **60,** 12 (1988).

[85] A. A. Gapud, J. Z. Wu, B. W. Kang, S. L. Yan, Y. Y. Xie, and M. P. Seigal, Phys. Rev. B **59**, 203 (1999).

[86] H. Uchiyama, W. Z. Hu, A. Yamamoto, S. Tajima, K. Saiki, and A. Koma, Phys. Rev. B **62**, 615 (2000).

[87] L. Krusin-Elbaum, C. C. Tsuei, and A. Gupta, Nature **373**, 679 (1995).

[88] H. Higuma, S. Miyashita, and F. Uchikawa, Appl. Phys. Lett. **65**, 743 (1994).

[89] M. Hirabayashi, K. Tokiwa, H. Ozawa, Yoshihiro, Y. Noguchi, M. Tokumoto, and H. Ihara, Physica C **219**, 6 (1994).

[90] Sung-Ik, Mun-Seog Kim, and A. Iyo, Physica C **341**, 379 (2000).

[91] A. Sacuto, A. Lebon, D. Colson, A. Bertinotti, J. F. Marucco, and V. Viallet, Physica C **259**, 209 (1996).

[92] M. T. D. Orlando, A. G. Cunha, E. V. L. de Mello, H. Belich, E. Baggio-Saitovitch, A. Sin, X. Obradors, T. Burghardt, and A. Eichler, Phys. Rev. B **61**, 15454 (2000).

[93] S. N. Putilin, E. V. Antipov, O. Chnaissem, and M. Marezio, Nature **362**, 226 (1993).

[94] A. Schilling, M. Cantoni, J. D. Cuo, and H. R. Ott, Nature **363**, 56 (1993).

[95] J. G. Correia, J. P. Araujo, S. M. Loureiro, P. Toulemonde, S. Le Floch, P. Bordet, J. J. Capponi, R. Gatt, W. Troger, B. Ctortecka, T. Butz, H. Hass, J. G. Marques, and J. C. Soares, Phys. Rev. B **61**, 11769 (2000).

[96] L. Gao, Y. Y. Xue, F. Chen, Q. Xiong, R. L. Meng, D. Ramirez, C. W. Chu, J. H. Eggert, and H. K. Mao, Phys. Rev. B **50**, 4260 (1994).

[97] X. Zhou, M. Cardona, C. W. Chu, Q. M. Lin, S. M. Loureiro, and M. Marezio, Physica C **270**, 193 (1996).

[98] J. H. Eggert, J. Z. Hu, H. K. Mao, L. Beauvais, R. L. Meng, and C. W. Chu, Phys. Rev. B **49**, 15299 (1994).

[99] C. W. Chu, Y. Y. Xue, Z. L. Du, Y. Y. Sun, L. Gao, N. L. Wu, Y. Cao, I. Rusakova, and K. Ross, Science **277**, 1081 (1997).

[100] Y. Kitaoka, H. Mukuda, S. Shimizu, M. Abe, A. Iyo, Y. Tanaka, H. Kito, K. Tokiwa, and T. Watanabe J. Magnetism and Magnetic Mats. **310**, 467 (2007).

[101] Z. Z. Sheng and A. M. Hermann, Nature **332**, 55 (1988).

[102] Z. Z. Sheng, A. M. Hermann, A. E. Ali, C. Almasan, J. Estrada, T. Datta, and R. J. Matson, Phys. Rev. Lett. **60**, 937 (1988).

[103] Z. Z. Sheng and A. M. Hermann, Nature **332**, 138 (1988).

[104] G. Malandrino, D. S. Richeson, T. J. Marks, D. C. De Groot, J. L. Schindler, and C. R. Kannewurf, Appl. Phys. Lett. **58**, 182 (1991).

[105] M. L. Chu, H. L. Chang, C. Wang, J. Y. Juang, T. M. Uen, and Y. S. Gou, Appl. Phys. Lett. **59**, 1123 (1991).

[106] W. L. Oslon, M. M. Eddy, T. W. James, R. B. Hammond, G. Gruner, and L. Drabeck, Appl. Phys. Lett. **55**, 188 (1989).

[107] M. Kikuchi, T. Kajitani, T. Suzuki, S. Nakajima, K. Hi-raga, N. Kobayashi, H. Iwasaki, Y. Syono, and Y. Muto, J. Appl. Phys. **28**, 382 (1989).

[108] S. S. P. Parkin, V. Y. Lee, E. M. Engler, A. I. Nazzal, T. C. Huang, G. Gormau, R. Savoy, and R. Beyer, Phys. Rev. Lett. **60**, 2539 (1988).

[109] J. Y. Juang, J. H. Horng, S. P. Chen, C. M. Fu, K. H. Wu, T. M. Uen, Y. S. Gou, Appl. Phys. Lett. **60**, 885 (1995).

[110] A. Sundaresan, H. Asada, A. Crisan, J. C. Nie, H. Kito, A. Iyo, T. Tanaka, M. Kusunoki, S. Oshima, Physica C **388**, 473 (2003).

[111] D. J. Miller, J. G. Hu, J. D. Hettinger, K. E. Gray, J. E. Tkaczyk, J. Deluca, P. L. Karas, J. A. Sutliff, M. F. Garauskas, Appl. Phys. Lett. **63**, 556 (1993).

[112] D. N. Zheng, J. D. Johnson, A. R. Jones, A. M. Campbell, W. Y. Liang, T. Doi, M. Okada, K. Higashyama, J. Appl. Phys. 77, 5287 (1995).

[113] R. T. Liu, S. L. Yan, L. Fang, M. He, Supercond. Sci. Technol. 14, 948 (2001).

[114] R. S. Liu, D. N. Zheng, J. W. Loram, K. A. Mirza, A. M. Campbell, P. P. Edwards, Appl. Phys. Lett. 60, 1019 (1992).

[115] A. Iyo, Y. Aizawa, Y. Tanaka, M. Tokumoto, K. Tokiwa, T. Watanabe, and H. Ihara, Physica C 357, 324 (2001).

[116] O. Heiml, G. Gritzner, S. Tonies, H. W. Weber, J. Keckes, and B. Ortner, Supercond. Sci. Technol. 15, 1592 (2002).

[117] R. E. Gladyshevskii, E. Bellingeri, F. Marti, and R. Flukiger, J. Supercond. 11, 109 (1998).

[118] M. Paranthaman, J. R. Thompson, A. Goyal, A. J. Pedraza, and M. Kroeger, Appl. Phys. Lett. 67, 294 (1995).

[119] A. M. Panich, S. D. Goren, L. Frenkel Ben-Yakar, M. Eder, and G. Gritzner, Physica C 356, 129 (2001).

[120] I. Hase, N. Hamada, A. Iyo, N. Terada, Y. Tanaka, and H. Ihara, Physica C 357, 153 (2001).

[121] H. Ibach, and H. Lüth, "Solid-State Physics: An Introduction to Principles of Material Science" Springer (2009).

[122] A. K. Saxena, "High-temperature superconductors" (Heidelberg: Springer, 2010).

[123] Q. Jin, S. Adachi, X. J. Wu, H. Yamauchi, and S. Tanaka, Physica C 223, 238 (1994).

[124] X. J. Wu, S. Adachi, C. Q. Jin, H. Yamauchi, and S. Ta-naka, Physica C 223, 243 (1994).

[125] X. J. Wu, C. Q. Jin, S. Adachi, and H. Yamauchi, Physica C 224, 175 (1994).

[126] H. Ihara, Adv. Supercond. 7, 255 (1995).

[127] H. Ihara, Solid State Phys. 35, 301 (2001).

[128] M. Karppinen, H. Yamauchi, Y. Morita, M. Kitabatake, T. Motohashi, R. S. Liu, J. M. Lee, and J. M. Chen, J. Solid State Chem. 177, 1037 (2004).

[129] N. Hassan, "Solid-state synthesis and studies of Ni doped $Cu_{0.5}Tl_{0.5}Ba_2Ca_2Cu_{3-x}Ni_xO_{10-\delta}$ superconductors", Ph.D Thesis QAU Islamabad (2010).

[130] H. Ihara, Physica C 364, 289 (2001).

[131] N. A .Khan, M. Mumtaz, K. Sabeeh, M. I. A, Khan, and M. Ahmed, Physica C 407,109 (2004).

[132] M. Mumtaz. N. A . Khan, and S. Khan. J. Appl. Phys. **107**, 103905 (2010).

[133] M. S. Vijaya, "Materials Science" McGraw-Hill Publishing Company Limited (2003).

[134] H. Alloul, J. Bobroff, M. Gabay, and P. J. Hirschfeld, Rev. Mod. Phys. **81**, 45 (2009).

[135] A. V. Balatsky, I. Vekhter, and J. X. Zhu, Rev. Mod. Phys. **78**, 373 (2006).

[136] K. V. Samokhin, "Lecture Notes in Physics" **847**, 269 (2012).

[137] N. Ni, "Structural/magnetic phase transitions and superconductivity in $Ba(Fe_{1-x}TM_x)_2As_2$ single crystals" A dissertation in Iowa State University, Ames, Iowa, (2009).

[138] P. W. Anderson, Phys. Rev. **124**, 41 (1961).

[139] C. C. Tsuei, and J. R. Kirtley, Rev. Mod. Phys. **72**, 969 (2000).

[140] G. V. M. Williams, J. L. Tallon, and R. Dupree, Phys. Rev. B **61**, 4319 (2000).

[141] C. Bernhard, Ch. Niedermayer, T. Blasius, G. V. M. Williams, R. De Renzi, C. Bucci, and J. L. Tallon, Phys. Rev. B **58**, R8937 (1998).

[142] J. M. Tarascon, P. Barboux, P. F. Miceli, L. H. Greene, G. W. Hull, M. Eibschutz and S. A. Sunshine, Phys. Rev. B **37**, 7458 (1988).

[143] M. H. Julien, T. Fehér, M. Horvatić, C. Berthier, O. N. Bakharev, P. Ségransan, G. Collin, and J. F. Marucco, Phys. Rev. Lett. **84**, 3422 (2000).

[144] J. M. Tarascon, E. Wang, S. Kivelson, B. G. Bagley, G. W. Hull, and R. Ramesh, Phys. Rev. B **42**, 218 (1990).

[145] N. P. Armitage, P. Fournier, and R. L. Greene, Rev. Mod. Phys. **82**, 2421 (2010).

[146] J. L. Tallon, Phys. Rev. B **58**, 5956 (1998).

[147] B. Vom Hedt, W. Lisseck, K. Westerholt, and H. Bach, Phys. Rev. B **49**, 9898 (1994).

[148] Y. K. Kuo, C. W. Schneider, M. J. Skove, M. V. Nevitt, G. X. Tessema, and J. J. McGee, Phys. Rev. B **56**, 6201(1997).

[149] M. F. Chisholm and D. A. Smith, Philos. Mag. A **59**, 181 (1989).

[150] M. F. Chisholm and S. J. Pennycook, Nature **351**, 47 (1991).

[151] J. P. Hirth, and J. Lothe, "Theory of dislocations" (Wiley, New York, 1982).

[152] D. Dimos, P. Chaudhari, and J. Mannhart, Phys. Rev. B **41**, 4038 (1990).

[153] H. Hilgenkamp, and J. Mannhart, Rev. Mod. Phys. **74**, 485 (2002).

[154] J. Paglione, and R. L. Greene, Nat. Phys. **6**, 645 (2010).

[155] I. Mazin, Physics **4**, 26 (2011).

[156] J. E. Hoffman, Science **328**, 441 (2010).

[157] J. H. Xu, J. L. Shen, J. H. Miller, Jr., and C. S. Ting, Phys. Rev. Lett. **73**, 2492 (1994).

[158] J. R. Kirtley, C. C. Tsuei, M. Rupp, J. Z. Sun, L. S. Yu-Jahnes, A. Gupta, M. B. Ketchen, K. A. Moler, and M. Bhushan, Phys. Rev. Lett. **76**, 1336 (1996).

[159] R. P. Robertazzi, A. W. Kleinsasser, R. B. Laibowitz, R. H. Koch, and K. G. Staniasz, Phys. Rev. B **46**, 8456 (1992).

[160] J. Mannhart, P. Chaudhari, D. Dimos, C. C. Tsuei, and T.R. McGuire, Phys. Rev. Lett. **61**, 2476 (1988).

[161] P. A. Rosenthal, E. N. Grossman, R. H. Ono, and L. R. Vale, Appl. Phys. Lett. **63**, 1984 (1993).

[162] A. Sugimoto, T. Yamaguchi, and I. Iguchi, Physica C **367**, 28 (2002).

[163] T. Katase, Y. Ishimaru, A. Tsukamoto, H. Hiramatsu, T. Kamiya, K. Tanabe, H. Hosono, Nat. Commun. **2**, 409 (2011).

[164] J. H. Durrell, C. B. Eom, A. Gurevich, E. E. Hellstrom, C. Tarantini, A. Yamamoto, and D. C. Larbalestier, Rep. Prog. Phys. **74**, 124511 (2011).

[165] C. L. Song, Y. L. Wang, P. Cheng, Y. P. Jiang, W. Li, T. Zhang, Z. Li, K. He, L. Wang, J. F. Jia, H. H. Hung, C. Wu, X. Ma, X. Chen, and Q. K. Xue, Science **332**, 1410 (2011).

[166] T. Katase, H. Hiramatsu, V. Matias, C. Sheehan, Y. Ishimaru, T. Kamiya, K. Tanabe, and H. Hosono, Appl. Phys. Lett. **98**, 242510 (2011).

[167] S. Tanaka, Jap. J. App. Phys. **45**, 12 (2006).

[168] http://www.mn.uio.no/research/groups/amks/superconductivity/images/pinn.jpg

[169] G. Blatter, M.V. Feigel'man, V. B. Geshkenbein, A. I. Larkin, and V. M. Vinokur, Rev. Mod. Phys. **66**, 1125 (1994).

[170] J. Sarrao, and W. K. Kwok, "Basic Research Needs for Superconductivity" (U.S. Department of Energy, 2006), www.er.doe.gov/bes/reports/files/sc_rpt.pdf.

[171] S. R. Foltyn, L. Civale, J. L. MacManus-Driscoll, Q. X. Jia, B. Maiorov, H. Wang, and M. Maley, Nat. Mater. **6**, 631 (2007).

[172] J. L. MacManus-Driscoll, S. R. Foltyn, Q. X. Jia, H. Wang, A. Serquis, L. Civale, B. Maiorov, M. E. Hawley, M. P. Maley, and D. E. Peterson, Nat. Mater. **3**, 439 (2004).

[173] T. Haugan, P. N. Barnes, R. Wheeler, F. Meisenkothen, and M. Sumption, Nature **430**, 867 (2004).

[174] Y. Yamada, K. Takahashi, H. Kabayashi, M. Konishi, T. Watanabe, A. Ibi, T. Muroga, and S. Miyata, Appl. Phys. Lett. **87**, 132502 (2005).

[175] A. Crisan, S. Fujiwara, J. C. Nie, A. Sundaresan, and H. Ihara, Appl. Phys. Lett. **79**, 4547 (2001).

[176] T. Aytug, M. Paranthaman, A. A. Gapud, S. Kang, H. M. Christen, K. J. Leonard, P. M. Martin, J. R. Thompson, D. K. Christen, R. Meng, I. Rusakova, C. W. Chu, and T. H. Johansen, J. Appl. Phys. **98**, 114309 (2005).

[177] K. Matsumoto, T. Horide, K. Osamura, M. Mukaida, Y. Yoshida, A. Ichinose, and S. Horii, Physica C **412-414**, 1267 (2004).

[178] J. C. Nie, H. Yamasaki, H. Yamada, Y. Nakagawa, K. Develos-Bagarinao, and Y. Mawatari, Supercond. Sci. Technol. **17**, 845 (2004).

[179] T. Schuster, H. Kuhn, M. R. Koblischka, H. Theuss, H. Kronmülle, M. Kraus, and G. Saemann-Ischenko, Phys. Rev. B **47**, 373 (1993).

[180] L. Civale, A. D. Marwick, T. K. Worthington, M. A. Kirk, J. R. Thompson, L. Krusin-Elbaum, Y. Sun, J. R. Clem, and F. Holtzberg, Phys. Rev. Lett. **67**, 648 (1991).

[181] A. M. Campbell, and J. E. Evetts, Adv. Phys. **21**, 194 (1972).

[182] C. Gerber, D. Anselmetti, J. G. Bednorz, J. Mannhart, and D. G. Schlom, Nature **350**, 279 (1991).

[183] M. Hawley, I. D. Raistrick, J. G. Beery, and R. J. Houlton, Science **251**, 1587 (1991).

[184] J. Mannhart, D. Anselmetti, J. G. Bednorz, A. Catana, C. Gerber, K. A. Muller, and D. G. Schlom, Zeitschrift Fur Physik B-Condensed Matter, **86**, 177 (1992).

[185] J. L. Macmanus-Driscoll, S. R. Foltyn, Q. X. Jia, H. Wang, A. Serquis, L. Civale, B. Maiorov, M. E. Hawley, M. P. Maley, and D. E. Peterson, Nature Materials **3**, 439 (2004).

[186] K. S. Harshavardhan, M. Rajeswari, D. M. Hwang, C. Y. Chen, T. Sands, T. Venkatesan, J. E. Tkaczyk, K. W. Lay, and A. Safari, Applied Physics Letters **60**, 1902 (1992).

[187] T. L. Hylton and M. R. Beasley, Phys. Rev. B **41**, 11669 (1990).

[188] T. Haage, J. Zegenhagen, J. Q. Li, H. U. Habermeier, M. Cardona, C. Jooss, R. Warthmann, A. Forkl, and H. Kronmuller, Phys. Rev. B **56**, 8404 (1997).

[189] C. Jooss, R. Warthmann, H. Kronmuller, T. Haage, H. U. Habermeier, and J. Zegenhagen, Phys. Rev. Lett. **82**, 632 (1999).

[190] C. Jooss, R. Warthmann, and H. Kronmuller, Phys. Rev. B **61**, 12433 (2000).

[191] P. C. Mcintyre, M. J. Cima, J. A. Smith, R. B. Hallock, M. P. Siegal, and J. M. Phillips, J. Appl. Phys. **71**, 1868 (1992).

[192] K. Matsumoto and P. Mele, Supercond. Sci. Technol. **23**, 014001 (2010).

[193] V. V. Moshchalkov, M. Baert, V. V. Metlushko, E. Rosseel, M. J. VanBael, K. Temst, R. Jonckheere, and Y. Bruynseraede, Phys. Rev. B **54**, 7385 (1996).

[194] A. Silhanek, L. Van Look, R. Jonckheere, B. Y. Zhu, S. Raedts, and V. V. Moshchalkov, Physica C-Superconductivity and Its Applications, **460**, 1434 (2007).

[195] W. Gillijns, A. V. Silhanek, and V. V. Moshchalkov, Appl. Phys. Lett. **91**, 202510 (2007).

[196] A. V. Silhanek, W. Gillijns, M. V. Milosevic, A. Volodin, V. V. Moshchalkov, and F. M. Peeters, Phys. Rev. B **76**, 100502 (2007).

[197] V. F. Solovyov, H. J. Wiesmann, L. Wu, Q. Li, L. D. Cooley, M. Suenaga, B. Maiorov, and L. Civale, Supercond. Sci. Technol. **20**, L20 (2007).

[198] A. Crisan, S. Fujiwara, J. C. Nie, A. Sundaresan, and H. Ihara, Appl. Phys. Lett. **79**, 4547 (2001).

[199] A. Crisan, P. Badica, S. Fujiwara, J. C. Nie, A. Sundaresan, Y. Tanaka, and H. Ihara, Appl. Phys. Lett. **80**, 3566 (2002).

[200] A. Crisan, P. Badica, S. Fujiwara, J. C. Nie, A. Sundaresan, A. Iyo, and Y. Tanaka, IEEE Transactions on Applied Superconductivity, **13**, 3726 (2003).

[201] P. Paturi, M. Peurla, K. Nilsson, and J. Raittila, Supercond. Sci. Technol. **17**, 564 (2004).

[202] C. Cai, J. Hanisch, R. Huhne, V. Stehr, C. Mickel, T. Gemming, and B. Holzapfel, J. Appl. Phys. **98**, (2005).

[203] H. Huhtinen, P. Paturi, and E. Lahderanta, Physics of Low-Dimensional Structures, **9-10**, 25 (1999).

[204] P. Paturi, H. Huhtinen, K. Laajalehto, and R. Laiho, Supercond. Sci. Technol. **13**, 622 (2000).

[205] J. Raittila, M. Peurla, H. Huhtinen, P. Paturi, and R. Laiho, Physica C Superconductivity and Its Applications, **408-10**, 647 (2004).

[206] H. Huhtinen, M. Peurla, M.A. Shakhov, Y.P. Stepanov, P. Paturi, J. Raittila, R. Palai, and R. Laiho, IEEE Transactions on Applied Superconductivity, **17**, 3620 (2007).

[207] S. Acharya, A. K. Biswal, J. Ray, and P. N. Vishwakarma, J. Appl. Phys. **112**, 053916 (2012).

[208] M. H. Pu, W. H. Song, B. Zhao, X. C. Wu, T. Hu, Y. P. Sun, and J. J. Du, Supercond. Sci. Tech. **14**, 305 (2001).

[209] M. Miura, T. Kato, M. Yoshizumi, Y. Yamada, T. Izumi, Y. Shiohara, and T. Hirayama, Appl. Phys. Express **1**, 051701 (2004).

[210] S. Engel, T. Thersleff, R. Huhne, L. Schultz, and B. Holzapfel, Appl. Phys. Lett. **90**, 102505 (2007).

[211] T. Puig, J. Gutierrez, A. Pomar, A. Llordes, J. Gazquez, S. Ricart, F. Sandiumenge, and X. Obradors, Supercond. Sci. Technol. **21**, 034008 (2008).

[212] N. M. Strickland, N. J. Long, E. F. Talantsev, P. Hoefakker, J. Xia, M. W. Rupich, T. Kodenkandath, W. Zhang, X. Li, and Y. Huang, Physica C **468**, 183 (2008).

[213] M. Miura, M. Yoshizumi, T. Izumi, and Y. Shiohara, Supercond. Sci. Tech. **23**, 014013 (2010).

[214] P. E. Kazin, m. jansen, A. larrea, G. F. de La Fuente, and Yu. D. Treyakov, Physica C, **253**, 391 (1995).

[215] S. Huang, D. Dew-Hughes, and R. Jenkins, Supercond. Sci Technol., **11**, 1359 (19960

[216] M. M. Elokr, R. Awad, A. Abd El-Ghany, A. Abou Shama, and A. Abd El-wanis, J. Supercond. Nov. Magn. **24**, 1345 (2011).

[217] I. E. Agranovski, A. Y. Ilyushechkin, I. S. Altman, T. E. Bostrom, and M. Choi, Physica C **434**, 115 (2006).

[218] N. H. Mohammad, A. I. Abou-Aly, R. Awad, I. H. Ibrahim, M. Roumie, and M. Rekaby, J. Low Temp. Phys. **172**, 234 (2013).

[219] A. Mellekh, M. Zouaoui, F. Ben Azzouz, M. Annabi, and M. Ben Salem, Solid State Commun. **140**, 318 (2006).

[220] A. Ghattas, F. Ben Azzouz, M. Annabi, M. Zouaoui, and M. Ben Salem, J. Phys.: Conference Series. **97**, 012175 (2008).

[221] A. H. Li, M. Ionescu, H. K. liu, T. Silver, X. L. Wang, and S. X. Dou, IEEE Trans. Appl. Supercond. **15**, 3046 (2005).

[222] P. M. Shirage, D. D. Shivagan, L. A. Ekal, N. V. Desai, S. B. Mane, and S. H. Pawar, . Appl. Surf. Sci. **182**, 403 (2001).

[223] M. Farbod, and M. R. Batvandi, Physica C **471**, 112 (2011).

[224] K. J. Song, S. W. Kim, C. Park, J. K. Chung, and G. H. Rim, IEEE Trans. Appl. Supercond. 15, 2 (2005).

[225] W. Abdeen, N. H. Mohammed, R. Awad, S. A. Mahmoud and M. Hasebbo, J. Supercond. Nov. Magn. 26, 3235 (2013).

[226] W. Kong, A. K. Koh and R. Abd-Shukor, Sains Malaysiana 38 (3), 419 (2009).

[227] M. Annabi, A. M. Chirgui, F. B. Azzuoz, and M. B. Salem, Physica C 25, 405 (2004).

[228] M. Annabi, A. Ghattas, M. Zouaoui, F. Ben Azzouz, and M. Ben Salem, Physica C 468, 31 (2008).

[229] N. H. Mohammad, A. I. Abou-Aly, R. Awad, I. H. Ibrahim, M. Roumie, and M. Rekaby, J. Physica C 172, 234 (2012).

[230] T. D. Dzhafarov, M. Altunbas and T. Kucukomeroglu, Mater. Lett. 25, 81 (1995).

[231] B. Zeimetz, S. X. Dou, and H. K. Liu, J. Supercond. Sci. Technol. 9, 888 (1996).

[232] T. D. Dzhafarov, M. Altunbas and T. Kucukomeroglu, Solid. St. Comm. 99, 839 (1996).

[233] F. M. Julian, S. Ricart, A. Pomer, and L. M. Marzan, J. Nanoscience Tech. 11, 3245 (2011).

[234] M. N. Khan, M. Khizar, and B. N. Mukeshev, J. Physica B 321, 257 (2002).

[235] H. Najafpour, S. R. Shojaei, and S. M. Shojaeiu, J. Supercond. Non. Magn. 23, 487 (2010).

Chapter 2

Synthesis, Characterization Techniques and Theoretical Models

2.1 Synthesis

Nowadays, researchers are facing challenges regarding the synthesis of materials with anticipated composition, structure and properties for precise application. For the synthesis and fabrication of nanostructures, different physical and chemical methods can be used. Physical methods involve subdivision of bulk material (i.e. including mechanical crushing) and chemical methods involve decomposition of precursors. There are two approaches for synthesis of nanostructures;

i) Top down approach ii) Bottom up approach

i) Top Down Approach:

To obtain nano-sized particles, this approach requires consecutive cutting of bulk materials. The major issue with this approach is the crystallographic destruction, impurity phases and inadequacy of surface of the nano-sized particles. Irrespective of these drawbacks in this approach, it still plays a significant role in the production of nanostructures. Ball milling and lithography are common examples of top down approach [1].

ii) Bottom Up Approach:

Constructing a material from the bottom as cluster by cluster, atom by atom or molecule by molecule is known as bottom up approach. Drexler [2, 3] presented the bottom up approach as molecular nanotechnology in which materials are manufactured through the process of assembly. The physical forces managing the nano-scale merge the basic units into larger stable structures during the self-assembly. This approach assures an improved possibility to acquire nanostructures that has more homogenous chemical composition. Sol-gel and co- precipitation methods are examples of bottom up approach [1-5].

Diagrammatical representation for fabrication of nanostructures by 'top down' and 'bottom up' approaches is shown in Fig. 2.1.

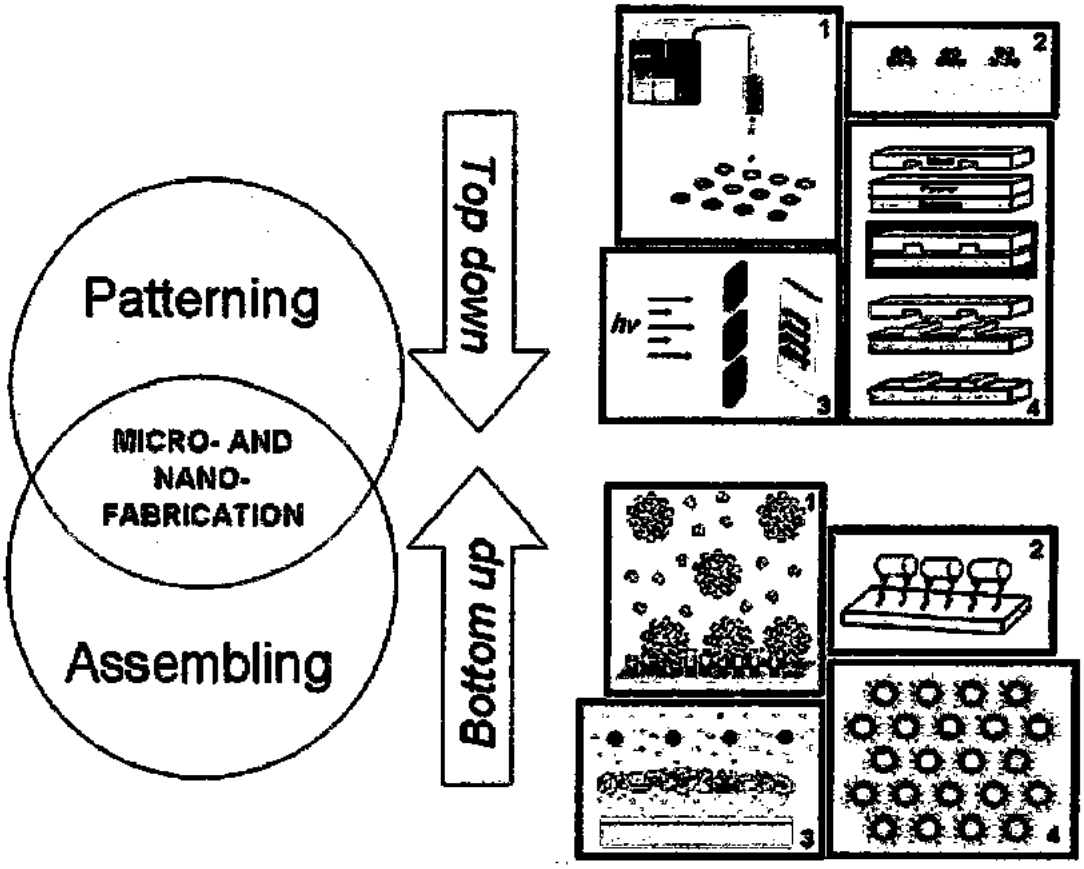

Fig. 2.1: Diagram of "top down" and "bottom up" approaches for fabrication of nanostructures [6].

2.1.1 Synthesis of Nanostructures

Many physical and chemical methods have been developed for the synthesis of nanostructures. Physical method in general includes, ball milling, arch discharge, spray pyrolysis and mechanical deformation techniques. Chemical methods comprise of many techniques like, hydrothermal, sol-gel, co-precipitation, thin film deposition, chemical vapor deposition, sono-chemical, sputtering and laser ablation. During synthesis of nanoparticles, some characteristics are important for better results. These characteristics include narrow particle size distribution, morphology, required chemical composition and crystal structure. Using chemical methods such as co-precipitation, sol-gel and hydrothermal, these characteristics can be attained [7, 8]. We used sol-gel and co-precipitation techniques to synthesize nanoparticles.

2.1.1.1 Sol- Gel Method

This method is very common and renowned amongst the scientists. This method is termed as; "an oxide network established by poly condensation reaction of a molecular precursor in a liquid". The starting materials used in the preparation of the "sol" are usually inorganic metal salts or metal organic compounds. A sol is a stable suspension of solid particles in a liquid, while

gel refers for solid network that has liquid phase. Sol-gel methods are commonly used to prepare nanostructure materials because these conversions occur readily with a wide range of precursors and can be conducted at low temperature [9-12].

Sol-gel has many advantages over other methods [13, 14].

- Better homogeneity compared to traditional mixed powder technology.
- High purity compared to mineral raw material sources.
- Lower temperature processing and consolidation is possible.
- More uniform phase distribution in multi-component systems.
- Better size and morphological control in powder synthesis.

2.1.1.2 Co-Precipitation Method

Co-precipitation method is an example of liquid phase synthesis technique. The reactions during co-precipitation method involve processes like simultaneous nucleation, growth and agglomeration of particles. In this method there is a reaction of metal salt solution with precipitating agent. Precipitation is the process which involves taking out the solute from solution which is insoluble in it. When the concentration of solute is made very high in the solution, the precipitation takes place and the solution gets super-saturated. The unstable solution leads toward agglomeration, as a result large clusters are produced. In order to control the size of nanostructures, the specific parameters are optimized to control the reaction. These parameters include reaction time, annealing temperature, pH value and ratio of reactants [15].

The advantages of co-precipitation method are:

- Very easy and cheap especially for the synthesis of metal oxide nanoparticles.
- Very efficient and quick, and particle size can easily be controlled.
- Environment friendly (it does not include any process which is hazardous for environment).
- It can be done easily in aqueous as well as non aqueous mediums.
- It does not require high temperature and thus it is less energy consuming.
- Large amount of products with high purity can be prepared.

2.1.2 Synthesis of High T_c Superconductors

For the preparation of high T_c superconductors, different methods of synthesis have been used. The main objective behind all of these synthesis techniques is to prepare single phase

materials having good superconducting properties [16, 17]. The solid state reaction method (also termed as ceramic method) is the most convincing and widely used conventional method. It is the most easy and straight forward synthesis procedure to get bulk samples such as high T_c superconductors. The solid state reaction is carried out at very high temperature with starting constituents in the solid form. If one of the compounds is volatile or sensitive to the atmosphere, then reaction is carried out in an evacuated sealed capsules normally made of gold. Alumina, gold, silica or platinum containers are generally used in the preparation of metal oxides. Normally, the starting materials are metal oxides, nitrates, carbonates or other salts, which are ground thoroughly to get homogeneous mixture. This homogeneous mixture is heated at an appropriate temperature for sufficient time to carry out reaction process. Some reactions require multi-step method for completion, the first step involves the synthesis of precursor material and the second step is to prepare the final compound by another heating process known as sintering process. The solid state reaction method has been successfully employed for the synthesis of large number of high T_c cuprate superconductors [18]. In spite of being popular and giving good results, this method has its own limitations. Therefore, some synthesis strategies have also been employed in the situations where it is required to control some factors such as oxygen stoichiometry, cation composition, cation oxidation state and carriers concentration.

There are also some disadvantages of the ceramic method:

i) To produce 100% homogeneous starting mixture is not possible. The purity of chemicals used as starting materials is still an issue for reproducible synthesis of high T_c cuprates.

ii) The entire reaction occurred in the solid state, first by phase boundary reaction and later by diffusion of constituents through the product phase. Diffusion path become longer and reaction rate slower with the progress of reaction. Between heating cycles, intermediate grinding can speed up the reaction up to some extent.

iii) To monitor the progress of the reaction, there is no simple and authentic way. Due to this complexity of the method, one can ends up with mixtures of reactants and products.

iv) So it is difficult to get a compositionally homogeneous product even at the completion of the reaction.

Regardless of the above mentioned limitations, the ceramic method is widely used for the synthesis of large variety of inorganic solids. A successful synthesis by the ceramic method depends on several factors, which includes the nature of the starting materials, the homogeneity of the mixture of powders, the rate of heating as well as the reaction temperature and duration.

2.1.3 Synthesis of CuTl-based Bulk Superconductors and Nano-superconductors Composites

The bulk superconductor of $Cu_{0.5}Tl_{0.5}Ba_2Ca_2Cu_3O_{10-\delta}$ was prepared adopting solid state reaction technique. Initially $Ca(NO_3)_2$, $Ba(NO_3)_2$ and Cu(CN) were used as initiating compounds to prepare host bulk's precursor material. These compounds were mixed in suitable ratios and ground in an agate mortar and pestle for 2 h. The mixed material was loaded in quartz boats and fired at 860°C for 24 h in furnace. The precursor material was cooled down to room temperature after 24 h. This precursor material was again ground for about 1 hour and again placed in the furnace under the same conditions (i.e. 860°C for 24 h). Later on, an appropriate amount of thallium oxide (Tl_2O_3) and already prepared nanoparticles (NP's) with different weight percent (x) were mixed in this precursor material and ground again for about 1 h. The ground material was then pelletized under 3.8 tons / cm^2 pressure and wrapped in gold capsule and finally sintered at 860°C for 10 minutes in preheated chamber furnace followed by quenching to room temperature. The final product obtained as "$(NP's)_x/Cu_{0.5}Tl_{0.5}Ba_2Ca_2Cu_3O_{10-\delta}$" nano-superconductor composite.

2.2 Experimental Characterization Techniques

The synthesized samples were then characterized using following techniques;

- X-ray diffraction (XRD),
- Scanning electron microscope (SEM),
- Energy dispersive X-ray analysis (EDX),
- Dc-resistivity measurements,
- Critical current measurements
- AC susceptibility measurements
- Fourier transform infrared (FTIR) spectroscopy

2.2.1 X-ray Diffraction (XRD)

XRD is a fundamental characterization technique, which gives detailed information about cell parameters of a unit cell, crystal structure, crystallite size and degree of crystallinity. Since the wave length (λ) of X-ray is in the range of 0.01-10nm, so it is a prime tool for probing structure of nano-materials. In 1912, the German physicist Max von Laue discovered diffraction of X-rays by crystals. This discovery revealed that crystal act as three-dimensional diffraction grating for X-rays beam. The most frequently used technique for the characterization of the material was XRD in those days. Using XRD, information about the crystalline nature of a material, nature of the phase present, lattice parameter and grain size can easily be acquired through this technique. The XRD is an appropriate technique for all form of samples such as powder, bulk as well as thin film [19, 20].

In 1912, W. L. Bragg explained the diffraction phenomenon very well that "the diffraction occurs only if the planes of the crystal act like mirrors when X-rays fall on them". When a monochromatic beam of X-rays is incident on the material placed under it, two types of interferences take place. The constructive interference takes place between those scattered waves which obeys the Bragg's law and for the others destructive interference is produced. X-rays can be reflected at many angles from a sequence of crystallographic planes but for the sake of simplicity only two diffracted rays are shown in Fig. 2.2.

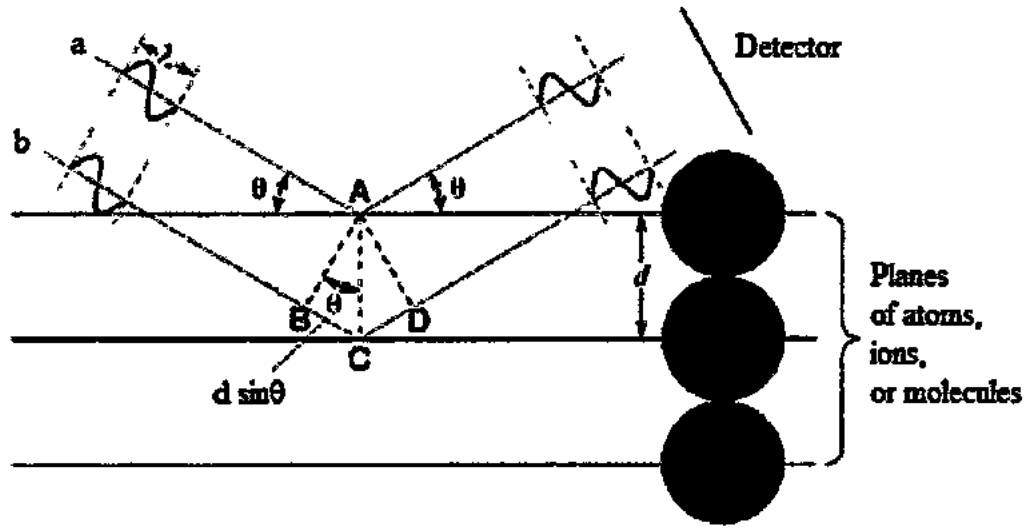

Fig. 2.2: Geometrical representation of Bragg's law and crystals planes [21].

Bragg's law can be expressed mathematically as;

$$2d\sin\theta = n\lambda \qquad 2.1$$

Here d and θ represent the inter planer spacing and Bragg angle respectively, while n has integral values, which give the order of diffraction.

For a crystalline sample this law connects the wavelength of electromagnetic radiation to the lattice spacing and diffraction angle. The diffracted $X-rays$ are then detected in a range of 2θ angles. In powder samples, all probable diffraction of the lattice must be achieved due to random orientations of the crystals. Every material has a specific set of d-spacing which permits detection of the materials by converting diffraction peaks to d-spacing. The size of the nanocrystals can be obtained by peak broadening by using Scherrer formula as given below;

$$D=\frac{k\lambda}{\beta cos\theta_B} \qquad 2.2$$

Where D is the average crystallite dimension perpendicular to the reflecting phases, "λ" is the X-ray wavelength, k is the Scherrer constant which is equal to 0.9 for the spherical particles, whose values depends on the shape of the particle, θ_B is Bragg angle and β is the full width at half maximum (FWHM) of the peaks [21, 22].

For the diffraction analysis, X-rays originating from K shell are used because of shorter wavelength as compared to the X-rays coming from L or M shell transition. In X-ray tubes, target materials are normally made of Cu or Mo, which produce X-rays with wavelengths of 1.54Å and 0.8Å respectively. The schematic diagram of an X-ray diffractometer is shown in Fig. 2.3.

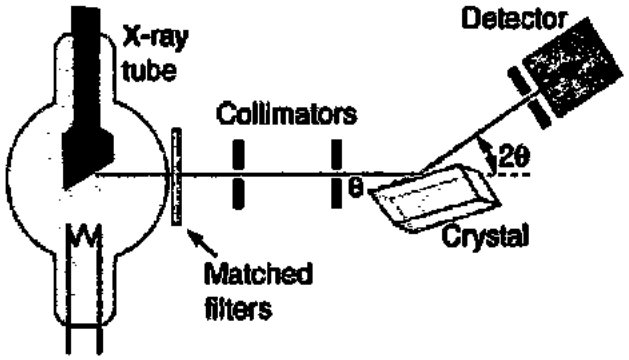

Fig. 2.3: Schematic diagram of X-ray diffractometer [23].

An evacuated glass tube fitted with a filament and a metal target is used for X-ray diffraction. Electrons produced from heated filament are accelerated by applying high voltage between the filament and metal target. The wavelength of the emitted X-rays depends on the nature of the target material. These rays are collimated in the form of a narrow beam focused on the sample

material. The rays diffracted at different angles are detected by the detector. The intensity of the diffracted rays along with diffracted angles is recorded carefully. We have performed these analyses on a diffractometer from "D/Max III Rigaku with a CuKα source of wavelength 1.54056Å". The XRD spectra were analyzed by using crystallography software "Check Cell".

2.2.2 Scanning Electron Microscopy (SEM)

SEM is a versatile instrument, which generates images of a sample under observation by probing its surface with high energy electrons. Light microscope creates magnified image using lenses where as SEM uses wave nature of electrons instead of light waves to create magnified image. Fig. 2.4 shows the schematic diagrams of these two microscopes. Electrons interact with the atoms of sample and produce different signals. These signals reveal important information about the sample including its chemical composition, external morphology and orientation of crystallites making the sample. SEM can produce three dimensional images with better resolution. Signals generated by SEM consists of secondary electrons, back scattered electrons (BSEs) and characteristic X-rays.

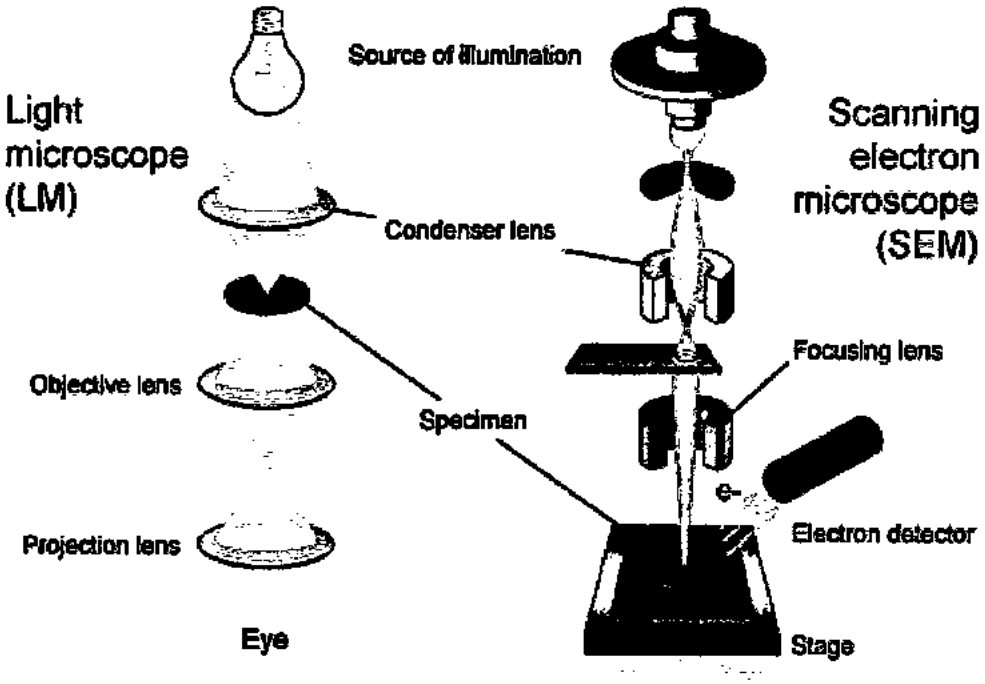

Fig. 2.4: Schematic diagrams of a light microscope compared to scanning electron microscope [24].

The most common detection mode is secondary electron imaging mode, which produces images with very high resolution and have wide range of magnification (10 times to 500,000

times). BSEs are those electrons which are reflected from surface of the sample by elastic scattering. Images formed by signals of back scattered electrons contain detailed information about the distribution of various elements in the sample. Characteristic X-rays are produced, when a beam of electron strikes with the inner shell electrons and remove them from the sample. These characteristic X-rays are important to categorize the elemental composition. Thermionically emitted electron beam from an electron gun (having tungsten filament) is used in scanning electron microscope. The vacuum pump is used to create vacuum in order to avoid interference of electrons with their surroundings. These electrons move through series of lens before approaching the target. Electron beam of high energy is focused to a small spot. When this energetic beam falls on surface of a sample, electrons begin to lose their energy due to scattering and absorption. The energy exchange between electrons and sample produces reflection and emission of electrons along with the emission of electromagnetic radiations. These reflected electrons, emitted electrons and emitted radiations can be detected by detectors to produce a magnified image [25, 26]. We have examined the composition and morphology of the materials with a JOEL Jed-2300.

2.2.3 Energy Dispersive X-ray Analysis (EDX)

EDX system works on the integrated characteristics of the SEM. It provides information about the elemental composition of a material. A beam of incident electrons is directed towards the sample under investigation, it may cause inter-shell transitions, which become responsible for electron hole pairing. When an electron from a higher energy orbit fills a hole in lower energy orbit, a difference of energies among the orbit might be emitted in the form of X-rays as shown in Fig. 2.5.

The number and energy of the obtained X-rays can be calculated by an energy dispersive spectrometer. Since the energy of the X-rays is a feature of the difference in energy between the orbits; this gives an opening for observation of the elemental composition of under observed sample [27, 28].

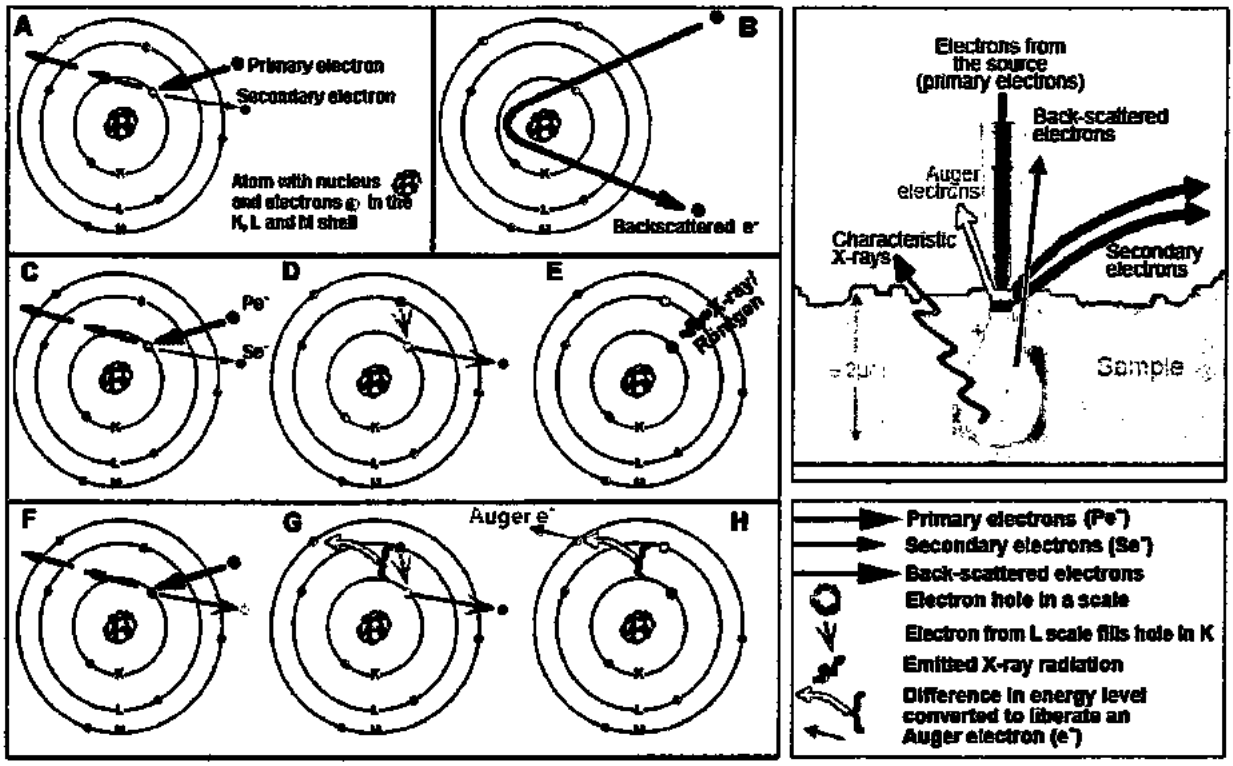

Fig. 2.5: Demonstration of shell transition and emission of X-rays [29].

2.2.4 DC Resistivity Measurements

Resistivity depends on the nature of the material and is different for different materials. The critical temperature $T_c(R=0)$, the onset temperature of superconductivity $T_c(onset)$ and their normal state properties can be found through the resistivity measurements. The scattering of electron due to defects in the lattice, electron-electron collision and lattice vibration are the main sources of resistivity in the normal state [30]. The electron-electron scattering is negligible as compared to scattering from the defects and lattice vibrations. So the resistivity can be calculated by adding the temperature independent residual resistivity ρ_{def} and temperature dependent phonon scattering resistivity $\rho_{ph}(T)$ as

$$\rho = \rho_{ph}(T) + \rho_{def} \qquad 2.3$$

Resistivity depends on the nature of the material. The four-probe method is one of the most extensively used techniques for the dc- resistivity measurements. In this technique, four leads are attached at sample surface at equal distances by using silver paint [31]. A schematic diagram of four-probe is shown in Fig. 2.6. A constant current is supplied by the two outer probes while the

resulting voltage drop is measured by the two inner probes. The dimensions of the slab-shaped samples were $1.2\times1.0\times4.0mm^3$. The resistivity is calculated by using the following relation

$$\rho = \frac{VA}{IL} \qquad 2.4$$

Where, 'V' is voltage drop across the sample, 'I' is current through the sample, 'L' is length and 'A' is the cross sectional area of the sample.

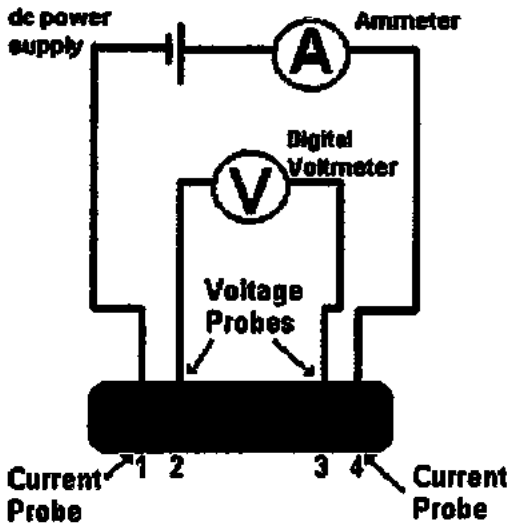

Fig. 2.6: Schematic of four-probe.

We have used Physical Properties Measurement System (PPMS-9) manufactured by Quantum Design for electrical dc-resistivity measurements. The Quantum Design PPMS measures DC Resistivity, AC Transport (AC Resistivity, Hall Coefficient, I-V Curve and Critical Current for superconductors), and Heat Capacity for small samples under user controlled magnetic field, pressure, gas composition, and temperature. The magnetic field may be programmed anywhere from 0 to 8 tesla and the sample's temperature can be programmed from 1.9 to 400 K. A PPMS set up is shown in Fig. 2.7. A measuring current of 1 mA was supplied during the dc-resistivity measurements. During these measurements, the temperature stability was kept at 2 mK. The dc-resistivity measurements were carried out during the heating cycle from 35 K to room temperature. The heating rate between 1 K/min to 3 K/min was applied during these measurements.

Fig. 2.7: Physical properties measurements system (PPMS) set up.

2.2.5 Critical Current Measurements

For a superconductor, the transport critical current measurements are very important. The maximum value of the current, which can flow through a superconducting sample without destroying its superconductivity, is known as critical current "I_c". Superconducting state of the material will convert to normal state when the value of current exceeds this critical value (I_c). For a superconductor, the transport critical current measurements are very important. The four probe method was also used for the critical current measurements. In this method, the sample was cooled down to 70 K and studied for different values of current. When voltage starts to appear across the voltage contacts, values of current recorded (the appearance of voltage reveals the transition of material from superconducting to normal state). IV measurements were carried out at 50 K below the zero resistivity critical temperature. The criterion of J_c for I-V measurements was kept at 1μV/cm at 50 K in a zero applied magnetic field.

2.2.6 AC Susceptibility Measurements

High temperature superconductors have also interesting magnetic properties such as Meissner's effect. For the characterization of high temperature superconductors, it is very necessary to study their magnetic properties. When a substance is placed in an applied magnetic field, it is magnetized in response to the applied field. The response of the material to an applied magnetic field is known as susceptibility. There are two types of magnetic susceptibilities; DC susceptibility and AC susceptibility. AC susceptibility is measure of the response of the material

in the presence of AC magnetic field and DC is measure of the material's response to DC magnetic field. In the case of a DC magnetic field, the susceptibility is given as

$$\chi_{dc} = \frac{M}{H_{dc}} \qquad 2.5$$

Where M is the magnetization of the material and H_{dc} is the applied field.

In the case of AC magnetic field, the sample's magnetic moment 'm' changes with the field. As magnetic moment 'm' is related with the spin motion or orbital motion of the electrons, it measures the magnetic field generated by the sample. The magnetization 'M' is the net magnetic moment/unit volume denoted by M as shown below

$$M = \frac{m}{V} \qquad 2.6$$

The expression for AC susceptibility is given by

$$\chi_{ac} = \frac{dM}{dH_{ac}} \qquad 2.7$$

The complex AC susceptibility has two parts, i.e. χ' and χ''.

$$\chi = \chi' + \chi'' \qquad 2.8$$

χ' is in phase with applied magnetic field H and is known as the real part of χ. While χ'' is 90° out of phase with the H and is known as imaginary part of χ. The χ' shows the shielding of superconducting volume fraction of the material from the AC field (diamagnetic effect), while imaginary part 'χ''' gives AC losses in the material. There can be two peaks in the imaginary part of AC susceptibility; first one is the intrinsic peak while the second one is coupling or inter-granular peak. The intrinsic peak appears at high temperature, gives losses due to screening of the magnetic flux by the superconducting surface currents, while other peak (coupling peak) appearing at low temperature, gives losses due to magnetic flux penetration in the given boundary regions. This coupling peak gives information about the weak links between the superconducting grains. The coupling peak shifts to lower temperature by increasing the applied field, while intrinsic peak position is independent of the strength of applied magnetic field and its frequency.

The AC susceptibility can be measured with the help of susceptometer, which consists of a primary coil and two secondary coils wound on non-magnetic material. The purpose of primary

coil is to produce AC magnetic field and two secondary coils wound oppositely to primary coil act as pick up coils to detect the diamagnetic signals. The linking flux in secondary coils is in opposite direction, so net induced *emf* becomes zero. When a superconducting material is put in one of the secondary coils and temperature is lowered below its critical value, voltage balance is disturbed between the two coils and a signal is observed, which is proportional to the susceptibility of the superconducting material. The voltage 'v' observed in the superconducting state is given as

$$v = VfH_a\chi \qquad 2.9$$

Where f is the frequency of the applied magnetic field H_a and V is the volume of the sample. From the Eq. 2.9, it is clear that the dependence of the resulting signal is on the volume of the sample and strength of the applied magnetic field. So, the sample should have such volume that it can occupy maximum space inside the coil.

The AC susceptibility technique is very important for the study of pinning properties, inter-granular coupling, transport critical current density and contact less resistivity measurements of superconductivity [32-36]. The system used for the AC susceptibility measurements is shown in the Fig.2.8.

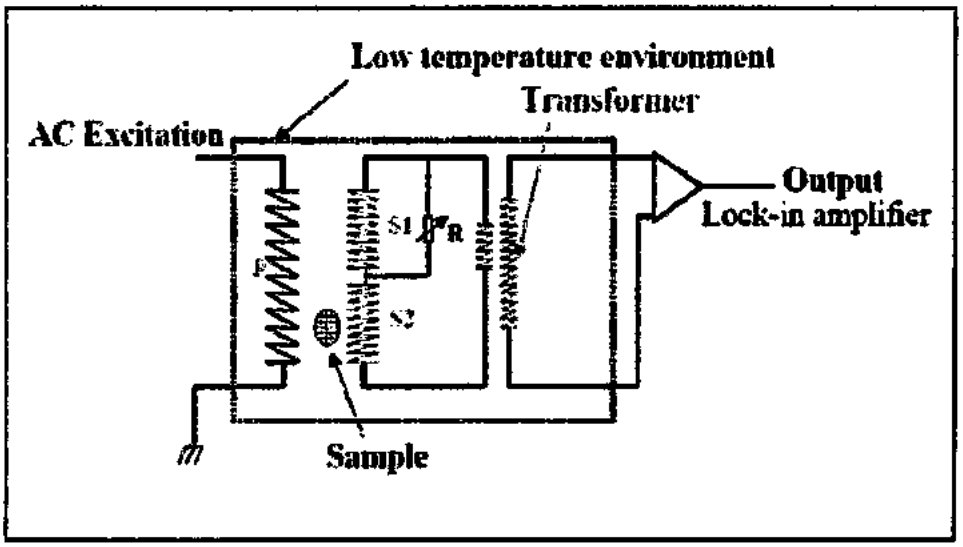

Fig. 2.8: Experimental setup for AC susceptibility measurements.

A copper wire of gauge 34 was used in susceptometer for primary as well as for secondary coils. The sample under observation was placed in lower parts of secondary coil and temperature lowered to 77 K by using liquid nitrogen Dewar. A function generator "Model HP 3314A" was used to produce signal of one volt (peak to peak) at 270 Hz and amplified from a lock-in

amplifier "Model SR 530". It was observed that when the values of frequency were higher than 270 Hz, the critical current decreased. For the measurements of temperature, a T-type (copper-constantan) thermocouple was fitted in the intermediate vicinity of the sample. The output of the lock-in amplifier is coupled to the XY graph plotter.

2.2.7 Fourier Transform Infrared Spectroscopy (FTIR)

FTIR spectroscopy is a technique used to get spectrum of absorption, emission or photoconductivity of the material. This spectroscopy carries advantages over dispersive spectroscopes, in range of wavelength of spectrum. As we know that, in solids, atoms and molecules are in state of continuous vibrations even at the temperature of absolute zero. A molecule can vibrate by bending, stretching and contraction of the bonds joining the two atoms. The energy associated with these vibrations, quantum mechanically, can be determined by simple harmonic oscillator approximation as;

$$E_n = (n+\frac{1}{2})\hbar\omega_o \qquad 2.10$$

For $n = 0$, $E_o = \frac{1}{2}\hbar\omega_o$ shows that ground state energy is non-zero for molecular vibrations. To detect these molecular vibrations and their measurements, spectrometer used is known as FTIR spectrometer. Basically, FTIR spectrometer consists of a Michelson interferometer, which separates the infrared radiation into its components of different wavelengths. A basic diagram of a Michelson interferometer is shown in Fig. 2.9 in which, one beam splitter and two mirrors (one is fixed and other is movable) are used. Beam splitter should be of such material, which is semi transparent to infrared light. When infrared radiations from the source enter into Michelson interferometer, beam splitter partially transmits the beam and reflects the remaining part of the beam. Transmitted part of beam strikes with fixed mirror and reflected part strikes with movable mirror. After reflection from mirrors, both beams combine with each other at beam splitter to produce interference and finally collect by the detector for sample analysis. A schematic diagram of FTIR system is shown in Fig. 2.10. As the frequency of the lattice vibrations lies in the infrared region, therefore the infrared radiations are used to detect these vibrations [37].

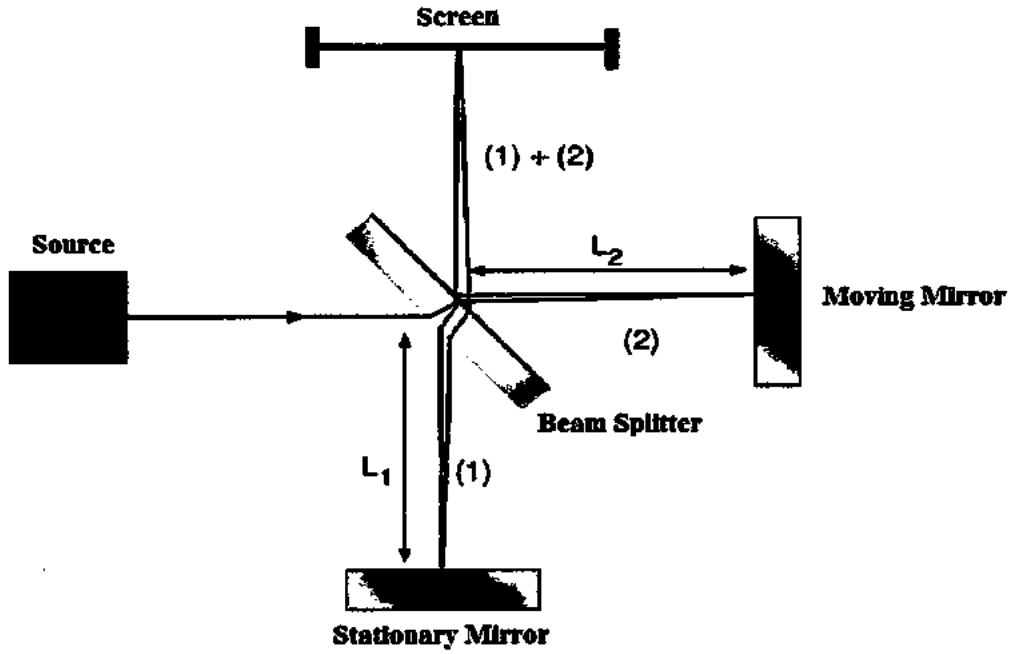

Fig. 2.9 A basic diagram of Michelson interferometer.

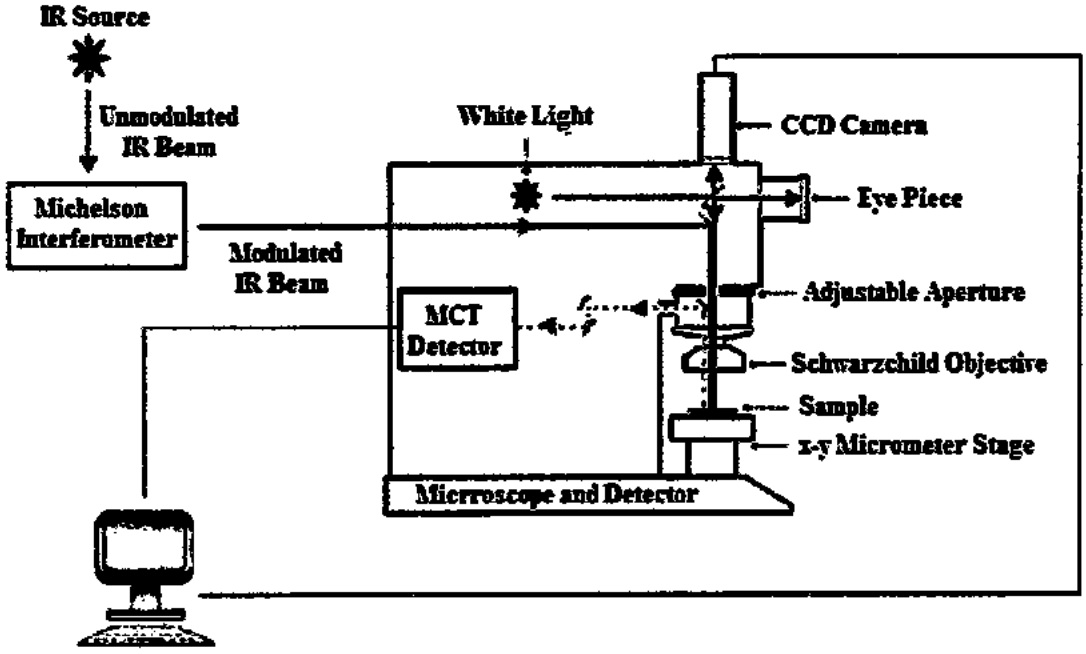

Fig. 2.10 A schematic diagram of FTIR system.

When infrared radiations fall on the material, these radiations interact with the molecules. If frequency of the infrared radiations matches with the natural frequency of the lattice vibration, the radiations will be absorbed and absorption peaks related to these vibrational modes will appear in the spectrum. All vibrational modes in the material are not active for infrared, but few vibrational modes producing fluctuating dipole moment and interacting with the electric field of

infrared radiations, are active for infrared. As the molecules of H_2, N_2, O_2, etc have no dipole moments, therefore these are inactive for infrared. For example, in case of CO_2, the symmetrical stretching or contraction does not produce oscillating electric field, so these modes do not appear in an infrared spectrum. But asymmetrical stretching or contraction can absorb infrared radiations due to fluctuating dipole moment [38]. The vibrational modes of CO_2 are shown in Fig. 2.11.

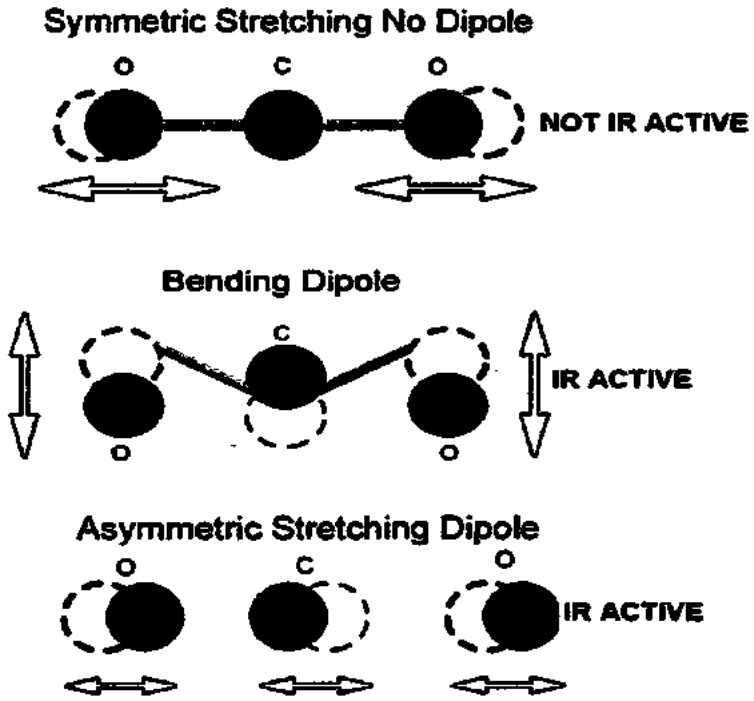

Fig. 2.11 Molecular vibration of CO_2.

Electron-phonon interaction is one of the possible origin of superconductivity in conventional superconductors. FTIR spectroscopy is very useful tool to study the possible correlation between lattice vibration and superconductivity An FTIR spectrometer "Nicolet 5700" was used for the study of absorption spectrum. In case of these superconducting samples, very small amount of the sample was mixed with *KBr*, and thin pellets were made. Before observing the sample spectrum, the background spectrum with *KBr* pellet was taken. The number of scans taken for the background and the sample spectrum were 10 and 50, respectively. The resolution of the spectrometer was 4 cm^{-1} in spectral range of 400-700 cm^{-1}. The resulted spectra were interpreted by using the lattice dynamical calculations of the optical modes of

vibrations in HTSCs. The lattice dynamical data is helpful in assigning vibrational modes to a particular atom in superconducting samples.

2.3 Theoretical Models

It is discussed in the first chapter that the Ginsburg Landau theory is one of the mathematical description of the superconductors. GL Theory also explains the thermodynamic fluctuation in the vicinity of transition temperature. This microscopic theory is the verification to the theoretical understanding of superconductivity [39]. According to this scenario, the HTSCs show a complex behavior that is linked with the thermodynamic fluctuation of the superconductivity order parameter. These thermodynamic fluctuations affect the electrical resistivity in general phase [40]. Ginsburg was the first one who calculates the fluctuation near the transition. He supposed the modification of fluctuation in type-I superconductors which marked in temperature regime.

$$\frac{\Delta T}{T_c} \sim \left[\frac{(T_c)^4}{\varepsilon f}\right] \sim \left[\frac{(a)^4}{\xi}\right] \sim 10^{-14} \text{ to } 10^{-16} \qquad 2.11$$

Where 'a' is inter-atomic distance, 'ξ' is coherence length and T_c is critical temperature. These microscopic values describe why for so long time, the fluctuation fact was distanced to experimental study in superconductors. Superconductor is made of various layers and these layers are responsible for disturbance in superconducting properties. Furthermore, these layers are placed one on the others; these layers hold up with the property of the superconductors, which makes them anisotropic. It is because of large anisotropy, fluctuations in the "order parameter" activate the effect on the cooper pairs. Here, the pairs are forced to move along c-axis and ab-plane with opposition along the major axis [41]. The studies of resistivity $\rho(T)$ versus temperature curve mark a bend of curve from linear state to nonlinear state. This change in the curve is result of superconducting fluctuation above critical region. The induced fluctuation in this (critical) region can be predicted by,

$$\Delta\sigma(T) = \frac{1}{\rho(T)} - \frac{1}{\rho_n(T)} \qquad 2.12$$

Here $\rho(T)$ is actually calculated resistivity which is equal to $\frac{1}{\sigma(T)}$, while $\rho_n(T)=\frac{1}{\sigma_n(T)}=\alpha+\beta T$ is extrapolated as normal-state resistivity with β is gradient of extrapolated curve.

In order to study excess conductivity, we use some theoretical models to dig out the parameter which are contributing in conductivity. These models are named as Aslamazov-Larkin (AL) model and Lawrence-Donaich (LD) model. Here it is noteworthy that for polycrystalline samples, AL model gives us a depiction of fluctuation in inter-grain and intra-grain regions [42], whereas, LD model is associated with fluctuation in intra-grain region of layered superconductor. Other contribution is because of Maki-Thompson (MT) which manifests effect of fluctuation on the "normal electron" [43-45].

2.3.1 Aslamazov-Larkin (AL) Model

AL model explains the effect of fluctuation on the conductivity or Para-conductivity. The excess conductivity is completely described by two contributions, which is given by

$$\Delta\sigma=\Delta\sigma_{AL}+\Delta\sigma_{MT} \qquad 2.13$$

The first contribution, according to AL model derived from the mean field theory is used to develop the excess conductivity '$\Delta\sigma$' above T_c. This is a direct contribution to the excess conductivity [46, 47] and mathematically it is given as

$$\Delta\sigma_{AL}(T)=A\varepsilon^{-\lambda} \qquad 2.14$$

Where 'A' is fluctuation amplitude, λ is related to dimensions of fluctuation and known as critical exponent and ε is the reduced temperature given by the mathematical relation as

$$\varepsilon=\ln\left[\frac{T-T_c^{mf}}{T_c^{mf}}\right] \qquad 2.15$$

Where T_c^{mf} is mean field critical temperature, at which change in value of resistivity is maximum with respect to temperature (separation between critical region and mean field region) [48, 49]. It can be determined from the point of variation of the temperature derivative of resistivity $(d\rho/dT)$. Critical exponent λ is given as λ= 2-D/2; λ= 3/2, λ= 1, and λ= 1/2 for one, two and three dimensional fluctuations, respectively. For all these dimensional fluctuations, the fluctuations amplitude 'A' is given by [50]

$$A(1D)=\frac{e^2\xi_c(0)}{32\hbar s} \quad \textit{for 1D fluctuation} \qquad 2.16$$

$$A(2D)=\frac{e^2}{16\hbar d} \quad \textit{for 2D fluctuation} \qquad 2.17$$

$$A(3D)=\frac{e^2}{32\hbar\xi_c(0)} \quad \textit{for 3D fluctuation} \qquad 2.18$$

Here $\xi_c(0)$ is zero coherence length in c-axis, 'd' represents the thickness of the 2D system, 'e' is electronic charge ,' $\hbar$ ' is the reduced Planks constant, and ' s ' is the cross-sectional area of the 1D system.

2.3.2 Lawrence-Donaich (LD) Model

LD model gives the complete description of fluctuation in intra-grain region. Here superconducting layers are coupled by the Josephson Effect. Here we obtain deviation of conductivity, which is the result of different temperature behaviors against different dimensions. The relation of Lawrence and Donaich for fluctuation induced conductivity ' $\Delta\sigma_{LD}$ ', and the fluctuation amplitude is given by

$$\Delta\sigma_{LD}=\frac{e^2}{16\hbar d\varepsilon}(1+2\alpha)^{\frac{-1}{2}} \qquad 2.19$$

$$A(3D)=\frac{e^2}{16\hbar d}\varepsilon^{-1}\left[1+\left(\frac{2\xi_c(0)}{d}\right)^2\right] \qquad 2.20$$

In Eq. 2.22, $\alpha=\frac{\alpha_o}{\varepsilon}=\left[\frac{\xi_c(0)}{d}\right]^2 2\varepsilon^{-1}$ is a dimensionless coupling parameter. Above the critical temperature (T_c), the cross-over mainly found from 2D to 3D is known as cross-over temperature (T_o). The system has 2D fluctuations above this temperature (T_o), and 3D fluctuations below T_o. According to LD model, the expression for T_o is

$$T_o=T_c\left[1+\left(\frac{2\xi_c(0)}{d}\right)^2\right] \qquad 2.21$$

The Lawrence-Doniach model predicts a change from 2D to 3D at T_{LD}. The value for T_{LD} is extracted from experimental data by extrapolation of straight lines and taking crossover point.

The study of LD framework reveals that in intra-grain region the non-superconducting region is sandwiched between two superconducting regions [45].

LD model suggested dimensional fluctuation with increasing temperature. In a nutshell, fluctuation induced conductivity (FIC) analysis is a best tool to abstract information at microscopic level. This analysis helps us to study coherence length $\xi_c(T)$, α (coupling parameter) and dimensionality of electronic state of system of superconductor. Other than this, different component of resistivity versus temperature curve are also focused [51].

2.3.3 Maki-Thompson (MT) Model

There is another region of fluctuations, known as critical region close to critical temperature (T_c) for which $\lambda = 1/3$. Few authors have determined cross-over to 0D fluctuations for $\lambda = 2$. Maki and Thompson calculated the indirect contribution to the excess conductivity [44]. Maki-Thompson (MT) contribution is coming from pair-breaking interaction [43]. MT contribution is minute and imperceptible in cuprate superconductors [45, 52].

Hikami and Larkin derived indirect contribution to excess conductivity for layered superconductors independently by Maki and Thompson [53, 54].

$$\Delta\sigma_{MT} = \left[\frac{e^2}{8\hbar d\varepsilon(1-\frac{\alpha}{\delta})}\right]\ln\left[\left(\frac{\delta}{\alpha}\right)\left(\frac{1+\alpha+(1+2\alpha)^{1/2}}{1+\delta+(1+2\delta)^{1/2}}\right)\right] \qquad 2.22$$

Where $\delta = \left[\left(\frac{4\xi_c(0)}{d}\right)^2\left(\frac{k_B T\tau_\varphi}{\pi\hbar}\right)\right]$, represents pair-breaking parameter, related to inelastic scattering process that bound the relaxation time (τ_φ) of quasi-particles involved in MT process and k_B is the Boltzmann constant. This parameter (δ) was introduced by Thompson. Non-magnetic impurities neither change the AL and MT terms nor affect T_c in s-wave BCS superconductors, whereas, these impurities may cause pair-breaking and suppression in the MT contributions, in P or d-wave superconductors [44, 55].

At a temperature when $\delta \approx \alpha$, the cross-over from 2D AL to 0D MT fluctuation contribution takes place [56], which is

$$\varepsilon_o \approx \left[\frac{\pi\hbar}{1.203(\frac{l}{\xi_{ab}})(8k_B T\tau_\varphi)}\right] \qquad 2.23$$

At this particular temperature, when mean free path 'l' of the Cooper pairs is nearly equal to ξ_{ab}, Cooper pairs are broken to Fermions. The phase relaxation time (τ_φ) at that temperature can be determined as

$$\tau_\varphi \approx \left[\frac{\pi\hbar}{8k_B T\varepsilon_o}\right] \qquad 2.24$$

While the Fermi velocity of the carriers can be estimated as

$$V_F \approx \left[\frac{5\pi k_B T_c \xi_c(0)}{2K\hbar}\right] \qquad 2.25$$

Where $K \approx 0.12$ is a coefficient of proportionality [57]. Fermi energy of the carriers can also be determined as

$$E_F = \frac{1}{2}m^* V_F^2 \qquad 2.26$$

Where $m^* = 10m_o$ is the effective mass of the carriers, while m_o is the carrier free mass [58].

2.4 References

[01] Alain Nouailhat, "An Introduction to Nanoscienceand Nanotechnology" John Wiley & Sons, Inc. USA (2008).

[02] K. E. Drexler, "Engines of Creation: The Coming Era of Nanotechnology" Anchor Press/Doubleday, New York (1986).

[03] K. E. Drexler, "Nanosystems: Molecular Machinery, Manufacturing and Computation" John Wiley & Sons, New York (1992).

[04] F.Sanchez, K.Sobolev, Construction and building materials **24**, 2060-2071 (2010).

[05] S. M. Lindsay, "Introduction to Nanoscience" Oxford University Press Inc; New York (2010).

[06] http://pubs.rsc.org/en/content/articlelanding/2010/cp/b926146j/unauth#!divAbstract

[07] T. Pradeep: "NANO: The ssentials: Understanding Nanoscience and Nanotechnology" Tata McGraw-Hill Publishing, New Delhi (2007).

[08] H. S. Nalwa, "Nanostructured Materials and Nanotechnology" Academic Press, Concise ed. (2002).

[09] G. Cao, "Nanostructures and Nanomaterials: Synthesis, Properties and Applications" Imperial College Press, London (2004).

[10] C. J. Brinker and G. W. Scherer, "Sol-Gel Science" Academic Press, Boston, (1990).

[11] R. J. P.Corriu and D. Leclercq, Angew. Chem., Int. Ed. Engl. **35**, 1420 (1996).

[12] J. Zarzycki, J. Sol-Gel Sci. Technol. **8**, 17 (1997).

[13] J. D. MacKenzie, J. Non-Cryst. Solids **48**, 1-10 (1982)

[14] D. R. Uhlmann, B. J. Zelinski& G. E. Wnek. In: C. J. Brinker, D. E. Clark, and D. R. Ulrich (Eds) "Better Ceramics Through Chemistry" North-Holland, New York, (1984).

[15] B. L Cushing, V. L. Kolesnichenko, C. J. O Connor, Chemical Reviews, **104**, 3893 (2004).

[16] C. N. R. Rao, "Chemistry of High Temperature Superconductors (Ed)" World Scientific, Singapore (1991).

[17] C. N. R. Rao, Phil. Trans. R. Soc. **A336**, 595 (1991).

[18] C. N. R. Rao, and J. Gopalakrishnan, "New Directions in Solid State Chemistry" Cambridge University Press, Cambridge 1989.

[19] C. Hammond, "The Basics of Crystallography and Diffraction" Oxford University Press Inc. New York (2009).

[20] B. D. Cullity, "Elements of X-Ray Diffraction, 2nd ed. Addison-Wesley Publishing Company, Inc. London (1977).

[21] Y. Leng, Material Chercteization, John Wiley & Sons (2008).

[22] L. Alexander, and H. P. Klug, J. Appl. Phys. **21**,126 (1969).

[23] http://www.asdlib.org/

[24] http://www.ammrf.org.au/myscope/sem/background

[25] J. I. Goldstein, D. E. Newbury, D. C. Joy, C. E. Lyman, P. Echlin, E. Lifshin, L. Sawyer, and J. R. Michael, "Scanning Electron Microscopy and X-Ray Microanalysis" Kluwer Academic/Plenum Publishers, New York, 3rd ed. (2003).

[26] M. T. Postek, K. S. Howard, A. H. Johnson, and K. L. Mcmichael, "Scanning Electron Microscopy", Ladd Research Ind., Inc. Williston (1980).

[27] M. Joshi, A. Bhattacharyya and S. Wazed Ali, Indian J. Fibre Text. **33**, 304 (2008).

[28] M. Rajendran, R. C. Pullar, A. K. Bhattacharya, D. Das, S. N. Chintalapudi, and C. K. Majumdar, Magn. Mater. **232**, 71 (2001).

[29] http://www.niton.com

[30] Haraldlbach, and Hans Luth, "Solid State Physics: An Introduction to Theory and Experiment" Spinger-Verlag, Berlin (1991).

[31] E. Ruckenstein, and S. Narain, Mater. Lett. **8**, 421 (1989).

[32] S. K. Agarwal, and B. V. Kumaraswang, J. Phys. Chem. Solids **66**, 729 (2005).

[33] M. I. Youssif, A. A. Bahgat, and A. Ali, Egypt. J. Sol. **23**, 231 (2000).

[34] F. Gomory, Supercond. Sci. Technol. **10**, 523 (1997).

[35] H. Salamati, P. Kameli, Physica C **403**, 60 (2004).

[36] H. Salamati, A. A. Babaei-Brojeny, and M. Safa, Supercond. Sci. Technol. **14**, 816 (2001).

[37] P. R. Griffiths, "Fourier Transform Infrared Spectroscopy" Plenum Press, New York, (1975).

[38] V. B. Patania, "Spectroscopy", Campus Books International, New Delhi (2002).

[39] V. L. Ginzburg, Fiz. Tverd.Tela (Leningrad) **2**, 2031 (1960).

[40] V. J. Emery, and S. Kivelson, Nature (London), **374**, 434 (1995).

[41] P. A. Lee, N. Nagaosa, and X. G. Wen, Rev. Mod. Phys. **78**, 17 (2006).

[42] L. G. Aslamazov and A. L. Larkin, Phys. Lett. A **26**, 238 (1968).

[43] K. Maki, Prog. Theo. Phys. **39**, 897 (1968).

[44] R. S. Thompson, Phys. Rev. B **1,** 327 (1970).

[45] W. E. Lawrence and S. Doniach, in proceedings of 12thinternational conference on Low Temperature Physics, Kyoto, Japan, edited by E. Kanda (Keigaku, Tokyo, 1971), p. 361.

[46] Q. Wang, G. A. Saunders, H. J. Liu, M. S. Acres and D. P. Almond, Phys. Rev. B **55,** 8529 (1997).

[47] M. V. Ramallo, A. Pomar, and F. Vidal, Phys. Rev. B **54,** 4341 (1996).

[48] A. L. Solovjov, H. U. Habermeier, and T. Haage, Low Temp. Phys. **28,** 17 (2002).

[49] C. A. C. Passos, M. T. D. Orlando, J. L. Passamai, Jr., E. V. L. de Mello, H. P. S. Correa, and L. G. Martinez, Phys. Rev. B **74,** 094514 (2006).

[50] S. R. Ghorbani and M. RahmatiTarki, J. Supercond. Novel Magn. **27,** 749(2014).

[51] S. Hikami and A. I. Larkin, Mod. Phys. Lett. B **2,** 693 (1998).

[52] S. H. Naqib, J. R. Cooper, J. L. Tallon, R. S. Islam, and R. A. Chakalov, Phys. Rev. B **71,** 054502 (2005).

[53] K. Maki and R. S. Thompson, Phys. Rev. B **39,** 2767 (1989).

[54] P. K. Nayak and S. Ravi, Supercond. Sci. Technol. **19,** 1209 (2006).

[55] W. Lang, G. Heine, W. Kula, and R. Sobolewski, Phys. Rev. B **51,** 9180 (1995).

[56] A. L. Solovjov, H. U. Habermeier, T. Haage, and F. Nizk, Low Temp.Phys. **28,** 99 (2002).

[57] J. Bardeen, L. N. Cooper, and J. R. Schrieffer, Phys. Rev. **108,** 1175 (1957).

[58] A. L. Solovjov, V. M. Dmitriev, and H. U. Habermeier, Phys. Rev. B **55,**8551 (1997).

Chapter 3

$(Ag)_x$/CuTl-1223 Nano-Superconductor Composites

In this chapter, we have discussed the effects of Ag nanoparticles addition on structural and superconducting transport properties of CuTl-1223 matrix. Series of samples added with different nano-Ag particles contents (0 ~ 4.0 wt. %) were synthesized to find out the optimal concentration level of these nanoparticles to obtain the maximum improvement in superconducting transport properties without affecting the crystal structure of CuTl-1223 phase. We used Ginzburg-Landau equations, Aslamazov-Larkin (AL), Lawrence-Doniach (LD) and Maki-Thompson models [46-49] on the experimental data to obtain the different microscopic superconducting parameters for understanding and explaining the role of Ag nanoparticles on superconductivity of host CuTl-1223 phase in detail. We tried to unfold the role of nano-Ag particles addition in CuTl-1223 matrix with a central objective to determine the dominant source and mechanism taking place affecting the superconducting properties.

3.1 Introduction

The impact of superconducting materials from their application point of view can be estimated from the values of superconducting critical parameters (i.e. critical temperature T_c, critical current density J_c, critical magnetic field H_c) and CuTl-based high temperature superconducting family has the highest values of these critical parameters after Hg-based superconductor [1, 2]. The main advantage for the selection of CuTl-1223 superconducting matrix is its ambient synthesis conditions especially pressure along with higher values of critical parameters [3-6]. But the performance of these compounds is badly affected by inter-grains voids, inhomogeneous micro-defects, etc, present in their bulk form. In polycrystalline bulk samples, the inter-granular superconducting transport properties have become limited by the weak-links caused by the grain-boundaries and the intra-granular critical current is impeded principally by the thermally activated flux flow at high temperatures and in applied magnetic fields. One of the most suitable and convenient way to address this issue is the inclusion of metallic nanoparticles at grain-boundaries of superconducting granular bulk materials for filling the pores and healing up the cracks to improve the weak-links. The second very important issue is the vortex motion in the applied magnetic field, which can easily damage the superconductivity. To avoid this situation of vortex motion and to improve the infield

superconducting transport properties, it is necessary to introduce artificial pinning centers in the superconducting matrices apart from those which occur naturally [3-14]. Different methods such as high energy ions irradiation [15], chemical doping and different types of additives were reported in literature for this purpose [16-18]. Nano-additives of different kinds in various high temperature superconductor matrices have shown positive effects on superconducting properties [10, 11, 18-20]. These additives improve the inter-grain connectivity by filling the pores and healing up the crakes as well as pinning ability acting as additional artificial pinning centers [21-23]. Significant improvement in superconducting parameters was observed by the inclusion of nanostructures of noble metals such as Ag and Au in many superconducting systems [24-26]. The addition of different sizes and concentrations of silver (Ag) nanoparticles in YBCO superconductor showed monotonic increase in superconducting properties particularly J_c by improving crystal structure in the form of higher crystallinity, crystallites connectivity and superconducting volume fraction [19, 27]. The improvement in inter-grains connectivity as well as in J_c was observed with increasing concentration of nano-Ag particles in Bi-2223 system [24, 25]. The improvement in mechanical properties of (Bi Pb)-Sr-Ca-Cu-O superconducting matrix was also observed by the inclusion of nano-Ag particles that was due to cementing effects of these additives at the grain-boundaries [28, 29]. The inclusion of different metals oxides MgO, ZrO_2 and Al_2O_3 nanoparticles in Bi-based systems showed the improvement in superconducting parameters [30-32]. The presence of MgO nanoparticles in Bi-2212 matrix has increased the transition sharpness and the superconductor volume fraction [33]. Significant improvement in infield J_c was observed by the addition of Al_2O_3 nanoparticles in $YBa_2Cu_3O_y$ superconducting phase without affecting the structural symmetry, which can be rendered to the existence of enhanced flux pinning centers [34]. The volume pinning force density, onset temperature of dissipation, activation energy, transport properties and J_c in applied magnetic field were also improved by the addition of nano-Al_2O_3 particles in polycrystalline (Bi, Pb)-2223 system [35]. The excess conductivity analysis showed that the width of three dimensional (3D) conductivity region was reduced by the addition of nano-Al_2O_3 particles in polycrystalline (Bi, Pb)-2223 superconducting matrix, which was explained on the basis of scattering of mobile carriers across the insulating nano-Al_2O_3 particles present at the grain-boundaries [36]. Mechanical properties were improved by the inclusion of Ag nanoparticles at the grain-boundaries of Bi-based superconducting systems acting as pores fillers and improving the inter-grains connections [37].

The superconducting transport properties were sufficiently improved by the addition of nano-Ag particles in $Bi_{1.8}Pb_{0.4}Sr_2Ca_2Cu_3O_{10+\delta}$ superconducting matrix without affecting the crystal structure, indicating more efficient pinning mechanisms [38]. The size of flux pinning centers is important in enhancing J_c and particle with size closer to the coherence length showed higher transport J_c [39]. But the size and homogenous distribution of nanoparticles at the grain-boundaries of the bulk high T_c superconducting matrix is the real challenge [40-45].

3.2 Theoretical Models for Analysis of Experimental Data

The fluctuation induced conductivity (FIC) analysis is a state of the art theoretical analysis on the experimental data of cuprates, which can play an essential role to unearth the intrinsic properties of the material well above the zero resistivity critical temperature T_c (0), where the Cooper pairs formation starts and imparts additional conductivity. There are two models that can give a very nice picture of superconducting fluctuations in inter-grains and intra-grains regions. Aslamasov-Larkin (AL) Model can be used for fluctuations both in inter-grains and intra-grains regions while Lawrence-Doniach (LD) Model can be used only for fluctuations in intra-grains regions of layered superconductors [46, 47].

The excess conductivity is given by;

$$\Delta\sigma(T) = \left[\frac{\rho_N(T) - \rho(T)}{\rho_N(T)\rho(T)}\right] \quad \text{..... (1)}$$

where 'ρ (T)' is the actually measured resistivity, and $\rho_N(T) = \alpha+\beta T$ is the normal-state resistivity of the samples extrapolated to resistivity at 0 K; the 'α' is a intercept and 'β' is a slope of straight line. The excess conductivity generally comprises on two contributions i.e.

$$\Delta\sigma = \Delta\sigma_{AL} + \Delta\sigma_{MT} \quad \text{..... (2)}$$

The first term, according to AL model, is derived using microscopic approach by mean field theory and is considered as a direct contribution to paraconductivity [48]. The fluctuation induced conductivity according to AL theory is given as;

$$\Delta\sigma_{AL} = A\varepsilon^{-\lambda} \quad \text{..... (3)}$$

where 'A' is the fluctuation amplitude, 'λ' is dimensional exponent, $\varepsilon = \ln\left[\frac{T - T_c^{mf}}{T_c^{mf}}\right]$ is the reduced temperature and 'T_c^{mf}' is usually referred to as the mean field critical temperature, which separates the mean field region from the critical region [48, 49] and is determined from

the point of inflection of the temperature derivative of resistivity (dρ/dT). The exponent 'λ' determines the dimensionality of the superconducting fluctuations and is given as λ = 2-D/2; λ = 3/2, 1, and 1/2 for one, two and three dimensional fluctuations, respectively. The fluctuation amplitude A for one, two and three dimensional fluctuations is given by [50];

$$A = \begin{cases} \frac{e^2}{32\hbar\xi_c(0)} & \text{for 3D fluctuation} \\ \frac{e^2}{16\hbar d} & \text{for 2D fluctuation} \\ \frac{e^2\xi_c(0)}{32\hbar s} & \text{for 1D fluctuation} \end{cases} \quad \ldots\ldots\ldots\ldots\ldots\ldots\ldots\ldots\ldots\ldots (4)$$

where *'e'* is the electron charge, '$\xi_c(0)$' is the zero-temperature coherence length along c-axis, '$\hbar$' is the reduced Planks constant, '*d*' is the effective layer thickness of the 2D system, and '*s*' is the cross-sectional area of the 1D system.

The physical microscopic parameters calculated from FIC analysis depend strongly on the dimensionality of the fluctuations. Lawrence-Doniach (LD) introduced the concept of interlayer coupling via Josephson coupling of adjacent layers close to the critical temperature [47]. According to the LD model for layered superconductors, the excess conductivity $\Delta\sigma_{LD}$ due to superconducting fluctuations is;

$$\Delta\sigma_{LD} = \frac{e^2}{16\hbar d\varepsilon}(1+2\alpha)^{-1/2} \quad \ldots\ldots\ldots\ldots\ldots\ldots\ldots\ldots\ldots\ldots (5)$$

where $\alpha = \frac{\alpha_o}{\varepsilon} = \left[\frac{\xi_c(0)}{d}\right]^2 2\varepsilon^{-1}$ is a dimensionless coupling parameter. The cross-over from 2D to 3D is mainly found above the critical temperature known as cross-over temperature (T_o). The system has 3D fluctuations below this temperature and 2D fluctuations above this temperature, and the expression for T_o according to the LD model is

$$T_o = T_c\left[1+\left(\frac{2\xi_c(0)}{d}\right)^2\right] \quad \ldots\ldots\ldots\ldots\ldots\ldots\ldots\ldots\ldots\ldots (6)$$

The second term is the inter-layer coupling strength, which is related to the reduced temperature 'ε' by $J = \varepsilon/4$. In layered superconductors at very low temperature close to zero resistivity temperature $\xi_c > d$; where '*d*' is the distance between the conducting layers of adjacent unit cells ('*d*' is approximately equal to the c-axis lattice parameter of the unit cell). The advantage of LD model is that it reduces to 2D AL model for large ε values where the coupling constant '*J*' is quite small and to 3D AL model for small 'ε' values where in some cases the coupling constant

'J' is quite strong. The above theoretical AL and LD models are based on direct contribution to the excess conductivity.

There is one more region of fluctuations close to critical temperature for which $\lambda = 1/3$ and is known as critical region [51]. Some authors have observed a cross-over to 0D fluctuations with critical exponent 2. In high T_c superconductors, the Maki and Thompson (MT) contribution, which is due to the interaction of fluctuating Cooper pairs with normal electrons, is not easily observable. Since the MT contribution is negligible in cuprate superconductors [52]. This indirect contribution to the excess conductivity was calculated by Maki [53] and later on modified by Thompson [54]. For layered superconductors, Hikami and Larkin [55] derived the indirect contribution to the excess conductivity independently by MT [56, 57].

$$\Delta\sigma_{MT} = \left[e^2 / 8\hbar d\varepsilon (1 - \alpha/\delta) \right] \ln\left[\left(\frac{\delta}{\alpha}\right) \left(\frac{1+\alpha+(1+2\alpha)^{1/2}}{1+\delta+(1+2\delta)^{1/2}} \right) \right] \quad \text{..... (7)}$$

where $\delta = \left[\left(\frac{4\xi_c(0)}{d} \right)^2 \left(\frac{\kappa_B T \tau_\varphi}{\pi\hbar} \right) \right]$ is the pair-breaking parameter, which was introduced by Thompson [49] and is related to inelastic scattering processes that limit the phase relaxation time τ_φ of the quasiparticles involved in MT process [58] and κ_B is the Boltzmann constant. In s-wave BCS superconductor, nonmagnetic impurities neither change T_c nor affect AL and MT terms while on the other hand in P or d-wave superconductor these impurities may act pair-breaking and are supposed to suppress the MT contribution [58].

The cross-over from 2D AL to 0D MT fluctuation contribution occurs at a temperature where $\delta \approx \alpha$, which gives [59];

$$\varepsilon_o \approx \left[\frac{\pi\hbar}{1.203(\ell/\xi_{ab})(8\kappa_B T \tau_\varphi)} \right] \quad \text{..... (8)}$$

When the mean free path ℓ of the Cooper pairs approaches to ξ_{ab} at a particular temperature then they (Cooper pairs) are broken to Fermions and at that temperature the phase relaxation time can be estimated as;

$$\tau_\varphi \approx \left[\frac{\pi\hbar}{8\kappa_B T \varepsilon_o} \right] \quad \text{..... (9)}$$

Fermi velocity of the carriers can also be estimated by;

$$V_F \approx \left[\frac{5\pi\kappa_B T_c \xi_c(0)}{2K\hbar}\right] \quad \text{..... (10)}$$

where $K \approx 0.12$ is a co-efficient of proportionality [60]. Fermi energy of the carriers can also be calculated by;

$$E_F = \tfrac{1}{2} m^* V_F^2 \quad \text{..... (11)}$$

where $m^* = 10\ m_o$ is the effective mass of the carrier and m_o is the carrier free mass [61].

Ginzburg and Landau observed the existence of two types of superconductors depending upon the energy of the interface between the normal and superconducting states. In 1957 Alexei Abrikosov used Ginzburg–Landau theory to explain the experimental data of superconducting alloys and thin films. He found that high magnetic field in a type-II superconductor penetrates in the form of magnetic flux quanta Φ_o. The thermodynamics magnetic field $B_c(0)$ can be estimated from Ginzburg number N_G, which is given by [61, 62];

$$N_G = \left|\frac{T_G - T_c^{mf}}{T_c^{mf}}\right| = \tfrac{1}{2}\left(\kappa_B T_c \gamma \Big/ \{B_c(0)\}^2 \{\xi_c(0)\}^3\right)^2 \quad \text{..... (12)}$$

where $\gamma = \xi_{ab}(0)/\xi_c(0)$ is anisotropy whose estimated value is '4' for CuTl-1223 superconducting system [63, 64] and T_G is the cross-over temperature from critical to 3D regime. We can estimate penetration depth $\lambda_{p.d.}$, lower critical magnetic field $B_{c1}(0)$, upper critical magnetic field $B_{c2}(0)$ and the critical current density $J_c(0)$ after determination of $B_c(0)$ as follows [65-68];

$$B_c = \frac{\Phi_o}{2\sqrt{2}\pi\lambda_{p.d.}\xi_{ab}(0)} \quad \text{..... (13)}$$

$$B_{c1} = \frac{B_c}{\kappa\sqrt{2}} \ln\kappa \quad \text{..... (14)}$$

$$B_{c2} = \sqrt{2}\kappa B_c \quad \text{..... (15)}$$

$$J_c = \frac{4\kappa B_{c1}}{3\sqrt{3}\lambda_{p.d.} \ln\kappa} \quad \text{..... (16)}$$

where $\Phi_o = \frac{\hbar}{2e}$ is the flux quantum and κ is the GL parameter, which is the ratio of penetration depth to coherence length.

3.3 Results and Discussion

3.3.1 X-Ray Diffraction (XRD)

The structure and phase purity of material was determined by XRD (D/Max IIIC Rigaku with a CuK_α source of wavelength 1.54056 Å). The XRD pattern of Ag nanoparticles is shown in Fig. 3.1. The prominent peaks are indexed according to face-centered cubic (FCC) structure of Ag and the average size of Ag nanoparticles calculated by Scherrer's formula is about 35 nm. The XRD analysis shows exquisitely indexed (1 1 1), (2 0 0), (2 2 0), and (3 1 1) planes of FCC structure The lattice parameter calculated for FCC pattern of Ag nanoparticles is about a = 4.09 Å. No peak of impurity crystalline phases was observed.

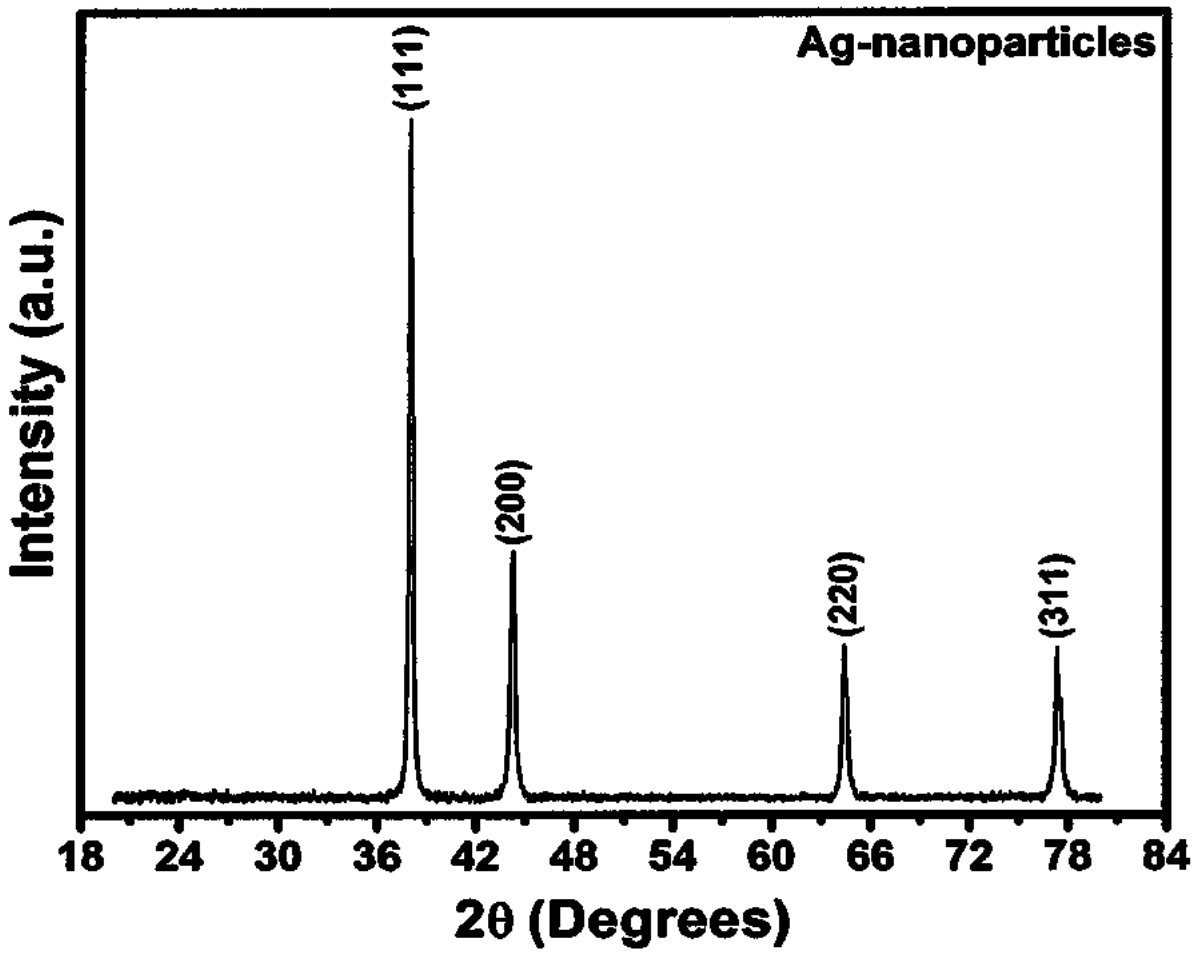

Fig. 3.1: XRD pattern of silver (Ag) nanoparticles.

Typical representative XRD patterns of $(Ag)_x$/CuTl-1223 composite samples with x = 0 and 2 wt. % is shown in Fig. 3.2. Most of the diffraction peaks are well indexed according to tetragonal structure following the P4/mmm space group indicating the dominance of CuTl-1223 phase along with very few peaks of some other superconducting phases as well as some unknown impurities. There is no change observed in the overall XRD pattern of Ag nanoparticles added samples, which gives a clue about the occupancy of these nanoparticles at the inter-crystallites sites in CuTl-1223 superconducting matrix. The presence of these nanoparticles at the grain-boundaries can help to heal up the voids and to improve the inter-grains weak-links as well as superconducting volume fraction due to which over all superconducting properties can be enhanced.

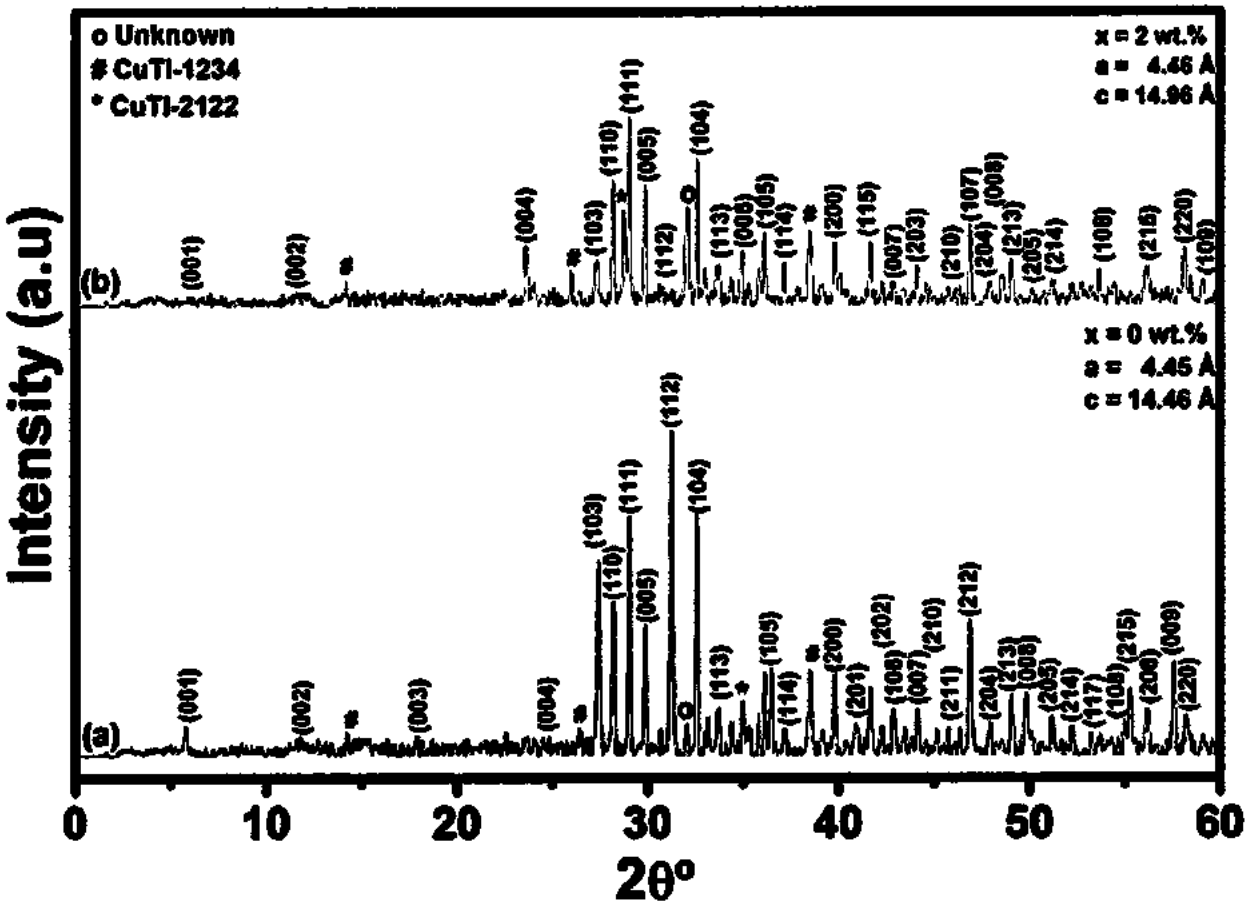

Fig. 3.2: X-ray diffraction (XRD) patterns of $(Ag)_x$/CuTl-1223 composites with (a) x = 0 and (b) x = 2 wt. %.

The unit cell parameters calculated by computer software (crystal) program are a = 4.45 Å, c = 14.46 Å for x = 0, and a = 4.46 Å, c = 14.96 Å for x = 2%, respectively and the stoichiometry of the CuTl-1223 matrix remains unaffected after the inclusion of these nanoparticles. However, the

slight shift in the diffraction peaks to lower angles is possibly due to the uniform strain produced in the materials after the addition of Ag nanoparticles. The slight increase in the c-axis length may also be due to increase of oxygen (O_δ) contents with the addition of these nanoparticles, which can relax the apical bond length.

3.3.2 Scanning Electron Microscopy (SEM) and Energy Dispersive X-ray (EDX) Spectra

The typical SEM images and EDX spectra of (Ag)$_x$/CuTl-1223 samples for x = 0, and 2 wt. % are shown in Fig. 3.3. The improvement of inter-grains weak-links as well as the grains size is obvious from these SEM images after the addition of Ag nanoparticles in the host CuTl-1223 superconducting phase. The improvement of inter-grains weak-links and the grains size may be due to cementing effects of Ag nanoparticles occupying the inter-grains boundaries by filling the voids and pores present in the bulk form of CuTl-1223 matrix. The improved grains size enhances the superconducting volume fraction and superconducting properties of the host material by the addition of Ag nanoparticles.

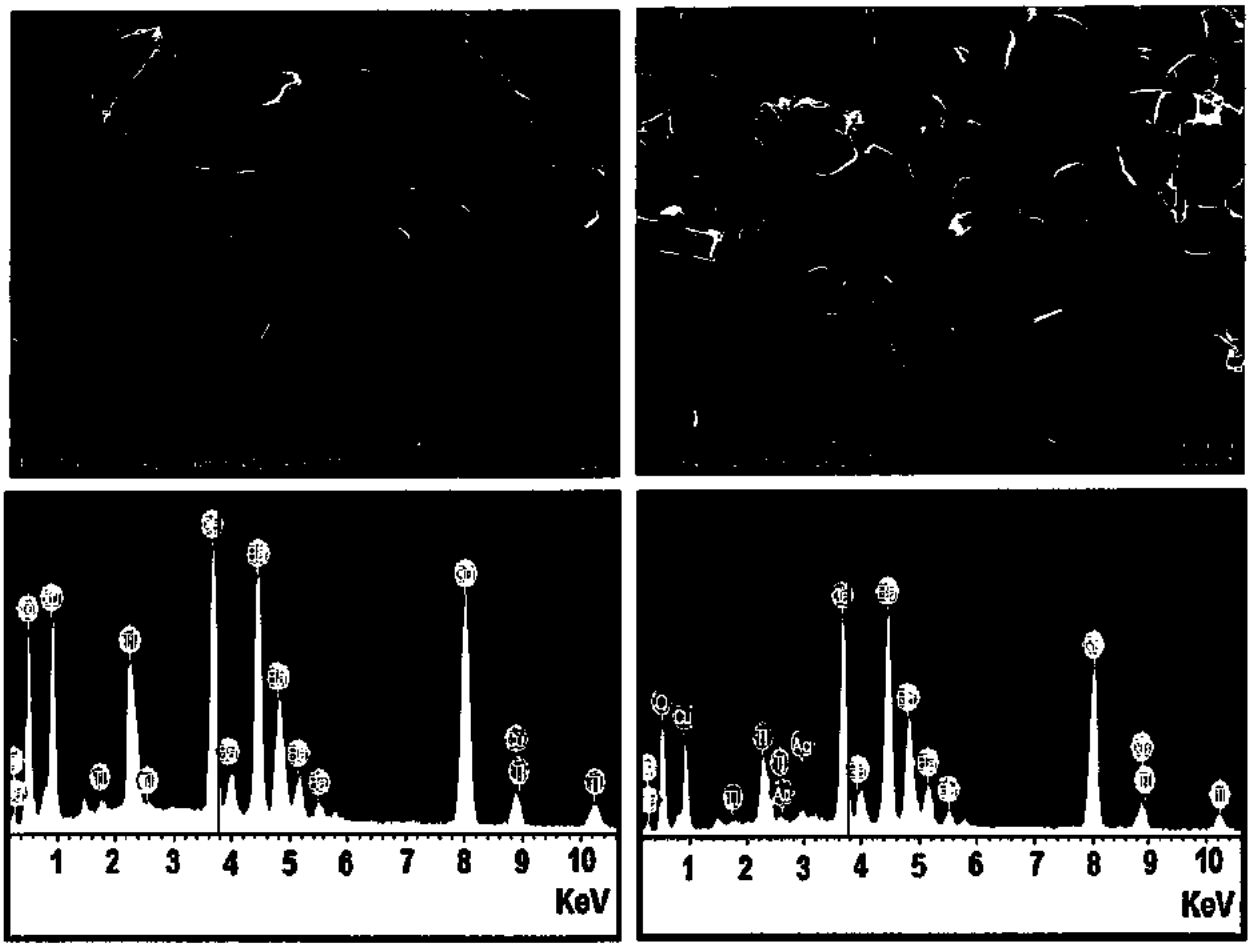

Fig. 3.3: Typical SEM images and EDX spectra of (Ag)$_x$/CuTl-1223 composites with (a) x = 0 and (b) x =2.0 wt.%.

The EDX spectra showed the presence of different elements in the composition. The mass percentages of different elements determined from the EDX analysis are listed in Table 3.1.

Table 3.1: Elemental analysis by EDX of $(Ag)_x$/CuTl-1223 composites with (a) 0 and (b) 2.0 wt.%.

Elements	(a) : x = 0			(b) : x = 2.0 wt.%		
	KeV	Mass%	Atom%	KeV	Mass%	Atom%
O K	0.535	20.68	58.05	0.540	20.22	55.96
Ca K	3.695	8.87	9.94	3.702	8.78	9.70
Cu L	0.952	26.93	19.03	0.960	27.48	19.15
Ba L	4.484	31.83	10.41	4.492	30.63	9.88
Tl M	2.325	11.70	2.57	2.315	11.12	2.41
Ag K	...	...	...	1.525	1.77	2.90
Total		**100.00**	**100.00**		**100.00**	**100.00**

3.3.3 Fourier Transform Infrared (FTIR) Spectroscopy

FTIR spectroscopy is very sensitive technique commonly used for detecting a trace amount of impurities along with the functional groups in the material. But here we are interested to observe the viberational modes of different oxygen atoms present in the unit cell with the help of FTIR absorption spectroscopy. The FTIR absorption spectra of $(Ag)_x$/CuTl-1223 composites with x = 0, 0.5, 1.0, 2.0 and 4.0 wt.%, in the range from 400-700 cm^{-1} are shown in Fig. 3.4. The absorption bands in the range from 400 to 540 cm^{-1} are associated with the apical oxygen atoms and in the range around from 541 to 600 cm^{-1} are associated with CuO_2 planar oxygen atoms [69, 70]. The absorption bands in the range from 670 to 700 cm^{-1} are associated with O_δ atoms in the charge reservoir layer [71-75]. The apical oxygen modes of type Tl-O_A-Cu(2) and Cu(1)-O_A-Cu(2) are observed around 430cm^{-1} and 460~499 cm^{-1} and CuO_2 planner oxygen mode is around 536 cm^{-1} in the pure $Cu_{0.5}Tl_{0.5}Ba_2Ca_2Cu_3O_{10-\delta}$ samples. The nominal variation in the position of the apical oxygen modes may be due to presence of stresses and strains in the bond lengths of the unit cells caused by the nano-Ag particles in the composites. The CuO_2 planner oxygen modes and O_δ modes remained almost unaffected after the addition of nano-Ag particles in the host CuTl-1223 matrix. The FTIR study also supports our claim and objective that the Ag

nanoparticles don't substitute the constituent atoms of CuTl-1223 unit cell but they occupy the inter-granular spaces, fill up the pores and heal up the cracks.

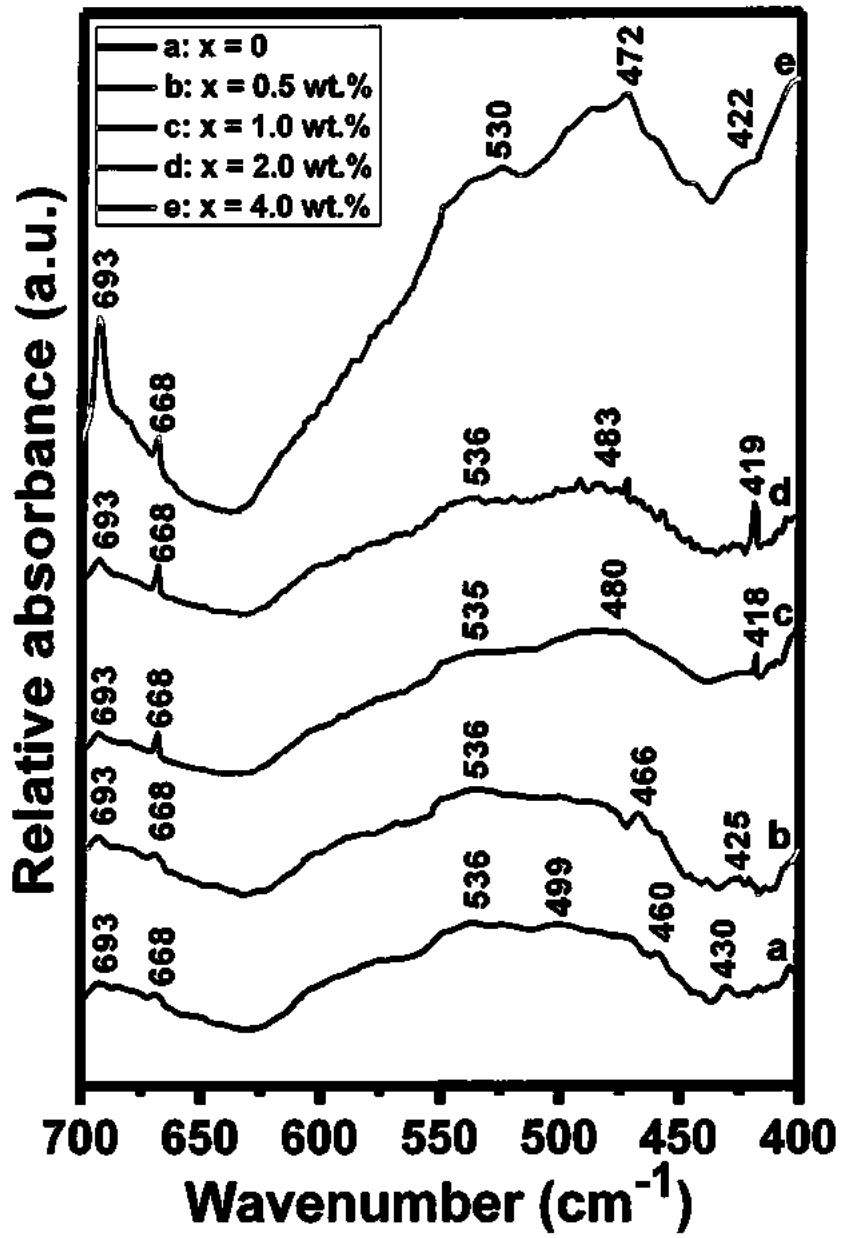

Fig. 3.4: FTIR absorption spectra of (Ag)$_x$/CuTl-1223 composites with (a) x = 0, (b) x = 0.5 wt.%, (c) x = 1.0 wt.%, (d) x = 2.0 wt.% and (e) x = 4.0 wt.% .

3.3.4 Resistivity versus Temperature, Arrhenius Plots and Activation Energy Measurements

The resistivity versus temperature measurements of (Ag)$_x$/CuTl-1223 composites with different contents of nano-Ag particles from x = 0 ~ 4.0 wt. % are shown in Fig. 3.5. All these samples have shown a metallic variation in the resistivity from room temperature down to onset

of superconductivity with zero resistivity critical temperature {T_c (R=0)} around 73 K, 95 K, 98 K, 102 K and 91 K for x = 0, 0.5, 1.0, 2.0 and 4.0 wt.%, respectively. These measurements show that the value of T_c (R=0) is increased after the addition of nano-Ag particles upto x = 2.0 wt. % concentration and then is suppressed on further increase of these nanoparticles concentration in CuTl-1223 matrix.

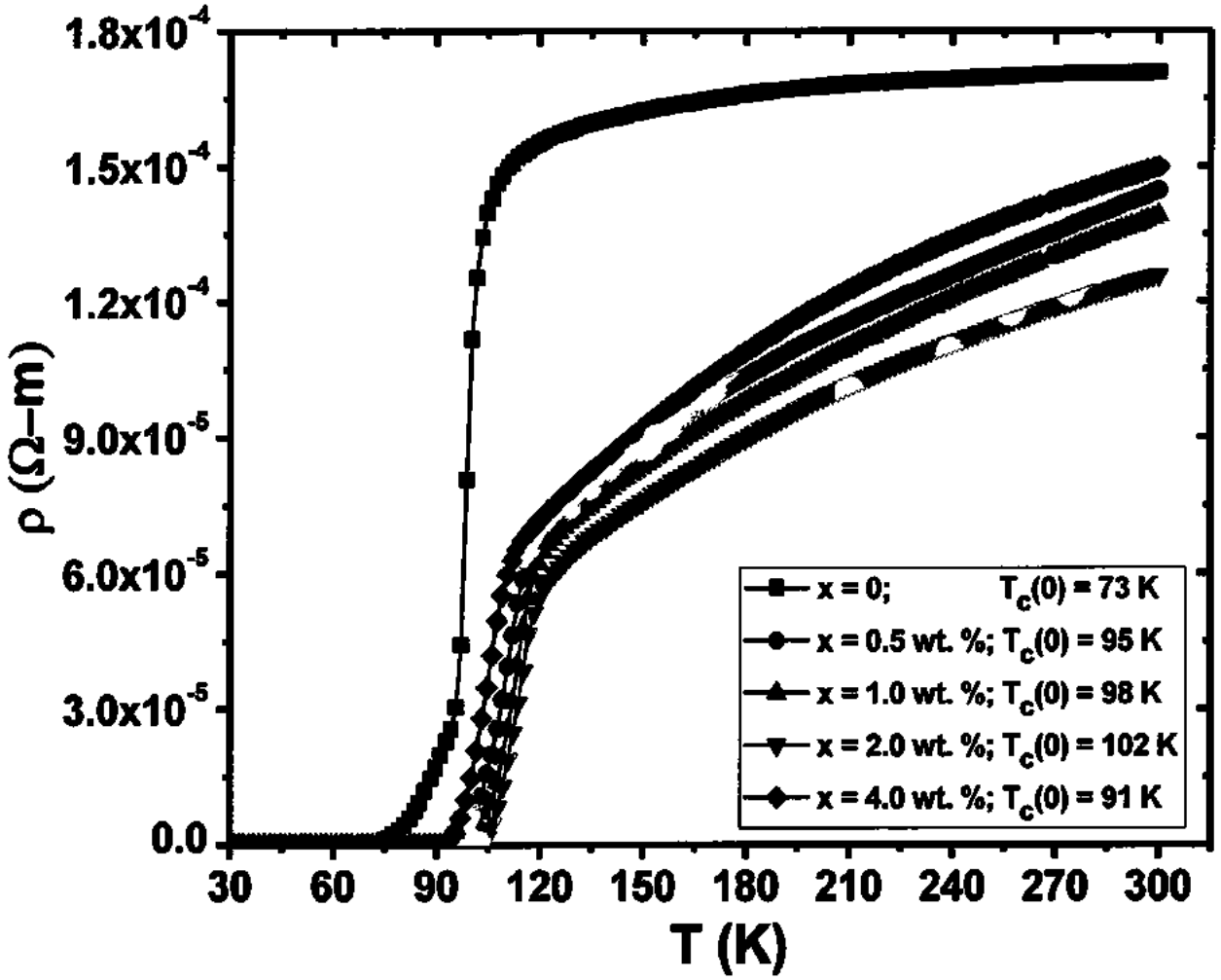

Fig. 3.5: Resistivity versus temperature measurements of $(Ag)_x$/CuTl-1223 composites with x = 0, 0.5, 1.0, 2.0 and 4.0 wt.%.

The increase in T_c is an evidence of improved superconducting volume fraction and carriers density after nano-Ag particles addition in the host CuTl-1223 superconducting matrix. The improved inter-grain weak-links facilitate the charge carriers transport processes and reduce the energy losses across the grain-boundaries. But the superconducting volume fraction starts to be decreased after certain optimum inclusion level of Ag nanoparticles, which causes the suppression of superconductivity parameters. The non-superconducting metallic Ag nanoparticles reduce the superconducting volume fraction beyond certain optimum level of Ag

nanoparticles inclusion in superconducting state of CuTl-1223 matrix. After a certain optimum level of Ag nanoparticles addition, the agglomeration and segregation of these nanoparticles result in the reduction of T_c by various mechanisms like scattering, pair-breaking, etc [76-78]. Still, there are many issues to be addressed in future studies like homogeneous and non-uniform distribution of Ag nanoparticles at the inter-grain boundaries of the host CuTl-1223 superconducting matrix.

The variation of superconducting transition region resistivity versus temperature measurements of $(Ag)_x$/CuTl-1223 composites with x = 0, 0.5, 1.0, 2.0 and 4.0 wt.%, is shown in Fig. 3.6. The Arrhenius plots of $(Ag)_x$/CuTl-1223 composites, activation energy U (eV), $\rho_{300\ K}$ (Ω-cm) and T_c (0) versus x (i.e. Ag nanoparticles contents in wt.%) are shown in the inset of Fig. 3.6.The systematic decrease in the normal state resistivity at 300 K and also a systematic increase in T_c (0) with the gradual increase of these nanoparticles contents in the composites up to x = 2.0 wt. % is also shown in the inset of Fig. 3.6. The systematic decrease in normal state resistivity and monotonic increase in T_c (0) with gradual increase of these nanoparticles contents is most probably due to somehow homogeneous and uniform distribution of these nanoparticles at the grain-boundaries of the bulk CuTl-1223 material. The activation energy required to overcome the barrier can be calculated by the Arrhenius law $\rho = \rho_o \exp\left(\frac{-U}{\kappa_B T}\right)$, where U is the activation energy and κ_B is the Boltzmann constant, for superconductors [79-81]. We used the superconducting transition region for the calculation of activation energy and observed an increase in the activation energy with the increase of Ag nanoparticles contents in the composites. Theories of high T_c superconductors so far developed believe that pairs of electrons (Cooper pairs) move freely without activation energy, which is the main source of superconductivity. In this study, it is observed that activation energy has been increased with the increase of Ag nanoparticles contents in these composites. When Cooper pairs interact with non-superconducting metallic Ag nanoparticles at the grain-boundaries during their transport in superconducting state of the host CuTl-1223 matrix, the pairing interaction is weakened and Cooper pairs could not exist in the low energy state and energy dissipation take place. But on the other hand the presence of metallic Ag nanoparticles at grain-boundaries can increase the inter-grain connectivity by filling the voids and pores, which may be the cause of an increase in T_c (0). Therefore, there are two possible mechanisms taking place due to the inclusion of Ag

nanoparticles, one is the formation of non-superconducting regions causing increase in activation energy and the other (dominating) is the improved inter-grain connectivity promoting T_c (0) of the samples.

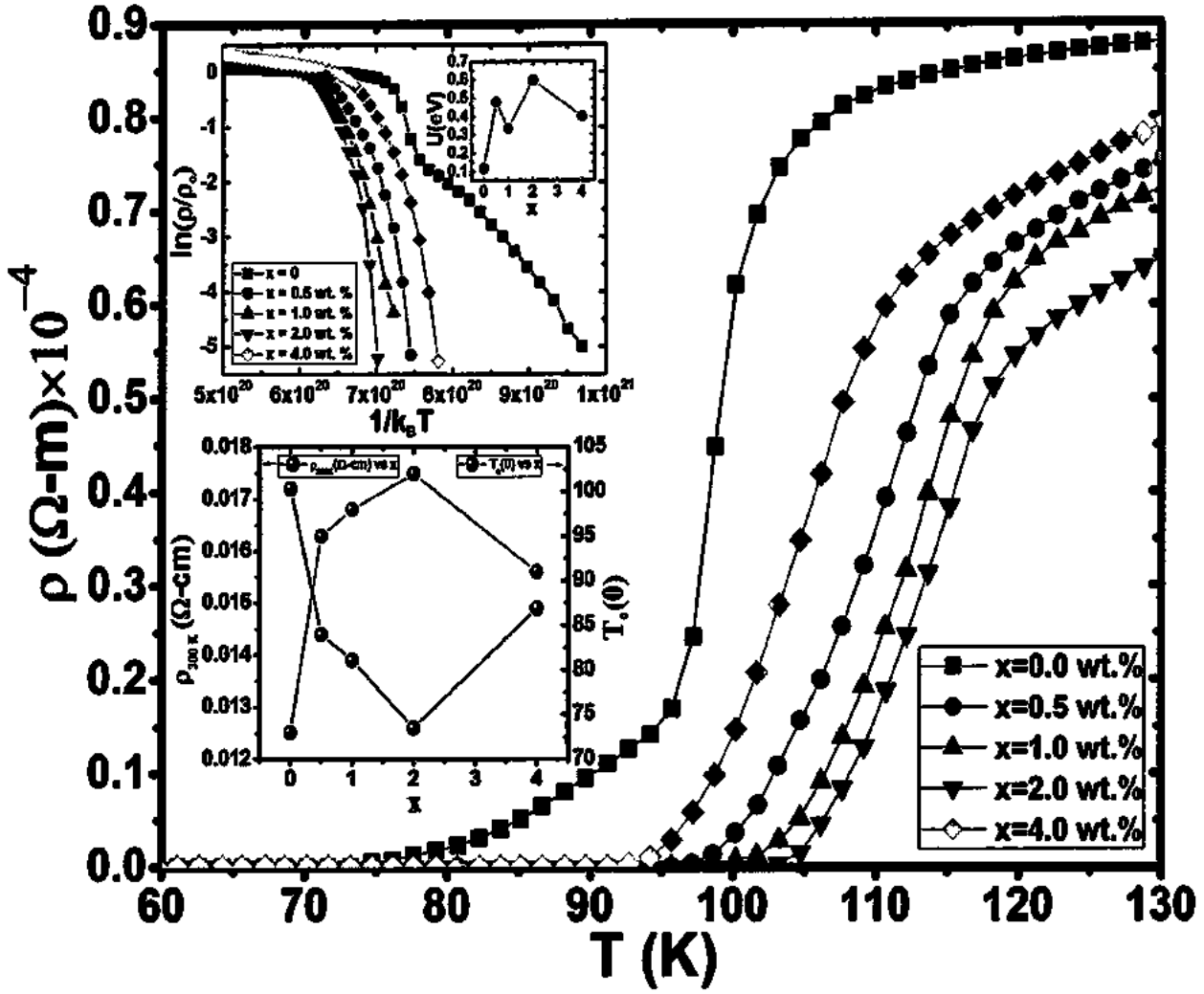

Fig. 3.6: Variation of superconducting transition region in resistivity versus temperature measurements of $(Ag)_x$/CuTl-1223 composites with x = 0, 0.5, 1.0, 2.0 and 4 wt.%. (In the inset are given the Arrhenius plots of $Ag)_x$/CuTl-1223 composites with x = 0, 0.5, 1.0, 2.0 and 4 wt.%, T_c (0), $\rho_{300\,K}$ (Ω-cm) and activation energy U (eV) versus x i.e. Ag nanoparticles contents in wt.%.)

3.3.5 Fluctuation Induced Conductivity (FIC) Analysis

The FIC analysis on the dc-resistivity versus temperature data of $(Ag)_x$/CuTl-1223 composite samples has been carried out by using the above mentioned models in the neighborhood of transition region. The plots of ln ($\Delta\sigma$) versus ln (ε) of $(Ag)_x$/CuTl-1223 composites samples with x = 0, 0.5, 1.0, 2.0, and 4.0 wt.% are shown in Fig. 3.7(a-e). The experimentally measured dc-resistivity $\rho(\Omega$-m) along with a straight line extrapolated from the room temperature (300 K) normal state resistivity to 0 K and derivative ($d\rho/dT$) of dc-resistivity versus temperature are shown in the insets of Fig. 3.7(a-e). The variation of zero temperature coherence length $\xi_c(0)$ along c-axis and inter-layer coupling constant (J) versus Ag nanoparticles contents (wt. %) in $(Ag)_x$/CuTl-1223 composites is also shown in Fig. 3.7 (f). The superconducting fluctuations starts at a particular temperature denoted by T^* from where the experimental dc-resistivity curve deviates from the straight line extrapolated from the room temperature normal state resistivity to 0 K. The values of T^* are around 170.74, 169.56, 189.63, 185.61 and 184. 61 K for x = 0, 0.5, 1.0, 2.0, and 4.0 wt. % respectively. The increase in T^* shows that the superconducting fluctuations starts at higher temperature values, which may be due to improved inter-grains coupling, zero temperature coherence length along c-axis $\xi_c(0)$, superconducting volume fraction etc, after the inclusion of Ag nanoparticles in the host CuTl-1223 matrix. The values of critical exponents (λ_{CR} λ_{3D} λ_{2D} and λ_{0D}), cross-over temperatures ($T_{CR\text{-}3D} = T_G$, $T_{3D\text{-}2D}$, and $T_{2D\text{-}SW}$), mean field critical temperature (T_c^{mf}), T^*, inter-grains coupling constant (α) and superconducting transition width ($W = \Delta T_c$) deduced from the FIC analysis on dc-resistivity versus temperature data of $(Ag)_x$/CuTl-1223 composites samples are given in Table 3.2. All the cross-over temperatures, T_c^{mf}, and T^* have been shifted to the higher values, which is theoretical evidence of improved superconducting properties of the host CuTl-1223 matrix after the addition of Ag nanoparticles. The increased values of 'α' is a theoretical evidence of improved non-superconducting inter-grains boundaries in the composites samples, which is in accordance to the increase in the activation energy after Ag nanoparticles addition. The increase in $W = \Delta T_c$ is another evidence of energy loss across the metallic non-superconducting grain-boundaries in $(Ag)_x$/CuTl-1223 composites samples.

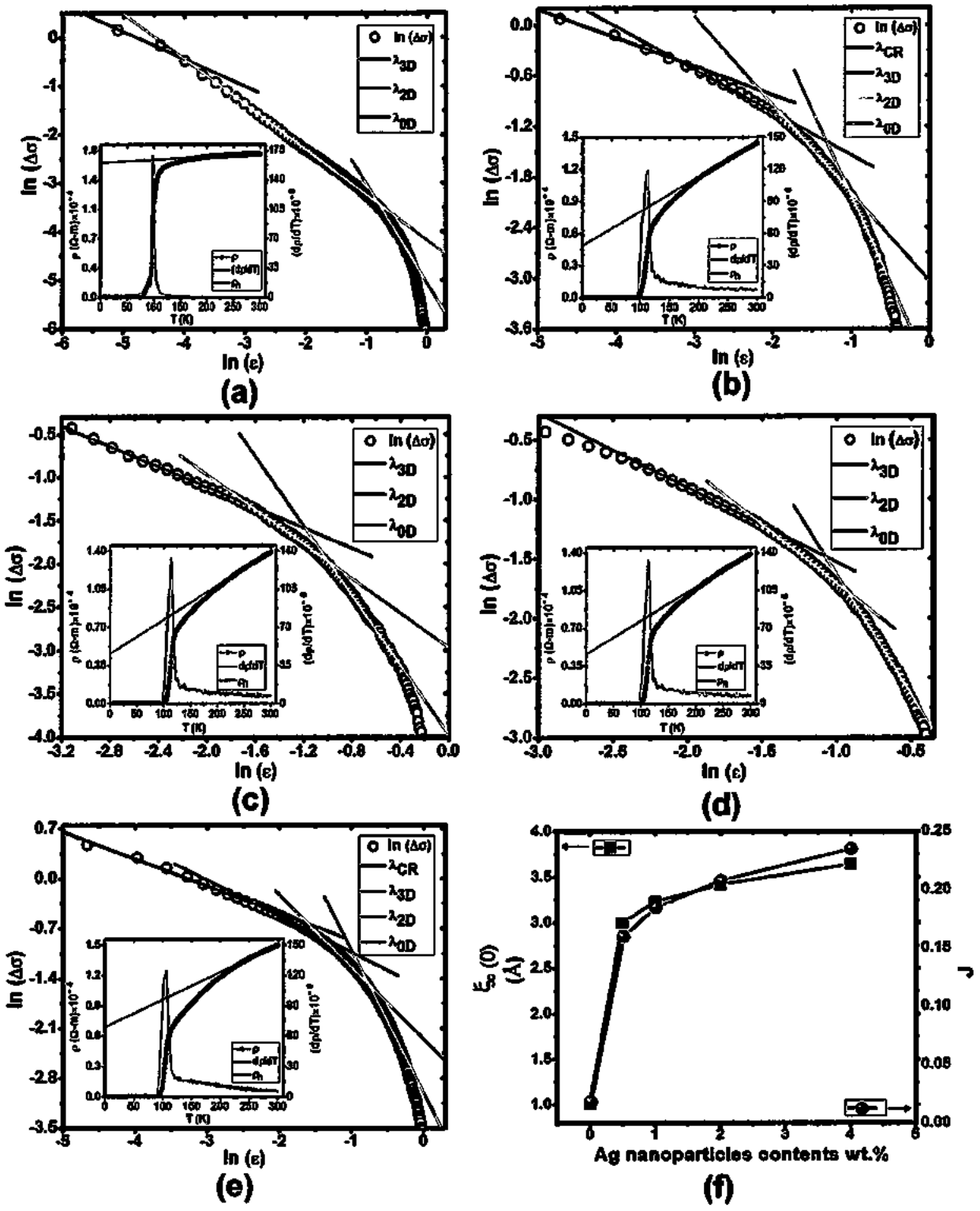

Fig. 3.7(a-f): ln (Δσ) versus ln (ε) plots of (Ag)$_x$/CuTl-1223 composites; (a) x = 0, (b) x = 0.5, (c) x = 1.0, (d) x = 2.0, and (e) x = 4.0 wt.% ; (In the insets are shown the experimentally measured dc-resistivity ρ(Ω-cm), derivative (dρ/dT) of dc-resistivity versus temperature, and the straight line extrapolated from the room temperature '300 K' normal state resistivity to 0 K). **(f)** Zero temperature coherence length ξ_c (0) and coupling constant (J) versus Ag nanoparticles contents wt. % in (Ag)$_x$/CuTl-1223 composites.

Table 3.2: Widths of critical 3D, 2D, and SW fluctuation regions deduced from the fitting of experimental resistivity versus temperature data of (Ag)$_x$/CuTl-1223 composites samples with x = 0, 0.5, 1.0, 2.0 and 4.0 wt.%.

Samples x = wt.%	λ_{CR}	λ_{3D}	λ_{2D}	λ_{SW}	$T_{CR3D}=T_G$ (K)	T_{3D-2D} (K)	T_{2D-SW} (K)	T_c^{mf} (K)	T^* (K)	$\alpha=\rho_n(0K)$ $(\Omega\text{-m})\times10^{-4}$	$W=\Delta T_c$ (K)
0	——	0.56	0.93	2.03	98.59	99.79	141.88	97.99	170.74	1.60	3.65
0.5	0.34	0.50	1.04	2.04	116.38	130.43	151.50	112.37	169.56	0.485	11.00
1.0	——	0.58	0.99	2.01	126.42	134.44	154.51	113.37	189.63	0.495	10.51
2.0	——	0.62	0.99	2.01	132.44	139.46	160.53	115.38	185.61	0.495	9.10
4.0	0.36	0.50	1.01	2.00	116.38	131.43	155.51	106.35	184.61	0.689	10.00

The various superconductivity parameters (i.e. $\xi_c(0)$, J, N_G, $\lambda_{p.d}$, $B_c(0)$, B_{c1}, B_{c2}, κ, J_c, V_F, E_F, and τ_φ) deduced from the FIC analysis of (Ag)$_x$/CuTl-1223 composites samples with x = 0, 0.5, 1.0, 2.0 and 4.0 wt.% are given in Table 3.3. The values of N_G, $B_c(0)$, B_{c1}, B_{c2}, J_c, and E_F have been decreased marginally, whereas $\xi_c(0)$, J, $\lambda_{p.d.}$, κ, V_F, E_F, and τ_φ have been enhanced after the inclusion of Ag nanoparticles. It is witnessed that $\xi_c(0)$ has been improved with the increase of 'J' values after the addition of Ag nanoparticles in CuTl-1223 superconducting matrix.

Table 3.3: The superconductivity parameters deduced from the FIC analysis of (Ag)$_x$/CuTl-1223 composites samples with x = 0, 0.5, 1.0, 2.0 and 4.0 wt.%.

Samples x = wt.%	$\xi_c(0)$ (Å)	J	N_G	$\lambda_{p.d}$ (Å)	$B_c(0)$ (T)	B_{c1} (T)	B_{c2} (T)	κ	$J_c(0)\times10^5$ (A/cm^2)	$V_F\times10^7$ (m/s)	E_F (eV)	$\tau_\varphi\times10^{-14}$ (s)
0	1.01	0.018	0.350	547.18	2.661	0.194	128.7	34.19	2.6462	0.63	0.183	2.25
0.5	3.00	0.160	0.225	2181.0	0.667	0.017	128.7	136.3	0.1664	2.44	0.123	3.34
1.0	3.23	0.185	0.290	2551.0	0.570	0.012	128.7	159.4	0.1216	2.71	0.122	3.38
2.0	3.42	0.208	0.298	2747.4	0.530	0.011	128.7	171.7	0.1048	2.99	0.126	3.27
4.0	3.64	0.235	0.278	3134.9	0.464	0.008	128.7	195.9	0.0805	2.83	0.151	2.73

The cross-over from 2D to 0D (from LD to MT contribution) takes place at a particular temperature where the mean free path l of the carriers approaches to ξ_{ab} and Cooper pairs are

broken to fermions. The values of phase relaxation time τ_φ calculated at this particular temperature are 2.25×10^{-14}, 3.34×10^{-14}, 3.38×10^{-14}, 3.27×10^{-14}, and 2.73×10^{-14} s for x = 0, 0.5, 1.0, 2.0, and 4.0 wt.%, respectively. The increase of τ_φ is an evidence of long life of Cooper pairs at certain high temperature values after Ag nanoparticles addition in CuTl-1223 superconducting matrix. The increase of ξ_c (0), J, V_F, and E_F shows the improvement of superconducting properties, which may be due to healing up the voids and improving the inter-grains connectivity after the inclusion of Ag nanoparticles. This also shows that the samples become more isotropic after the addition Ag nanoparticles. The variation in microscopic parameters extracted from FIC analysis explained the overall improvement of superconductivity up to certain optimum level of Ag nanoparticles addition in CuTl-1223 superconducting matrix.

3.4 References

[1] Nawazish A. Khan, Y. Sekita, H. Ihara, and A. Maqsood, Physica C 377, 43 (2002).

[2] E. V. Antipov, A. M. Abakumov, and S. N. Putilin, Supercond. Sci. Technol. 15, R31 (2002).

[3] Nawazish A. Khan, Y. Sekita, F. Tateai, T. Kojima, K. Ishida, N. Terada, and H. Ihara, Physica C 320, 39 (1999).

[4] K. Tokiwa, H. Aota, C. Kunugi, K. Tanaka, Y. Tanaka, A. Iyo, H. Ihara, and T. Watanabe, Physica B 284, 1077 (2000).

[5] K. Tanaka, A. Iyo, N. Terada, K. Tokiwa, S. Miyashita, Y. Tanaka, T. Tsukamoto, S. K. Agarwal, T. Watanabe, and H. Ihara, Phys. Rev. B 63, 064508 (2001).

[6] Nawazish A. Khan, and M. Mumtaz, Phy. Rev. B 77, 054507 (2008).

[7] T. Matsushita, Supercond. Sci. Technol. 13,730 (2000).

[8] D. Larbalestier, A. Gurevich, D. M. Feldmann, and A. Polyanski, Nature 414, 368 (2001).

[9] R. Goswami, T. J. Haugan, P. N. Barnes,G. Spanos, and R. L. Holtz, Physica C 470, 318 (2010).

[10] F. Ben Azzouz, M. Zouaoui, A. Mellekh, M. Annabi, G. Van Tendeloo, and M. Ben Salem, Physica C 455, 19 (2007).

[11] Y. Zhao, C. H. Chen, and J. Wang, Supercond. Sci. Technol. 18, S43 (2005).

[12] J. Plain, T. Puig, F. Sandiumenge, X. Obradors, and J. Rabier, Phys. Rev. B 65, 104526 (2002).

[13] S. Y. Chen, and I. G. Chen, Supercond. Sci. Technol. 17, 7 (2004).

[14] N. Hari Babu, E. S. Reddy, D. A. Cardwell, A. M. Campbell, C. D. Tarrant, and K. R. Schneider, Appl. Phys. Lett. 83, 4806 (2003)

[15] K. Nakashima, N. Chikumoto, A. Ibi, S. Miyata, Y. Yamada, T. Kubo, A. Suzuki, T. Terai, Physica C 463–465, 665 (2007).

[16] A. Hamrita, F. Ben Azzouz, W. Dachraoui, and M. Ben Salem, J. Supercond. Nov. Magn. 26, 879 (2013).

[17] S. Patnaik, A. Gurevich, S. D Bu, S. D. Kaushik, J. Choi, C. B. Eom, and D. C. Larbalestier, Phys. Rev. B 70, 064503 (2004).

[18] S. Dadras, Y. Liu, Y. S. Chai, V. Daadmehr, and K. H. Kim, Physica C 469, 55 (2009).

[19] M. Farbod, and R. M. Batvandi, Physica C 471, 112 (2011).

[20] I. E. Agranovski, Y. Ilyushechkin, I. S. Altman, T. E. Bostrom, and M. Choi, Physica C **434**, 115 (2006).

[21] A. Goyal, S. Kang, K. J. Leonard, P. M. Martin, A. A. Gapud, M. Varela, M. Paranthaman, A. O. Ijaduola, E. D. Specht, J. R. Thompson, D. K. Christen, S. J. Pennycook, and F. A. List, Supercond. Sci. Technol. **18**, 1533(2005).

[22] P. Mele, K. Matsumoto,T. Horide, A. Ichinose, M. Mukaida, Y. Y. Oshida, S. Horii, and R. Kita, Supercond. Sci. Technol. **21**, 032002 (2008).

[23] K. Yamada, A. Ichinose, S. Horii, H. Kai, R. Teranishi, M. Mukaida, R. Kita, S. Kato, Y. Yoshida, K. Matsumoto, and S. Toh, Physica C **468**, 1638 (2008).

[24] M. N. Khan, M. Khizar and B. N. Mukeshev, Physica B **321**, 257 (2002).

[25] H. Najafpour, S. H. R. Shojaei and S. M. Shojaeiu, J. Supercond. Non. Magn. **23**, 487 (2010).

[26] F. M. Julian, S. Ricart, A. Pomer, and L. M. Marzan and J. Nanoscience Tech. **11**, 3245 (2011).

[27] A. H. Li, M. Ionescu, H. k. Liu, T. Silver, X. L. wang, and S. X. Dou, IEEE Trans. Appl. Supercond. **15**, 2 (2005).

[28] S. Sakiroglu, and K. Kocabas, J. Supercond. Nov. Magn. **24**, 1321 (2011).

[29] W. Abdeen, N. h. Mohammed, R. Awad, S. A. Mahmoud, and M. Hasebbo, J. Supercond. Nov. Magn. **26**, 3235 (2013).

[30] W. D. Huang, W. H. Song, Z, Cui, B. Zhao, M. H. Pu, X. C. Wu, Y. P. Sun, and J. J. Du, Phy. Stat. Sol. (a) **179**, 189 (2000).

[31] Z. Y. Jia, H. Tang, Z. Q. Yang, Y. T. Xing, Y.Z. Wang, and G.W. Qiao, Physica C **337**, 130 (2000).

[32] M. Annabi, A. M'chirgui, F. Ben Azzouz, M. Zouaoui, M. Ben Salem, Physica C **405**, 25 (2004).

[33] K. Christova , A. Manov, J. Nyhus, U. Thisted, O. Herstad, S. E. Foss, K. N. Haugen, and K. Fossheim, J. Alloy.Compound. **340**, 1 (2002).

[34] A. Mellekh, M. Zouaoui, F. Ben Azzouz, M. Annabi, and M. Ben Salem, Solid Stat. Commun. **140**, 318 (2006).

[35] A. Ghattas, F. Ben Azzouz, M. Annabi, M. Zouaoui, and M. Ben Salem, Journal of Physics: Conference Series. **97**, 012175 (2008).

[36] M. Annabi, A. Ghattas, M. Zouaoui, F. Ben Azzouz, and M. Ben Salem, Journal of Physics: Conference Series **150**, 052008 (2009).

[37] V. Bartůněk, and O. Smrčková, J. Supercond. Nov. Magn. **24 (4)**, 1241 (2011).

[38] R. Mawassi, S. Marhaba, M. Roumié, R. Awad, M. Korek, and I. Hassan, J. Supercond. Nov. Magn. **27 (5)**, 1131 (2014).

[39] R. Abd-Shukor, Nabil A. A. Yahya, and A. Agail, AIP Conf. Proc. **1588**, 35 (2014)

[40] J. Gutiérrez, A. Llordés, J. Gazquez, M. Gibert, N. Romá, S. Ricart, A. Pomar, F. Sandiumenge, N. Mestres, T. Puig, and X. Obradors, Nat. Mater. **6**, 367 (2007).

[41] T. G. Holesinger, L. Civale, B. Maiorov, D. M. Feldmann, J. Y. Coulter, J. Miller, V. A. Maroni, Z. J. Chen, D. C. Larbalestier, R. Feenstra, X. P. Li, M. B. Huang, T. Kodenkandath, W. Zhang, M. W. Rupich, and A. P. Malozemoff, Adv. Mater. **20**, 391 (2008)

[42] S. Engel, T. Thersleff, R. Huhne, L. Schultz, and B. Holzapfel, Appl. Phys. Lett. **90**, 102505 (2007).

[43] T. Puig, J. Gutierrez, A. Pomar, A. Llordes, J. Gazquez, S. Ricart, F. Sandiumenge, and X. Obradors, Supercond. Sci. Technol. **21**, 034008 (2008).

[44] N. M. Strickland, N. J. Long, E. F. Talantsev, P. Hoefakker, J. Xia, M. W. Rupich, T. Kodenkandath, W. Zhang, X. Li, and Y. Huang, Physica C **468**, 183 (2008).

[45] M. Miura, M. Yoshizumi, T. Izumi, and Y. Shiohara, Supercond. Sci. Tech. **23**, 014013 (2010).

[46] L. G. Aslamazov, and A. L. Larkin, Phys. Lett. A **26**, 238 (1968).

[47] W. E. Lawrence, and S. Doniach, in Proceedings of the 12th International Conference on Low Temperature Physics, Keigaku, Tokyo, (1971), p. 361.

[48] A. L. Solovjov, H. -U. Habermeier, and T. Haage, Low Temp. Phys. **28**, 17 (2002).

[49] C. A. C. Passos, M. T. D. Orlando, J. L. Passamai, Jr., E. V. L. de Mello, H. P. S. Correa, L. G. Martinez, Phys. Rev. B **74**, 094514 (2006).

[50] S. R. Ghorbani, and M. Rahmati Tarki, J. Supercond. Nov. Magn. **27**, 749 (2014).

[51] S. H. Han, Yu. Eltseu, and Ō. Rapp, Phys. Rev. B **61**, 11776 (2000).

[52] S. H. Naqib, J. R. Cooper, J. L. Tallon, R. S. Islam, and R. A. Chakalov, Phys. Rev. B **71**, 054502 (2005).

[53] K. Maki, Prog. Theor. Phys. **39**, 897 (1968).

[54] R. S. Thompson, Phys. Rev. B **1**, 327 (1970).

[55] S. Hikami and A. I. Larkin, Mod. Phys. Lett. B **2**, 693 (1988).

[56] K. Maki, and R. S. Thompson, Phys. Rev. B **39**, 2767 (1989).

[57] P. K. Nayak and S. Ravi, Supercond. Sci. Technol. **19**, 1209 (2006).

[58] W. Lang, G. Heine, W. Kula, and Roman Sobolewski, Phys. Rev. B **51**, 9180 (1995).

[59] A. L. Solovjov, H.-U. Habermeier, T. Haage, and Fiz Nizk, Low Temp. Phys. **28**, 99 (2002).

[60] J. Bardeen, L. N. Cooper, and J. R. Schrieffer, Phys. Rev. **108**, 1175 (1957).

[61] A. L. Solovjov, V. M. Dmitriev, and H.-U. Habermeier, Phys. Rev. B **55**, 8551 (1997).

[62] H. Ihara, A. Iyo, K. Tanaka, K. Tokiwa, K. Ishida, N. Terada, M. Tokumoto, Y. Sekita, T. Tsukamoto, T. Watanabe, and M. Umeda, Physica C **282-287**, 1973 (1997).

[63] H. Hayakawa, and Y. Enomoto, in Advances in Superconconductivity VIII: Proceedings of the 8th Int. Symposium on Superconductivity, Hamamatsu, (1995), pp. 247–249.

[64] A. K. Ghosh and A. N. Basu, Phys. Rev. B **59**, 11193 (1999).

[65] A. I. Abou Aly, I. H. Ibrahim, R. Awad, and A. EL-Harizy, J. Supercond. Nov. Magn. **23**, 1325 (2010).

[66] J. F. Annet, Superconductivity, Superfluids and Condensates (Oxford University Press, London, 2004).

[67] N. A. Khan, and Shakil Ahmad, J. Appl. Phys. **112**, 033912 (2012).

[68] N. H. Mohammad, A. I. Abou-Aly, R. Awad, I. H. Ibrahim, M. Roumie, and M. Rekaby, J. Low Temp. Phys. **172**, 234 (2013).

[69] M. Mumtaz, M. Zubair, Nawazish A. Khan, and K. Nadeem, Ceram. Int. **40**, 6655 (2014).

[70] M. Mumtaz, Nawazish A. Khan, Saleem Abbas, and Khurram Shehzad, Ceram. Int. **40**, 4187 (2014).

[71] Nawazish A. Khan, M. Mumtaz, K. Sabeeh, M. I. A. Khan, and Mushtaq Ahmad, Physica C **407**, 103 (2004).

[72] Nawazish A. Khan, and M. Mumtaz, Eur. Phys. J. Appl. Phys. **38**, 47 (2007).

[73] M. Mumtaz, M. Kamran, K. Nadeem, Abdul Jabbar, Nawazish A. Khan, Abida Saleem, S. Tajammul Hussain, and M. Kamran, Low Temp. Phys./ Fiz. Nizk. Temp. **39**, 806 (2013).

[74] M. Mumtaz, and Nawazish A. Khan, Supercond. Sci. Technol. **21** ,065015 (2008).

[75] M. Mumtaz, and Nawazish A. Khan, Phys. Scr. **80**, 025702 (2009).

[76] J. C. Zhang, F. Q. Liu, G.S. Cheng, J. X. Shang, J. Z. Liu, S. X. Cao, and Z. X. Liu, Phys, Lett. A **201**, 70 (1995).

[77] P. F. Miceli, J. M. Tarascon, L. H. Greene, H. P. Barbou, F. J. Rotella, and J. D. Jorgensen, Phys. Rev. B **37**, 5932 (1988).

[78] S. J. Feng, J. Ma, H.D. Zhou, G. Li, L. Shi, Y. Liu, J. Fang, and X.G. Li, Physica C **386**, 22 (2003).

[79] A. J. Batista-Leyva, M. T. D. Orlando, L. Rivero, R. Cobas, and E. Altshuler, Physica C **383**, 365 (2003).

[80] M. Tinkham, Phys. Rev. Lett. **61**, 1658 (1988).

[81] T. M. Palstra, B. Batlogg, L. F. Schneemeyer, and J. V. Waszczak, Phys. Rev. Lett. **61**, 1662 (1988).

Chapter 4

$(Au)_x$/CuTl-1223 Nano-Superconductor Composites

In this chapter, we have investigated the effect of Au nanoparticles addition on superconducting properties of CuTl-1223 matrix in detail. The present work is concerned with the effect of nano-Au particles addition on the phase formation and characteristics superconducting parameters. We have reported the influence of Au nanoparticles addition on structure, morphology and superconducting transport properties. The main objective of this work is to improve the inter-grains connectivity, superconducting volume fraction, and to investigate their effects on superconductivity. This can be due to the reduction of defects in the form of voids and oxygen deficiencies by filling the voids and pores with these nanoparticles. We have also determined the optimum level of Au nanoparticles inclusion for the maximum improvement in the superconducting properties of CuTl-1223 matrix.

4.1 Introduction

$(Cu_{0.5}Tl_{0.5})Ba_2Ca_2Cu_3O_{10-\delta}$ (CuTl-1223) is the most attractive phase of $Cu_{0.5}Tl_{0.5}Ba_2Ca_{n-1}Cu_nO_{2n+4-\delta}$ (CuTl-12(n-1)n); n = 2, 3, 4,..., high temperature superconductors (HTSCs) family due to its higher critical temperature, lower superconducting anisotropy, and longer coherence length along c-axis [1]. But the performance of this compound in bulk form may be reduced mainly due to inter-grain voids and pores. The presence of inter-grain weak links diminishes the critical parameters of superconductivity. Also the motion of the vortices in HTSCs creates resistance and causes energy dissipation. These facts restrict their applications such as superconducting magnetic field sensors. There has been consistent effort in enhancing the current carrying capacity of the superconducting materials, which may be achieved by incorporating extended defects acting as pinning centers. The effect of pinning center is at its best when their sizes are of the order of coherence length [2]. It is important that the density of these pinning centers should be as high as 10^{11} cm^{-2}. Large number of defects created to achieve large densities of pinning centers degrades the superconducting properties. It was found that magnetic nanoparticles may act as efficient pinning centers at much lower density [2-4]. In order to enhance the transport properties, many attempts have been made to introduce artificial defects of nanometer order of magnitude into the bulk HTSCs as extra effective pinning centers under applied field, such as by nanoparticles addition in the bulk or by post-annealing of the

superconducting samples [5, 6]. The superconducting properties of granular bulk HTSCs can be improved by the inclusion of nanoparticles at the grain-boundaries. But the size and homogenous distribution of nanoparticles at the grain-boundaries of the bulk HTSCs is the real challenge [7-13]. The sizes and densities of defects are critical factors to be adjusted for effective vortex pinning. It was observed that magnetic nanoparticles such as Fe_2O_3 embedded in to the bulk HTSCs act as efficient pinning centers [3, 14]. The improvement of critical current density (J_c) was observed in Bi-based HTSC by the inclusion of MgO, ZrO_2 and Al_2O_3 nanoparticles [15-17]. Transmission Electron Microscopy (TEM) has showed that MgO nanoparticles could be embedded within the superconducting Bi-2212 grains. The presence of MgO nanoparticles has increased the transition sharpness, and the superconductor volume fraction in the sample [18]. The addition of ZrO_2 and ZnO nanoparticles in Gd-123 superconductor has improved the critical current density (J_c) but suppressed zero resistivity critical temperature (T_c) [19]. The addition of SnO_2 nanoparticles increases the microstructure density and reduces porosity among the grains of $Cu_{0.5}Tl_{0.5}$-1223 superconductor [20]. The improvement of T_c, J_c and phase volume fraction is obtained on different concentrations of ZnO nanoparticles in $(Cu_{0.5}Tl_{0.25}Pb_{0.25})$-1223 [21]. The superconducting properties (i.e. T_c, J_c, etc) of CuTl-1223 were enhanced with the addition of CuO, CaO_2 and BaO nanoparticles [22, 23]. The addition of nanoparticles like $NiFe_2O_4$, Al_2O_3, ZrO_2, Ag etc in suitable amount helps in creating the effective flux pinning centers, which can enhance the critical superconductivity parameters [24-26]. The addition of nanostructures of noble metals such as Ag and Au has shown the significant improvement in superconducting parameters in many superconducting systems [27-30]. Increased nano-Ag content in Bi-2223 improves the connectivity among the grains and enhances superconductivity [31, 32].

4.2 Results and Discussion

4.2.1 X-Ray Diffraction (XRD)

The XRD pattern of Au nanoparticles exhibits prominent sharp diffraction peaks indexed with face-centered cubic (FCC) structure as shown in Fig. 4.1. Also XRD analysis showed the distinct diffraction peaks at 38.22°, 44.35° 64.67°, and 77.62°, which corresponds to (1 1 1), (2 0 0), (2 2 0) and (3 1 1) planes respectively of FCC structure. The FCC structures of Au nanoparticles matches well with the database of Joint Committee on Powder Diffraction Standards (JCPDS No. 00-004-0784), revealing that the synthesized Au nanoparticles are

composed of pure crystalline gold. The Au nanoparticles size can be calculated by Sherrer's formula and the average size of Au nanoparticles is about 39 nm.

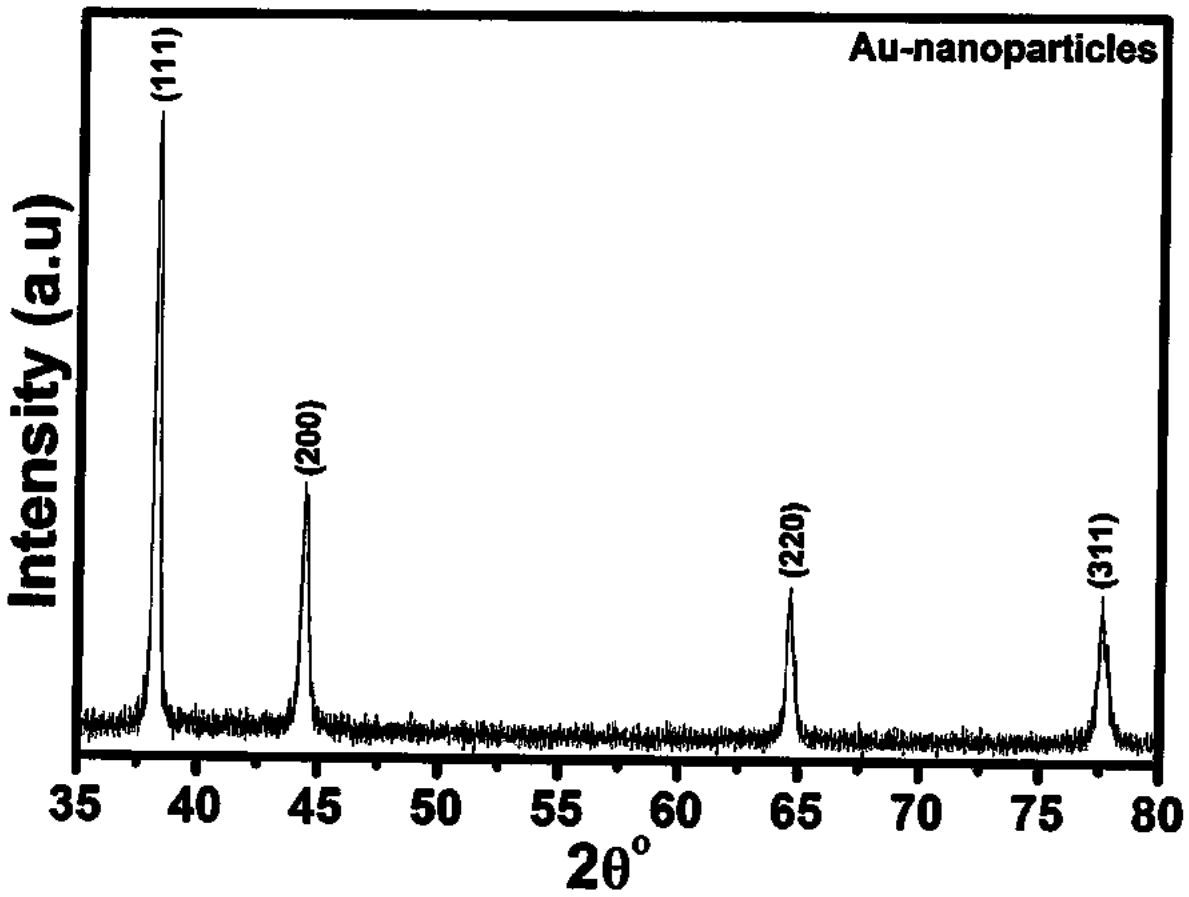

Fig. 4.1: XRD pattern of gold (Au) nanoparticles.

The XRD patterns of $(Au)_x$/CuTl-1223 for x= 0, 0.5 and 1.0 wt.% composites are shown in Fig. 4.2. The composites have shown the tetragonal structure following P4/mmm symmetry. Majority of the diffraction peaks corresponds to the CuTl-1223 phase with lattice parameters a = 4.20 Å and c = 15.31 Å for x = 0. The addition of Au nanoparticles in CuTl-1223 phase has slightly decreased the cell parameters lengths i.e. a = 4.20 Å, c = 15.30 Å and a = 4.19 Å and c = 15.25 Å for x = 0.5 and x = 1.0 wt.%, respectively, which might be due to variation of oxygen contents or stresses and strains in the polycrystalline lattice. The slight decrease in the c-axis length is most probably due to the compression of apical bond length by the effect of variation in O_δ oxygen and stresses produced by the addition of these nanoparticles. The un-indexed peaks are possibly due to presence of some impurities and some other superconducting phases as given in the in set of Fig. 4.2.

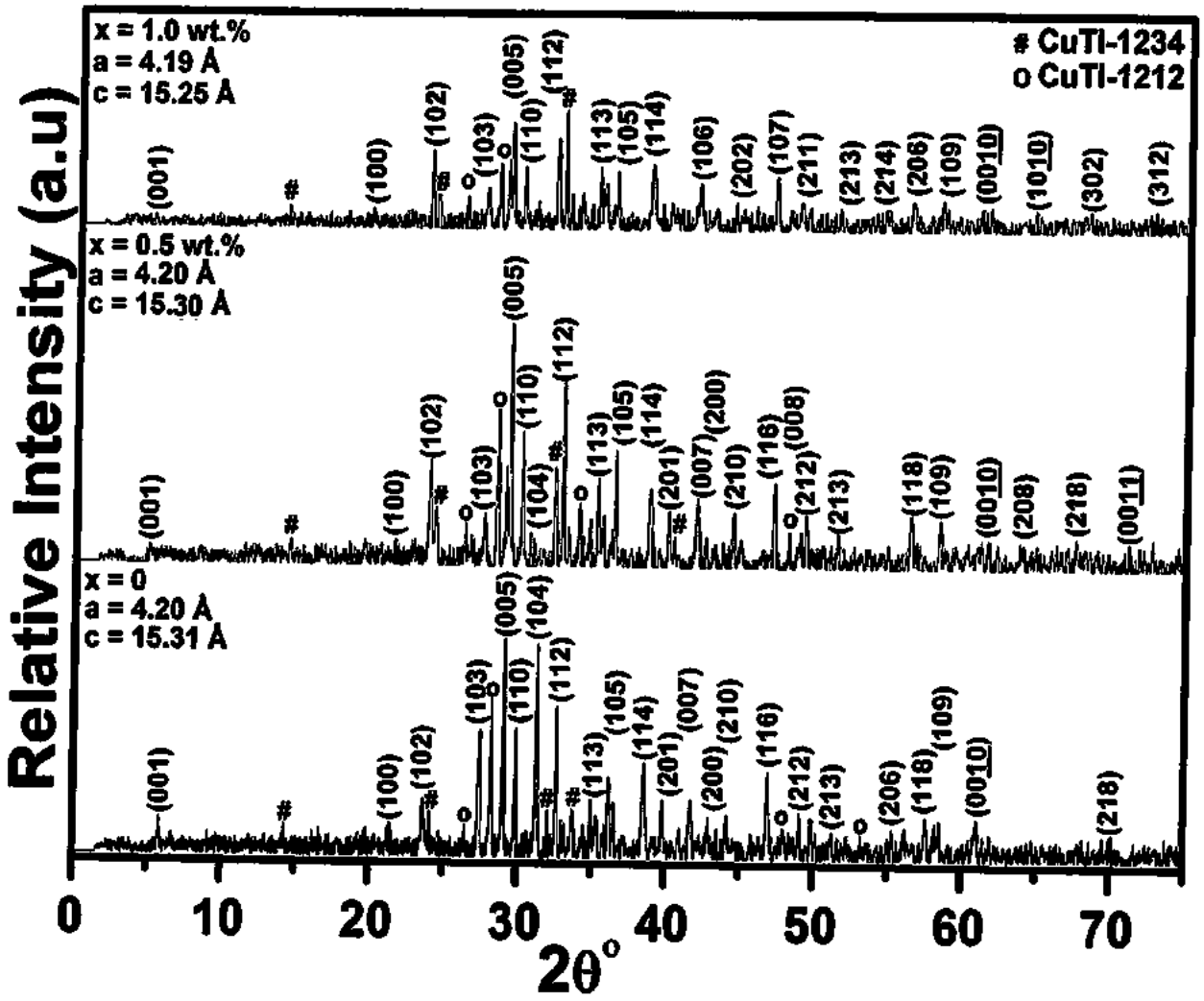

Fig. 4.2: XRD patterns of (Au)$_x$/CuTl-1223 composites with x = 0, 0.5, 1.0 wt.% .

4.2.2 Scanning Electron Microscopy (SEM)

The surface morphology was examined by SEM images of the (Au)$_x$/CuTl-1223 composites as shown in Fig. 4.3. The granular nature and porosity of samples are obvious from these micrographs. There is an improvement in the inter-grain connectivity as well as in the grain size after the addition of Au nanoparticles in the matrix. The main problem is the inhomogeneous mixing of Au nanoparticles in the matrix.

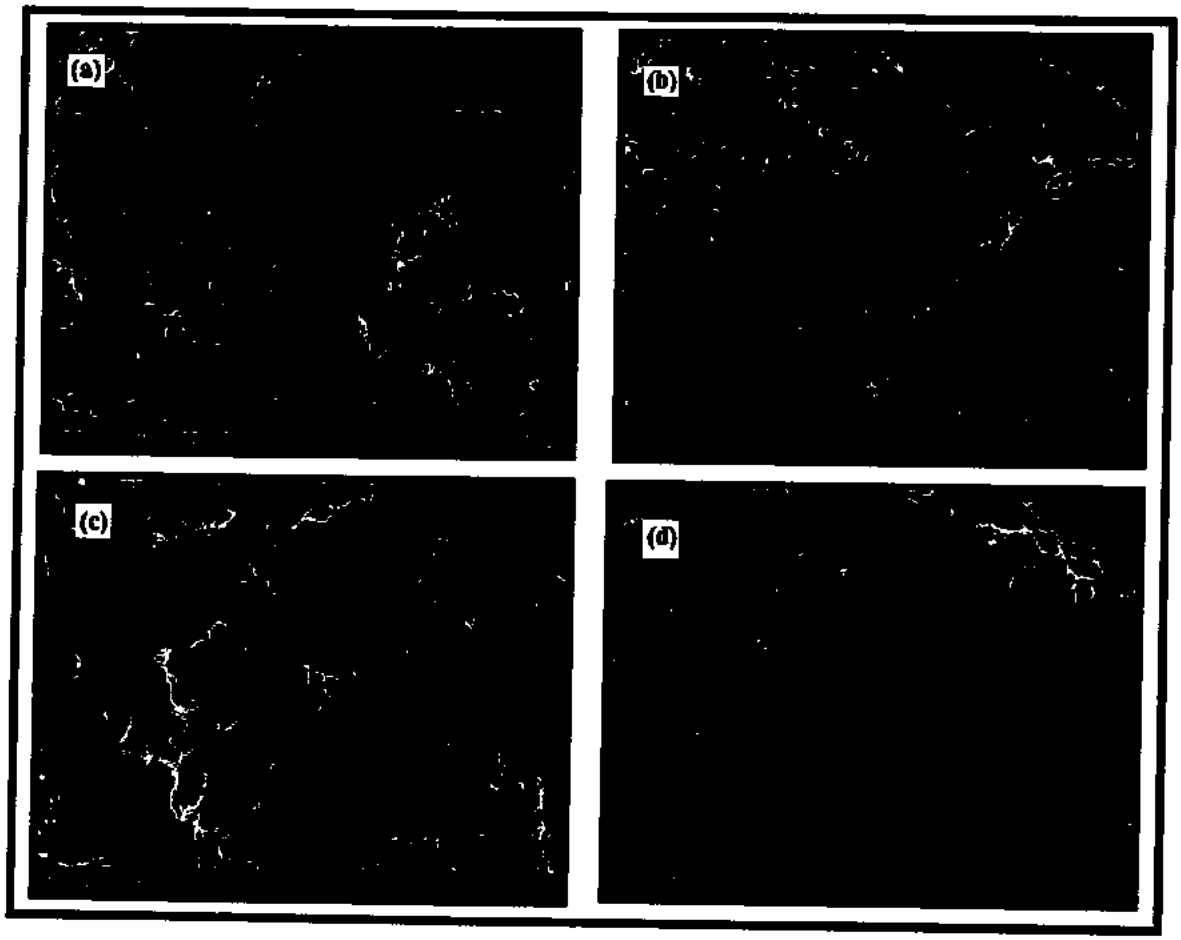

Fig. 4.3 (a-d): Typical SEM images of $(Au)_x$/CuTl-1223 composites (a) x = 0, (b) x = 0.5 wt.%, (c) x = 1.0 wt.% and (d) x = 1.5 wt.%.

4.2.3 Fourier Transform Infrared (FTIR) Spectroscopy

The FTIR absorption spectra of $(Au)_x$/CuTl-1223 (x = 0, 0.5, 1.0 and 1.5 wt.%) composites in the range from 400-700 cm^{-1} and the unit cell of CuTl-1223 superconductor are shown in Fig. 4.4 (a, b). The nomenclature of different oxygen atoms in the unit cell of CuTl-1223 superconductor has been demonstrated in Fig. 4.4(b). The bands in the range from 400 to 540 cm^{-1} are associated with the apical oxygen atoms and in the range from 541 to 600 cm^{-1} are associated with CuO_2 planar oxygen atoms. The bands in the range from 670 to 700 cm^{-1} are associated with O_δ atoms in the $Cu_{0.5}Tl_{0.5}Ba_2O_{4-\delta}$ charge reservoir layer [33-35]. But in the pure $Cu_{0.5}Tl_{0.5}Ba_2Ca_2Cu_3O_{10-\delta}$ samples, the apical oxygen modes of type Tl–O_A–Cu(2) and Cu(1)–O_A–Cu(2) are observed around 427 cm^{-1} and 458~492 cm^{-1} and CuO_2 planner mode is around 526 cm^{-1}. The apical mode of type Tl–O_A–Cu(2) is slightly softened from 427 cm^{-1} to 420~421 cm^{-1} and the position Cu(1)–O_A–Cu(2) remained around 458~490 cm^{-1} after nano-Au particles

addition. The position of Cu(2) –O_P–Cu(2) planner oxygen mode is also slightly softened from 526 cm^{-1} to 520 cm^{-1} after nano-Au particles addition. The slight shifting of the positions of different oxygen modes represents the presence of strains in the materials, which affects the bond lengths. But overall the positions of all the oxygen vibrational phonon modes remained almost unaltered after nano-Au particles addition in CuTl-1223 matrix. This gives us a clue that nano-Au particles did not substitute any atom in the unit cell and remained at the grain-boundaries of (Au)$_x$/CuTl-1223 composites.

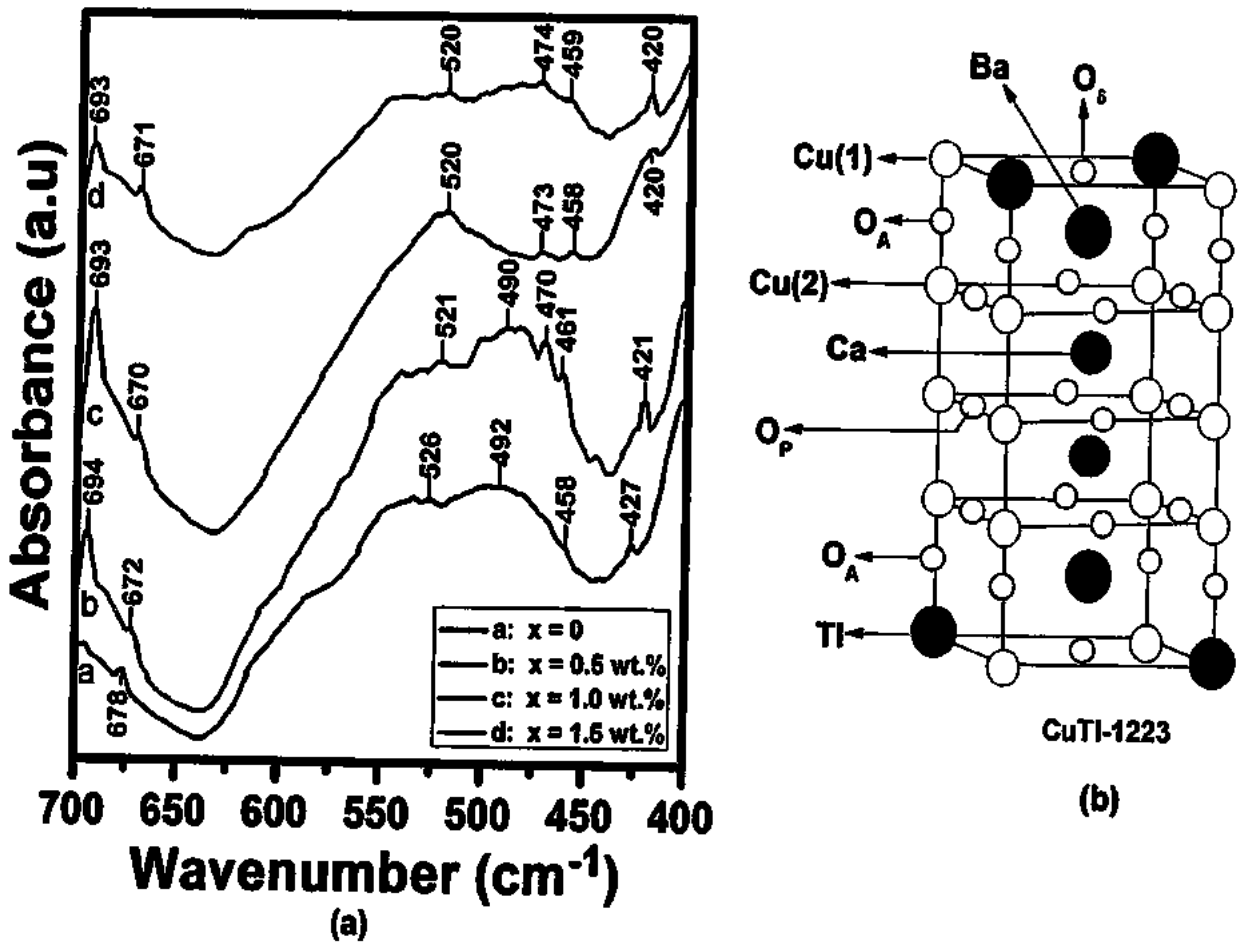

Fig. 4.4 (a, b): (a) FTIR absorption spectra of (Au)$_x$/CuTl-1223 composites, (a) x = 0, (b) x = 0.5 wt.% (c) x = 1.0 wt.%, and (d) x = 1.5 wt.%. **(b)** Unit cell of CuTl-1223 superconductor.

4.2.4 Resistivity versus Temperature Measurements

The resistivity versus temperature measurements of (Au)$_x$/CuTl-1223 (x = 0, 0 .5, 1.0 and 1.5 wt.%) composites are shown in the Fig. 4.5. All the samples exhibit metallic behavior in the variation of resistivity versus temperature measurements at high temperatures before superconducting transition temperatures. The variation of $T_c(0)$ and normal state resistivity $\rho_{(300}$

K) (Ω-cm) versus x (i.e. Au contents) is given in the inset of Fig. 4.5. The value of T_c (0) increases up to x = 1.0 wt. % and then decreases, which predicts the optimum inclusion level of Au nanoparticles in CuTl-1223 matrix. The value of T_c has increased from 88 K of un-doped sample (x = 0) to 99 K and 101 K for x = 0.5 and 1.0 wt. % addition of Au nanoparticles, respectively. The value of T_c has been decreased to 96 K for x = 1.5 wt. %. The initial increase in T_c is possibly due to improved weak links among the superconducting grains by healing up the voids and pores with nano-Au particles. But after certain optimum inclusion level of Au-nanoparticles, the superconducting volume fraction start to be decreased, which causes the suppression of superconductivity parameters. Normally the zero resistivity critical temperature T_c (0) of cuprates depends upon the carriers' density in their CuO_2 planes [36]. The carriers supplied by the charge reservoir layer to the CuO_2 planes depend upon the oxygen contents in the charge reservoir layer [37]. As with the addition of Au nanoparticles, the T_c (0) increases, this is due to optimization of carriers' density in the CuO_2 planes supplied by the charge reservoir layer. Therefore, it is obvious that the oxygen contents in the charge reservoir layer depends upon Au nanoparticles contents in the CuTl-1223 matrix. The superconducting volume fraction can also be improved by the optimization of oxygen, which can occupy the oxygen vacancies in the bulk CuTl-1223 matrix. The initial increase in T_c (0) is possibly due to increased superconducting volume fraction and improved weak links by the addition of nano-Au particles at the grain-boundaries. The decreasing trend in T_c (0) beyond certain optimum limit of Au nanoparticles addition may be due to agglomeration and segregation of these nanoparticles at the grain-boundaries in the bulk CuTl-1223 matrix, which can cause the degradation of the quality of the samples and reduces the superconducting bulk volume fraction of the samples. The initial increase in T_c (0) is possibly due to improved weak-links among the superconducting grains by nano-Au particles at the grain-boundaries. But after certain optimum inclusion level of Au-nanoparticles, the superconducting volume fraction and density of mobile charge carriers start to be decreased, which causes the suppression of superconductivity parameters. The normal state resistivity is very high for the sample with x = 1.5, which is the finger print of the enhanced scattering cross-section of the carriers and reduced superconducting volume fraction. Usually, the trend in the variation of superconductivity onset temperature T_c^{onset} (K) is similar to zero resistivity critical temperature T_c (0) of cuprates, which depends upon the carriers' density in CuO_2 planes. Superconducting fluctuations near the superconducting transition contribute to the

T_c^{onset} (K) and the Au nanoparticles addition may enhance these fluctuations and can affect T_c^{onset} (K) of these composites [38].

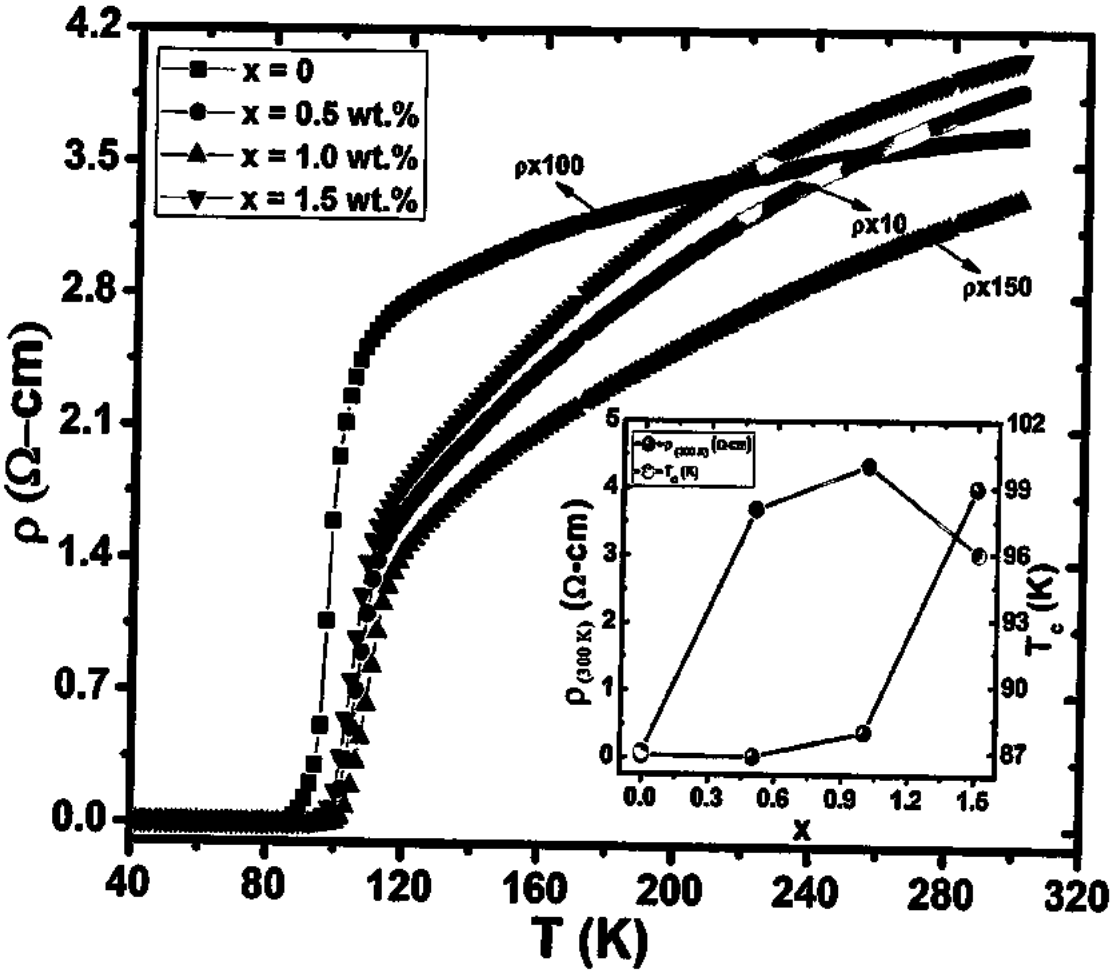

Fig. 4.5: Resistivity versus temperature measurements of $(Au)_x$/CuTl-1223 composites with x = 0.0, 0.5, 1.0and 1.5 wt.%. In the inset T_c (K) and $\rho_{(300K)}$ (Ω-cm) versus x (i.e. Au nanoparticles contents).

4.2.5 Magnetic Ac-Susceptibility Measurements

Magnetic ac-susceptibility measurements of $(Au)_x$/CuTl-1223 (x = 0, 0 .5, 1.0 and 1.5 wt.%) composites are shown in Fig. 4.6. The ac-susceptibility measurements of these samples were carried out in field cooled (FC) conditions by the mutual inductance method using an SR530 Lock-in Amplifier working at a frequency of 270 Hz with H_{AC} = 0.07 Oe of primary coil. Single peak above the transition temperature in the ac-susceptibility measurements is observed for all the samples. There are two components of magnetic ac-susceptibility, in-phase component (χ') and out of phase component (χ''). The magnitude of diamagnetism of the superconducting materials is represented by the real part (χ') of the ac-susceptibility and the ac-losses corresponding to the flux penetration into superconductor sample is represented by imaginary

part (χ''). The imaginary part of the ac-susceptibility provides the inter-granular contribution and therefore, gives information about the nature of inter-grains weak links and pinning strength [39-41]. The suppression of superconductivity within the grains decreases the magnitude of χ'. It is observed that the onset temperature as well as magnitude of diamagnetism initially increases and then decreases beyond certain optimum limit of Au nanoparticles addition. Similarly, the peak position in χ'' initially shifts to higher temperature values and then shifts to lower temperature values beyond certain optimum limit of Au nanoparticles addition.

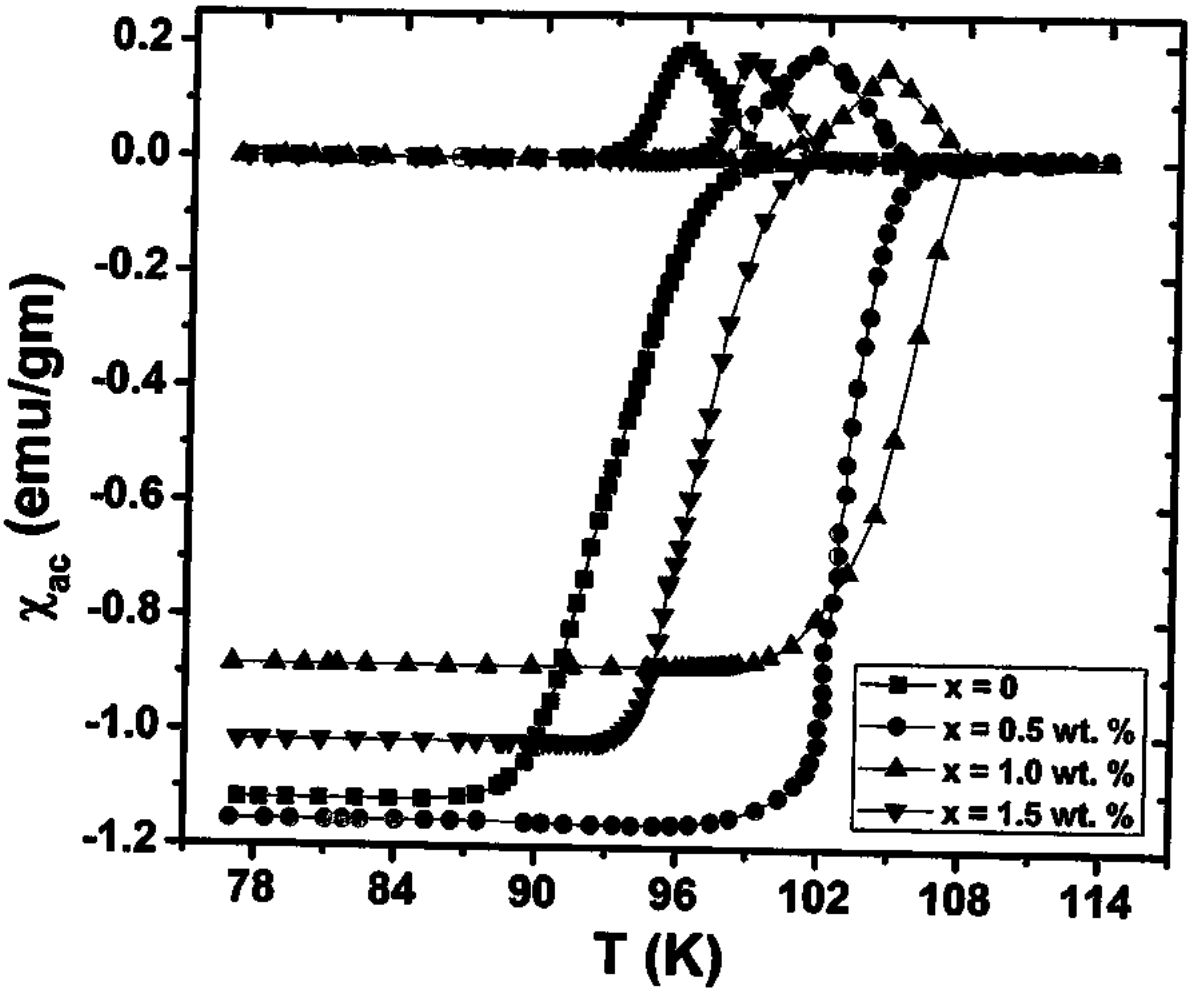

Fig. 4.6: Ac-susceptibility measurements of (Au)$_x$/CuTl-1223 composites with x = 0, 0.5, and 1.0 wt.%.

The value of onset of diamagnetism {T_c^{onset} (K)} increases up to x = 1.0 wt. % and then decreases, which predicts the optimum inclusion level of Au nanoparticles in CuTl-1223 matrix for maximum improvement of superconductivity. The initial increase in T_c^{onset} (K) is possibly due to improved superconducting volume fraction and carriers density with the increase of Au

nanoparticles. The suppression of T_c^{onset} (K) and diamagnetic signal beyond a certain level of Au nanoparticles inclusion can be due to reduction of superconducting volume fraction and carriers density. The relatively higher density of voids and pores in pure un-added Au nanoparticles samples can be the cause of reduction of superconducting volume fraction and superconductivity. The other defects in the form of oxygen deficiencies can cause the reduction of carriers' density from the optimum level. By the incorporation of Au nanoparticles at the grain-boundaries, the voids and pores can be filled and can improve the inter-grains weak-links. In this way, we can reduce the defects in the material and can improve the superconducting properties. The enhancement of T_c^{onset} (K) can be the indication of enhanced carriers' density towards optimization after Au nanoparticles addition. This can be due to the reduction of defects in the form of voids and oxygen deficiencies by filling the pores with these nanoparticles. But the non-superconducting metallic Au nanoparticles reduces the superconducting volume fraction in the superconducting state of CuTl-1223 matrix beyond the certain optimum level of Au nanoparticles inclusion i.e. x = 1.5 wt. % in this case.

The overall superconducting properties of CuTl-1223 matrix have been improved up to certain optimum level of Au nanoparticles addition that can be attributed to an increase in the inter-grains connectivity and enhanced superconducting volume fraction. The increase in superconducting properties can also be associated with the optimization of carriers' density in the CuO_2 planes supplied by the charge reservoir layer, which depends upon the optimum oxygen contents in the charge reservoir layer. Therefore, we can relate the oxygen contents with Au nanoparticles contents in the CuTl-1223 matrix. We have planned to carry out the infield measurement (i.e. J_c, ρ etc) to investigate the role of Au nanoparticles as additional flux pining centers. The uniform distribution and controlled size of nanostructures added in the HTSCs matrices are still unresolved problems in this area of research. We are trying to address these issues in our future research work.

4.3 References

[1] H. Ihara, K. Tanaka, Y. Tanaka, A. Iyo, N. Terada, M. Tokumoto, M. Ariyama, I. Hase, A. Sundaresan, N. Hamada, S. Miyashita, K. Tokiwa, and T. Watanabe, Physica C **341-348,** 487 (2000).

[2] S. Acharya, A. K. Biswal, J. Ray, and P. N. Vishwakarma, J. Appl. Phys. **112,** 053916 (2012).

[3] A. Snezhko, T. Prozorov, and R. Prozorov, Phys. Rev. B **71,** 024527 (2005).

[4] L. N. Bulaevskii, E. M. Chudnovsky, and M. P. Maley, Appl. Phys. Lett. **76,** 2594 (2000).

[5] M. H. Pu, W. H. Song, B. Zhao, X. C. Wu, T. Hu, Y. P. Sun, and J. J. Du, Supercond. Sci. Tech. **14,** 305 (2001).

[6] K. T. Lau, S. Y. Yahya, and R. Abd-Shukor, J. Appl. Phys. **99,** 123904 (2006).

[7] J. Gutiérrez, A. Llordés, J. Gazquez, M. Gibert, N. Romá, S. Ricart, A. Pomar, F. Sandiumenge, N. Mestres, T. Puig, and X. Obradors, Nat. Mater. **6,** 367 (2007).

[8] T. G. Holesinger, L. Civale, B. Maiorov, D. M. Feldmann, J. Y. Coulter, J. Miller, V. A. Maroni, Z. J. Chen, D. C. Larbalestier, R. Feenstra, X. P. Li, M. B. Huang, T. Kodenkandath, W. Zhang, M. W. Rupich, and A. P. Malozemoff, Adv. Mater. **20,** 391 (2008)

[9] M. Miura, T. Kato, M. Yoshizumi, Y. Yamada, T. Izumi, Y. Shiohara, and T. Hirayama, Appl. Phys. Express **1,** 051701 (2004).

[10] S. Engel, T. Thersleff, R. Huhne, L. Schultz, and B. Holzapfel, Appl. Phys. Lett. **90,** 102505 (2007).

[11] T. Puig, J. Gutierrez, A. Pomar, A. Llordes, J. Gazquez, S. Ricart, F. Sandiumenge, and X. Obradors, Supercond. Sci. Technol. **21,** 034008 (2008).

[12] N. M. Strickland, N. J. Long, E. F. Talantsev, P. Hoefakker, J. Xia, M. W. Rupich, T. Kodenkandath, W. Zhang, X. Li, and Y. Huang, Physica C **468,** 183 (2008).

[13] M. Miura, M. Yoshizumi, T. Izumi, and Y. Shiohara, Supercond. Sci. Tech. 23, 014013 (2010).

[14] R. Prozorov, T. Prozorov, and A. Snezhko, IEEE Tran. Appl. Supercond. **15,** 3277 (2005).

[15] W. D. Huang, W. H. Song, Z, Cui, B. Zhao, M. H. Pu, X. C. Wu, Y. P. Sun, and J. J. Du, Phy. Stat. Sol. (a) **179,** 189 (2000).

[16] Z. Y. Jia, H. Tang, Z. Q. Yang, Y. T. Xing, Y.Z. Wang, and G.W. Qiao, Physica C **337,** 130 (2000).

[17] M. Annabi, A. M'chirgui, F. Ben Azzouz, M. Zouaoui, M. Ben Salem, Physica C **405**, 25 (2004).

[18] K. Christova , A. Manov, J. Nyhus, U. Thisted, O. Herstad, S. E. Foss, K. N. Haugen, and K. Fossheim, J. Alloy.Compound. **340,** 1 (2002).

[19] Y. Xu, A. Hu, C. Xu, N. Sakai, I. Hirabayashi, M. Izumi, Physica C **468,** 1363 (2008).

[20] N. H. Mohammed, A. I. Abou-Aly, I. H. Ibrahim, R. Awad, and M. Rekaby, J. Alloy. Compound. **486,** 733 (2009).

[21] M. M. Elokret, R. Awad, A. A. El-Ghany, A. A. Shama, and A. El-wanis, J. Supercond. Nov. Magn. **24,** 1345 (2011).

[22] N. A. Khan, A. Saleem, and S. T. Hussain, J. Supercond. Nov. Magn. **25,** 1725 (2012).

[23] M. Mumtaz, Asif I. Bhatti, K. Nadeem, Nawazish A. Khan, Abida Saleem, and S. Tajammul Hussain, J. Low Temp. Phys. **170,** 185 (2013).

[24] M. Annabi, A. M. Chirgui, F. B. Azzuoz, and M. B. Salem, Physica C **25,** 405 (2004).

[25] M. Annabi, A. Ghattas, M. Zouaoui, F. Ben Azzouz, and M. Ben Salem, Physica C **468,** 31 (2008).

[26] N. H. Mohammad, A. I. Abou-Aly, R. Awad, I. H. Ibrahim, M. Roumie, and M. Rekaby, J. Physica C **172,** 234-255 (2012).

[27] T. D. Dzhafarov, M. Altunbas and T. Kucukomeroglu, Mater. Lett. **25,** 81 (1995).

[28] B. Zeimetz, S. X. Dou, and H. K. Liu, J. Supercond. Sci. Technol. **9,** 888 (1996).

[29] T. D. Dzhafarov, M. Altunbas and T. Kucukomeroglu, Solid. Stat. Comm. **99,** 839 (1996).

[30] F. M. Julian, S. Ricart, A. Pomer, and L. M. Marzan and J. Nanosci. Tech. **11,** 3245 (2011).

[31] M. N. Khan, M. Khizar and B. N. Mukeshev, J. Physica B **321,** 257 (2002).

[32] H. Najafpour, S. H. R. Shojaei and S. M. Shojaeiu, J. Supercond. Non. Magn. **23,** 487 (2010).

[33] M. Mumtaz, Nawazish A. Khan, and E.U. Khan, Physica C **470,** 428 (2010)

[34] M. Mumtaz, M. Kamran, K. Nadeem, Abdul Jabbar, Nawazish A. Khan, Abida Saleem, S. Tajammul Hussain, and M. Kamran, Low Temp. Phys./ Fiz. Nizk. Temp. **39,** 806 (2013).

[35] M. Mumtaz and Nawazish A. Khan, Fiz. Nizk. Temp. **36,** 196 (2010).

[36] N. A. Khan and M. Mumtaz, Phys. Rev. B **77,** 054507 (2008)

[37] M. Mumtaz, N. A. Khan, and Sajid Khan, J. Appl. Phys. **107,** 103905 (2010)

[38] M. Mumtaz, Asif I. Bhatti, K. Nadeem, Nawazish A. Khan, Abida Saleem, S. Tajammul Hussain, J. Low Temp. Phys. **170**,185 (2013).

[39] F. Gomory, Supercond. Sci. Technol. **10**, 523 (1997).

[40] R.V. Sarmago, K.L.C. Molina, L. J. D. Guerra, Physica C **364**, 239 (2001).

[41] N. A. Khan, M. Mumtaz, A. A. Khurram and P. Kameli, Physica C **468**, 233 (2008).

Chapter 5

$(CoFe_2O_4)_x$/CuTl-1223 Nano-Superconductor Composites

In this chapter, we have investigated the effects of $CoFe_2O_4$ nanoparticles addition on structural, morphological and superconducting transport properties of CuTl-1223 matrix. The main objective of this work was to improve the inter-grain weak-links by filling the pores and voids present in bulk form of the host CuTl-1223 matrix by the inclusion of these nanoparticles. The second objective was to increase the number of flux pinning centers to the optimum level by the addition of these magnetic nanoparticles. The suppression of superconducting properties in zero field with increasing $CoFe_2O_4$ nanoparticles contents is most probably due to localization and pair-breaking mechanisms of carriers across these highly coercive magnetic $CoFe_2O_4$ nanoparticles having net magnetic moments. In the present study our focus was to see the effects of magnetic $CoFe_2O_4$ nanoparticles on the superconducting transport properties of CuTl-1223 matrix.

5.1 Introduction

Normally, cuprate high temperature superconductors (HTSCs) are synthesized at very high pressure (3~5 GPa) but the compounds of $Cu_{0.5}Tl_{0.5}Ba_2Ca_{n-1}Cu_nO_{2n+4-\delta}$ (CuTl-12(n-1)n); n = 2, 3, 4,..., high temperature superconducting family can be easily synthesized at ambient pressure [1]. The superconducting parameters of this HTSCs family have the second highest values after Hg-based superconductors. Also $Cu_{0.5}Tl_{0.5}Ba_2Ca_2Cu_3O_{10-\delta}$ (CuTl-1223) phase with three CuO_2 planes has highest values of almost all superconducting parameters as compared to other phases of this HTSCs family [2, 3]. Therefore, this class of superconductors is one of the most promising candidates for further investigation and technological applications. The overall structure is granular and porous in nature for large scale production in bulk form [2, 3]. In order to enhance the superconducting properties, many attempts have been made by the different research groups working in this area. Post-annealing and creation of artificial defects by different techniques of the order of nanometer scale acting as extra effective pinning centers under the applied external field have been exercised [4, 5]. Main objective of creation of additional effective pinning centers by different techniques is to enhance the critical current density (J_c) under the applied external magnetic field. These pinning centers are more effective when their sizes are of the order of coherence length [6]. The easy and very useful technique for the creation

of artificial pinning centers is the addition of magnetic nanoparticles in the bulk superconducting materials [7].

The enhancement of critical current density (J_c) in many HTSCs families have been observed by the inclusion of nano-oxides of different nature, sizes and concentrations, which act as flux pinning centers in the applied external field [8-11]. The addition of Al_2O_3 and ZrO_2 nanoparticles acted as effective flux pinning centers in (Bi, Pb)-2223 superconductor and improved the infield J_c [12-14]. The lower addition of ZnO nanoparticles in $(Cu_{0.5}Tl_{0.25}Pb_{0.25})$-1223 matrix improved the superconducting transition temperature, J_c and superconducting volume fraction [15]. Also the addition of In_2O_3 and SnO_2 in CuTl-1223 matrix improved the superconducting volume fraction and reduced the porosity [16, 17]. The improvement of J_c and suppression of T_c were also observed by the addition of ZrO_2 and ZnO in Gd-123 superconductor [18]. The superconducting properties (i.e. T_c, J_c etc) of CuTl-1223 were improved by the addition of CuO, CaO_2 and BaO nanoparticles [19, 20].

Recently, it was shown that magnetic nanoparticles play an important role as efficient pinning centers at lower densities [21, 22]. $BiFeO_3$ (BFO) nanoparticles are the promising candidate for the various applications in recent years due to their large magneto-electric coupling [23]. Nano-BFO exhibits super-paramagnetism, which is very suitable for flux pinning centers in superconductors [24, 25]. Enhancement in T_c was observed by the doping of paramagnetic Cr impurities in Pd films up to certain level in applied external magnetic fields [26]. The electrical resistivity versus temperature measurements showed that T_c has been increased up to 0.2 wt.% addition of nano-Fe_2O_3 in CuTl-1223 matrix. The suppression in T_c on further increase of Fe_2O_3 nanoparticles concentration was due to Cooper pair-breaking mechanism or due to decrease in the volume fraction [27]. In recent years, the interest in creating the artificial pinning centers by the inclusion of magnetic nanoparticles in MgB_2 superconductor was also observed in literature [28]. Several models have been proposed to investigate the effects of the inclusion of magnetic nanoparticles within the bulk superconductors transport properties [29]. However, magnetic flux pinning depends on the magnitude and orientation of magnetization vector, which is a challenging problem for both theoretical and experimental investigations. The effects of magnetic nanoparticles addition on superconductivity in MgB_2 was investigated experimentally as well as theoretically but reported results were contradictory, which provide no evidence of magnetic pinning [30-36]. We have already reported the effect of addition of $ZnFe_2O_4$

nanoparticles in CuTl-1223 superconducting matrix. We have observed the improvement of the grain size with the addition of $ZnFe_2O_4$ nanoparticles. But after the addition of $ZnFe_2O_4$ nanoparticles, $T_c(0)$ and magnitude of diamagnetism were suppressed. The suppression of superconductivity was most likely due to trapping or localization of mobile free carriers and reflection of spin charge due to paramagnetic nature of $ZnFe_2O_4$ nanoparticles. Also, the reduction of $T_c(0)$ may be due to the possibility of Fe and Zn incorporation in lattice sites [37].

5.2 Results and Discussion

5.2.1 X-Ray Diffraction (XRD), Scanning Electron Microscopy (SEM) and MH-Loop of $CoFe_2O_4$ Nanoparticles

XRD pattern of cobalt ferrite ($CoFe_2O_4$) nanoparticles is shown in Fig. 5.1(a). The characteristic peaks in XRD pattern of $CoFe_2O_4$ nanoparticles are in accordance with standard data values given in International Center for Diffraction Data (ICDD) record. The prominent peaks are indexed with cubic spinal structure and average size of $CoFe_2O_4$ nanoparticles calculated by using Debye-Scherrer's formula is 36 nm. XRD analysis shows exquisitely indexed (2 2 0), (3 1 1), (2 2 2), (4 0 0), (4 2 2), (5 1 1), (4 4 0), and (5 3 3) planes and sharpness of these peaks confirms that $CoFe_2O_4$ nanoparticles are better crystallized. Major phase has been observed at (h k l) value of (3 1 1). No peak of other impurity crystalline phases has been detected. The lattice parameter calculated to be a = 0.8392 nm. SEM image of $CoFe_2O_4$ nanoparticles at 500 nm scale is shown in Fig. 5.1(b). It shows that nanoparticles are nearly spherical in shape and agglomerated due to magnetic inter-particle interactions. We have measured MH-loop of $CoFe_2O_4$ nanoparticles at T = 50 K by using SQUID magnetometer to confirm their magnetic behavior as shown in Fig. 5.1(c). These nanoparticles exhibit high saturation magnetization (86 emu/g) and high coercivity (3350 Oe) as evident in the inset of Fig. 5.1(c). Ammar *et al.* [38] reported a high saturation magnetization (85.1 emu/g) for chemically prepared $CoFe_2O_4$ nanoparticles. Liu *et al.* [39] reported the high saturation magnetization (83.6 emu/g) of nano-sized $CoFe_2O_4$ particles prepared by co-precipitation method and annealed at 1300 °C.

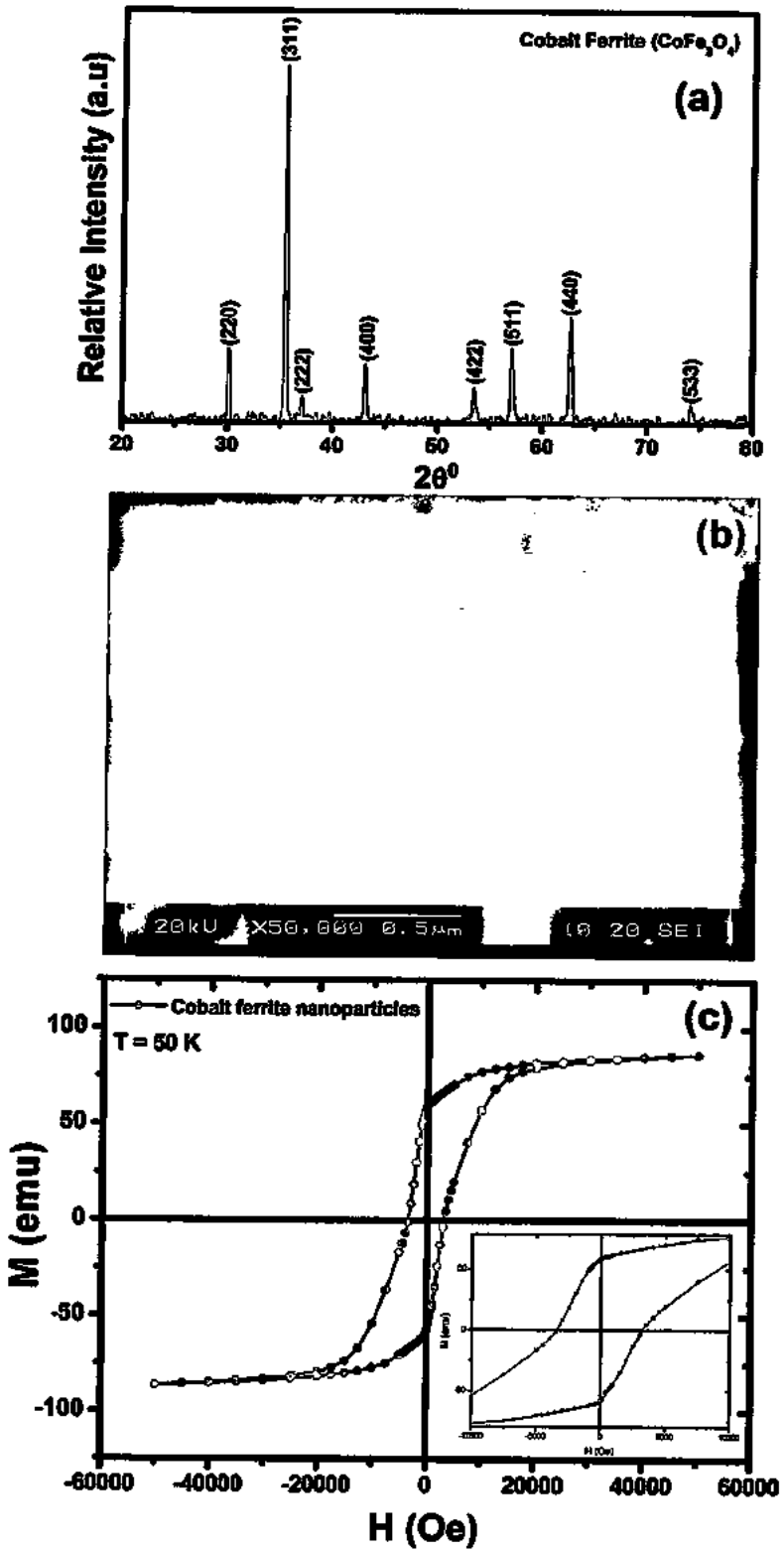

Fig. 5.1(a-c): (a) XRD patterns of $CoFe_2O_4$ nanoparticles, (b) SEM image of $CoFe_2O_4$ nanoparticles at 500 nm scale, and (c) MH-loop of $CoFe_2O_4$ nanoparticles at T = 50 K. (In the inset of (c) shows the coercivity region).

5.2.2 X-ray Diffraction of $(CoFe_2O_4)_x$/CuTl-1223 Composites

Typical XRD patterns of $(CoFe_2O_4)_x$/CuTl-1223 composites with x = 0, 1.0 and 2.0 wt.%, are shown in Fig. 5.2. The diffraction patterns indicate the dominance of CuTl-1223 phase as most of the peaks are well indexed according to tetragonal structure of this phase following the P4/mmm space group. The characteristic (001) peak of this CuTl-1223 phase appeared at 2θ = 5.84° and the stoichiometry remains unchanged after the addition of these nanoparticles, which may be an evidence that there is no variation in structural chemistry of the host CuTl-1223 compound. Structure of CuTl-1223 phase remains preserved even with the existence of $CoFe_2O_4$ nanoparticles, which clearly indicates that these nanoparticles occupy the positions at the inter-crystallite boundaries of CuTl-1223 matrix and help in improving the inter-grain weak-links.

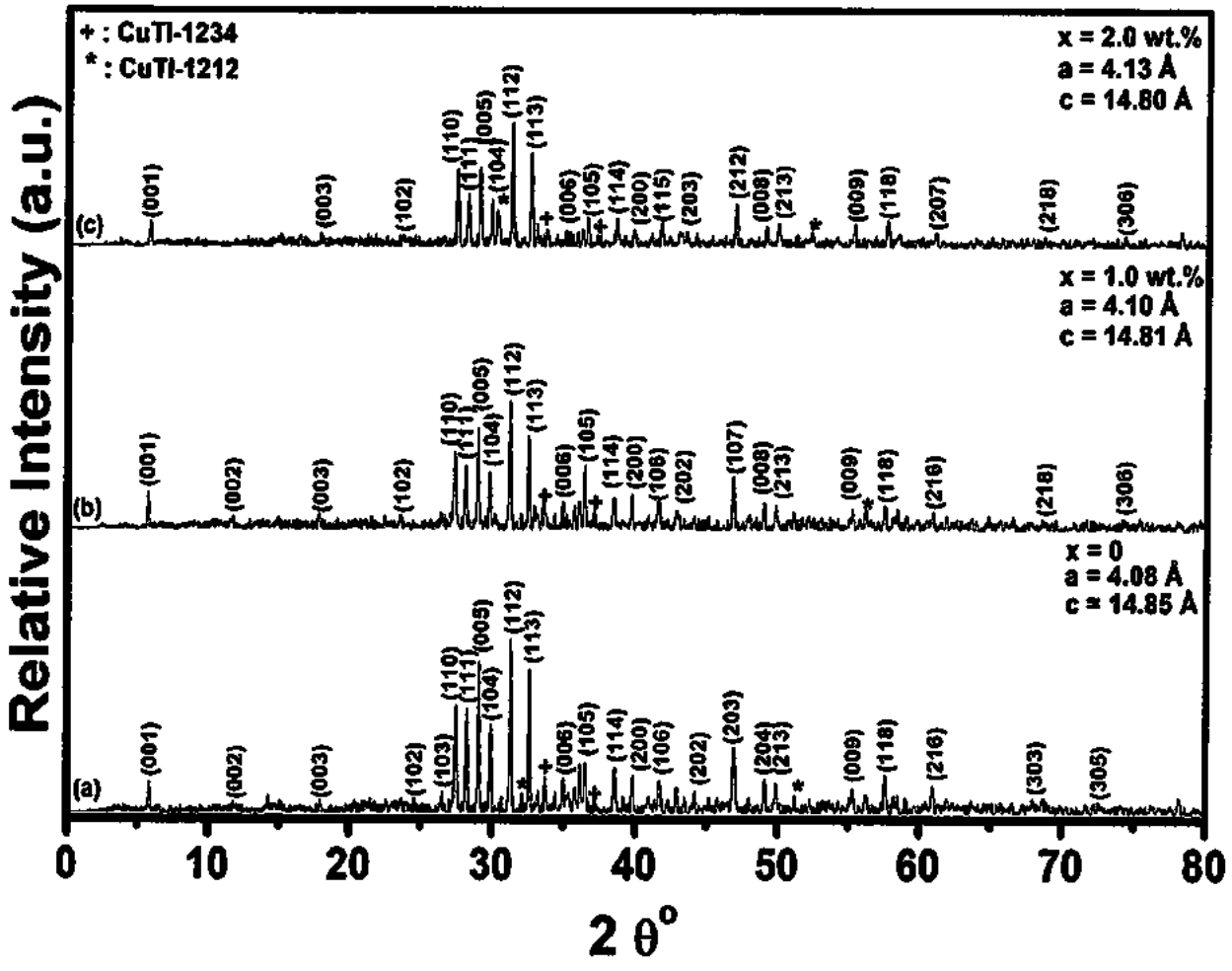

Fig. 5.2: XRD patterns of $(CoFe_2O_4)_x$/CuTl-1223 composites with (a) x = 0, (b) x = 1.0 wt.%, and (c) x = 2.0 wt.%.

Beside the dominant CuTl-1223 phase, few un-indexed peaks appeared which are possibly due to presence of some impurities and some other superconducting phases. Extremely small variation in c-axis length was observed, which may possibly be due to some strains and change in oxygen (O_δ) contents after nanoparticles addition. The slight shift in the diffraction peaks to lower angles, which is due to uniform strain produced in the materials after the addition of $CoFe_2O_4$ nanoparticles. Also the slight decrease in the c-axis length and an increase in a-axis length are due to the slight compression in apical bond length and relaxation in CuO_2 planner bond lengths.

5.2.3 Scanning Electron Microscopy (SEM) of $(CoFe_2O_4)_x$/CuTl-1223 Composites

SEM images of $(CoFe_2O_4)_x$/CuTl-1223 composite samples are shown in Fig. 5.3. Some impression of agglomeration of magnetic nanoparticles have been observed in the composite sample with x = 2.0 wt. %. Similar results were already observed by M. Hafiz and R. Abd-Shukor [40] for nano-sized NiF_2 addition in $Bi_{1.4}Pb_{0.6}Sr_2Ca_2Cu_3O_{10+\delta}$ superconductor samples and N. H. Mohammad *et al* [27] in studying the effect of nano-SnO_2 inclusion into the CuTl-1223 superconducting phase on superconducting properties.

5.2.4 FTIR Absorption Spectra of $(CoFe_2O_4)_x$/CuTl-1223 Composites

FTIR is very sensitive technique used to detect a trace amount of impurities along with functional groups in the material. The FTIR absorption spectra of $(CoFe_2O_4)_x$/CuTl-1223 composites with x = 0, 0.5, 1.0, 1.5 and 2.0 wt.%, in the far infrared range from 400-700 cm^{-1} are shown in Fig. 5.4. The bands in the range from 400 to 540 cm^{-1} are associated with the apical oxygen atoms and in the range from 541 to 600 cm^{-1} are associated with CuO_2 planar oxygen atoms. The bands in the range from 670 to 700 cm^{-1} are associated with O_δ atoms in the charge reservoir layer [41-43]. Apical oxygen modes of type Tl–O_A–Cu(2) and Cu(1)–O_A–Cu(2) are observed around 418 cm^{-1} and 483 cm^{-1} and CuO_2 planner modes are observed around 533 cm^{-1} in pure $Cu_{0.5}Tl_{0.5}Ba_2Ca_2Cu_3O_{10-\delta}$ samples. The positions of both the apical oxygen modes were not altered significantly with the addition of $CoFe_2O_4$ nanoparticles. The CuO_2 planner oxygen modes also did not change their positions with the addition of $CoFe_2O_4$ nanoparticles. The slight variation in these modes can be possibly due to stresses and strains produced in material after addition of these nanoparticles. The almost unchanged position of various oxygen modes with the addition of these nanoparticles showed that the unit cell structure of the host CuTl-1223 matrix remained unaltered. This is another indirect evidence of the occupancy of $CoFe_2O_4$

nanoparticles at the grain-boundaries. Therefore, these nanoparticles healed up the voids and improved the inter-grain coupling.

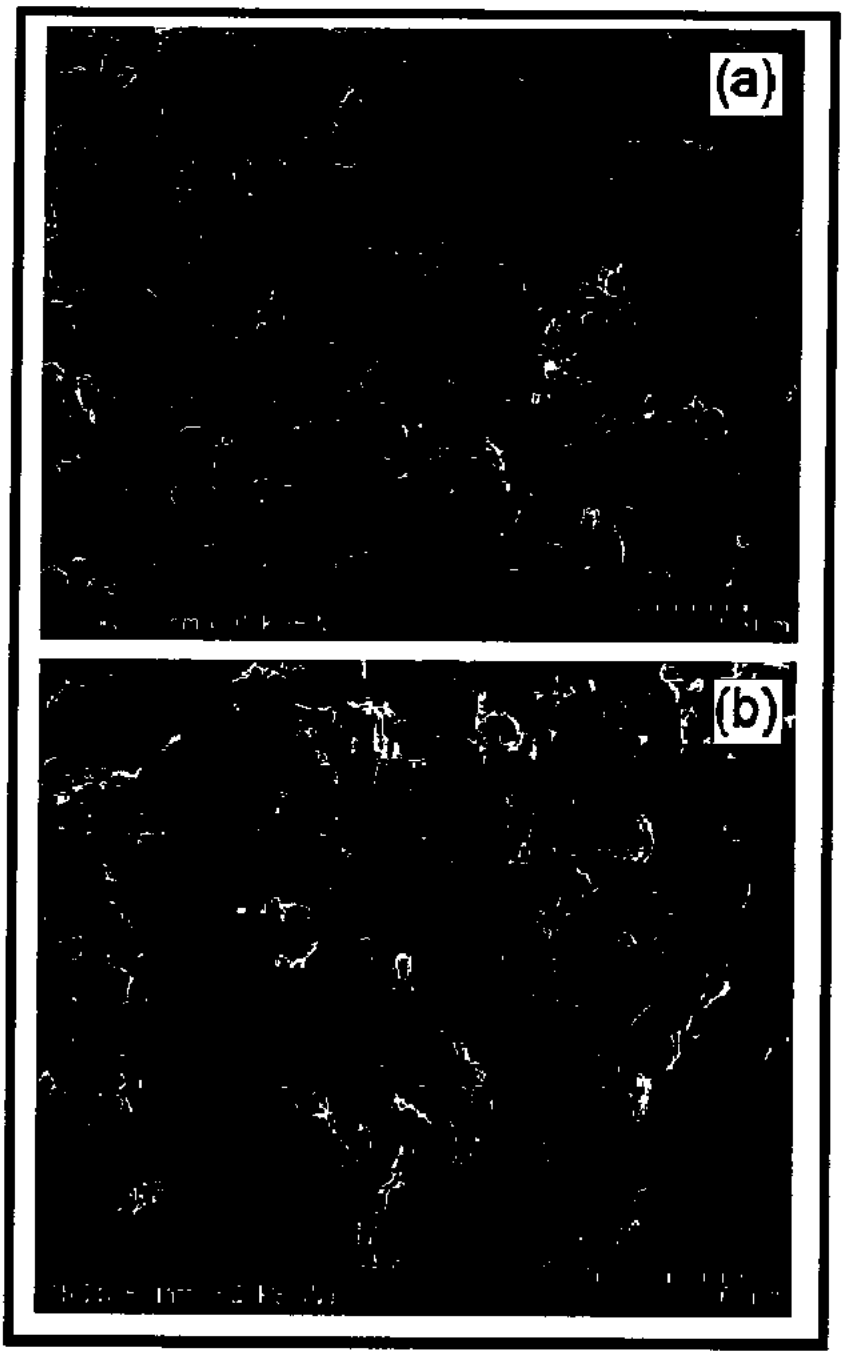

Fig. 5.3: SEM images of $(CoFe_2O_4)_x$/CuTl-1223 composites with (a) x = 0 and (b) x = 2.0 wt.%.

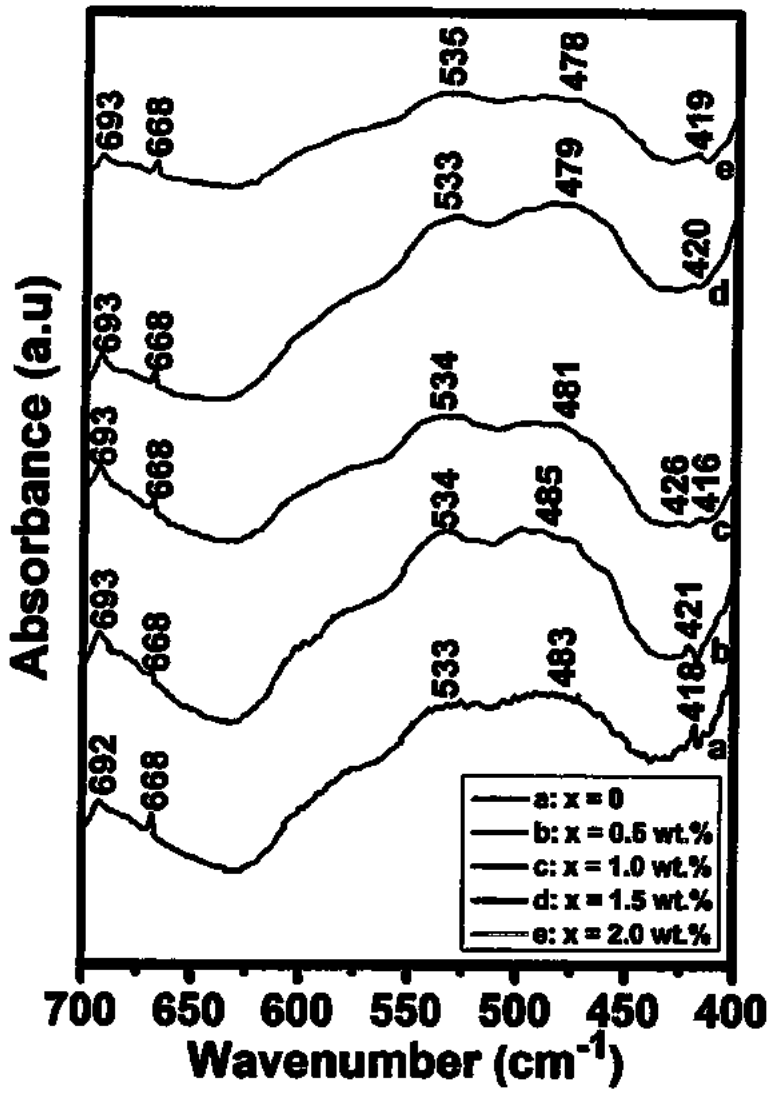

Fig. 5.4: FTIR absorption spectra of $(CoFe_2O_4)_x$/CuTl-1223 composites with (a) x = 0, (b) x = 0.5 wt.%, (c) x = 1.0 wt.%, (d) x = 1.5 wt.%, and (e) x = 2.0 wt.%.

5.2.5 Resistivity versus Temperature Measurements

Resistivity versus temperature measurements of $(CoFe_2O_4)_x$/CuTl-1223 (x = 0, 0.5, 1.0, 1.5 and 2.0 wt.%) composites samples with various amounts of $CoFe_2O_4$ nanoparticles are shown in Fig. 5.5. The variation of T_c (0) versus $CoFe_2O_4$ nanoparticles content is shown in the inset (a) of Fig. 5.5. The values of T_c (0) for the samples with x = 0, 0.5, 1.0, 1.5 and 2.0 wt.% are around 66 K, 68 K, 69 K, 78 K and 60 K respectively. These measurements show that the value of T_c(0) is increased after the addition of $CoFe_2O_4$ nanoparticles into CuTl-1223 superconducting

matrix till x = 1.5 wt. % concentration and then suppressed on further increase in the amount of nanoparticles. The increase in T_c (0) after the inclusion of $CoFe_2O_4$ nanoparticles up to x = 1.5 wt.% is due improvement in the inter-grains connectivity and after certain optimum level of $CoFe_2O_4$ nanoparticles addition, the agglomeration starts which deteriorates the samples quality and produces stresses and strains in the materials [44, 45].

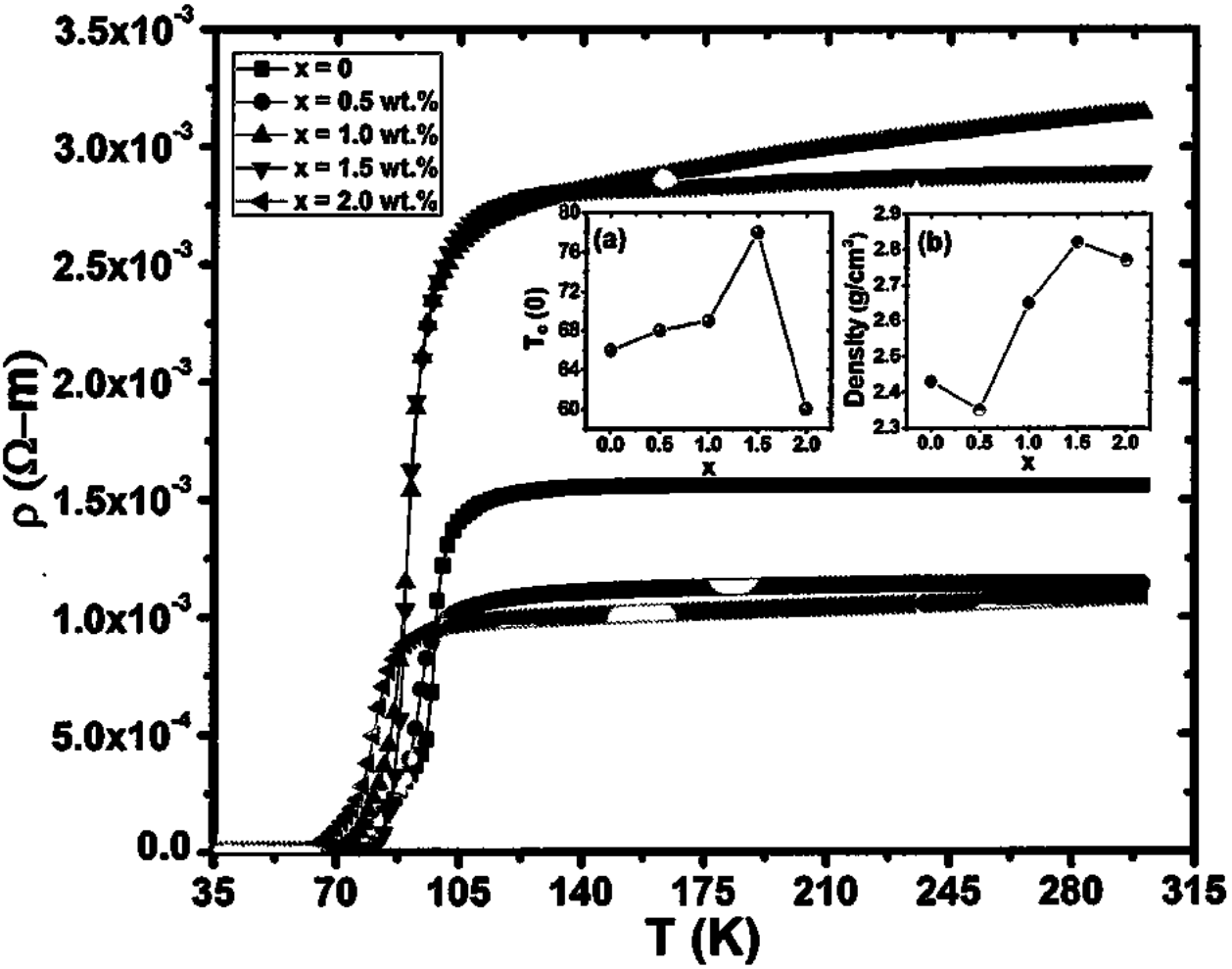

Fig. 5.5: Resistivity versus temperature measurements of $(CoFe_2O_4)_x$/CuTl-1223 composites; x = 0, 0.5 wt.%, 1.0 wt.%, 1.5 wt.% , and 2.0 wt.%. In the inset (a) the variation of $T_c(0)$ versus x and in the inset (b) the variation of massive density versus x (i.e. $CoFe_2O_4$ nanoparticles).

In ceramic high T_c superconductors, there is always a resistive broadening due to two critical temperatures, one is the T_c^{onset}(K) at which Cooper pair formation starts and the second is the T_c (0) at which the materials goes into bulk superconducting state. The T_c^{onset}(K) depends on the electronic properties of the material, whereas $T_c(0)$ depends on the microstructure of the material and carriers density in the CuO_2 planes. The material with weak inter-grain connectivity and voids tends to have lower $T_c(0)$, as compared to that of a material with well connected and

packed grains in spite of their equal T_c^{onset} (K). In the present article the T_c^{onset} (K) is monotonically decreasing with the increase of magnetic $CoFe_2O_4$ nanoparticles content, which is not surprising because magnetic nanoparticles have the ability to suppress the superconductivity. The reason behind the increase in $T_c(0)$ might be the improvement of the inter-grain connectivity, which is essential to get higher $T_c(0)$. The main problem is to make the distribution of $CoFe_2O_4$ nanoparticles uniform and homogeneous across the grain-boundaries of CuTl-1223 superconducting matrix. The non-monotonic variation of the normal state resistivities with magnetic $CoFe_2O_4$ nanoparticles content is most probably due to the inhomogeneous distribution of these nanoparticles at the grain-boundaries of the bulk material. The variation of mass density of $(CoFe_2O_4)_x$/CuTl-1223 composites with different content of $CoFe_2O_4$ nanoparticles is shown in the inset (b) of the Fig. 5.5. The overall slightly increasing trend in mass density is observed with increasing content of these nanoparticles in the matrix, which is an evidence of filling the voids in the bulk samples. Slightly non-monotonic variation in mass density can be most probably due to inhomogeneous distribution of these nanoparticles at the grain-boundaries of the samples.

5.3 References

[1] H. Ihara, K. Tanaka, Y. Tanaka, A. Iyo, N. Terada, M. Tokumoto, M. Ariyama, I. Hase, A. Sundaresan, N. Hamada, S. Miyashita, K. Tokiwa, and T. Watanabe, Physica C **341-348**, 487 (2000).

[2] M. Mumtaz, S. M. Hasnain, A. A. Khurram, and Nawazish A. Khan, J. Appl. Phys. **109**, 023906 (2011).

[3] H. Ihara, K. Tokiwa, K. Tanaka, T. Tsukamoto, T. Watanabe, H. Yamamoto, A. Iyo, M. Tokumoto, and M. Umeda, Physica C **282-287**, 957 (1997).

[4] M. H. Pu, W. H. Song, B. Zhao, X. C. Wu, T. Hu, Y. P. Sun, and J. J. Du, Supercond. Sci. Tech. **14**, 305 (2001).

[5] K. T. Lau, S. Y. Yahya, and R. Abd-Shukor, J. Appl. Phys. **99**, 123904 (2006).

[6] T. Haugan, P. N. Barnes, R. Wheeler, F. Meisenkothen, and M. Sumption, Nature **430**, 867 (2004).

[7] K. Togano, H. Kumakura, H. Maeda, E. Yanagisawa, and K. Takahashi, Appl. Phys. Letters **53**, 1329 (1988).

[8] Y. C. Guo, Y. Tanaka, T. Kuroda, S. X. Dou, and Z. Q. Yang, Physica C **311**, 65 (1999).

[9] E. Guilmeau, B. Andrzejewski, and J. G. Noudem, Physica C **387**, 382 (2003)

[10] T. Haugan, W. Wong-Ng, L. P. Cook, H. J. Brown, L. Swartzendruber, and D. T. Shaw, Physica C **335**, 129 (2000).

[11] S. Sengupta, V. R. Todt, P. Kostic, Y. L. Chen, M. T. Lanagan, and K. C. Goretta, Physica C **264**, 34 (1996).

[12] M. Annabi, A. M'chirgui, F. Ben Azzouz, M. Zouaoui, and M. Ben Salem, Physica C **405**, 25 (2004).

[13] A. Ghattas, M. Annabi, M. Zouaoui, F. Ben Azzouz, and M. Ben Salem, Physica C **468**, 31 (2008).

[14] Z. Y. Jia, H. Tang, Z. Q. Yang, Y. T. Xing, Y. Z. Wang, and G. W. Qiao, Physica C **337**, 130 (2000).

[15] M. M. Elokret, R. Awad, A. A. El-Ghany, A. A. Shama, and A. El-wanis, J. Supercond. Nov. Magn. **24**, 1345 (2011).

[16] N. H. Mohammed, A. I. Abou-Aly, I. H. Ibrahim, R. Awad, and M. Rekaby, J. Supercond. Nov. Magn. **24**, 1463 (2011).

[17] N. H. Mohammed, A. I. Abou-Aly, I. H. Ibrahim, R. Awad, and M. Rekaby, J. Alloy. Compound. **486,** 733 (2009).

[18] Y. Xu, A. Hu, C. Xu, N. Sakai, I. Hirabayashi, and M. Izumi, Physica C **468,** 1363 (2008).

[19] Nawazish. A. Khan, A. Saleem, and S. T. Hussain, J. Supercond. Nov. Magn. **25,** 1725 (2012).

[20] M. Mumtaz, Asif I. Bhatti, K. Nadeem, Nawazish A. Khan, Abida Saleem, and S. Tajammul Hussain, J. Low Temp. Phys. **170,** 185 (2013).

[21] A. Snezhko, T. Prozorov, and R. Prozorov, Phys. Rev. B **71,** 024527 (2005).

[22] L. N. Bulaevskii, E. M. Chundnovsky, and M. P. Maley, Appl. Phys. Lett. **76,** 2594 (2000).

[23] T. Zhao, A. Scholl, F. Zavaliche, K. Lee, M. Barry, A. Doran, M. P. Cruz, Y. H. Chu, C. Ederer, N. A. Spaldin, R. R. Das, D. M. Kim, S. H. Baek, C. B. Eom, and R. Ramesh, Nature Mater. **5,** 823 (2006).

[24] T. J. Park, G. C. Papaefthymiou, A. J. Viescas, A. R. Moodenbaugh, and S. S. Wong, Nano Lett. **7,** 766 (2007).

[25] S. Acharya, A. K. Biswal, J. Ray, and P. N. Vishwakarma, J. Appl. Phys. **112,** 053916 (2012).

[26] H. J. Gardner, A. Kumar, L. Yu, P. Xiong, M. P. Warusawithana, L. wang, O. Vafek, and D. G. Schlom, Nature Phys. **7,** 895 (2011).

[27] N. H. Mohammad, A. I. Abou-Aly, R. Awad, I. H. Ibrahim, M. Roumie, and M. Rekaby, J. Low Temp. Phys. **172,** 234-255 (2013).

[28] N. Novosel, S. Galic , D. Pajic, Z. Skoko, I. Loncarek, M. Mustapic , K. Zadro, and E. Babic , Supercond. Sci. Technol. **25,** 095018 (2012).

[29] M. G. Blamire, R. B. Dinner, S.C. Wimbush, and J. L. MacManus-Driscoll, Supercond. Sci. Technol. **22,** 025017 (2009).

[30] B. Qu, X. D. Sun, J.-G. Li, Z. M. Xiu, S.H. Liu, and C. P. Xue, Supercond. Sci.Technol. **22,** 015027 (2009).

[31] C. Cheng, and Y. Zhao, Physica C **463–465,** 220 (2007).

[32] V. P. S. Awana, M. Isobe, K.P. Singh, E. Takayama-Muromachi, and H. Kishan, Supercond. Sci. Technol. **19,** 551 (2006).

[33] S. X. Dou, S. Soltanian, Y. Zhao, E. Getin, Z. Chen, O. Shcherbakova, and J. Horvat, Supercond. Sci. Technol. **18,** 710 (2005).

[34] T. Kuroda, T. Nakane, H. Uematsu, and K. Kumakura, Supercond. Sci. Technol. **19,** 1152 (2006).

[35] O. F. de Lima, K.B. Vieira, E. Moschim, V.P.S. Awana, and H. Kishan, J. Mater. Sci. **45,** 4929 (2010).

[36] N. Novosel, and E. Babic, Physica C, **493,** 119 (2013).

[37] M. Mumtaz, S. Naeem, K. Nadeem, F. Naeem, Abdul Jabbar, Y. R. Zheng, Nawazish A. Khan, and M. Imran, Solid.Stat. Sci. **22,** 21 (2013).

[38] S. Ammar, A. Helfen, N. Jouini, F. Fievet, I. Rosenman, F. Villain, P. Molinie, and M. Danot, J. Mater. Chem., **11,** 186-192 (2001)

[39] B. H. Liu, J. Ding, Z. L. Dong, C. B. Boothroyd, J. H. Yin, and J. B. Yi, Phys. Rev. B **74,** 184427 (2006).

[40] M. Hafiz and R. Abd-Shukor, Adv. Matr. Research, **895,** 87-90 (2014).

[41] Nawazish A. Khan, M. Mumtaz, K. Sabeeh, M. I. A. Khan, and. Mushtaq Ahmad, Physica C **407,** 103-114 (2004).

[42] Nawazish A. Khan, and M. Mumtaz, Eur. Phys. J. Appl. Phys. **38,** 47-51(2007).

[43] M. Mumtaz, and Nawazish A. Khan, Supercond. Sci. Technol. **21,** 065015 (2008).

[44] J. C. Zhang, F. Q. Liu, G.S. Cheng, J. X. Shang, J. Z. Liu, S.X. Cao, and Z. X. Liu, Phys, Lett. A **201,** 70 (1995).

[45] P. F. Miceli, J. M. Tarascon, L. H. Greene, H. P. Barbou, F. J. Rotella, and J. D. Jorgensen, Phys. Rev. B **37,** 5932 (1988).

Chapter 6

$(Al_2O_3)_y$/CuTl-1223 Nano-Superconductor Composites

We studied the effects of nano-Al_2O_3 particles addition on superconductivity as well as on crystal structure of CuTl-1223 phase in this chapter. We have presented our experimental results on the superconducting properties and the changes in microstructure correlated with nano-sized Al_2O_3 addition in CuTl-1223 matrix. The presence of nano-Al_2O_3 particles embedded in the superconductor matrix was investigated by X-rays diffraction (XRD), scanning electron microscopy (SEM) and energy dispersive x- rays (EDX) spectroscopy. The resistivity versus temperature, current versus voltage (IV) and Fourier Transform Infrared (FTIR) absorption measurements were carried out on these samples.

6.1 Introduction

$(Cu_{0.5}Tl_{0.5})Ba_2Ca_2Cu_3O_{10-\delta}$ (CuTl-1223) phase of $(Cu_{0.5}Tl_{0.5})Ba_2Ca_nCu_{n+1}O_{2n+4-\delta}$ high T_c superconducting family is the most attractive due to its relatively larger critical current density (J_c), high superconducting transition temperature (T_c) and low superconducting anisotropy ($\gamma = \frac{\xi_{ab}}{\xi_c}$) [1-3]. Two main constituents of the unit cell of this phase are $Cu_{0.5}Tl_{0.5}Ba_2O_{4-\delta}$ charge reservoir layer (CRL) and $nCuO_2$ conducting planes [4, 5]. The effects of the substitution of impurities within the unit cell and the addition of suitable nanostructures (nanoparticles, nanorods, etc) on the physical and structural properties of different superconducting families were investigated by different research groups working in this area [6-10]. The addition of nanoparticles affects the superconducting properties by creating the surface defects in the materials and varying the number of charge carriers in CuO_2 planes. It was observed in many superconducting families that superconductivity parameters vary by varying the oxygen contents [11-15]. The addition of elemental and oxides nanoparticles into the high temperature superconductors (HTSCs) matrices plays a vital role in increasing the critical current density (J_c) by the different mechanisms (i.e. flux pinning, inter-grain improved connectivity etc) occurring in the materials [16-20]. It was reported that low concentration of nano-ZnO addition in $(Cu_{0.5}Tl_{0.25}Pb_{0.25})$-1223 matrix enhanced the superconducting transition temperature (T_c), critical current density (J_c) and melting point, while high concentration of nano-ZnO enhanced the secondary phases and grain boundary resistance. This was possibly due to large agglomeration of

nano-ZnO particles [21]. Microhardness of CuTl-1223 superconducting phase was significantly improved by nano-SnO_2 particles addition [22]. It was also observed that superconducting properties were improved by nano-Fe_2O_3 particles addition up to certain concentration level and then started to decrease with higher concentration of nano-Fe_2O_3 particles in CuTl-1223 superconductor [23]. The suppression of superconducting properties was explained in terms of enhanced pair-breaking mechanism due to scattering phenomenon at higher concentration of nano-Fe_2O_3 particles in CuTl-1223 superconductor. The nano-MgO particles addition up to 0.6 wt. % in CuTl-1234 superconducting phase improved the phase formation, grain-connectivity, electrical transport properties and reduced the thermal expansion co-efficient [24]. The improvement in J_c was believed to be due to enhanced pinning effects of nano-MgO particles in the CuTl-1234 superconducting matrix [25]. There was also no change observed in the tetragonal crystal structure of CuTl-1234 superconducting phase after the addition of nano-MgO particles. The study of the effects of Al_2O_3 nanoparticles addition on the superconducting properties of $YBa_2Cu_3O_y$ showed that there was no change in the structural symmetry, while the orthorhombicity slightly decreased with the increase of nano-Al_2O_3 particles content in the matrix. In applied magnetic field, J_c of the superconducting material was observed to be enhanced significantly by nano-Al_2O_3 particles addition, which can be rendered to the existence of the flux pinning centers [26]. The substitution of nano-Al_2O_3 particles did not affect the structural symmetry of the parent $YBa_2Cu_3O_y$ system but the oxygen content were affected and therefore the superconductivity altered as it is sensitive to oxygen contents especially in this system. The effects of nano-Al_2O_3 particles addition in the polycrystalline (Bi, Pb)-2223 superconductors also illustrated the improvement of transport properties. The volume pinning force density, onset temperature of dissipation, activation energy and J_c in applied magnetic field were found to be improved [27]. The fluctuation induced conductivity (FIC) analysis demonstrated that three dimensional (3D) conductivity region has been reduced, which is possibly due to scattering of mobile carriers across the nano-Al_2O_3 particles at the grain-boundaries of (Bi, Pb)-2223 superconducting matrix [28]. The small amount of nano-Al_2O_3 particles addition in $YBa_2Cu_3O_{7-\delta}$ (Y123) textured bulk superconductor has increased the J_c values that may be due to improved flux pinning after the inclusion of these insulating nanoparticles [29]. The structural symmetry of Y123 superconducting matrix was also not affected after the inclusion of Al_2O_3 nanoparticles [30]. The improvement of J_c was most likely

due to enhanced pinning effects by the insulating nano-Al_2O_3 particles acting as effective pinning centers in Y123 superconducting matrix. The value of the J_c depends upon the size, density of pinning centers and flux pinning strength. The values of J_c and H_{irr} were enhanced due to the presence of nano-Al_2O_3 particles at the grain-boundaries of MgB_2 acting as strong pinning centers [31]. Some amount of aluminum (Al) was doped into the lattice and more Al_2O_3 nanoparticles were present at grain-boundaries in the bulk at higher level of nano-Al_2O_3 particles addition in MgB_2 matrix.

6.2 Theoretical Model for Analysis of Experimental Data

The dc-resistivity measured data were analyzed with the help of Aslamasov-Larkin (AL) Model. FIC analysis gives information about the scattering and superconducting pairing in cuprates as T approaches T_c^{onset} (K). The excess conductivity is;

$$\Delta\sigma(T) = \left[\frac{\rho_n(T) - \rho(T)}{\rho_n(T)\rho(T)}\right] \quad \text{..... (1)}$$

where ρ (T) is the actually measured resistivity, and ρ_n (T) = αT + b is the normal-state resistivity of the sample extrapolated to resistivity at 0 K. The fluctuation conductivity according to AL theory is given as;

$$\Delta\sigma(T) = A\varepsilon^{-\lambda} \quad \text{..... (2)}$$

where A is the fluctuation amplitude, λ is dimensional exponent, and $\varepsilon = \ln[T/T_c^{mf}]$ is the reduced temperature and T_c^{mf} is usually referred to as the mean field critical temperature [32, 33]. The exponent λ determines the dimensionality of the superconducting fluctuations and is given as λ =2-D/2; λ =1/2, 1, 3/2 for three, two and one dimensional fluctuations, respectively. A cross-over from two dimensional (2D) to three dimensional (3D) conductivity occurs at a cross-over temperature;

$$T_o = T_c\left[1 + \left(\frac{2\xi_c(0)}{d}\right)^2\right] \quad \text{..... (3)}$$

The second term is the inter-layer coupling strength, which is related to the reduced temperature ε by J = ε /4. In layered superconductors at very low temperature close to zero resistivity temperature ξ_c > d; where d is the distance between the conducting layers of adjacent unit cells (d is approximately equal to the c-axis lattice parameter of the unit cell).

6.3 Results and Discussion

6.3.1 X-Ray Diffraction (XRD)

XRD pattern of nano-Al_2O_3 particles is shown in Fig. 6.1. The various crystal features of Al_2O_3 nanoparticles like crystal structure, crystallite size and diffraction pattern are determined from the XRD spectrum. The random orientation of crystals, smaller crystallite size, strains and structural faults lead to the peak broadening. The peaks are indexed with cubic structure and the average size of Al_2O_3 nanoparticles calculated by Sherrer's formula is found to be 5 nm. XRD analysis shows cubic structure and crystallinity with exquisitely indexed planes (3 1 1), (2 2 2), (4 0 0), (5 1 1) and (4 4 1), which are completely in accordance with International Center for Diffraction Data (ICDD).

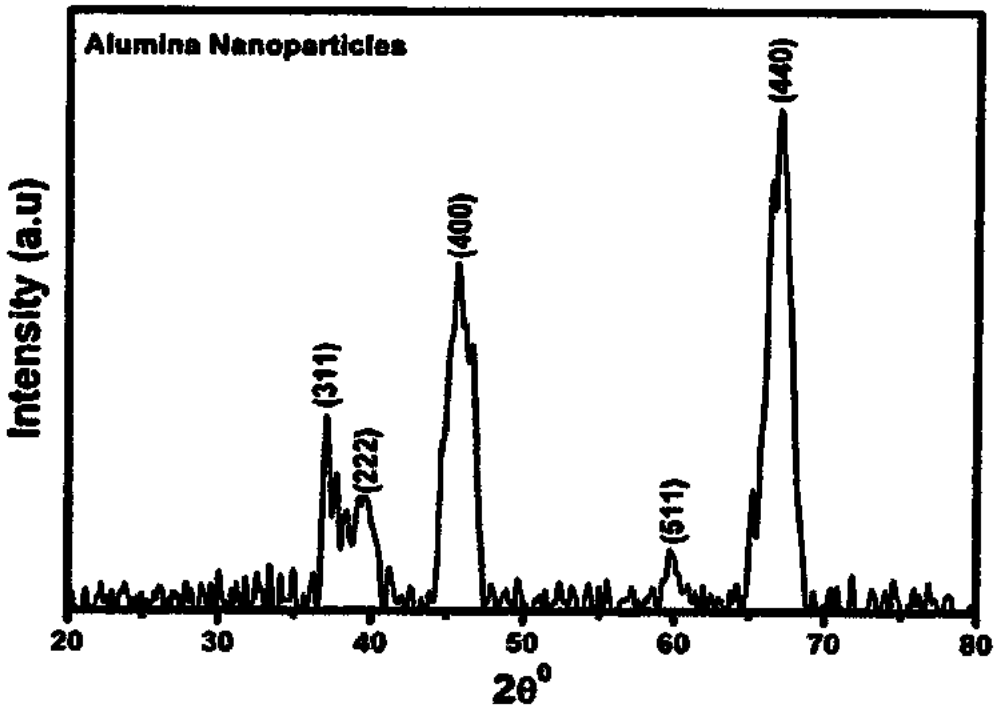

Fig. 6.1: XRD pattern of alumina (Al_2O_3) nanoparticles

The typical XRD patterns of $(Al_2O_3)_y$/CuTl-1223 composites with y = 0 and 1.5 wt.%, are shown in Fig. 6.2. The XRD patterns indicate the dominance of CuTl-1223 phase as most of the diffraction peaks are well indexed according to tetragonal structure following the P4/mmm space group. The characteristic (001) peak of CuTl-1223 phase appeared at $2\theta = 5.75^\circ$ and also there is no change in the overall XRD patterns of nano-Al_2O_3 particles added samples. The unit cell parameters calculated by computer software (crystal) program are a = 4.01 Å, c = 14.95 Å

for y = 0, and a = 4.13 Å, c = 15.16 Å for y = 1.5%, respectively. The structure of CuTl-1223 phase remains preserved even with the presence of Al_2O_3 nano-particles in the matrix. Therefore, the nano-particles can occupy the positions at the inter-crystallite boundaries of CuTl-1223 superconducting matrix and help in improving the inter-grain weak links. Beside the dominant CuTl-1223 phase, few non indexed peaks may possibly be due to presence of impurities as well as some other superconducting phases. Therefore, the stoichiometry of the host CuTl-1223 compound remains unchanged after the addition of these nanoparticles. The slight shift in the diffraction peaks to lower angles is due to the uniform strain produced in the materials after the addition of Al_2O_3 nanoparticles. Also the slight variation in the c-axis length may be due to variation of O_δ oxygen, which can change the apical bond length.

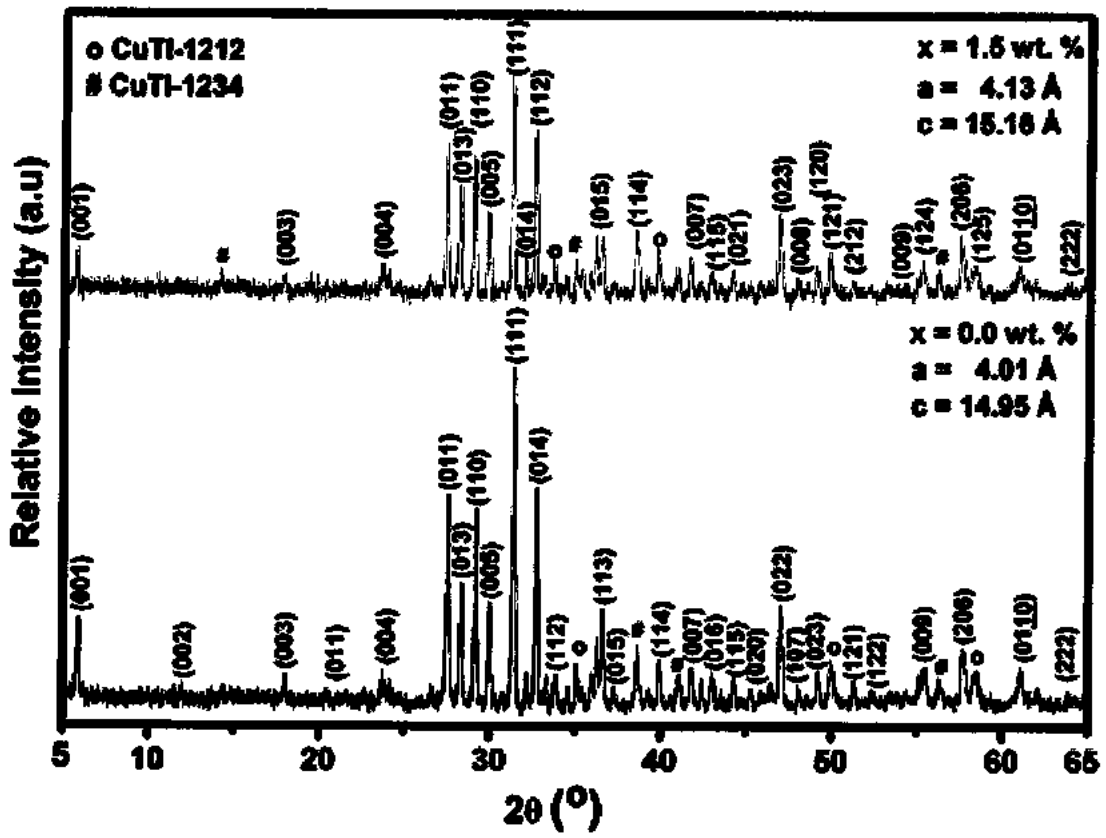

Fig. 6.2: XRD patterns of $(Al_2O_3)_y$/CuTl-1223 composites (a) y = 0, (b) y = 1.5 wt.%

6.3.2 Scanning Electron Microscopy (SEM) and Energy Dispersive X-Ray (EDX) Analysis

SEM images and EDX spectra of $(Al_2O_3)_y$/CuTl-1223 samples with y = 0 and 1.5 wt. % are shown in Fig. 6.3. The improvement in the grains size after the addition of nano-Al_2O_3 particles is possibly due to the presence of these nano-particles at the inter-grain boundaries that can heal up the inter-grain voids in CuTl-1223 superconducting matrix. The EDX spectra show the mass percentages of different elements in the composition.

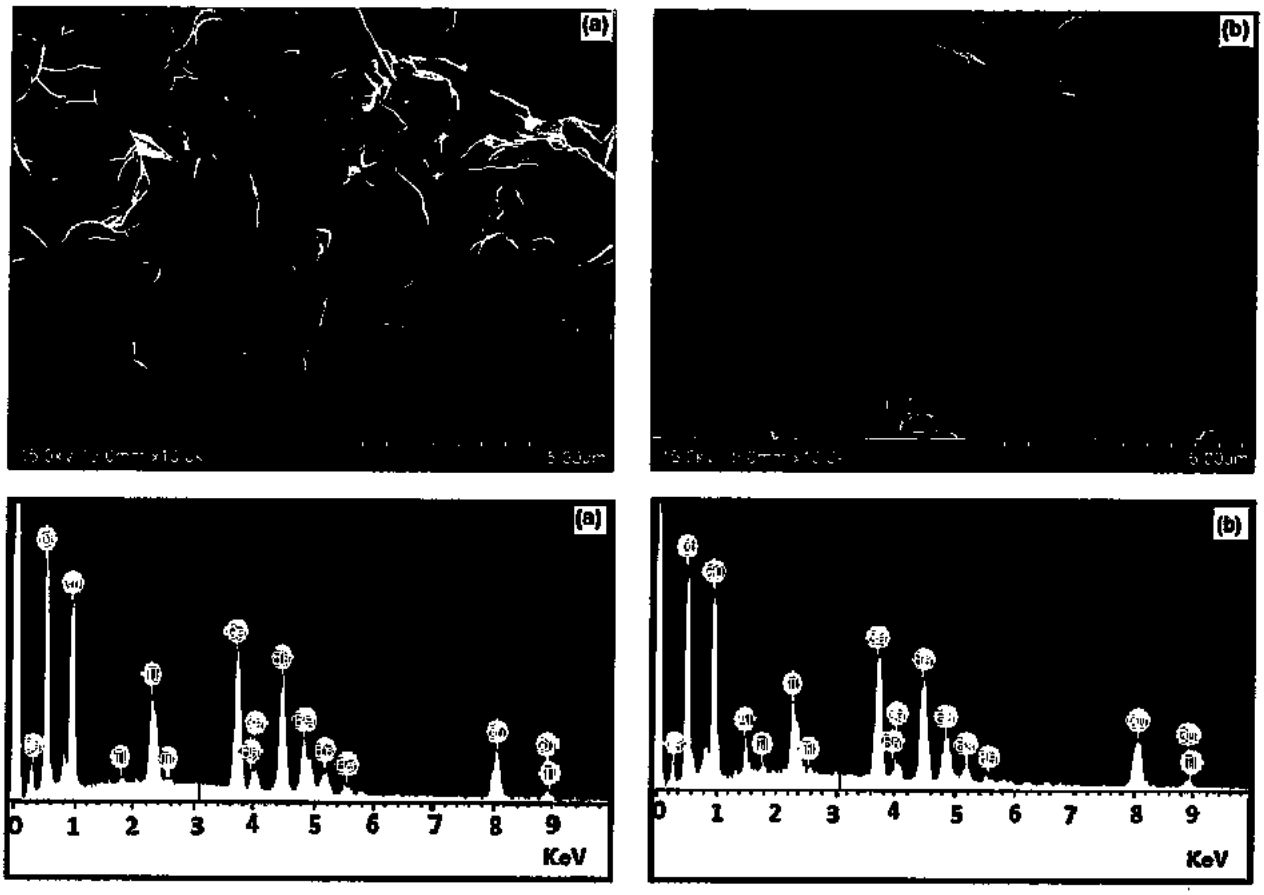

Fig. 6.3: Typical SEM micrographs and EDX spectra of $(Al_2O_3)_x$/CuTl-1223 composites (a) x = 0.0%, (b) x = 1.5%.

SEM and XRD indicate that the nano-Al_2O_3 particles just occupy the interstitial spaces amongst the grains and do not enter into the structure of CuTl-1223 phase. Similar results were observed by A. Mellekh *et al* [26] for Al_2O_3 nanoparticles added $YBa_2Cu_3O_y$ phase and N. H. Mohammad *et al* [22] in studying the effect of nano-SnO_2 particles inclusion into CuTl-1223 superconducting phase. The mass percentages of different elements present in $(Al_2O_3)_y$/CuTl-1223 composition determined by the EDX analysis are listed in Table 6.1.

Table 6.1: Elemental analysis by EDX of $(Al_2O_3)_y$/CuTl-1223 composites with y = 0, 0.5, 1.0 and 1.5 wt.%.

Elements	y = 0			y = 0.5 wt.%			y = 1.0 wt.%			y = 1.5 wt.%		
	KeV	Mass%	Atom%	KeV	Mass%	Atom%	KeV	Mass%	Atom%	KeV	Mass%	Atom%
O K	0.535	20.68	58.05	0.536	18.78	54.65	0.538	20.40	57.08	0.540	20.22	55.96
Ca K	3.695	8.87	9.94	3.696	9.16	10.64	3.698	7.67	8.57	3.702	8.78	9.70
Cu L	0.952	26.93	19.03	0.955	26.00	19.05	0.958	27.85	19.62	0.960	27.48	19.15
Ba L	4.484	31.83	10.41	4.486	33.55	11.37	4.488	30.16	9.83	4.492	30.63	9.88
Tl M	2.325	11.70	2.57	3.321	11.54	2.63	2.318	12.64	2.77	2.315	11.12	2.41
Al K	—	—	—	1.495	0.96	1.66	1.510	1.28	2.13	1.525	1.77	2.90
Total		**100**	**100**		**100**	**100**		**100**	**100**		**100**	**100**

6.3.3 Fourier Transform Infrared (FTIR) Absorption Spectra

FTIR is a very sensitive technique used to detect a trace amount of impurities along with functional groups in the material. FTIR absorption spectra of $(Al_2O_3)_y$/CuTl-1223 composites with y = 0, 0.5, 1.0 and 1.5 wt.%, in the infrared range from 400-700 cm^{-1} are shown in Fig. 6.4. The bands in the range from 400 to 540 cm^{-1} are associated with the apical oxygen atoms and in the range from 541 to 600 cm^{-1} are associated with CuO_2 planar oxygen atoms [34, 35]. The bands in the range from 670 to 700 cm^{-1} are associated with O_δ oxygen atoms in the charge reservoir layer [36]. In pure $Cu_{0.5}Tl_{0.5}Ba_2Ca_2Cu_3O_{10-\delta}$ samples, the apical oxygen modes of type Tl–O_A–Cu(2) and Cu(1)–O_A–Cu(2) are observed around 418 cm^{-1} and 537 cm^{-1} and CuO_2 planner mode is around 580 cm^{-1}. The apical oxygen modes remain unchanged in nano-Al_2O_3 particles added samples. The CuO_2 planner mode is harden to 591 cm^{-1} for y = 1.0 wt. % and slightly softened to 575 and 576 cm^{-1} for y = 0.5 and 1.5 wt. %, respectively. The softening and hardening of these modes is most likely associated with the stresses and strains produced in the materials after the addition of Al_2O_3 nanoparticles, which may affect the different bond length in the unit cell. There was no significant change in peak positions of oxygen modes after nanoparticles addition but the shapes of FTIR spectra are slightly different from one another with respect to relative intensity for different samples. Different bond lengths in the unit cell can be affected due to stresses and strains produced in the materials by the inclusion of these nanoparticles as well as due to small variation in the O_δ oxygen in the CRL of the unit cell. This gives evidence that no decomposition of Al_2O_3 nanoparticles and no diffusion of Al in the unit

cell of the host CuTl-1223 matrix have been taken place. Therefore the most suitable place of these nanoparticles in the CuTl-1223 matrix is the grain-boundaries.

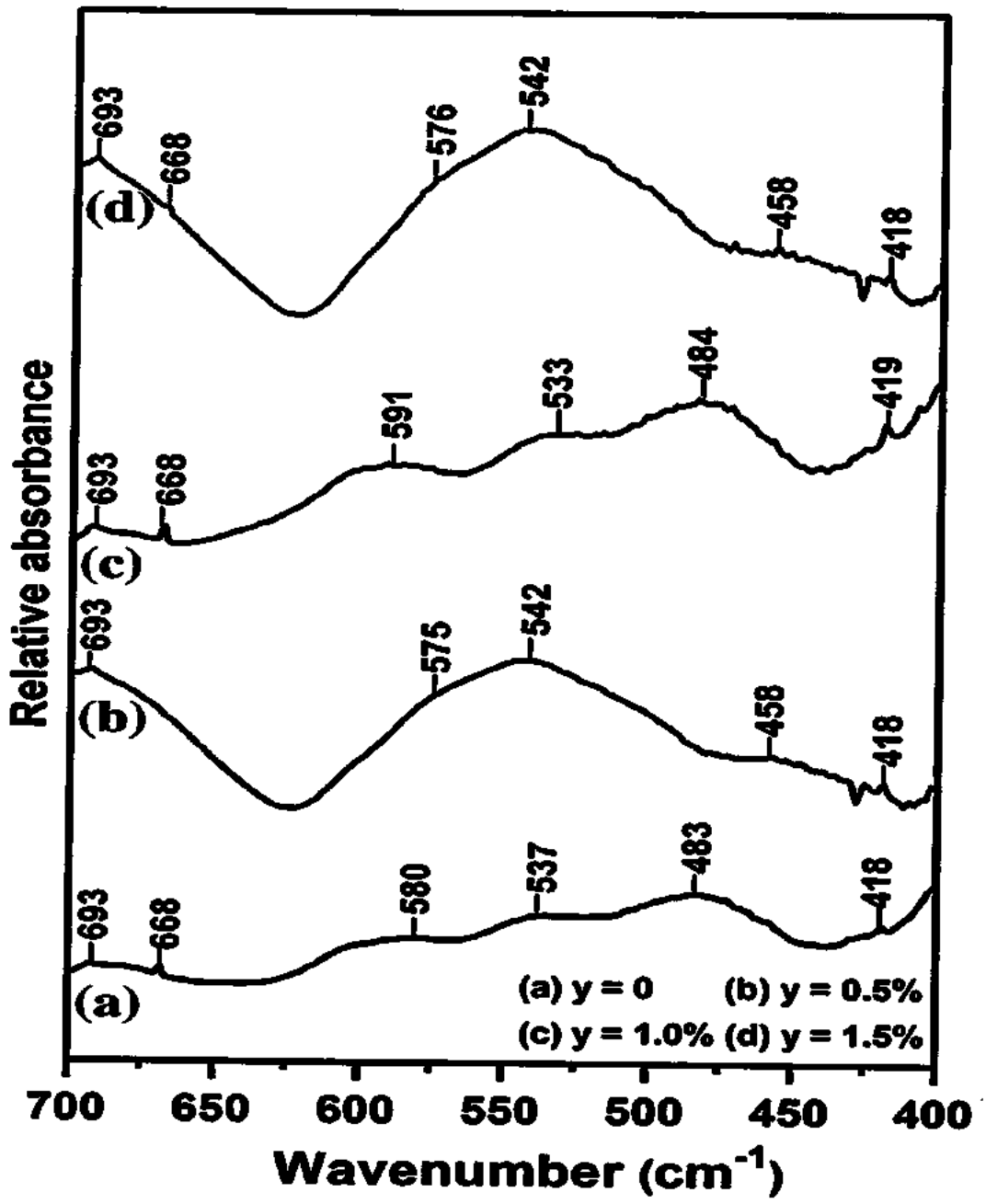

Fig. 6.4: FTIR absorption spectra of $(Al_2O_3)_y$/CuTl-1223 composites with (a) y = 0, (b) y = 0.5 wt. %, (c) y = 1.0 wt.%, and (d) y = 1.5 wt. %.

6.3.4 Resistivity versus Temperature, Arrhenius Plots and Activation Energy Measurements

The resistivity versus temperature measurements of $(Al_2O_3)_y$/CuTl-1223 (y = 0, 0.5, 1.0 and 1.5 wt.%) nano-superconductor composites are shown in Fig. 6.5. All these samples have shown a metallic variation in resistivity from room temperature down to onset of superconductivity with zero resistivity critical temperature $\{T_c(0)\}$ around 86 K, 74 K, 75 K and 64 K.

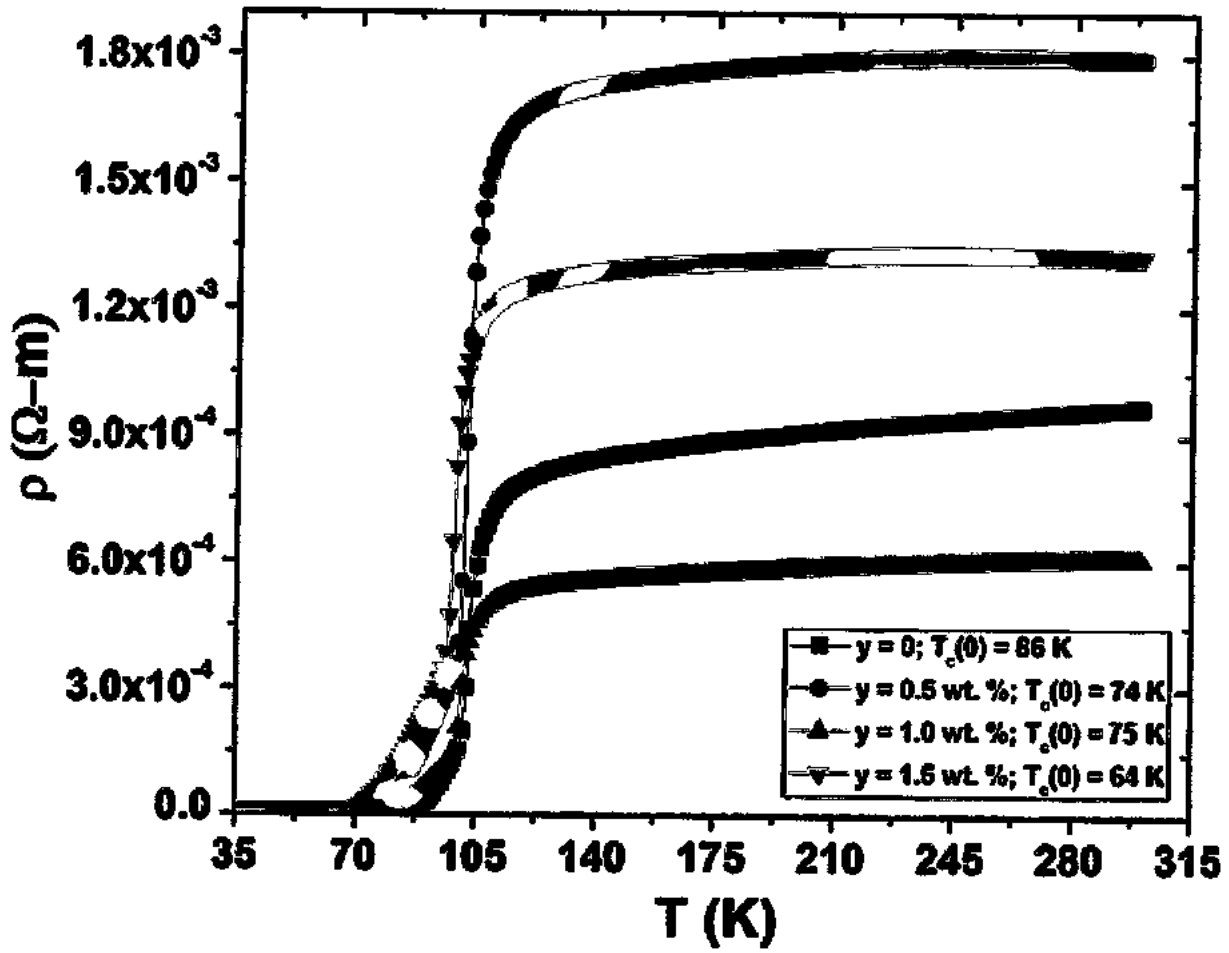

Fig. 6.5: Resistivity versus temperature measurements of $(Al_2O_3)_y$/CuTl-1223 composites with y = 0.0, 0.5, 1.0 and 1.5 wt.%.

There is non-monotonic variation in T_c (R=0) with the increase of nano-Al_2O_3 particles concentration in the composites as shown in the inset of Fig.6.6. It is assumed that this non-monotonic variation in T_c (0) K is mainly because of non-uniform distribution of Al_2O_3 nanoparticles at the grain boundaries of the host CuTl-1223 superconducting matrix. The overall suppression of T_c (0) K with Al_2O_3 nanoparticles addition is either due to oxygen vacancy

disorder or due to mobile holes trapping [37-40] or due to lesser oxygen content in CuO_2 planes [41]. The main problem is to make the distribution of Al_2O_3 nanoparticles uniform and homogeneous across the grain-boundaries of CuTl-1223 superconducting matrix. It can be seen from the superconducting transition region in resistivity versus temperature measurements that there is no clear relationship between the Al_2O_3 content and normal state resistivity at 300 K as shown in Fig.6.6, which is most probably due to the inhomogeneous distribution of these nanoparticles at the grain-boundaries of the bulk CuTl-1223 material.

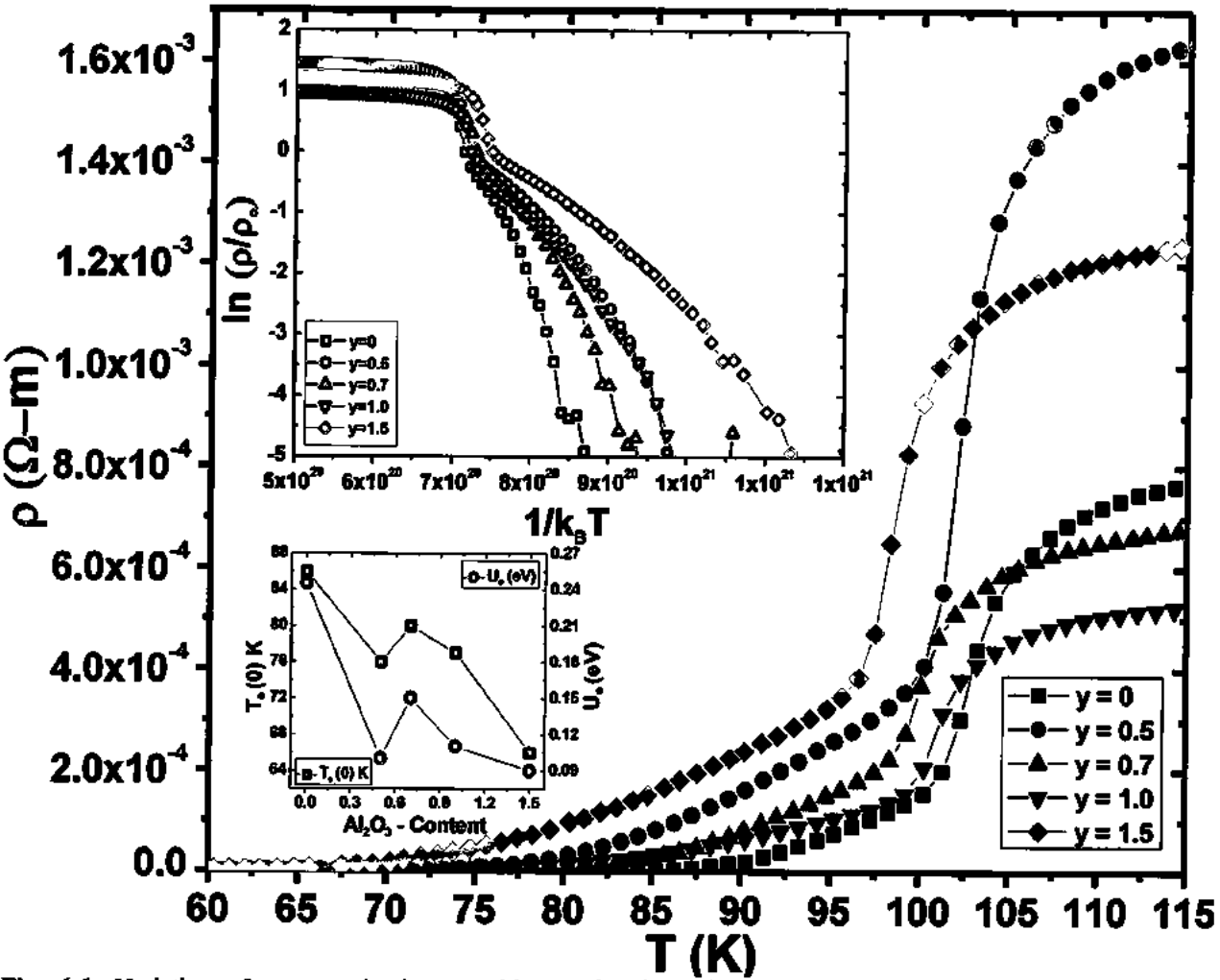

Fig. 6.6: Variation of superconducting transition region in resistivity versus temperature measurements of $(Al_2O_3)_y$/CuTl-1223 composites with y = 0, 0.5, 0.7, 1.0 and 1.5 wt.%. In the inset are given the Arrhenius plots of $(Al_2O_3)_y$/CuTl-1223 composites with y = 0, 0.5, 0.7, 1.0 and 1.5 wt.%, activation energy and T_c versus nano-Al_2O_3 contents.

The possibility of the Al_2O_3 material dissolved into the matrix of CuTl-1223 superconductor cannot be eliminated as it was synthesized at higher temperature for elongated time (860°C, 24 hours). Since the vortex motion in high T_c superconductors is thermally assisted phenomena, therefore, we can use the Arrhenius Law to calculate the activation energy required to overcome the pinning barrier [42-45]. The Arrhenius Law for superconductors is $\rho = \rho_o \exp(-U/k_BT)$; where U is the activation energy and k_B is the Boltzmann constant. The Arrhenius plots of $(Al_2O_3)_y$/CuTl-1223 composites are shown in the inset of Fig. 6.6. We used the region close to T_c (0) K to calculate the activation energy. The plot of activation energy versus nano-Al_2O_3 particles contents is also shown in the inset of Fig. 6.6. It can be seen that activation energy has been decreased with the increase of nano-Al_2O_3 particles contents in the composites. The decrease of the activation energy with the increase of nano-Al_2O_3 contents is possibly due to enhanced insulating nature of inter-granular regions. These insulating weak-links between the superconducting grains cause resistive broadening as the energy dissipation takes place during the transport of mobile carriers. The lower values of the activation energies also show the weak flux pinning in these samples.

6.3.5 Current versus Voltage (IV) Measurements

The current versus voltage (IV) measurements of $(Al_2O_3)_y$/CuTl-1223 (y = 0, 0.5, 1.0 and 1.5 wt.%) composites are shown in Fig. 6.7. These IV measurements were carried out at 50 K below the zero resistivity critical temperature for the samples. The criterion of J_c for the IV measurements was kept 1 μV/cm at 50 K in zero external applied magnetic field for all the samples. The IV characteristics curves show the suppression of critical current (I_c) with the addition of nano-Al_2O_3 particles in CuTl-1223 superconducting matrix. The variation of J_c with different concentrations of nano-Al_2O_3 particles is shown in the inset of Fig. 6.7. This decreasing trend of J_c with increasing Al_2O_3 nanoparticles concentration is possibly due to the formation of superconductor-insulator-superconductor junctions in the composites. The insulating Al_2O_3 nanoparticles present at the grain-boundaries reduce the activation energy of the carriers due to which pair-breaking of carriers occurs and superconducting parameters are suppressed [46]. But, we expect that Al_2O_3 nanoparticles will act as active pinning centers in the external applied magnetic field measurements [26-31]. The pinning effects of these nanoparticles will be explored by infield measurements of these composites, which are under way. Presently, we only reported the effects of Al_2O_3 nanoparticles addition on the structural and superconducting transport

properties of CuTl-1223 matrix without external applied magnetic field. All the experimental results are very consistent and supporting each other.

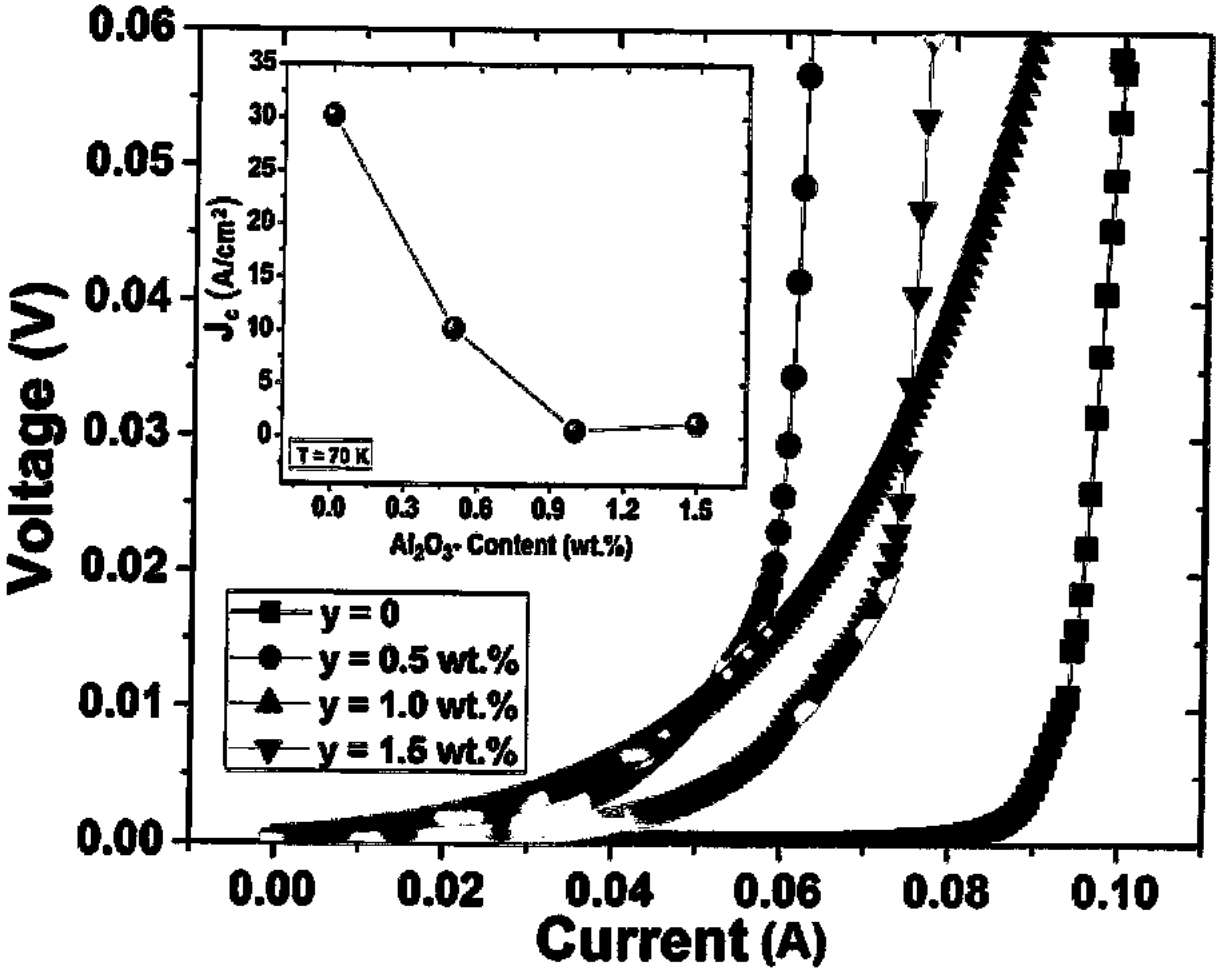

Fig. 6.7: Current versus voltage (IV) measurements of $(Al_2O_3)_y$/CuTl-1223 composites with y = 0, 0.5, 1.0 and 1.5 wt.%. (In the inset J_c(A/cm^2) versus nano-Al_2O_3 particles content is shown).

6.3.6 Fluctuation Induced Conductivity (FIC) Analysis

The FIC analysis on the resistivity versus temperature data of $(Al_2O_3)_y$/CuTl-1223 composites are carried out by using AL model in the mean field regime. The values of critical exponent (λ_{2D} and λ_{3D}), cross-over temperature (T_o), mean field critical temperature (T_c^{mf}), zero temperature coherence length along c-axis $\{\xi_c(0)\}$, inter-layer coupling (J) are given in Table 6.2. The increased values of 'α' after nano-Al_2O_3 particles addition is a theoretical evidence of insulating inter-grain boundaries in the composites samples. Moreover it is also witnessed that $\xi_c(0)$ has been improved with the increase of 'J' values with the nano-Al_2O_3 particles addition in CuTl-1223 superconducting matrix. The plots of ln($\Delta\sigma_{AL}$) versus ln(ε) of $(Al_2O_3)_y$/CuTl-1223 composite samples for; (a) y = 0, (b) y = 1.5% are shown in Fig. 6.8(a, b) and in the insets are

shown the experimentally measured dc-resistivity ρ(Ω-cm) along with a straight line extrapolated from the room temperature (300 K) normal state resistivity to 0 K and derivative (dρ/dT) of dc-resistivity versus temperature.

Table 6.2: The superconductivity parameters observed from the FIC analysis of $(Al_2O_3)_y$/CuTl-1223 composites with y = 0.0, 0.5, 0.7, 1.0 and 1.5 wt.%.

Samples	ρ_n(300K) (Ω-cm)$\times 10^{-4}$	T_c (K)	T_o (K)	T_c^{mf}(K)	$\alpha=\rho_n(0K)$ (Ω-cm) $\times 10^{-4}$	λ_{3D} slope	λ_{2D} slope	$\xi_c(0)$ (Å)	$J=[2\xi_c(0)]^2/d^2$
y= 0.0	9.650	86	104.34	102.31	7.79	0.52	1.05	3.664	0.238
y= 0.5	17.9	74	104.38	102.31	17.21	0.48	1.07	4.741	0.399
y= 0.7	6.105	79	103.34	101.31	5.316	0.5	1.02	4.91	0.429
y =1.0	13.33	75	101.33	98.34	12.83	0.47	1.97	5.857	0.609
y =1.5	13.33	64	101.33	98.34	12.752	0.48	1.99	6.181	0.679

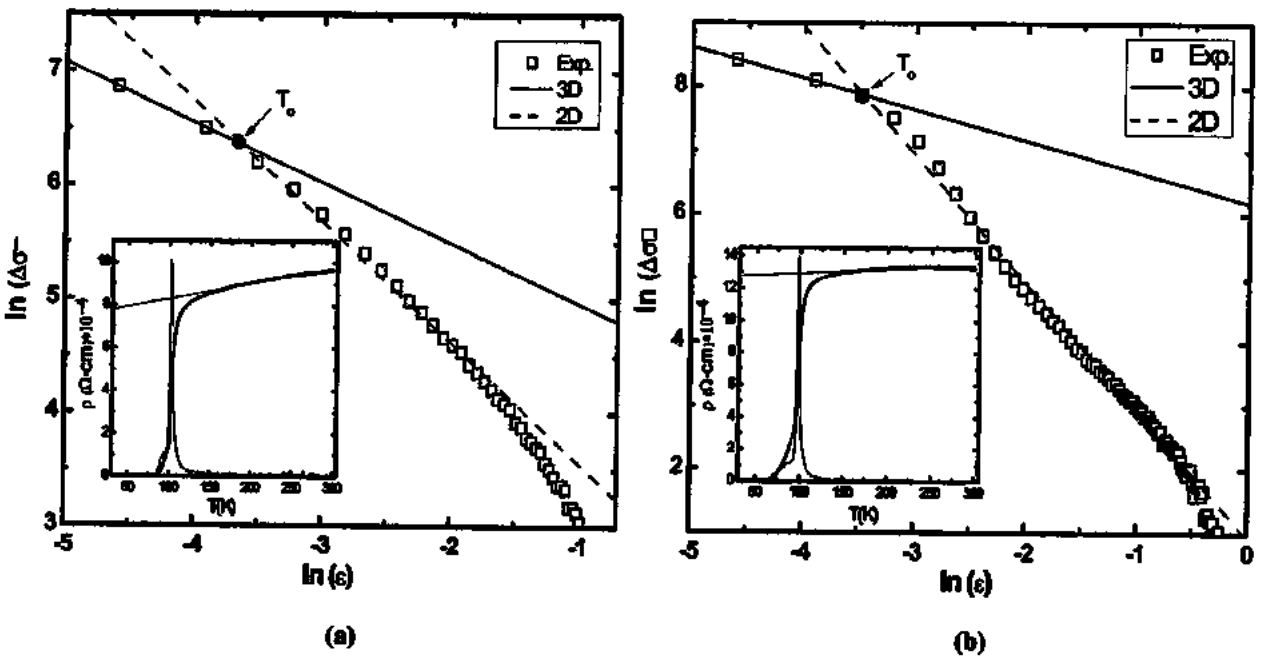

Fig. 6.8(a, b): ln (Δσ) versus ln(ε) plot of $(Al_2O_3)_y$/CuTl-1223 composites; (a) y = 0, (b) y = 1.5 wt.% ; (In the insets are shown the experimentally measured dc resistivity ρ(Ω-cm), derivative (dρ/dT) of dc resistivity versus temperature, and the straight line extrapolated from the room temperature '300 K' normal state resistivity to 0 K).

The fitting of experimental curves shows the existence of two different fluctuation regions in these samples. The values of critical exponent (λ_D) derived from the slopes of sample with y = 0

is found to be 0.52 and 1.05, which correspond to 3D and 2D AL fluctuations respectively. Also, the value of λ_D were found to be (0.48, 1.07), (0.5, 1.02), (0.47, 1.97) and (0.48, 1.99) with y = 0. 5, y = 0.7, y = 1.0, and y = 1.5 wt.%, respectively for 3D and 2D fluctuations. There is a cross-over temperature (T_o) at which fluctuations have been changed from 2D to 3D in low temperature region. The widths of these fluctuation regions are given in Table 6.3. It can be seen from the data that T_o has been shifted toward lower temperature with nano-Al_2O_3 particles addition. On the other hand the increased values of $\{\xi_c(0)\}$ and (J) show that samples become more isotropic after nano-Al_2O_3 particles addition.

Table 6.3: Widths of critical 3D and 2D fluctuation regions observed from fitting of the experimental data of $(Al_2O_3)_y$/CuTl-1223 composites with y = 0.0, 0.5, 0.7, 1.0 and 1.5 wt.%.

Sample	λ_{3D} T(K)	ln ε (range in 3D)	λ_{2D} T(K)	ln ε (range in 2D)
y = 0.0	103.34- 104.34	-4.59 < ln < -3.91	104.34 – 121.40	-3.91 < ln ε < -1.67
y = 0.5	103.37-105.38	-4.56 < ln ε < -3.50	105.38 – 129.47	-3.50 < ln ε < -1.32
y =0.7	102.34-103.34	-4.58 < ln ε < -3.50	103.34 – 131.43	-3.50 < ln ε < -1.21
y =1.0	99.39-101.33	-4.59 < ln ε < -3.49	101.33 – 154.51	-3.49 < ln ε < -0.55
y =1.5	99.33-101.33	-4.60 < ln ε < -3.49	101.33 – 159.53	-3.49 < ln ε < -0.47

The shift of 3D regime to lower temperature indicates that inter-grain boundaries become more insulating due to which T_c and T_o have been decreased. The variation in microscopic parameters extracted from FIC analysis verifies the overall suppression of superconductivity after nano-Al_2O_3 particles addition in CuTl-1223 superconducting matrix.

6.4 References

[1] H. Ihara, K. Tokiwa, H. Ozawa, M. Hirabayashi, A. Negishi, H. Matuhata, and Y. S. Song, Jpn. J. Appl. Phys. **33**, L503 (1994).

[2] H. Ihara, Physica C **364-365**, 289 (2001).

[3] Z. Z. Sheng, and A. M. Hermann, Nature **332**, 55 (1988).

[4] Z. Z. Sheng, A. M. Hermann, A. E. Ali, C. Almasan, J. Estrada, T. Datta, and R. J. Matson, Phys. Rev. Lett. **60**, 937 (1988).

[5] Z. Z. Sheng, and A. M. Hermann, Nature **332**, 138 (1988).

[6] G. Malandrino, D. S. Richeson, T. J. Marks, D. C. De Groot, J. L. Schindler, and C. R. Kannewurf, Appl. Phys. Lett. **58**, 182 (1991).

[7] M. L. Chu, H. L. Chang, C. Wang, J. Y. Juang, T. M. Uen, and Y. S. Gou, Appl. Phys. Lett. **59**, 1123 (1991).

[8] W. L. Oslon, M. M. Eddy, T. W. James, R. B. Hammond, G. Gruner, and L. Drabeck, Appl. Phys. Lett. **55**, 188 (1989).

[9] S. H. Yun, and J. Z. Wu, Appl. Phys. Lett. **68**, 862 (1996).

[10] M. Annabi, A. M. Chirgui, F. B. Azzuoz, and M. B. Salem, Physica C **25**, 405 (2004).

[11] Nawazish A. Khan, M. Mumtaz, K. Sabeeh, M. I. A. Khan, and M. Ahmed, Physica C **407**, 103 (2004).

[12] K. Semba, A. Matsuda, and T. Ishii, Phys. Rev. B **49**, 10043 (1996).

[13] M. K. Wu, J. R. Ashburn, C. J. Torng, P. H. Hor, R. L. Meng, L. Gao, Z. J. Huang,Y. Q. Wang, and C.W. Chu, Phys. Rev. Lett. **58**, 908 (1987).

[14] K. Heine, J. Tenbrink, and M. Thoner, Appl. Phys. Lett. **55**, 2441 (1989).

[15] J. Y. Yuang, J. H. Horng, S. P. Chen, C. M. Fu, K. H. Wu, T. M. Uen, and Y. S. Gou, Appl. Phys. Lett. **66**, 885 (1995).

[16] M. Mumtaz, Nawazish A. Khan, and S. Khan, J. Appl. Phys. **107**, 103905 (2010).

[17] M. Mumtaz, Nawazish A. Khan, and E. U. Khan, Physica C **470**, 428 (2010).

[18] Nawazish A. Khan, and M. Mumtaz, *J. Low Temp. Phys.* **151**, 1221 (2008).

[19] C. Wang, Z. Gao, L. Wang, Y. Qi, D. Wang, C. Yao, Z. Zhang, and Y. Ma, Supercond. Sci. Technol. **23**, 055002 (2010).

[20] B. P. Mikhailov, G. S. Burkhanov, G. M. Leitus G. N. Mikhailova, A. M. Prokhorov, A. S. Seferov, A. V. Troitskii, and I. E. Lapshina, Inorganic Mater. **32** (10), 1073 (1996).

[21] M. M. Elokr, R. Awad, Asmaa Abd El-Ghany, A. Abou Shama, and A, Abd El-wanis, J. Supercond. Nov. Magn. **24,** 1345 (2011).

[22] N. H. Mohammad, A. I. Abou-Aly, I. H. Ibrahim, R. Awad, and M. Rek-aby, J. Alloys Comp. **486,** 733 (2009).

[23] N. H. Mohammad, A. I. Abou-Aly, R. Awad, I. H. Ibrahim, M. Roumie, and M. Rekaby, J. Low Temp. Phys. **172,** 234 (2013).

[24] S. G. Elsharkawy, and R. Awad, J. Alloys Comp. **478,** 642-647 (2009).

[25] R. Awad, J. Supercond. Nov. Magn. **21,** 461 (2013).

[26] A. Mellekh, M. Zouaoui, F. Ben Azzouz, M. Annabi, and M. Ben Salem, Solid Stat. Comm. **140,** 318 (2006).

[27] A. Ghattas, F. Ben Azzouz, M. Annabi, M. Zouaoui, and M. Ben Salem, Journal of Physics: Conference Series. **97,** 012175 (2008).

[28] M. Annabi, A. Ghattas, M. Zouaoui, F. Ben Azzouz, and M. Ben Salem, Journal of Physics: Conference Series **150,** 052008 (2009).

[29] N. Moutalibi, A. M'chirgui, and J. Noudem, Physica C **470,** 568 (2010).

[30] A. Mellekh, M. Zouaoui, F. Ben Azzouz, M. Annabi, and M. Ben Salem, Physica C **460-462,** 426 (2007).

[31] X. F. Rui, J. Chen, X. Chen, W. Guo, and H. Zhang, Physica C **412-414,** 312-315 (2004).

[32] A. L. Solovjov, H. -U. Habermeier, and T. Haage, Low Temp. Phys. **28,** 17 (2002)

[33] C. A. C Passos, M. T. D. Orlando, J. L. Passamai, Jr., E. V. L. de Mello, H. P. S. Correa, L. G. Martinez, Phys. Rev. B **74,** 094514 (2006).

[34] K. Nadeem, F. Naeem, M. Mumtaz, S. Naeem, Abdul Jabbar, Irfan Qasim, and Nawazish A. Khan, Ceram. Int. **40,** 13819 (2014).

[35] M. Mumtaz, M. Zubair, Nawazish A. Khan, and Saleem Abbas, Low Temp. Phys./Fizika Nizkikh Temperatur **40,** 259 (2014).

[36] M. Mumtaz, S. Naeem, K. Nadeem, F. Naeem, Abdul Jabbar, Y. R. Zheng, Nawazish A. Khan, and M. Imran, Solid Stat. Sci. **22,** 21 (2013).

[37] J. C. Zhang, F. Q. Liu, G.S. Cheng, J. X. Shang, J. Z. Liu, S.X. Cao, and Z. X. Liu, Phys, Lett. A **201,** 70 (1995).

[38] P. F. Miceli, J. M. Tarascon, L. H. Greene, H. P. Barbou, F. J. Rotella, and J. D. Jorgensen, Phys. Rev. B **37,** 5932 (1988).

[39] S. Cao, L. Li, F. Liu, W. Li, C. Chi, C. Jing, and J. Zhang, Supercond. Sci. Technol. **18**, 606 (2005).

[40] V. P. S. Awana, S. K. Malik, W. B. Yelon, C. A. Cardoso, O. F. de Lima, Anurag Gupta, A. Sedky, and A. V. Narlikar, Physica C **338**, 197 (2000).

[41] E. Brecht, W. W. Schmahl, G. Miehe, M. Rodewald, H. Fuess, N. H. Andersen, J. Hanβmann, and Th. Wolf, Physica C **265**, 53 (1996).

[42] S. J. Feng, J. Ma, H.D. Zhou, G. Li, L. Shi, Y. Liu, J. Fang, and X.G. Li, Physica C **386**, 22 (2003).

[43] A. J. Batista-Leyva, M. T. D. Orlando, L. Rivero, R. Cobas, and E. Altshuler, Physica C **383**, 365 (2003).

[44] M. Tinkham, Phys. Rev. Lett. **61**, 1658 (1988).

[45] T. M. Palstra, B. Batlogg, L. F. Schneemeyer, and J. V. Waszczak, Phys. Rev. Lett. **61**, 1662 (1988)

[46] Abdul Jabbar, Irfan Qasim, M. Mumtaz, M. Zubair, K. Nadeem, and A. A. Khurram, J. Appl. Phys. **115**, 203904 (2014).

Chapter 7

General Conclusions and Future Prospects

7.1 General Conclusions

In order to study the variations in superconducting properties of $(Cu_{0.5}Tl_{0.5})Ba_2Ca_2Cu_3O_{10-\delta}$ (CuTl-1223) matrix by the inclusion of different types and sizes of nanoparticles (i.e. Al_2O_3, Ag, Au and $CoFe_2O_4$) with different wt. %, we successfully synthesized four series of samples by solid-state reaction method and characterized them by different experimental techniques such as XRD, SEM, EDX, TEM, FTIR, RT-measurements, IV-measurements, etc. We analyzed our experimental data with the help of well-established theoretical models (AL, LD and MTmodels) in this area of research.

Following conclusions can be drawn from our investigations.

i) In case of $(Ag)_x$/CuTl-1223 (x = 0, 0.5, 1.0, 2.0 and 4.0 wt.%) nanoparticles-superconductor composites, the crystal structure of host CuTl-1223 superconducting matrix was not affected after the addition of Ag nanoparticles. The activation energy {U (eV)} and zero resistivity critical temperature $\{T_c(0)\}$ were increased with increasing contents of Ag nanoparticles up to x = 2.0 wt. %. The systematic increase in $T_c(0)$ and decrease in $\rho_{300\,K}$ (Ω-cm) may be due to improved inter-grains coupling by healing up the voids after the addition of Ag nanoparticles at the grain-boundaries of CuTl-1223 phase. The suppression of superconducting properties after the addition of these nanoparticles beyond the certain optimum level is most probably due to agglomeration and segregation of these nanoparticles at the grain-boundaries. The microscopic parameters deduced from the FIC analysis are in accordance with the experimental findings. The increase in ξ_c (0)and J indicates the reduction of anisotropic nature of CuTl-1223 phase after Agnanoparticles addition.

ii) In case of $(Au)_x$/CuTl-1223 (x = 0, 0 .5, 1.0 and 1.5 wt.%) nanoparticles-superconductor composites, the tetragonal structure of CuTl-1223 matrix remained unaltered after nano-Au particles addition. It provides an evidence of the presence of nano-Au particles at inter-granular spaces (inter-grain boundaries). The systematic decrease in normal state resistivity and monotonic increase in T_c (0) with gradual increase of these nanoparticles contents up to certain optimum level is most probably

due to somehow homogeneous and uniform distribution of these nanoparticles at the grain-boundaries of the bulk CuTl-1223 material.The improvement in the superconducting properties can be attributed to an increase in the inter-grains connectivity by healing up the inter-grains voids and pores by the addition of Au nanoparticles. The improved inter-grains connections can facilitate the carriers transport across the inter-crystallite sites. But the superconducting volume fraction starts to be reduced after certain optimum inclusion level of non-superconducting metallic Au nanoparticles, which causes the suppression of superconductivity parameters of CuTl-1223 phase.

iii) In case of $(CoFe_2O_4)_x$/CuTl-1223 (x = 0, 0.5, 1.0, 1.5 and 2.0 wt.%) nanoparticles-superconductor composites, the stoichiometry and crystal structure of the host CuTl-1223 matrix remained unchanged after the addition of highly coercive$CoFe_2O_4$ nanoparticles. The enhancement in $T_c(0)$ was observed with increasing contents of $CoFe_2O_4$ nanoparticles due to improvement of weak-links by filling the pores and crakes present in the bulk CuTl-1223 matrix. The increase in mass density after addition of these nanoparticles can also be due to filling of pores. The addition of these nanoparticles beyond a certain optimum concentration level causes agglomeration and produces additional stresses and strains in the bulk material and suppresses the superconducting properties. The suppression of $T_c(0)$ may due to pair-breaking mechanism caused by reflection/scattering of carriers and trapping/localization of mobile free carriers across the agglomerated magnetic $CoFe_2O_4$ nanoparticles present at grain-boundaries of the host CuTl-1223 superconducting matrix.

iv) In case of $(Al_2O_3)_y$/CuTl-1223 (y = 0.0, 0.5, 0.7, 1.0 and 1.5 wt.%) nanoparticles-superconductor composites, XRD scans revealed that the tetragonal structure of CuTl-1223 matrix was not affected by the inclusion of Al_2O_3 nanoparticles, which provided a clue about the occupancy of these nanoparticles at the grain-boundaries. The EDX spectra confirmed the presence of Al_2O_3 nanoparticles in CuTl-1223 matrix. The suppression of $T_c(0)$ and J_c was observed with increasing contents of Al_2O_3 nanoparticles, which was most probably due to pair-breaking mechanism caused by the reflection/scattering of carriers during their transport across these

insulating nano-Al_2O_3 particles present at the grain-boundaries. The insulating nano-Al_2O_3 particles forming the superconductor-insulator-superconductor junctions in the $(Al_2O_3)_y$/CuTl-1223 composites has suppressed the superconductivity parameters. The decrease of the activation energy with the increase of nano-Al_2O_3particles contents is possibly due to enhanced insulating nature of inter-granular regions. These insulating weak-links between the superconducting grains cause resistive broadening as the energy dissipation takes place during the transport of carriers. The lower values of the activation energies also show the weak flux pinning in these samples. The dc-resistivity data seems to be fitted very well with 3D and 2D Aslamasov-Larkin equations. The cross-over temperature (T_o) is shifted towards lower temperature values with the enhanced nano-Al_2O_3 particles concentration. The increase in $\xi_c(0)$and J indicates the reduction of anisotropic nature of the material after nano-Al_2O_3 particles addition.

7.2 Future Prospects

We have planned to address the following unresolved and unaddressed issues in this area;

1) Uniform distribution of nanostructures at the grain-boundaries of the host HTSCs matrix.
2) Tuning of superconducting properties of the host HTSCs matrix by varying the sizes of nanostructures (nanoparticles, nanorodesetc).
3) Infield measurements (i.e. RT, IV, RH etc) to explore the influence of nanostructures on the artificial flux pinning centers in the host HTSCs matrix.

Research Articles Published in ISI Indexed Impact Factor International Journals from the Research Work of this PhD Thesis

Available online at www.sciencedirect.com

ScienceDirect

Progress in Natural Science: Materials International 25 (2015) 204–208

Progress in Natural Science Materials International

www.elsevier.com/locate/pnsmi
www.sciencedirect.com

Original Research

Synthesis and superconductivity of $(Ag)_x$/CuTl-1223 composites

Abdul Jabbar, Irfan Qasim, M. Mumtaz[1], K. Nadeem

Materials Research Laboratory, Department of Physics, Faculty of Basic and Applied Sciences (FBAS), International Islamic University (IIU), Islamabad 44000, Pakistan

Received 27 August 2014; accepted 21 December 2014
Available online 9 July 2015

Abstract

Series of $(Ag)_x/(Cu_{0.5}Tl_{0.5}Ba_2Ca_2Cu_3O_{10-\delta})$ {$(Ag)_x$/CuTl-1223} nano-superconductor composites were synthesized with different concentrations (i.e. $x=0\sim4.0$ wt%) of silver (Ag) nanoparticles. Low anisotropic CuTl-1223 superconducting matrix was prepared by solid-state reaction and Ag nanoparticles were prepared by a sol–gel method separately. The required $(Ag)_x$/CuTl-1223 composition was obtained by the inclusion of Ag nanoparticles in CuTl-1223 superconducting matrix. Structural, morphological, compositional and superconducting transport properties of these composites were investigated in detail by x-ray diffraction (XRD), scanning electron microscopy (SEM), energy dispersive x-rays (EDX) spectroscopy and four-point probe electrical resistivity (ρ) measurements. The inclusion of Ag nanoparticles enhanced the superconducting properties without affecting the tetragonal structure of the host CuTl-1223 matrix. The improvement in superconducting properties of $(Ag)_x$/CuTl-1223 composites is most likely due to enhanced inter-grains coupling and increased superconducting volume fraction after the addition of metallic Ag nanoparticles at the inter-crystallite sites in the samples. The presence of Ag nanoparticles at the grain-boundaries may increase the number of flux pinning centers, which were present in the form of weak-links in the pure CuTl-1223 superconducting matrix.

Keywords: $(Ag)_x$/CuTl-1223 composites; Ag nanoparticles; weak-links; superconducting properties

1. Introduction

The selection of superconducting materials for their practical applications demands higher values of critical transition temperature (T_c), critical current density (J_c) and critical magnetic field (H_c). It is obvious from literature that in spite of granular and porous nature of bulk $(Cu_{0.5}Tl_{0.5})Ba_2Ca_2Cu_3O_{10-\delta}$ (CuTl-1223) phase of $(Cu_{0.5}Tl_{0.5})Ba_2Ca_nCu_{n+1}O_{2n+4-\delta}$ high T_c superconducting family has relatively higher values of J_c, T_c, H_c and lower superconducting anisotropy ($\gamma=\xi_{ab}/\xi_c$) [1–3]. Therefore, it is necessary to study in the selected CuTl-1223 superconducting phase. The presence of inter-grain voids, impurity phases, oxygen vacancies, inhomogeneous microdefects, etc., in its bulk form due to granular nature affects the performance of this compound. This issue can, however, be resolved up to some extent by filling the pores with some suitable nanostructures (nanoparticles, nanorods, etc.) at inter-granular sites in the bulk superconductor [4]. The effects of nanostructures addition on physical and structural properties of different high temperature superconducting (HTSC) families in their bulk as well as thin films were studied by different research groups [5–9]. Generally, it is observed from the literature reviews that the addition of nanostructures in HTSCs improves the inter-grain connectivity and superconductivity parameters up to certain extent without affecting the crystal structures of superconducting phases [10–19]. The addition of nanoparticles also enhances the additional pinning effects in the bulk polycrystalline samples for the improvement of infield superconducting properties [20–22]. It was observed that low concentration of nano-ZnO addition in $(Cu_{0.5}Tl_{0.25}Pb_{0.25})$-1223 matrix enhanced superconducting properties, while high concentration of nano-ZnO enhanced the secondary phases and grain-boundaries resistance due to agglomeration of nano-ZnO particles [23]. The addition of

[1]Tel.: +92 51 9019926; fax: +92 51 9210256.
E-mail address: mmumtaz75@yahoo.com (M. Mumtaz).
Peer review under responsibility of Chinese Materials Research Society.

http://dx.doi.org/10.1016/j.pnsc.2015.06.001

MgO nanoparticles in Bi-2212 superconducting matrix improved J_c by enhancing the grains morphology due to improved inter-grains weak-links without altering the crystal structure [16]. It was observed that superconducting properties were improved by nano-Fe_2O_3 particles addition in CuTl-1223 superconductor up to certain concentration level and then started to decrease with higher concentration [24]. There was also no effect on the structural symmetry of $YBa_2Cu_3O_y$ superconducting phase after the addition of Al_2O_3 nanoparticles. In applied magnetic field, J_c of the superconducting material was enhanced significantly by nano-Al_2O_3 particles addition, which can be rendered to the existence of enhanced flux pinning centers in the superconducting matrix [25]. The values of pinning force density, onset temperature, activation energy and J_c in the applied magnetic field were improved by the addition of nano-Al_2O_3 particles in polycrystalline (Bi, Pb)-2223 superconductor [26]. The addition of Ag nanoparticles in YBCO superconducting thin films reveals greater J_c values and improved crystal structure in the form of higher crystallinity [27]. Bulk superconductor YBCO doped by Ag nanoparticles of different sizes and concentrations showed monotonic increase in superconducting properties especially J_c, which is attributed to the improvement of crystallites connectivity and superconducting volume fraction [10]. Optimal addition of Ag and SiC nano-powder of size 30–130 nm in MgB_2 superconductor has increased the artificial pinning centers along with the increase of infield superconducting properties. A further increase of SiC and Ag nano-powder above 16 wt% decreases the superconductivity of MgB_2 [28]. The improvement of mechanical properties of (Bi Pb)–Sr–Ca–Cu–O superconducting matrix was also observed after nano-Ag particles addition that may be due to cementing effects of these additives at the grains boundaries [29–31].

In literature, the optimal concentration of nano-Ag particles in different superconducting families that can enhance the superconducting properties without affecting the crystal chemistry was not yet clearly determined. In this paper, we reported that effects of the nano-Ag particles addition on structural and superconducting properties of CuTl-1223 matrix. We also tried to find out the optimal concentration of Ag nanoparticles to obtain the maximum improvement in superconducting transport properties without affecting the crystal structure of CuTl-1223 phase. The appropriate concentration of Ag nanoparticles' addition heals up inter-grains voids to improve the weak-links and act as facilitators for the carrier transport in bulk superconductors.

2. Experimental details of samples' synthesis and characterization

The nano-Ag particles added bulk ceramic CuTl-1223 superconductor composites were synthesized by two-cycle solid-state reaction method. Initially, $Ba(NO_3)_2$, $Ca(NO_3)_2$ and Cu(CN) compounds were used as starting compounds to prepare $Cu_{0.5}Ba_2Ca_2Cu_3O_{10-\delta}$ precursor. These starting compounds were mixed in appropriate ratios and ground in an agate mortar and pestle for 2 h. The mixed and ground material was loaded in quartz boats and calcinated in chamber furnace at 860 °C for 24 h followed by furnace cooling to room temperature. The calcination steps were repeated twice following 1 h intermediate grinding each time to get the fine $Cu_{0.5}Ba_2Ca_2Cu_3O_{10-\delta}$ precursor material. The nano-Ag particles were prepared by a sol-gel method separately. The precursor material was mixed with Tl_2O_3 and different wt% of Ag nanoparticles of 35 nm in average size at second stage and then ground again for 1 h to get $(Ag)_y$/CuTl-1223 (y=0.0, 0.5, 1.0, 2.0, 4.0) wt% superconductor composites. The material was then pelletized under 3.8 tons/cm^2 pressure and the pellets were enclosed in gold capsules for sintering at 860 °C for 10 min followed by quenching to room temperature.

The structure and phase purity of material was determined by XRD (D/Max IIIC Rigaku with a CuKα source of wavelength 1.54056 Å). The morphology and composition of material were determined by SEM and EDX, respectively. A conventional four-point probe method was used for dc-resistivity measurements. The phonon modes related to the vibrations of various oxygen atoms were observed by Fourier Transform Infrared (FTIR) spectroscopy in the wavenumber range of 400–700 cm^{-1}.

3. Results and discussion

The XRD pattern of Ag nanoparticles is shown in Fig. 1. The prominent peaks are indexed according to face-centered cubic (FCC) structure of Ag and the average size of Ag nanoparticles calculated by Sherrer's formula is about 35 nm. The XRD analysis shows exquisitely indexed (111), (200), (220), and (311) planes of FCC structure. The lattice parameter calculated for FCC pattern of Ag nanoparticles is about $a=4.09$ Å. No peak of impurity crystalline phases was observed.

The typical XRD patterns of $(Ag)_x$/CuTl-1223 composites with $x=0$, 1.0 and 2.0 wt%, are shown in Fig. 2. Most of the diffraction peaks are well indexed according to the tetragonal structure of CuTl-1223 phase following the P4/mmm space group and the characteristic (001) diffraction peak of this phase appeared at $2\theta=5.79°$. The stoichiometry and crystal structure of CuTl-1223 phase remained preserved even after the addition

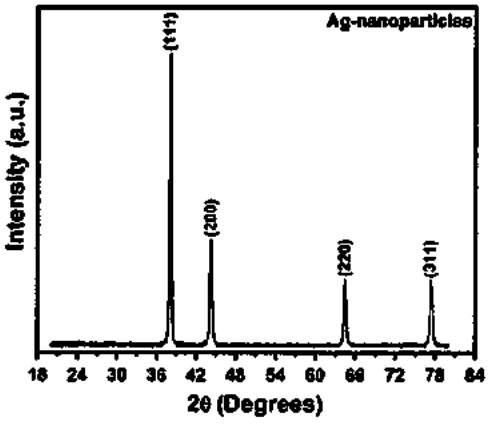

Fig. 1. XRD pattern of silver (Ag) nanoparticles.

of Ag nanoparticles. This provides evidence about the occupancy of these nanoparticles at the inter-crystallite sites and the improvement of inter-grain weak-links by filling the pores and voids. Besides the dominance of CuTl-1223 phase, few un-indexed diffraction peaks appearing in XRD patterns are possibly due to the presence of some impurities and other superconducting phases mentioned in the inset of Fig. 2. The calculated cell parameters are (a=4.45 Å, c=14.45 Å), (a=4.46 Å, c=14.96 Å), and (a=4.46 Å, c=14.97 Å) for x=0, 1.0, and 2.0 wt%, respectively. Slight variation in c-axis length may be due to some strains and variation of O_δ oxygen contents after Ag nanoparticles addition in CuTl-1223 superconducting matrix.

The typical SEM images and EDX spectra of $(Ag)_x$/CuTl-1223 samples for x=0, and 2 wt% are shown in Fig. 3. The improvement of inter-grains weak-links as well as the grains size is obvious from these SEM images after the addition of Ag nanoparticles in the host CuTl-1223 superconducting phase. The improvement of inter-grains weak-links and the grains size may be due to cementing effects of Ag nanoparticles occupying the inter-grains boundaries by filling the voids and pores present in the bulk form of CuTl-1223 matrix. The improved grains size enhances the superconducting volume fraction and superconducting properties of the host material by the addition of Ag nanoparticles. The EDX spectra show the presence of different elements in the composition. The mass percentages of different elements determined from the EDX analysis are listed in Table 1.

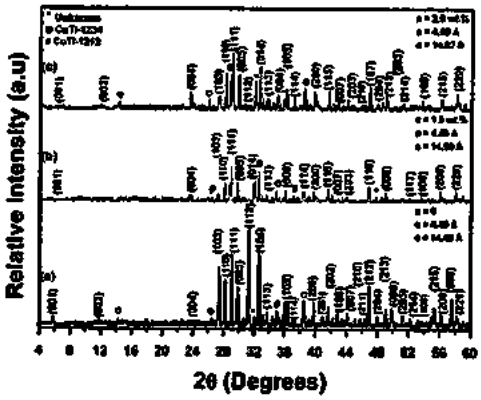

Fig. 2. XRD patterns of $(Ag)_x$/CuTl-1223 composites with (a) x=0, (b) x=1.0 wt%, and (c) x=2.0 wt%.

The FTIR absorption spectra of $(Ag)_x$/CuTl-1223 composites with x=0, 0.5, 1.0, 2.0 and 4.0 wt%, in the range from 400–700 cm^{-1} are shown in Fig. 4. The absorption bands in the range from 400 to 540 cm^{-1} are associated with the apical oxygen atoms and in the range around from 541 to 600 cm^{-1} are associated with CuO_2 planar oxygen atoms [32,33]. The absorption bands in the range from 670 to 700 cm^{-1} are associated with O_δ atoms in the charge reservoir layer [34–38]. The apical oxygen modes of type Tl–OA–Cu(2) and Cu(1)–O_A–Cu(2) are observed around 430 cm^{-1} and 460–499 cm^{-1} and CuO_2 planner oxygen mode is around 536 cm^{-1} in the pure $Cu_{0.5}Tl_{0.5}Ba_2Ca_2Cu_3O_{10-\delta}$ samples. The nominal variation in the position of the apical oxygen modes may be due to the presence of stresses and strains in the bond lengths of the unit cells caused by the nano-Ag particles in the composites. The CuO_2 planner oxygen modes and O_δ modes remained almost unaffected after the addition of nano-Ag particles in the host CuTl-1223 matrix. The FTIR study also supports our claim and objective that the Ag nanoparticles do not substitute the constituent atoms of CuTl-1223 unit cell but they occupy the inter-granular spaces, fill up the pores and heal up the cracks.

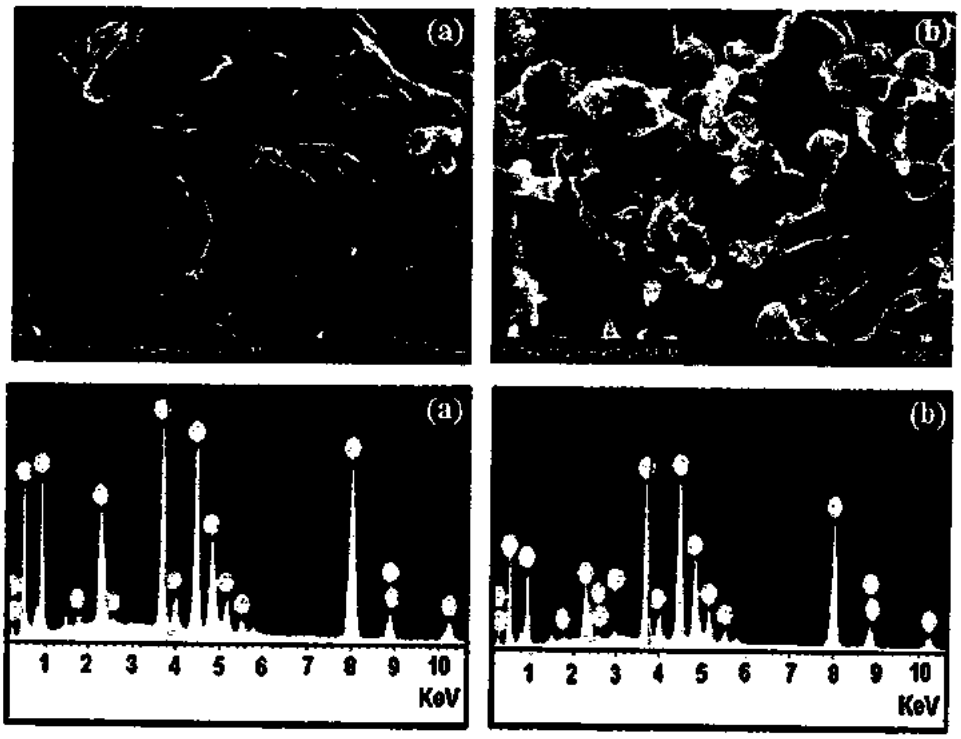

Fig. 3. Typical SEM images and EDX spectra of $(Ag)_x$/CuTl-1223 composites with (a) x=0 and (b) x=2.0 wt%.

Table 1
Elemental analysis by EDX of $(Ag)_x$/CuTl-1223 composites with (a) 0 and (b) 2.0 wt%.

Elements	(a): $x=0$			(b): $x=2.0$ wt%		
	KeV	Mass%	Atom%	KeV	Mass%	Atom%
O K	0.535	20.68	58.05	0.540	20.22	55.96
Ca K	3.695	8.87	9.94	3.702	8.78	9.70
Cu L	0.952	26.93	19.03	0.960	27.48	19.15
Ba L	4.484	31.83	10.41	4.492	30.63	9.88
Tl M	2.325	11.70	2.57	2.315	11.12	2.41
Ag K	–	–	–	1.525	1.77	2.90
Total		100.00	100.00		100.00	100.00

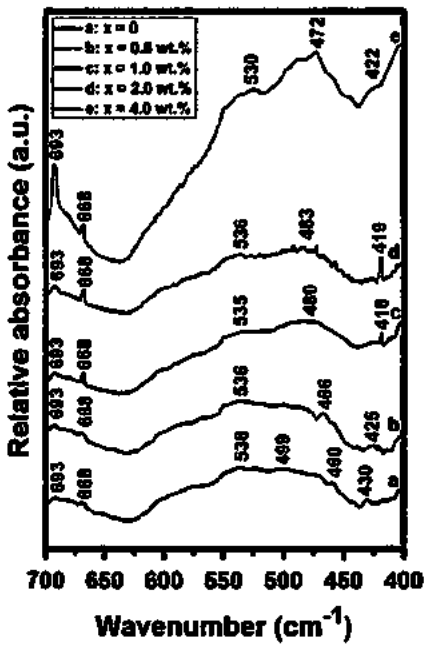

Fig. 4. FTIR absorption spectra of $(Ag)_x$/CuTl-1223 composites with (a) $x=0$, (b) $x=0.5$ wt%, (c) $x=1.0$ wt%, (d) $x=2.0$ wt% and (e) $x=4.0$ wt%.

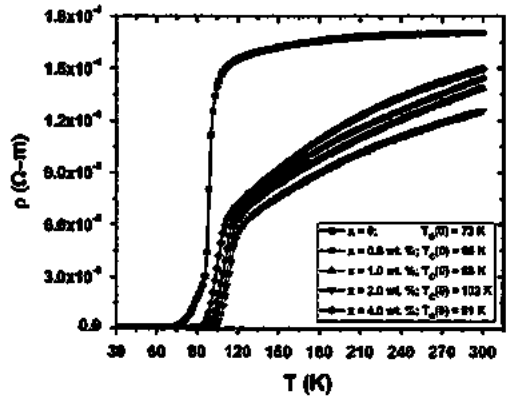

Fig. 5. Resistivity versus temperature measurements of $(Ag)_x$/CuTl-1223 composites with $x=0$, 0.5, 1.0, 2.0 and 4.0 wt%.

The resistivity versus temperature measurements of $(Ag)_x$/CuTl-1223 composites with different contents of nano-Ag particles from $0 \le x \le 4.0$ wt% are shown in Fig. 5. All these samples have shown a metallic variation in the resistivity from room temperature down to onset of superconductivity with zero resistivity critical temperature $\{T_c\ (R=0)\}$ around 73 K, 95 K, 98 K, 102 K and 91 K for $x=0$, 0.5, 1.0, 2.0 and 4.0 wt %, respectively. These measurements show that the value of T_c $(R=0)$ is increased after the addition of nano-Ag particles matrix till $x=2.0$ wt% concentration and then is suppressed on further increase of nanoparticles concentration into CuTl-1223. The increase in T_c is an evidence of improved superconducting volume fraction after nano-Ag particles addition in the host CuTl-1223 superconducting matrix. The improved inter-grain weak-links facilitate the charge carriers transport processes and reduce the energy losses across the grain-boundaries. But the superconducting volume fraction starts to decrease after certain optimum inclusion level of Ag nanoparticles, which causes the suppression of superconductivity parameters. The non-superconducting metallic Ag nanoparticles reduce the superconducting volume fraction beyond certain optimum level of Ag nanoparticles inclusion in superconducting state of CuTl-1223 matrix. After a certain optimum level of Ag nanoparticles addition, the agglomeration and segregation of these nanoparticles result in the reduction of T_c by various mechanisms like scattering, pair-breaking, etc. [39,40]. Still, there are many issues to be addressed in future studies like homogeneous and uniniform distribution of Ag nanoparticles at the inter-grain boundaries of the host CuTl-1223 superconducting matrix. The effects on the superconductivity of the host $(Cu_{0.5}Tl_{0.5})$ $Ba_2Ca_nCu_{n+1}O_{2n+4-\delta}$ superconducting family with addition of different sizes and concentrations of nanoparticles and their response in applied magnetic field will also be addressed in our future research work in this area.

4. Conclusion

Ag nanoparticles are metallic in nature and their influence on structural and superconducting properties of CuTl-1223 matrix has been investigated thoroughly to locate the optimal conditions for the enhanced superconducting parameters. The addition of nano-Ag particles in the host CuTl-1223 superconducting matrix shows no change in the stoichiometry and crystal structure. The added Ag nanoparticles occupy inter-crystallite sites and improve the weak links. This improvement leads to the enhancement of superconducting properties of $(Ag)_x$/CuTl-1223 composite matrix, increased inter-grains coupling and superconducting volume fraction. The systematic increase in T_c and decrease in $\rho_{300\,K}$ (Ω-cm) of $(Ag)_x$/CuTl-1223 composites after addition of Ag nanoparticles has been observed up to some optimum level of concentration which is $x=2.0$ wt%. Suppression of superconducting properties after the addition of the nanoparticles beyond this optimum level has been observed, which is probably due to degradation of samples quality, non homogeneous distribution of Ag nanoparticles causing agglomeration and segregation at the grain-boundaries of host CuTl-1223 matrix. Electrically Conductive nature of metallic Ag nanoparticles is responsible for the reduction in normal state resistivity and improvement in superconducting volume fraction due to their facilitating

behavior for charge carrier transport across the grains in bulk superconducting matrix.

Acknowledgments

We are thankful to the Higher Education Commission (HEC) of Pakistan for continuous financial support. We are also highly grateful to Dr. Nawazish A. Khan and Prof. Qiu Xiang Gang for providing the characterization facilities at Material Science Laboratory, Department of Physics QAU Islamabad, Pakistan and Beijing National Laboratory of Condensed Matter Physics, Institute of Physics (IOP), Chinese Academy of Sciences (CAS) Beijing, China.

References

[1] Z.Z. Sheng, A.M. Hermann, Nature 332 (1988) 55–58.
[2] H. Ihara, Physica C 364–365 (2001) 289–297.
[3] H. Ihara, K. Tokiwa, H. Ozawa, M. Hirabayashi, A. Negishi, H. Matsuhata, Y.S. Song, Jpn. J. Appl. Phys. 33 (1994) L503–L506.
[4] V. Pillai, P. Kumar, M.J. Hou, P. Ayyub, D.O. Shah, Adv. Colloid Interface Sci. 55 (1995) 241–269.
[5] G. Malandrino, D.S. Richeson, T.J. Marks, D.C. De Groot, J.L. Schindler, C.R. Kannewurf, Appl. Phys. Lett. 58 (1991) 182–184.
[6] M.L. Chu, H.L. Chang, C. Wang, J.Y. Juang, T.M. Uen, Y.S. Gou, Appl. Phys. Lett. 59 (1991) 1123–1125.
[7] W.L. Oslon, M.M. Eddy, T.W. James, R.B. Hammond, G. Gruner, L. Drabeck, Appl. Phys. Lett. 55 (1989) 188–190.
[8] S.H. Yun, J.Z. Wu, Appl. Phys. Lett. 68 (1996) 862–864.
[9] M. Annabi, F. A. M'chirgui, M. Ben Azzouz, M. Zouaoui, B.e.n. Salem, Physica C 405 (2004) 25–28.
[10] M. Farbod, M.R. Barvandi, Physica C 471 (2011) 112–117.
[11] Z.Y. Jia, H. Tang, Z.Q. Yang, Y.T. Xing, Y.Z. Wang, G.W. Qiao, Physica C 337 (2000) 130–132.
[12] M. Miura, M. Mukaida, K. Matsumoto, Y. Yoshida, A. Ichinose, S. Horii, R. Kita, A. Saito, K. Kaneko, K. Yamada, N. Mori, Physica C 445–448 (2006) 845–848.
[13] X.M. Cui, G.Q. Liu, J. Wang, Z.C. Huang, Y.T. Zhao, B.W. Tao, Y.R. Li, Physica C 466 (2007) 1–4.
[14] Z.H. He, T. Habisreuther, G. Bruchlos, D. Litzkendorf, W. Gawalek, Physica C 356 (2001) 277–284.
[15] M. Mumtaz, N.A. Khan, E.U. Khan, Physica C 470 (2010) 428–434.
[16] N.A. Khan, M. Mumtaz, J. Low Temp. Phys. 151 (2008) 1221–1229.
[17] C. Wang, Z. Gao, L. Wang, Y. Qi, D. Wang, C. Yao, Z. Zhang, Y. Ma, Supercond. Sci. Technol. 23 (2010) 055002.
[18] M. Mumtaz, N.A. Khan, S. Khan, J. Appl. Phys. 107 (2010) 103905.
[19] K. Nadeem, F. Naeem, M. Mumtaz, S. Naeem, A. Jabbar, I. Qasim, N.A. Khan, Ceram. Int. 40 (2014) 13819–13825.
[20] P.E. Kazin, M. Jansen, A. Larrea, G.F. de la Fuente, Y.D. Tretyakov, Physica C 253 (1995) 391–400.
[21] I.E. Agranovski, A.Y. Ilyushechkin, I.S. Altman, T.E. Bostrom, M. Choi, Physica C 434 (2006) 115–120.
[22] S. Pavard, C. Villard, D. Bourgault, R. Tournier, Supercond. Sci. Technol. 11 (1998) 1359–1366.
[23] M.M. Elokret, R. Awad, A.A. El-Ghany, A.A. Shama, A. El-wanis, J. Supercond. Nov. Magn. 24 (2011) 1345–1352.
[24] N.H. Mohammad, A.I. Abou-Aly, R. Awad, I.H. Ibrahim, M. Roumie, M. Rekaby, J. Low Temp. Phys. 172 (2013) 234–255.
[25] A. Mellekh, M. Zouaoui, F. Ben Azzouz, M. Annabi, M. Ben Salem, Solid State Commun. 140 (2006) 318–323.
[26] A. Ghattas, M. Annabi, M. Zouaoui, F. Ben Azzouz, M. Ben Salem, Physica C 468 (2008) 31–38.
[27] A.H. Li, M. Ionescu, H.K. Liu, T. Silver, X.L. Wang, S.X. Dou, IEEE Trans. Appl. Supercond. 15 (2005) 3046–3049.
[28] K.J. Song, S.W. Kim, C. Park, J.K. Chung, J.S. Yang, J.H. Joo, R.K. Ko, H.S. Ha, H.S. Kim, D.W. Ha, S.S. Oh, E.Y. Lee, Y.K. Kwon, IEEE Trans. Appl. Supercond. 15 (2005) 3288–3291.
[29] V. Bartůněk, O. Smrčková, J. Supercond. Nov. Magn. 24 (2011) 1241–1244.
[30] W. Abdeen, N.H. Mohammed, R. Awad, S.A. Mahmoud, M. Hasebbo, J. Supercond. Nov. Magn. 26 (2013) 3235–3245.
[31] W. Kong, A.K. Koh, R. Abd-Shukor, Sains Malays. 38 (2009) 419–422.
[32] M. Mumtaz, M. Zubair, N.A. Khan, K. Nadeem, Ceram. Int. 40 (2014) 6655–6662.
[33] M. Mumtaz, N.A. Khan, S. Abbas, K. Shehzad, Ceram. Int. 40 (2014) 4187–4191.
[34] N.A. Khan, M. Mumtaz, K. Sabeeh, M.I.A. Khan, M. Ahmad, Physica C 407 (2004) 103–114.
[35] N.A. Khan, M. Mumtaz, Eur. Phys. J. Appl. Phys. 38 (2007) 47–51.
[36] M. Mumtaz, M. Kamran, K. Nadeem, A. Jabbar, N.A. Khan, A. Saleem, S.T. Hussain, M. Kamran, Low Temp. Phys./Fiz. Nizk. Temp. 39 (2013) 806–813.
[37] M. Mumtaz, N.A. Khan, Supercond. Sci. Technol. 21 (2008) 065015.
[38] M. Mumtaz, N.A. Khan, Phys. Scr. 80 (2009) 025702.
[39] J.C. Zhang, F.Q. Liu, G.S. Cheng, J.X. Shang, J.Z. Liu, S.X. Cao, Z.X. Liu, Phys. Lett. A 201 (1995) 70–76.
[40] P.F. Miceli, J.M. Tarascon, L.H. Greene, H.P. Barbou, F.J. Rotella, J.D. Jorgensen, Phys. Rev. B 37 (1988) 5932–5935.

JOURNAL OF APPLIED PHYSICS 116, 103911 (2014)

Activation energy and excess conductivity analysis of $(Ag)_x$/CuTl-1223 nano-superconductor composites

Ghulam Hussain,[1] Abdul Jabbar,[1] Irfan Qasim,[1] M. Mumtaz,[1,a)] K. Nadeem,[1] M. Zubair,[1] S. Qamar Abbas,[2] and A. A. Khurram[3]
[1]*Materials Research Laboratory, Department of Physics FBAS, International Islamic University (IIU), Islamabad 44000, Pakistan*
[2]*Materials Science Lab, Department of Physics, Quaid-i-Azam University, Islamabad 45320, Pakistan*
[3]*Experimental Physics Labs, National Centre for Physics, Islamabad, Pakistan*

(Received 30 June 2014; accepted 27 August 2014; published online 12 September 2014)

Silver (Ag) nanoparticles were added into $(Cu_{0.5}Tl_{0.5})Ba_2Ca_2Cu_3O_{10-\delta}$ (CuTl-1223) high T_c superconducting matrix to get $(Ag)_x$/CuTl-1223, $x = 0$, 0.5, 1.0, 2.0, and 4 wt. %, nano-superconductor composites. The activation energy {U (eV)} and zero resistivity critical temperature {T_c (0)} were increased with increasing contents of Ag nanoparticles in (CuTl-1223) phase up to $x = 2.0$ wt. %. The increase of activation energy is most probably due to interaction of carriers with the metallic Ag nanoparticles present at grain boundaries of the host CuTl-1223 superconducting matrix. The systematic increase in T_c (0) and gradual decrease in normal state resistivity {ρ_{300K} (Ω cm)} may be due to improved inter-grains coupling by filling up the voids and pores with the inclusion of metallic Ag nanoparticles at the grain-boundaries. There are two possible mechanisms associated with the inclusion of Ag nanoparticles, one is the formation of non-superconducting regions causing the increase of activation energy and other (dominating) is the improved inter-grains connectivity promoting T_c (0). The microscopic parameters (i.e., zero temperature coherence length along c-axis {ξ_c (0)}, inter-layer coupling (J), inter-grain coupling (α), etc.) deduced from the fluctuation induced conductivity analysis reasonably explained the experimental findings. © *2014 AIP Publishing LLC*. [http://dx.doi.org/10.1063/1.4895051]

I. INTRODUCTION

The impact of superconducting materials from their application point of view can be estimated from the values of superconducting critical parameters (i.e., critical temperature T_c, critical current density J_c, critical magnetic field, H_c) and CuTl-based high temperature superconducting family has the highest values of these critical parameters after Hg-based superconductor.[1,2] The main advantage for the selection of CuTl-1223 superconducting matrix is its ambient synthesis conditions especially pressure along with higher values of critical parameters.[3–6] But the performance of these compounds is badly affected by inter-grains voids, inhomogeneous micro-defects, etc., present in their bulk form. In polycrystalline bulk samples, the inter-granular superconducting transport properties have become limited by the weak-links caused by the grain-boundaries and the intra-granular critical current is impeded principally by the thermally activated flux flow at high temperatures and in applied magnetic fields. One of the most suitable and convenient way to address this issue is the inclusion of metallic nanoparticles at grain-boundaries of superconducting granular bulk materials for filling the pores and healing up the cracks to improve the weak-links and superconducting volume fraction. The second very important issue is the vortex motions in the applied magnetic field, which can easily damage the superconductivity. To avoid this situation of vortex motion and to improve the infield superconducting transport properties, it is necessary to introduce artificial pinning centers in the superconducting matrices apart from those which occur naturally.[3–14] Different methods such as high energy ions irradiation,[15] chemical doping, and different types of additives were reported in the literature for this purpose.[16–18] Nano-additives of different kinds in various high temperature superconductor matrices have shown positive effects on superconducting properties.[10,11,18–20] These additives improve the inter-grain connectivity by filling the pores and healing up the cracks as well as pinning ability acting as additional artificial pinning centers.[21–23] Significant improvement in superconducting parameters was observed by the inclusion of nanostructures of noble metals such as Ag and Au in many superconducting systems.[24–26] The addition of different sizes and concentrations of silver (Ag) nanoparticles in YBCO superconductor showed monotonic increase in superconducting properties particularly J_c by improving crystal structure in the form of higher crystallinity, crystallites connectivity, and superconducting volume fraction.[19,27] The improvement in inter-grains connectivity as well as in J_c was observed with increasing concentration of nano-Ag particles in Bi-2223 system.[24,25] The improvement in mechanical properties of (Bi Pb)-Sr-Ca-Cu-O superconducting matrix was also observed by the inclusion of nano-Ag particles that was due to cementing effects of these additives at the grain-boundaries.[28,29] The inclusion of different metals oxides MgO, ZrO_2, and Al_2O_3 nanoparticles in Bi-based systems showed the improvement in superconducting parameters.[30–32] The presence of MgO nanoparticles in

a)E-mail: mmumtaz75@yahoo.com. Telephone: +92-51-9019926. Fax: +92-51-9210256.

Bi-2212 matrix has increased the transition sharpness and the superconductor volume fraction.[33] Significant improvement in infield J_c was observed by the addition of Al_2O_3 nanoparticles in $YBa_2Cu_3O_y$ superconducting phase without affecting the structural symmetry, which can be rendered to the existence of enhanced flux pinning centers.[34] The volume pinning force density, onset temperature of dissipation, activation energy, transport properties, and J_c in applied magnetic field were also improved by the addition of nano-Al_2O_3 particles in polycrystalline (Bi, Pb)–2223 system.[35] The excess conductivity analysis showed that the width of three dimensional (3D) conductivity region was reduced by the addition of nano-Al_2O_3 particles in polycrystalline (Bi, Pb)–2223 superconducting matrix, which was explained on the basis of scattering of mobile carriers across the insulating nano-Al_2O_3 particles present at the grain-boundaries.[36] Mechanical properties were improved by the inclusion of Ag nanoparticles at the grain-boundaries of Bi-based superconducting systems acting as pores fillers and improving the inter-grains connections.[37] The superconducting transport properties were sufficiently improved by the addition of nano-Ag particles in $Bi_{1.8}Pb_{0.4}Sr_2Ca_2Cu_3O_{10+\delta}$ superconducting matrix without affecting the crystal structure, indicating more efficient pinning mechanisms.[38] The size of flux pinning centers is important in enhancing J_c and particle with size closer to the coherence length showed higher transport J_c.[39] But the size and homogeneous distribution of nanoparticles at the grain-boundaries of the bulk high T_c superconducting matrix are the real challenge.[40–45]

In this paper, we reported the effects of Ag nanoparticles addition on structural and superconducting transport properties of CuTl-1223 matrix. Series of samples added with different nano-Ag particles contents ($0 \sim 4.0$ wt. %) were synthesized to find out the optimal concentration level of these nanoparticles to obtain the maximum improvement in superconducting transport properties without affecting the crystal structure of CuTl-1223 phase. We used Ginzburg-Landau equations, Aslamazov-Larkin (AL), Lawrence-Doniach (LD), and Maki-Thompson (MT) models[46–49] on the experimental data to obtain the different microscopic superconducting parameters for understanding and explaining the role of Ag nanoparticles on superconductivity of host CuTl-1223 phase in detail. We tried to unfold the role of nano-Ag particles addition in CuTl-1223 matrix with a central objective to determine the dominant source and mechanism taking place affecting the superconducting properties.

II. EXPERIMENTAL DETAILS

Nano-superconductor $(Ag)_x$/CuTl-1223 ($x = 0$, 0.5, 1.0, 2.0, and 4.0 wt. %) composites were synthesized by the solid-state reaction method. Initially, $Ba(NO_3)_2$, $Ca(NO_3)_2$, and Cu(CN) compounds were mixed in appropriate ratios and ground in an agate mortar and pestle for about 2 h to prepare $Cu_{0.5}Ba_2Ca_2Cu_3O_{10-\delta}$ precursor material. The ground material was loaded in quartz boats for firing in chamber furnace at 860 °C for 24 h. The furnace is switched off for cooling the samples gradually to room temperature. The firing steps were repeated twice following 1 h intermediate grinding each time to get the fine $Cu_{0.5}Ba_2Ca_2Cu_3O_{10-\delta}$ precursor material. The nano-particles of Ag were prepared separately by sol-gel method. Later on, at second stage appropriate amount of thallium oxide (Tl_2O_3) and Ag nanoparticles of 35 nm in size with different wt. % were mixed in this precursor material and then ground again for 1 h. This ground material was pressed under 3.8 tons/cm^2 pressure in the form of pellets and the pellets were enclosed in gold capsules for sintering at 860 °C for 10 min followed by quenching to room temperature to get $(Ag)_x$/CuTl-1223 nano-superconductor composites.

The structure and phase purity of the samples were examined by X-ray diffraction (XRD) (D/Max IIIC Rigaku with a CuKα source of wavelength 1.54056 Å). The cell parameters were determined by cell refinement computer program. The morphology was examined by scanning electron microscopy (SEM) and composition was determined by energy dispersive x-ray (EDX) spectroscopy of the materials. The dc-resistivity versus temperature measurements of the samples were carried out by conventional four-probe method with the help of commercial Physical Properties Measurement System (PPMS) manufactured by Quantum Design. Four low resistance contacts with silver paint were made on the surface of the slab shaped samples with dimensions of $1.2 \times 1.0 \times 4.0$ mm^3. The temperature stability was kept 2 mK during the transport measurements on these samples.

III. THEORETICAL MODELS FOR ANALYSIS OF EXPERIMENTAL DATA

The fluctuation induced conductivity (FIC) analysis is a state of the art theoretical analysis on the experimental data of cuprates, which can play an essential role to unearth the intrinsic properties of the material well above the zero resistivity critical temperature T_c (0), where the Cooper pair formation starts and imparts additional conductivity. There are two models that can give a very nice picture of superconducting fluctuations in inter-grains and intra-grains regions. AL Model can be used for fluctuations both in inter-grains and intra-grains regions, while LD can be used only for fluctuations in intra-grains regions of layered superconductors.

The excess conductivity is given by

$$\Delta\sigma(T) = \left[\frac{\rho_N(T) - \rho(T)}{\rho_N(T)\rho(T)}\right], \quad (1)$$

where ρ(T) is the actually measured resistivity, and $\rho_N(T) = \alpha + \beta T$ is the normal-state resistivity of the samples extrapolated to resistivity at 0 K; the α is a intercept and β is a slope of straight line. The excess conductivity generally comprises on two contributions, i.e.,

$$\Delta\sigma = \Delta\sigma_{AL+}\Delta\sigma_{MT}. \quad (2)$$

The first term, according to AL model, is derived using microscopic approach by mean field theory and is considered as a direct contribution to paraconductivity.[50] The fluctuation induced conductivity according to AL theory is given as

$$\Delta\sigma_{AL} = A\varepsilon^{-1}, \tag{3}$$

where A is the fluctuation amplitude, λ is dimensional exponent, $\varepsilon = \ln\left[\frac{T-T_c^{mf}}{T_c^{mf}}\right]$ is the reduced temperature, and T_c^{mf} is usually referred to as the mean field critical temperature, which separates the mean field region from the critical region[50,51] and is determined from the point of inflection of the temperature derivative of resistivity ($d\rho/dT$). The exponent λ determines the dimensionality of the superconducting fluctuations and is given as $\lambda = 2-D/2$; $\lambda = 3/2$, 1, and 1/2 for one, two, and three dimensional fluctuations, respectively. The fluctuation amplitude A for one, two, and three dimensional fluctuations is given by[52]

$$A = \begin{cases} \dfrac{e^2}{32\hbar\xi_c(0)} & \text{for 3D fluctuation} \\ \dfrac{e^2}{16\hbar d} & \text{for 2D fluctuation} \\ \dfrac{e^2\xi_c(0)}{32\hbar s} & \text{for 1D fluctuation} \end{cases}, \tag{4}$$

where e is the electron charge, $\xi_c(0)$ is the zero-temperature coherence length along c-axis, $\hbar$ is the reduced Planks constant, d is the effective layer thickness of the 2D system, and s is the cross-sectional area of the 1D system.

The physical microscopic parameters calculated from FIC analysis depend strongly on the dimensionality of the fluctuations. LD introduced the concept of interlayer coupling via Josephson coupling of adjacent layers close to the critical temperature.[47] According to the LD model for layered superconductors, the excess conductivity $\Delta\sigma_{LD}$ due to superconducting fluctuations is

$$\Delta\sigma_{LD} = \frac{e^2}{16\hbar d\varepsilon}(1+2\alpha)^{\frac{-1}{2}}, \tag{5}$$

where $\alpha = \frac{a_o}{\varepsilon} = \left[\frac{\xi_c(0)}{d}\right]^2 2\varepsilon^{-1}$ is a dimensionless coupling parameter. The cross-over from 2D to 3D is mainly found above the critical temperature known as cross-over temperature (T_o). The system has 3D fluctuations below this temperature and 2D fluctuations above this temperature, and the expression for T_o according to the LD model is

$$T_o = T_c\left[1+\left(\frac{2\xi_c(0)}{d}\right)^2\right]. \tag{6}$$

The second term is the inter-layer coupling strength, which is related to the reduced temperature ε by $J = \varepsilon/4$. In layered superconductors at very low temperature close to zero resistivity temperature $\xi_c > d$, where d is the distance between the conducting layers of adjacent unit cells (d is approximately equal to the c-axis lattice parameter of the unit cell). The advantage of LD model is that it reduces to 2D AL model for large ε values where the coupling constant J is quite small and to 3D AL model for small ε values where in some cases the coupling constant J is quite strong. The above theoretical AL and LD models are based on direct contribution to the excess conductivity.

There is one more region of fluctuations close to critical temperature for which $\lambda = 1/3$ and is known as critical region.[53] Some authors have observed a cross-over to 0D fluctuations with critical exponent 2. In high T_c superconductors, the MT contribution, which is due to the interaction of fluctuating Cooper pairs with normal electrons, is not easily observable. Since the MT contribution is negligible in cuprate superconductors.[54] This indirect contribution to the excess conductivity was calculated by Maki[48] and later on modified by Thompson.[49] For layered superconductors, Hikami and Larkin[55] derived the indirect contribution to the excess conductivity independently by Maki and Thompson.[56,57]

$$\Delta\sigma_{MT} = \left[\frac{e^2}{8\hbar d\varepsilon\left(1-\frac{\varepsilon}{\delta}\right)}\right]\ln\left[\left(\frac{\delta}{\alpha}\right)\left(\frac{1+\alpha+(1+2\alpha)^{1/2}}{1+\delta+(1+2\delta)^{1/2}}\right)\right], \tag{7}$$

where $\delta = \left[\left(\frac{4\xi_c(0)}{d}\right)^2\left(\frac{\kappa_B T\tau_\varphi}{\pi\hbar}\right)\right]$ is the pair-breaking parameter, which was introduced by Thompson[49] and is related to inelastic scattering processes that limit the phase relaxation time τ_φ of the quasiparticles involved in MT process[58] and κ_B is the Boltzmann constant. In s-wave BCS superconductor, nonmagnetic impurities neither change T_c nor affect AL and MT terms, while on the other hand in P or d-wave superconductor these impurities may act pair-breaking and are supposed to suppress the MT contribution.[58]

The cross-over from 2D AL to 0D MT fluctuation contribution occurs at a temperature where $\delta \approx \alpha$, which gives[59]

$$\varepsilon_o \approx \left[\frac{\pi\hbar}{1.203\left(\frac{\ell}{\xi_{ab}}\right)(8\kappa_B T\tau_\varphi)}\right]. \tag{8}$$

When the mean free path ℓ of the Cooper pairs approaches to ξ_{ab} at a particular temperature then they (Cooper pairs) are broken to Fermions and at that temperature the phase relaxation time can be estimated as

$$\tau_\varphi \approx \left[\frac{\pi\hbar}{8\kappa_B T\varepsilon_o}\right]. \tag{9}$$

Fermi velocity of the carriers can also be estimated by

$$V_F \approx \left[\frac{5\pi\kappa_B T_c\xi_c(0)}{2K\hbar}\right], \tag{10}$$

where $K \approx 0.12$ is a co-efficient of proportionality.[60] Fermi energy of the carriers can also be calculated by

$$E_F = \frac{1}{2}m^* V_F^2, \tag{11}$$

where $m^* = 10\,m_o$ is the effective mass of the carrier and m_o is the carrier free mass.[61]

Ginzburg and Landau observed the existence of two types of superconductors depending upon the energy of the interface between the normal and superconducting states. In

1957, Alexei Abrikosov used Ginzburg–Landau theory to explain the experimental data of superconducting alloys and thin films. He found that high magnetic field in a type-II superconductor penetrates in the form of magnetic flux quanta Φ_o. The thermodynamics magnetic field B_c (0) can be estimated from Ginzburg number N_G, which is given by[61,62]

$$N_G = \left|\frac{T_G - T_c^{inf}}{T_c^{inf}}\right| = \frac{1}{2}\left(\frac{\kappa_B T_c \gamma}{\{B_c(0)\}^2\{\xi_c(0)\}^3}\right)^2, \quad (12)$$

where $\gamma = \frac{\xi_{ab}(0)}{\xi_c(0)}$ is anisotropy whose estimated value is "4" for CuTl-1223 superconducting system[63,64] and T_G is the cross-over temperature from critical to 3D regime. We can estimate penetration depth $\lambda_{p.d.}$, lower critical magnetic field $B_{c1}(0)$, upper critical magnetic field $B_{c2}(0)$, and the critical current density $J_c(0)$ after determination of $B_c(0)$ as follows:[65–68]

$$B_c = \frac{\Phi_o}{2\sqrt{2}\pi\lambda_{p.d.}\xi_{ab}(0)}, \quad (13)$$

$$B_{c1} = \frac{B_c}{\kappa\sqrt{2}}\ln\kappa, \quad (14)$$

$$B_{c2} = \sqrt{2}\kappa B_c, \quad (15)$$

$$J_c = \frac{4\kappa B_{c1}}{3\sqrt{3}\lambda_{p.d.}\ln\kappa}, \quad (16)$$

where $\Phi_o = \frac{h}{2e}$ is the flux quantum and κ is the GL parameter, which is the ratio of penetration depth to coherence length.

IV. RESULTS AND DISCUSSION

Typical representative XRD patterns of $(Ag)_x$/CuTl-1223 composite samples with x = 0 and 2 wt. % are shown in Fig. 1 and in the inset the XRD pattern of Ag nanoparticles is also shown. Most of the diffraction peaks are well indexed according to tetragonal structure following the P4/mmm space group indicating the dominance of CuTl-1223 phase along with very few peaks of some other superconducting phases as well as some unknown impurities. There is no change observed in the overall XRD pattern of Ag nanoparticles added samples, which gives a clue about the occupancy of these nanoparticles at the inter-crystallites boundaries of CuTl-1223 superconducting matrix. The presence of these nanoparticles at the grain-boundaries can help to heal up the voids and to improve the inter-grains weak-links as well as superconducting volume fraction due to which over all superconducting properties can be enhanced. The unit cell parameters calculated by computer software (crystal) program are a = 4.45 Å, c = 14.46 Å for x = 0, and a = 4.46 Å, c = 14.96 Å for x = 2%, respectively, and the stoichiometry of the CuTl-1223 matrix remains unaffected after the inclusion of these nanoparticles. However, the slight shift in the diffraction peaks to lower angles is possibly due to the uniform strain produced in the materials after the addition of Ag nanoparticles. The slight increase in the c-axis length may also be due to increase of oxygen (O_δ) contents with the addition of these nanoparticles, which can relax the apical bond length. The XRD pattern of Ag nanoparticles shown in the inset of Fig. 1 illustrates the characteristic peaks in accordance with the standard data values in ICDD record. The prominent peaks are indexed with FCC structure and the average size of Ag nanoparticles calculated by Sherrer's formula ($t = \frac{0.9\lambda}{B\cos\theta_B}$) is around 35 nm. The XRD analysis shows neatly indexed (1 1 1), (2 0 0), (2 2 0), and (3 1 1) planes and sharpness of the peaks confirms that Ag nanoparticles are well crystallized. Major phase is observed at (h k l) value of (3 1 1) and no peak of other impurity crystalline phases is detected. The lattice parameter is calculated to be a = 4.09 Å for FCC pattern of Ag nanoparticles.

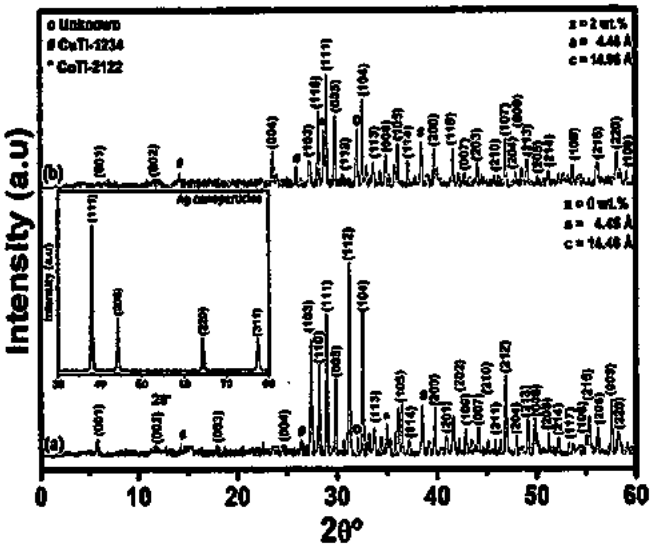

FIG. 1. XRD patterns of $(Ag)_x$/CuTl-1223 composites with (a) x = 0 and (b) x = 2 wt. %. (In the inset, the XRD pattern of Ag nanoparticles is shown.)

The morphology of material was examined by SEM images of $(Ag)_x$/CuTl-1223 samples with x = 0 and 2 wt. % as shown in Fig. 2. The presence of these nanoparticles at the inter-grains boundaries can be easily visualized that can heal up the inter-grains voids and improve the inter-grains weak-links in CuTl-1223 superconductor matrix. It can be verified from the SEM and XRD that the nano-Ag particles just occupy the interstitial spaces and do not enter into the structure of CuTl-1223 phase. In the literature, similar findings were reported by different groups working in this area.[34,69] The mass percentages of different elements present in $(Ag)_x$/CuTl-1223 composition determined by the EDX analysis for x = 0 and 2 wt. % are listed in Table I.

The dc-resistivity versus temperature measurements of $(Ag)_x$/CuTl-1223 composites samples with various concentrations (i.e., x = 0, 0.5, 1.0, 2.0, and 4.0 wt. %) of Ag nanoparticles are shown in Fig. 3. The Arrhenius plots of $(Ag)_x$/CuTl-1223 composites, activation energy U (eV), ρ_{300K} (Ω cm), and T_c (0) versus x (i.e., Ag nanoparticles contents in wt. %) are also shown in the inset of Fig. 3. The variation in dc-resistivity with temperature is metallic from room temperature down to onset of superconductivity for all these composite samples with T_c (0) around 73, 95, 98, 102, and 91 K for x = 0, 0.5, 1.0, 2.0, and 4.0 wt. %, respectively. The

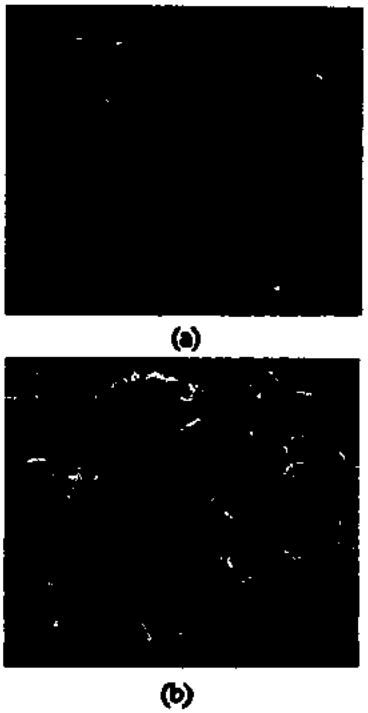

FIG. 2. Scanning electron micrographs (SEMs) of $(Ag)_x$/CuTl-1223 composites with (a) x = 0 and (b) x = 2 wt. %.

value of T_c (0) increases with increasing Ag nanoparticles contents up to x = 2.0 wt. % and then start to decrease beyond this limit of these nanoparticles contents in host CuTl-1223 superconducting matrix. The inclusion of Ag nanoparticles enhances the superconducting properties without affecting the tetragonal structure and stoichiometry of the host CuTl-1223. The improvement in superconducting properties of $(Ag)_x$/CuTl-1223 composites is most likely due to enhanced inter-grains coupling and increased superconducting volume fraction by the addition of metallic Ag nanoparticles at the inter-crystallite sites in the samples. The systematic decrease in the normal state resistivity at 300 K and also a systematic increase in T_c (0) with the gradual increase of these nanoparticles contents in the composites up to x = 2.0 wt. % are shown in the inset of Fig. 3. The systematic decrease in normal state resistivity and monotonic increase in T_c (0) with gradual increase of these nanoparticles contents are most probably due to somehow

TABLE I. Elemental analysis by EDX of $(Ag)_x$/CuTl-1223composites with (a) 0 wt. % and (b) 2.0 wt. % of Ag nanoparticles.

	(a) x = 0 wt. % Ag nanoparticles			(b) x = 2.0 wt. % Ag nanoparticles		
Elements	KeV	Mass%	Atom%	KeV	Mass%	Atom%
O K	0.535	20.68	58.05	0.540	20.22	55.96
Ca K	3.695	8.87	9.94	3.702	8.78	9.70
Cu L	0.952	26.93	19.03	0.960	27.48	19.15
Ba L	4.484	31.83	10.41	4.492	30.63	9.88
Tl M	2.325	11.70	2.57	2.315	11.12	2.41
Ag K	...	...	...	1.525	1.77	2.90
Total	...	100.00	100.00	...	100.00	100.00

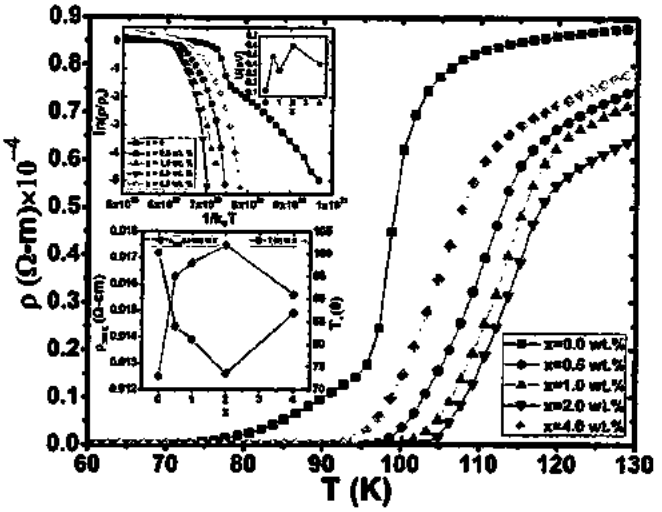

FIG. 3. Resistivity versus temperature measurements of (Ag)x/CuTl-1223 composites with x = 0, 0.5, 1.0, 2.0, and 4 wt. %. (In the inset are given the Arrhenius plots of (Ag)x/CuTl-1223 composites with x = 0, 0.5, 1.0, 2.0, and 4 wt. %, T_c (0), ρ_{300K} (Ω cm), and activation energy U (eV) versus x, i.e., Ag nanoparticles contents in wt. %.)

homogeneous and uniform distribution of these nanoparticles at the grain-boundaries of the bulk CuTl-1223 material. The improved inter-grains weak-links facilitate the charge carriers transport processes and reduce the energy losses across the grain-boundaries. But after a certain optimum level of Ag nanoparticles addition, the agglomeration and segregation of nanoparticles at the grain-boundaries reduce the superconducting volume fraction and degrade the quality of the samples resulting in the reduction of T_c (0) by various mechanisms like scattering, pair-breaking, etc.[70,71] The activation energy required to overcome the barrier can be calculated by the Arrhenius law $\rho = \rho_o \exp\left(\frac{-U}{\kappa_B T}\right)$, where U is the activation energy and κ_B is the Boltzmann constant, for superconductors.[72–74] We used the superconducting transition region for the calculation of activation energy and observed an increase in the activation energy with the increase of Ag nanoparticles contents in the composites. Theories of high T_c superconductors so far developed believe that pairs of electrons (Cooper pairs) move freely without activation energy, which is the main source of superconductivity. In the present article, it is observed that activation energy has been increased with the increase of Ag nanoparticles contents in the composites. When Cooper pairs interact with non-superconducting metallic Ag nanoparticles at the grain-boundaries during their transport in superconducting state of the host CuTl-1223 matrix, the pairing interaction is weakened and Cooper pairs could not exist in the low energy state and energy dissipation takes place. But on the other hand, the presence of metallic Ag nanoparticles at grain-boundaries can increase the inter-grain connectivity by filling the voids and pores, which may be the cause of an increase in T_c (0). Therefore, there are two possible mechanisms in play due to the inclusion of Ag nanoparticles, one is the formation of non-superconducting regions causing increase in activation energy and the other (dominating) is the improved inter-grain connectivity promoting T_c (0) of the samples.

The FIC analysis on the dc-resistivity versus temperature data of $(Ag)_x$/CuTl-1223 composite samples has been carried out by using the above mentioned models in the neighborhood of transition region. The plots of ln ($\Delta\sigma$) versus ln (ε) of $(Ag)_x$/CuTl-1223 composites samples with x = 0, 0.5, 1.0, 2.0, and 4.0 wt. % are shown in Figs. 4(a)–4(e). The experimentally measured dc-resistivity ρ (Ω m) along with a straight line extrapolated from the

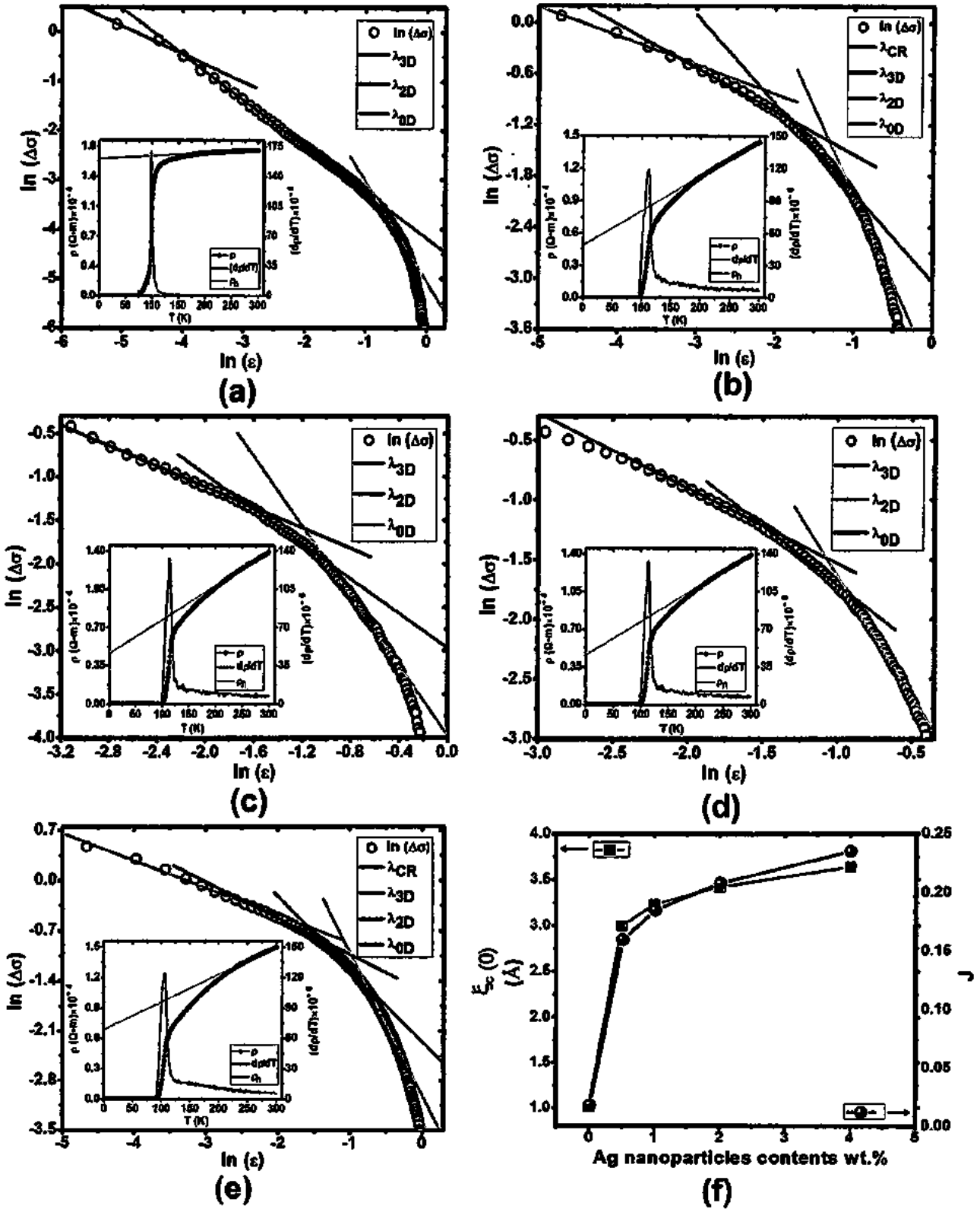

FIG. 4. (a)-(f) ln ($\Delta\sigma$) versus ln (ε) plots of $(Ag)_x$/CuTl-1223 composites; (a) x = 0, (b) x = 0.5, (c) x = 1.0, (d) x = 2.0, and (e) x = 4.0 wt. % (In the insets are shown the experimentally measured dc-resistivity ρ (Ω m), derivative ($d\rho/dT$) of dc-resistivity versus temperature, and the straight line extrapolated from the room temperature "300 K" normal state resistivity to 0 K). (f) Zero temperature coherence length ξ_c (0) and coupling constant (J) versus Ag nanoparticles contents wt. % in $(Ag)_x$/CuTl-1223 composites.

TABLE II. Widths of critical 3D, 2D, and SW fluctuation regions deduced from the fitting of experimental-resistivity versus temperature data of $(Ag)_x$/CuTl-1223 composites samples with x = 0, 0.5, 1.0, 2.0, and 4.0 wt. %.

Samples x = wt.%	λ_{CR}	λ_{3D}	λ_{2D}	λ_{SW}	$T_{CR\text{-}3D} = T_G$ (K)	$T_{3D\text{-}2D}$ (K)	$T_{2D\text{-}SW}$ (K)	T_c^{mf} (K)	T* (K)	$\alpha = \rho_n(0\,K)$ (Ω m) $\times 10^{-4}$	$W = \Delta T_c$ (K)
0	...	0.56	0.93	2.03	98.59	99.79	141.88	97.99	170.74	1.60	3.65
0.5	0.34	0.50	1.04	2.04	116.38	130.43	151.50	112.37	169.56	0.485	11.00
1.0	...	0.58	0.99	2.01	126.42	134.44	154.51	113.37	189.63	0.495	10.51
2.0	...	0.62	0.99	2.01	132.44	139.46	160.53	115.38	185.61	0.495	9.10
4.0	0.36	0.50	1.01	2.00	116.38	131.43	155.51	106.35	184.61	0.689	10.00

TABLE III. The superconductivity parameters deduced from the FIC analysis of $(Ag)_x$/CuTl-1223 composites samples with x = 0, 0.5, 1.0, 2.0, and 4.0 wt. %.

Samples x = wt.%	ξ_c (0) (Å)	J	N_G	$\lambda_{p.d}$ (Å)	$B_c(0)$ (T)	B_{c1} (T)	B_{c2} (T)	κ	$J_c(0) \times 10^3$ (A/cm^2)	$V_F \times 10^7$ (m/s)	E_F (eV)	$\tau_\varphi \times 10^{-14}$ (s)
0	1.01	0.018	0.350	547.18	2.661	0.194	128.7	34.19	2.6462	0.63	0.183	2.25
0.5	3.00	0.160	0.225	2181.0	0.667	0.017	128.7	136.3	0.1664	2.44	0.123	3.34
1.0	3.23	0.185	0.290	2551.0	0.570	0.012	128.7	159.4	0.1216	2.71	0.122	3.38
2.0	3.42	0.208	0.298	2747.4	0.530	0.011	128.7	171.7	0.1048	2.99	0.126	3.27
4.0	3.64	0.235	0.278	3134.9	0.464	0.008	128.7	195.9	0.0805	2.83	0.151	2.73

room temperature (300 K) normal state resistivity to 0 K and derivative ($d\rho/dT$) of dc-resistivity versus temperature are shown in the insets of Figs. 4(a)–4(e). The variation of zero temperature coherence length ξ_c (0) along c-axis and inter-layer coupling constant (J) versus Ag nanoparticles contents (wt. %) in $(Ag)_x$/CuTl-1223 composites is also shown in Fig. 4(f). The superconducting fluctuations start at a particular temperature denoted by T* from where the experimental dc-resistivity curve deviates from the straight line extrapolated from the room temperature normal state resistivity to 0 K. The values of T* are around 170.74, 169.56, 189.63, 185.61, and 184. 61 K for x = 0, 0.5, 1.0, 2.0, and 4.0 wt. %, respectively. The increase in T* shows that the superconducting fluctuations start at higher temperature values, which may be due to improved inter-grains coupling, zero temperature coherence length along c-axis $\xi_c(0)$, superconducting volume fraction, etc., after the inclusion of Ag nanoparticles in the host CuTl-1223 matrix. The values of critical exponents (λ_{CR}, λ_{3D}, λ_{2D}, and λ_{0D}), cross-over temperatures ($T_{CR\text{-}3D} = T_G$, $T_{3D\text{-}2D}$, and $T_{2D\text{-}SW}$), mean field critical temperature (T_c^{mf}), T*, inter-grains coupling constant (α), and superconducting transition width ($W = \Delta T_c$) deduced from the FIC analysis on dc-resistivity versus temperature data of $(Ag)_x$/CuTl-1223 composites samples are given in Table II. All the cross-over temperatures, T_c^{mf}, and T* have been shifted to the higher values, which is theoretical evidence of improved superconducting properties of the host CuTl-1223 matrix after the addition of Ag nanoparticles. The decreased values of "α" is a theoretical evidence of improved non-superconducting inter-grains boundaries in the composites samples, which is in accordance to the increase in the activation energy after Ag nanoparticles addition. The increase in $W = \Delta T_c$ is another evidence of energy loss across the metallic non-superconducting grain-boundaries in $(Ag)_x$/CuTl-1223 composites samples. The various superconductivity parameters (i.e., $\xi_c(0)$, J, N_G, $\lambda_{p.d}$, $B_c(0)$, B_{c1}, B_{c2}, κ, J_c, V_F, E_F, and τ_φ) deduced from the FIC analysis of $(Ag)_x$/CuTl-1223 composites samples with x = 0, 0.5, 1.0, 2.0, and 4.0 wt.% are given in Table III. The values of N_G, B_c (0), B_{c1}, B_{c2}, J_c, and E_F have been decreased marginally, whereas ξ_c (0), J, $\lambda_{p.d.}$, κ, V_F, E_F, and τ_φ have been enhanced after the inclusion of Ag nanoparticles. It is witnessed that $\xi_c(0)$ has been improved with the increase of "J" values after the addition of Ag nanoparticles in CuTl-1223 superconducting matrix. The cross-over from 2D to 0D (from LD to MT contribution) takes place at a particular temperature where the mean free path *l* of the carriers approaches to ξ_{ab} and Cooper pairs are broken to fermions. The values of phase relaxation time τ_φ calculated at this particular temperature are 2.25×10^{-14}, 3.34×10^{-14}, 3.38×10^{-14}, 3.27×10^{-14}, and 2.73×10^{-14} s for x = 0, 0.5, 1.0, 2.0, and 4.0 wt. %, respectively. The increase of τ_φ is an evidence of long life of Cooper pairs at certain high temperature values after Ag nanoparticles addition in CuTl-1223 superconducting matrix. The increase of ξ_c (0), J, V_F, and E_F shows the improvement of superconducting properties, which may be due to healing up the voids and improving the inter-grains connectivity after the inclusion of Ag nanoparticles. This also shows that the samples become more isotropic after the addition Ag nanoparticles. The variation in microscopic parameters extracted from FIC analysis explained the overall improvement of superconductivity up to certain optimum level of Ag nanoparticles addition in CuTl-1223 superconducting matrix.

V. CONCLUSION

Series of $(Ag)_x$/CuTl-1223 composites samples were successfully synthesized by solid-state reaction to confirm their reproducibility. The crystal structure of the host CuTl-1223 superconducting matrix was not affected with the addition of Ag nanoparticles. The activation energy {U (eV)} and zero resistivity critical temperature {T_c (0)} were increased with increasing contents of Ag nanoparticles up to x = 2.0 wt. %. The increase of activation energy is most probably due to interaction of mobile free carriers with the non-superconducting metallic Ag nanoparticles present at the grain-boundaries of the host CuTl-1223 matrix. The systematic increase in T_c (0) and decrease in $\rho_{300\,K}$ (Ω cm) may

be due to improved inter-grains coupling by healing up the voids after the addition of Ag nanoparticles at the grain-boundaries of CuTl-1223 phase. The suppression of superconducting properties after the addition of these nanoparticles beyond the certain optimum level is most probably due to agglomeration and segregation of these nanoparticles at the grain-boundaries. The microscopic parameters deduced from the FIC analysis are in accordance with the experimental findings. The increase in ξ_c (0) and J indicates the reduction of anisotropic nature of CuTl-1223 phase after Ag nanoparticles addition.

ACKNOWLEDGMENTS

We acknowledge Higher Education Commission (HEC) of Pakistan for continuous financial support. We are also highly thankful to Dr. Nawazish A. Khan and Professor Qiu Xiang-Gang for providing the characterization facilities at Materials Science Laboratory, Department of Physics QAU Islamabad, Pakistan and Beijing National Laboratory of Condensed Matter Physics, Institute of Physics (IOP), Chinese Academy of Sciences (CAS) Beijing, China.

[1]N. A. Khan, Y. Sekita, H. Ihara, and A. Maqsood, Physica C 377, 43–48 (2002).
[2]E. V. Antipov, A. M. Abakumov, and S. N. Putilin, Supercond. Sci. Technol. 15, R31 (2002).
[3]N. A. Khan, Y. Sekita, F. Tateai, T. Kojima, K. Ishida, N. Terada, and H. Ihara, Physica C 320, 39 (1999).
[4]K. Tokiwa, H. Aota, C. Kunugi, K. Tanaka, Y. Tanaka, A. Iyo, H. Ihara, and T. Watanabe, Physica B 284–288, 1077 (2000).
[5]K. Tanaka, A. Iyo, N. Terada, K. Tokiwa, S. Miyashita, Y. Tanaka, T. Tsukamoto, S. K. Agarwal, T. Watanabe, and H. Ihara, Phys. Rev. B 63, 064508 (2001).
[6]N. A. Khan and M. Mumtaz, Phys. Rev. B 77, 054507 (2008).
[7]T. Matsushita, Supercond. Sci. Technol. 13, 730 (2000).
[8]D. Larbalestier, A. Gurevich, D. M. Feldmann, and A. Polyanski, Nature 414, 368 (2001).
[9]R. Goswami, T. J. Haugan, P. N. Barnes, G. Spanos, and R. L. Holtz, Physica C 470, 318 (2010).
[10]F. Ben Azzouz, M. Zouaoui, A. Mellekh, M. Annabi, G. Van Tendeloo, and M. Ben Salem, Physica C 455, 19 (2007).
[11]Y. Zhao, C. H. Chen, and J. Wang, Supercond. Sci. Technol. 18, S43 (2005).
[12]J. Plain, T. Puig, F. Sandiumenge, X. Obradors, and J. Rabier, Phys. Rev. B 65, 104526 (2002).
[13]S. Y. Chen and I. G. Chen, Supercond. Sci. Technol. 17, 71 (2004).
[14]N. Hari Babu, E. S. Reddy, D. A. Cardwell, A. M. Campbell, C. D. Tarrant, and K. R. Schneider, Appl. Phys. Lett. 83, 4806 (2003).
[15]K. Nakashima, N. Chikumoto, A. Ibi, S. Miyata, Y. Yamada, T. Kubo, A. Suzuki, and T. Terai, Physica C 463–465, 665 (2007).
[16]A. Hamrita, F. Ben Azzouz, W. Dachraoui, and M. Ben Salem, J. Supercond. Nov. Magn. 26, 879 (2013).
[17]S. Patnaik, A. Gurevich, S. D. Bu, S. D. Kaushik, J. Choi, C. B. Eom, and D. C. Larbalestier, Phys. Rev. B 70, 064503 (2004).
[18]S. Dadras, Y. Liu, Y. S. Chai, V. Daadmehr, and K. H. Kim, Physica C 469, 55 (2009).
[19]M. Farbod and R. M. Batvandi, Physica C 471, 112 (2011).
[20]I. E. Agranovski, Y. Ilyushechkin, I. S. Altman, T. E. Bostrom, and M. Choi, Physica C 434, 115 (2006).
[21]A. Goyal, S. Kang, K. J. Leonard, P. M. Martin, A. A. Gapud, M. Varela, M. Paranthaman, A. O. Ijaduola, E. D. Specht, J. R. Thompson, D. K. Christen, S. J. Pennycook, and F. A. List, Supercond. Sci. Technol. 18, 1533 (2005).
[22]P. Mele, K. Matsumoto, T. Horide, A. Ichinose, M. Mukaida, Y. Y. Oshida, S. Horii, and R. Kita, Supercond. Sci. Technol. 21, 032002 (2008).
[23]K. Yamada, A. Ichinose, S. Horii, H. Kai, R. Teranishi, M. Mukaida, R. Kita, S. Kato, Y. Yoshida, K. Matsumoto, and S. Toh, Physica C 468, 1638 (2008).
[24]M. N. Khan, M. Khizar, and B. N. Mukeshev, Physica B 321, 257 (2002).
[25]H. Najafpour, S. H. R. Shojaei, and S. M. Shojaeiu, J. Supercond. Novel Magn. 23, 487 (2010).
[26]F. Martínez-Julián, S. Ricart, A. Pomar, M. Coll, P. Abellán, F. Sandiumenge, M. J. Casanove, X. Obradors, T. Puig, I. Pastoriza-Santos, and L. M. Liz-Marzán, J. Nanosci. Nanotechnol. 11(4), 3245–3255 (2011).
[27]A. H. Li, M. Ionescu, H. K. Liu, T. Silver, X. L. Wang, and S. X. Dou, IEEE Trans. Appl. Supercond. 15, 2 (2005).
[28]S. Şakiroğlu and K. Kocabaş, J. Supercond. Nov. Magn. 24, 1321 (2011).
[29]W. Abdeen, N. h. Mohammed, R. Awad, S. A. Mahmoud, and M. Hasebbo, J. Supercond. Novel Magn. 26, 3235–3245 (2013).
[30]W. D. Huang, W. H. Song, Z. Cui, B. Zhao, M. H. Pu, X. C. Wu, Y. P. Sun, and J. J. Du, Phys. Status Solidi A 179, 189 (2000).
[31]Z. Y. Jia, H. Tang, Z. Q. Yang, Y. T. Xing, Y. Z. Wang, and G. W. Qiao, Physica C 337, 130 (2000).
[32]M. Annabi, A. M'chirgui, F. Ben Azzouz, M. Zouaoui, and M. Ben Salem, Physica C 405, 25 (2004).
[33]K. Christova, A. Manov, J. Nybus, U. Thisted, O. Herstad, S. E. Foss, K. N. Haugen, and K. Fossheim, J. Alloys Compd. 340, 1 (2002).
[34]A. Mellekh, M. Zouaoui, F. Ben Azzouz, M. Annabi, and M. Ben Salem, Solid State Commun. 140, 318 (2006).
[35]A. Ghattas, F. Ben Azzouz, M. Annabi, M. Zouaoui, and M. Ben Salem, J. Phys.: Conf. Ser. 97, 012175 (2008).
[36]M. Annabi, A. Ghattas, M. Zouaoui, F. Ben Azzouz, and M. Ben Salem, J. Phys.: Conf. Ser. 150, 052008 (2009).
[37]V. Bartůněk and O. Smrčková, J. Supercond. Novel Magn. 24(4), 1241–1244 (2011).
[38]R. Mawassi, S. Marhaba, M. Roumié, R. Awad, M. Korek, and I. Hassan, J. Supercond. Novel Magn. 27(5), 1131–1142 (2014).
[39]R. Abd-Shukor, N. A. A. Yahya, and A. Agail, AIP Conf. Proc. 1588, 35 (2014).
[40]J. Gutiérrez, A. Llordés, J. Gazquez, M. Gibert, N. Romá, S. Ricart, A. Pomar, F. Sandiumenge, N. Mestres, T. Puig, and X. Obradors, Nature Mater. 6, 367 (2007).
[41]T. G. Holesinger, L. Civale, B. Maiorov, D. M. Feldmann, J. Y. Coulter, J. Miller, V. A. Maroni, Z. J. Chen, D. C. Larbalestier, R. Feenstra, X. P. Li, M. B. Huang, T. Kodenkandath, W. Zhang, M. W. Rupich, and A. P. Malozemoff, Adv. Mater. 20, 391 (2008).
[42]S. Engel, T. Thersleff, R. Huhne, L. Schultz, and B. Holzapfel, Appl. Phys. Lett. 90, 102505 (2007).
[43]T. Puig, J. Gutierrez, A. Pomar, A. Llordes, J. Gazquez, S. Ricart, F. Sandiumenge, and X. Obradors, Supercond. Sci. Technol. 21, 034008 (2008).
[44]N. M. Strickland, N. J. Long, E. F. Talantsev, P. Hoefakker, J. Xia, M. W. Rupich, T. Kodenkandath, W. Zhang, X. Li, and Y. Huang, Physica C 468, 183 (2008).
[45]M. Miura, M. Yoshizumi, T. Izumi, and Y. Shiohara, Supercond. Sci. Technol. 23, 014013 (2010).
[46]L. G. Aslamazov and A. L. Larkin, Phys. Lett. A 26, 238 (1968).
[47]W. E. Lawrence and S. Doniach, in *Proceedings of the 12th International Conference on Low Temperature Physics, Keigaku, Tokyo, (1971)*, p. 361.
[48]K. Maki, Prog. Theor. Phys. 39, 897 (1968).
[49]R. S. Thompson, Phys. Rev. B 1, 327 (1970).
[50]A. L. Solovjov, H.-U. Habermeier, and T. Haage, Low Temp. Phys. 28, 17–24 (2002).
[51]C. A. C. Passos, M. T. D. Orlando, J. L. Passamai, Jr., E. V. L. de Mello, H. P. S. Correa, and L. G. Martinez, Phys. Rev. B 74, 094514 (2006).
[52]S. R. Ghorbani and M. Rahmati Tarki, J. Supercond. Novel Magn. 27, 749 (2014).
[53]S. H. Han, Yu. Eltsev, and Ö. Rapp, Phys. Rev. B 61, 11776 (2000).
[54]S. H. Naqib, J. R. Cooper, J. L. Tallon, R. S. Islam, and R. A. Chakalov, Phys. Rev. B 71, 054502 (2005).
[55]S. Hikami and A. I. Larkin, Mod. Phys. Lett. B 2, 693 (1988).
[56]K. Maki and R. S. Thompson, Phys. Rev. B 39, 2767 (1989).
[57]P. K. Nayak and S. Ravi, Supercond. Sci. Technol. 19, 1209 (2006).
[58]W. Lang, G. Heine, W. Kula, and R. Sobolewski, Phys. Rev. B 51, 9180 (1995).
[59]A. L. Solovjov, H.-U. Habermeier, T. Haage, and F. Nizk, Low Temp. Phys. 28, 99 (2002).
[60]J. Bardeen, L. N. Cooper, and J. R. Schrieffer, Phys. Rev. 108, 1175 (1957).

[61]A. L. Solovjov, V. M. Dmitriev, and H.-U. Habermeier, Phys. Rev. B **55**, 8551 (1997).
[62]H. Ihara, A. Iyo, K. Tanaka, K. Tokiwa, K. Ishida, N. Terada, M. Tokumoto, Y. Sekita, T. Tsukamoto, T. Watanabe, and M. Umeda, Physica C **282–287**, 1973 (1997).
[63]H. Hayakawa and Y. Enomoto, "Advances in Superconductivity VIII," in *Proceedings of the 8th International Symposium on Superconductivity, Hamamatsu (1995)*, pp. 247–249.
[64]A. K. Ghosh and A. N. Basu, Phys. Rev. B **59**, 11193–11196 (1999).
[65]A. I. Abou Aly, I. H. Ibrahim, R. Awad, A. El-Harizy, and A. Khalaf, J. Supercond. Novel Magn. **23**(7), 1325–1332 (2010).
[66]J. F. Annet, *Superconductivity, Superfluids and Condensates* (Oxford University Press, London, 2004).
[67]N. A. Khan and S. Ahmad, J. Appl. Phys. **112**, 033912 (2012).
[68]N. H. Mohammad, A. I. Abou-Aly, R. Awad, I. H. Ibrahim, M. Roumie, and M. Rekaby, J. Low Temp. Phys. **172**, 234–255 (2013).
[69]J. C. Zhang, F. Q. Liu, G. S. Cheng, J. X. Shang, J. Z. Liu, S. X. Cao, and Z. X. Liu, Phys. Lett. A **201**, 70 (1995).
[70]P. F. Miceli, J. M. Tarascon, L. H. Greene, H. P. Barbou, F. J. Rotella, and J. D. Jorgensen, Phys. Rev. B **37**, 5932 (1988).
[71]S. J. Feng, J. Ma, H. D. Zhou, G. Li, L. Shi, Y. Liu, J. Fang, and X. G. Li, Physica C **386**, 22 (2003).
[72]A. J. Batista-Leyva, M. T. D. Orlando, L. Rivero, R. Cobas, and E. Altshuler, Physica C **383**, 365 (2003).
[73]M. Tinkham, Phys. Rev. Lett. **61**, 1658 (1988).
[74]T. M. Palstra, B. Batlogg, L. F. Schneemeyer, and J. V. Waszczak, Phys. Rev. Lett. **61**, 1662 (1988).

Journal of Alloys and Compounds 618 (2015) 110–114

Contents lists available at ScienceDirect

Journal of Alloys and Compounds

journal homepage: www.elsevier.com/locate/jalcom

Synthesis and superconducting properties of $(Au)_x$/CuTl-1223 composites

Abdul Jabbar [a], Irfan Qasim [a], Khalid M. Khan [a], Zulqurnain Ali [b], K. Nadeem [a], M. Mumtaz [a,*]

[a] Materials Research Laboratory, Department of Physics, FBAS, International Islamic University (IIU), Islamabad 44000, Pakistan
[b] Department of Physics, Air University E-9 Complex, Islamabad, Pakistan

ARTICLE INFO

Article history:
Received 14 March 2014
Received in revised form 18 August 2014
Accepted 19 August 2014
Available online 27 August 2014

Keywords:
$(Au)_x$/CuTl-1223 nano-superconductor composites
Au nanoparticles
Grain-boundaries
Inter-grain connectivity

ABSTRACT

We explored the feasibility of synthesizing $(Au)_x/(Cu_{0.5}Tl_{0.5})Ba_2Ca_2Cu_3O_{10-\delta}$ ($(Au)_x$/CuTl-1223); $x = 0$, 0.5, 1.0, and 1.5 wt.%, nano-superconductor composites by two steps solid-state reaction. We investigated the effect of gold (Au) nanoparticles on the structural and superconducting properties of CuTl-1223 matrix. These composites were characterized by X-ray diffraction (XRD), scanning electron microscopy (SEM), Fourier transform infrared (FTIR) absorption spectroscopy, ac-susceptibility (χ_{ac}) and dc-resistivity (ρ) measurements. We observed the tendency of Au nanoparticles to occupy the inter-granular spaces (grain-boundaries) as the tetragonal structure of CuTl-1223 superconducting matrix remained unaltered after the addition of Au nanoparticles. The improvement in the superconducting properties after the addition of Au nanoparticles can be attributed to an increase in the inter-grains connectivity by healing up the inter-grains voids and pores by these nanoparticles. The improved inter-grains connections can facilitate the carriers transport across the inter-crystallite sites. But the superconducting volume fraction starts to be decreased after certain optimum inclusion level of Au nanoparticles, which causes the suppression of superconductivity parameters. The non-superconducting metallic Au nanoparticles reduce the superconducting volume fraction beyond certain optimum level of Au nanoparticles inclusion in superconducting state of CuTl-1223 matrix.

1. Introduction

$(Cu_{0.5}Tl_{0.5})Ba_2Ca_2Cu_3O_{10-\delta}$ (CuTl-1223) is the most attractive phase of $Cu_{0.5}Tl_{0.5}Ba_2Ca_{n-1}Cu_nO_{2n+4-\delta}$ (CuTl-12(n−1)n): $n = 2$, 3, 4,..., high temperature superconductors (HTSCs) family due to its higher critical temperature, lower superconducting anisotropy, and longer coherence length along c-axis [1]. But the performance of this compound in bulk form may be reduced mainly due to inter-grain voids and pores. The presence of inter-grain weak links diminishes the critical parameters of superconductivity. Also the motion of the vortices in HTSCs creates resistance and causes energy dissipation. These facts restrict their applications such as superconducting magnetic field sensors. There has been consistent effort in enhancing the current carrying capacity of the superconducting materials, which may be achieved by incorporating extended defects acting as pinning centers. The effect of pinning center is at its best when their sizes are of the order of coherence length [2]. It is important that the density of these pinning centers should be as high as 10^{11} cm^{-2}. Large number of defects created to achieve large densities of pinning centers degrades the superconducting properties. It was found that magnetic nanoparticles may act as efficient pinning centers at much lower density [3,4,2]. In order to enhance the transport properties, many attempts have been made to introduce artificial defects of nanometer order of magnitude into the bulk HTSCs as extra effective pinning centers under applied field, such as by nanoparticles addition in the bulk or by post-annealing of the superconducting samples [5,6]. The superconducting properties of granular bulk HTSCs can be improved by the inclusion of nanoparticles at the grain-boundaries. But the size and homogenous distribution of nanoparticles at the grain-boundaries of the bulk HTSCs is the real challenge [7–13]. The sizes and densities of defects are critical factors to be adjusted for effective vortex pinning. It was observed that magnetic nanoparticles such as Fe_2O_3 embedded into the bulk HTSCs act as efficient pinning centers [14,3]. The improvement of critical current density (J_c) was observed in Bi-based HTSC by the inclusion of MgO, ZrO_2 and Al_2O_3 nanoparticles [15–17]. Transmission Electron Microscopy (TEM) has showed that MgO nanoparticles could be embedded within the superconducting Bi-2212 grains [18]. The presence of MgO nanoparticles has increased the transition sharpness, and the superconductor volume fraction in the sample

* Corresponding author. Tel.: +92 51 9019926 (Office); fax: +92 51 9210256.
E-mail address: mmumtaz75@yahoo.com (M. Mumtaz).

http://dx.doi.org/10.1016/j.jallcom.2014.08.162
0925-8388/

[18]. The addition of ZrO_2 and ZnO nanoparticles in Gd-123 superconductor has improved the critical current density (J_c) but suppressed zero resistivity critical temperature (T_c) [19]. The addition of SnO_2 nanoparticles increases the microstructure density and reduces porosity among the grains of $Cu_{0.5}Tl_{0.5}$-1223 superconductor [20]. The improvement of T_c, J_c and phase volume fraction is obtained on different concentrations of ZnO nanoparticles in $(Cu_{0.5}Tl_{0.25}Pb_{0.25})$-1223 [21]. The superconducting properties (i.e. T_c, J_c, etc.) of CuTl-1223 were enhanced with the addition of CuO, CaO_2 and BaO nanoparticles [22,23]. The addition of nanoparticles like $NiFe_2O_4$, Al_2O_3, ZrO_2, Ag etc. in suitable amount helps in creating the effective flux pinning centers, which can enhance the critical superconductivity parameters [24–26]. The addition of nanostructures of noble metals such as Ag and Au has shown the significant improvement in superconducting parameters in many superconducting systems [27–30]. Increased nano-Ag content in Bi-2223 improves the connectivity among the grains and enhances superconductivity [31,32].

In this article, we have investigated the effect of Au nanoparticles addition on superconducting properties of CuTl-1223 matrix in detail. The present work is concerned with the effect of nano-Au particles addition on the phase formation and characteristics superconducting parameters. We have reported the influence of Au nanoparticles addition on structure, morphology and superconducting transport properties. The main objective of this work is to improve the inter-grains connectivity, superconducting volume fraction, and to investigate their effects on superconductivity. This can be due to the reduction of defects in the form of voids and oxygen deficiencies by filling the voids and pores with these nanoparticles. We have also determined the optimum level of Au nanoparticles inclusion for the maximum improvement in the superconducting properties of CuTl-1223 matrix.

2. Experimental details for sample preparation and characterizations

We used $Ba(NO_3)_2$ (99.50%, UNI-Chem), $Ca(NO_3)_2{\cdot}4H_2O$ (99%, AppliChem), $Cu_2(CN)_2 + H_2O$ (99%, BDH) to synthesize Cu:Ba:Ca:Cu = 0.5:2:2:3 precursor material. These compounds were mixed in appropriate ratios, and were ground in mortar and pestle for about 2 h. The mixture after grinding was put into quartz boat and placed in a chamber furnace for 24 h heat-treatment at 860 °C. The furnace was switched off and the precursor material was cooled down to room temperature after 24 h firing at 860 °C. The fired material was again ground for about one hour and placed into the chamber furnace for second time heat-treatment under the same conditions.

The precursor material after double heat-treatment was mixed with thallium oxide (Tl_2O_3) (99%, BDH) and ground to get $Cu_{0.5}Tl_{0.5}Ba_2Ca_2Cu_3O_{10-\delta}$ superconducting phase. At this stage Au nanoparticles extracted from the colloidal gold solution were also added into the precursor material in appropriate ratios to get the required composition. The precursor material mixed with Tl_2O_3 and Au nanoparticles was ground again for about an hour and then pelletized under 3.8 tons/cm^2 pressure. The pellets were wrapped in gold capsules and sintered at 860 °C for nearly 10 min in pre-heated chamber furnace followed by quenching to room temperature to obtain the final product $(Au)_x/(Cu_{0.5}Tl_{0.5})Ba_2Ca_2Cu_3O_{10-\delta}$ (x = 0, 0.5, 1.0, and 1.5 wt.%) nano-superconductor composites.

These composites samples were characterized by X-ray diffraction (XRD), scanning electron microscopy (SEM), Fourier transform infrared (FTIR) spectroscopy, ac-susceptibility (χ_{ac}) and dc-resistivity (ρ) measurements. The structure and phase purity of the nanoparticles and composites were determined by XRD scans (D/Max IIIC Rigaku with a Cu Kα source of wavelength 1.54056 Å). The cell parameters were determined by cell refinement computer program. The ac-susceptibility measurements were carried out by the mutual inductance method using an SR530 Lock-in Amplifier at a frequency of 270 Hz with H_{AC} = 0.07 Oe of primary coil. The conventional four-probe technique was used for dc-resistivity measurements with the help of commercial Physical Properties Measurement System (PPMS) manufactured by Quantum Design and the value of current during the measurements was kept 10 μA. Four low resistance contacts with silver paint were made on the surface of the slab shaped samples with dimensions of 1.2 × 1.0 × 4.0 mm^3. The dc-resistivity measurements were carried out during the heating cycle from 30 K to room temperature i.e. nearly 300 K. The rate of heating was kept 1 K/min during these measurements. The morphology of the material has been studied through Scanning Electron Microscopy (SEM) by JOEL Jed-2300. The Fourier transform infrared (FTIR) absorption measurements were carried out using by Nicolet 5700 Fourier Transform Infrared (FTIR) spectrometer in the 400–700 cm^{-1} wave number range. The FTIR absorption spectroscopy was carried out using KBr as a background material.

3. Results and discussions

The XRD pattern of Au nanoparticles exhibits prominent sharp diffraction peaks indexed with face-centered cubic (FCC) structure as shown in Fig. 1. Also XRD analysis showed the distinct diffraction peaks at 38.22°, 44.35°, 64.67°, and 77.62°, which corresponds to (111), (200), (220) and (311) planes respectively of FCC structure. The FCC structures of Au nanoparticles matches well with the database of Joint Committee on Powder Diffraction Standards (JCPDS No. 00-004-0784), revealing that the synthesized Au nanoparticles are composed of pure crystalline gold. The Au nanoparticles size can be calculated by Sherrer's formula and the average size of Au nanoparticles is about 39 nm. The XRD patterns of $(Au)_x$/CuTl-1223 for x = 0, 0.5 and 1.0 wt.% composites are shown in Fig. 2. The composites have shown the tetragonal structure following P4/mmm symmetry. Majority of the diffraction peaks corresponds to the CuTl-1223 phase with lattice parameters a = 4.20 Å and c = 15.31 Å for x = 0. The addition of Au nanoparticles in the CuTl-1223 has slightly decreased the cell parameters lengths i.e. a = 4.20 Å, c = 15.30 Å and a = 4.19 Å and c = 15.25 Å for x = 0.5 and x = 1.0 wt.% respectively, which might be due to variation of oxygen contents or stress–strains in the polycrystalline lattice. The slight decrease in the c-axis length is most probably due to the compression of apical bond length by the effect of variation in O_δ oxygen and stresses produced by the addition of these nanoparticles. The un-indexed peaks are possibly due to presence of some impurities and some other superconducting phases as given in the in set of Fig. 2.

The surface morphology was examined by SEM images of the $(Au)_x$/CuTl-1223 composites as shown in Fig. 3. The granular nature and porosity of samples are obvious from these micrographs. There is an improvement in the inter-grain connectivity as well as in the grain size after the addition of Au nanoparticles in the matrix. The main problem is the inhomogeneous mixing of Au nanoparticles in the matrix.

The FTIR absorption spectra of $(Au)_x$/CuTl-1223 (x = 0, 0.5, 1.0 and 1.5 wt.%) composites in the range from 400 to 700 cm^{-1} and the unit cell of CuTl-1223 superconductor are shown in Fig. 4(a and b). The nomenclature of different oxygen atoms in the unit cell of CuTl-1223 superconductor has been demonstrated in Fig. 4(b). The bands in the range from 400 to 540 cm^{-1} are associated with the apical oxygen atoms and in the range around from 541 to 600 cm^{-1} are associated with CuO_2 planar oxygen atoms. The bands in the range from 670 to 700 cm^{-1} are associated with O_δ atoms in the charge reservoir layer [33–35]. But in the pure

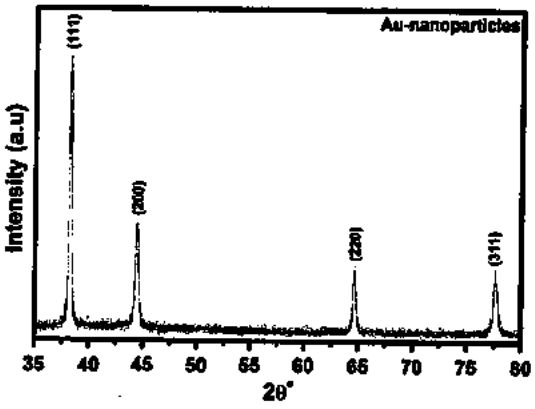

Fig. 1. XRD pattern of gold (Au) nanoparticles.

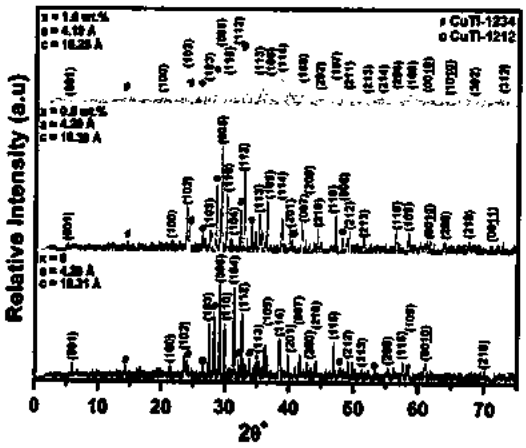

Fig. 2. XRD patterns of $(Au)_x$/CuTl-1223 composites with $x = 0$, 0.5, 1.0 wt.%.

$Cu_{0.5}Tl_{0.5}Ba_2Ca_2Cu_3O_{10-\delta}$ samples, the apical oxygen modes of type Tl–O_A–Cu(2) and Cu(1)–O_A–Cu(2) are observed around 427 cm^{-1} and 458–492 cm^{-1} and CuO_2 planner mode is around 526 cm^{-1}. The apical mode of type Tl–O_A–Cu(2) is slightly softened from 427 cm^{-1} to 420–421 cm^{-1} and the position Cu(1)–O_A–Cu(2) remained around 458–490 cm^{-1} after nano-Au particles addition. The position of Cu(2)–O_P–Cu(2) planner oxygen mode is also slightly softened from 526 cm^{-1} to 520 cm^{-1} after nano-Au particles addition. The slight shifting of the positions of different oxygen modes represents the presence of strains in the materials, which affects the bond lengths. But overall the positions of all the oxygen vibrational phonon modes remained almost unaltered after nano-Au particles addition in CuTl-1223 matrix. This gives us a clue that nano-Au particles did not substitute any atom in the unit cell and remained at the grain-boundaries of $(Au)_x$/CuTl-1223 composites.

The resistivity versus temperature measurements of $(Au)_x$/CuTl-1223 ($x = 0$, 0.5, 1.0 and 1.5 wt.%) composites are shown in the Fig. 5. All the samples exhibit metallic behavior in the variation of resistivity versus temperature measurements at high temperatures before superconducting transition temperatures. The variation of T_c (0) and normal state resistivity $\rho_{(300K)}$ (Ω-cm) versus x (i.e. Au contents) is given in the inset of Fig. 5. The value of T_c (0) increases up to $x = 1.0$ wt.% and then decreases, which predicts the optimum inclusion level of Au nanoparticles in CuTl-1223 matrix. The value of T_c has increased from 88 K of un-doped sample ($x = 0$) to 99 K and 101 K for $x = 0.5$ and 1.0 wt.% addition of Au nanoparticles respectively. The value of T_c has decreased to 96 K for $x = 1.5$ wt.%. The initial increase in T_c is possibly due to improved weak links among the superconducting grains by healing up the voids and pores with nano-Au particles. But after certain optimum inclusion level of Au-nanoparticles, the superconducting volume fraction start to be decreased, which causes the suppression of superconductivity parameters. Normally the zero resistivity critical temperature T_c (0) of cuprates depends upon the carriers' density in their CuO_2 planes [36]. The carriers supplied by the charge reservoir layer to the CuO_2 planes depend upon the oxygen contents in the charge reservoir layer [37]. As with the addition of Au nanoparticles, the T_c (0) increases, this is due to optimization of carriers' density in the CuO_2 planes supplied by the charge reservoir layer. Therefore, it is obvious that the oxygen contents in the charge reservoir layer depends upon Au nanoparticles contents in the CuTl-1223 matrix. The superconducting volume fraction can also be improved by the optimization of oxygen, which can occupy the oxygen vacancies in the bulk CuTl-1223 matrix. The initial increase in T_c (0) is possibly due to increased superconducting volume fraction and improved weak links by the addition of nano-Au particles at the grain-boundaries. The decreasing trend in T_c (0) beyond certain optimum limit of Au nanoparticles addition may be due to agglomeration and segregation of these nanoparticles at the grain-boundaries in the bulk CuTl-1223 matrix, which can cause the degradation of the quality of the samples and reduces the superconducting bulk volume fraction of the samples. The initial increase in T_c (0) is possibly due to improved weak-links among the superconducting grains by nano-Au particles at the grain-boundaries. But after certain optimum inclusion level of Au-nanoparticles, the superconducting volume fraction and density of mobile charge carriers start to be decreased, which causes the suppression of superconductivity parameters. The normal state resistivity is very high for the sample with $x = 1.5$, which is the finger print of the enhanced scattering cross-section of the carriers and reduced superconducting volume fraction. Usually, the trend in the variation of superconductivity onset temperature T_c^{onset} (K) is similar to zero resistivity critical temperature T_c (0) of cuprates, which depends upon the carriers' density in CuO_2 planes.

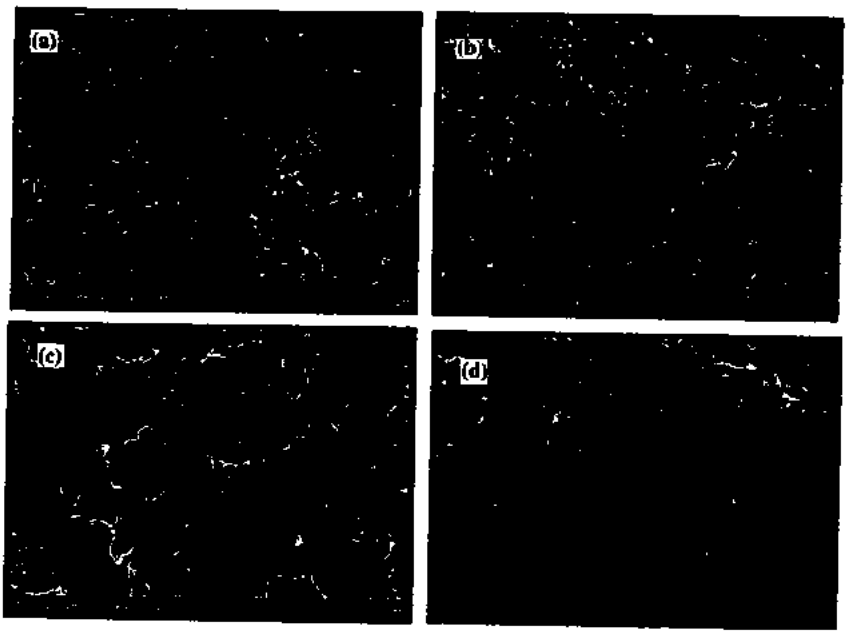

Fig. 3. Typical SEM images of $(Au)_x$/CuTl-1223 composites (a) $x = 0$, (b) $x = 0.5$ wt.%, (c) $x = 1.0$ wt.% and (d) $x = 1.5$ wt.%.

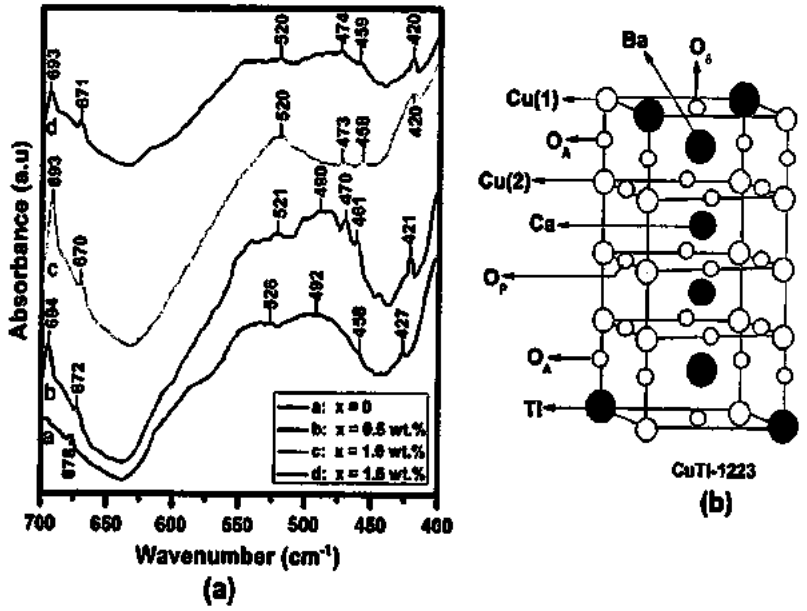

Fig. 4. (a) FTIR absorption spectra of $(Au)_x$/CuTl-1223 composites, (a) $x = 0$, (b) $x = 0.5$ wt.% (c) $x = 1.0$ wt.% and (d) $x = 1.5$ wt.%. (b) Unit cell of CuTl-1223 superconductor.

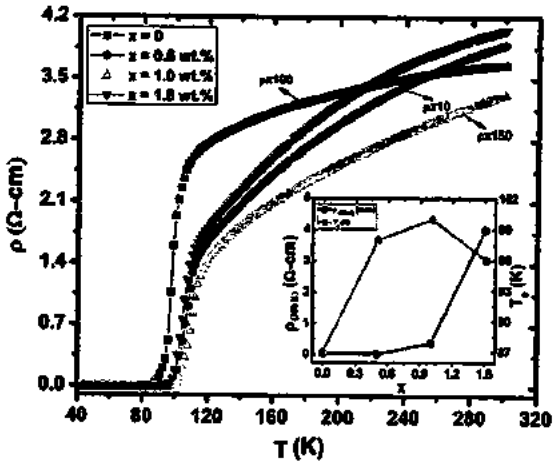

Fig. 5. Resistivity versus temperature measurements of $(Au)_x$/CuTl-1223 composites with $x = 0.0$, 0.5, 1.0 and 1.5 wt.%. In the inset T_c (K) and $\rho_{(300K)}$ (Ω-cm) versus x (i.e. Au nanoparticles contents).

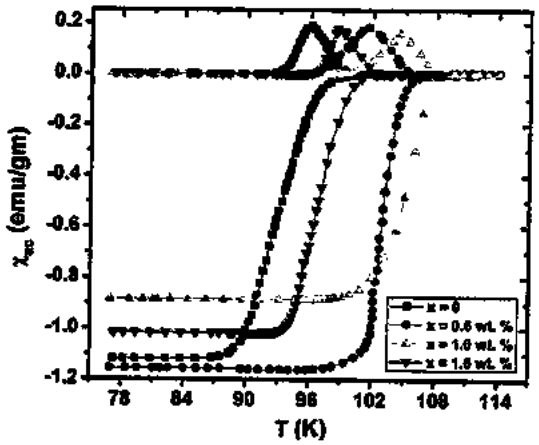

Fig. 6. Ac-susceptibility measurements of $(Au)_x$/CuTl-1223 composites with $x = 0$, 0.5, and 1.0 wt.%.

Superconducting fluctuations near the superconducting transition contribute to the T_c^{onset} (K) and the Au nanoparticles addition may enhance these fluctuations and can affect T_c^{onset} (K) of these composites [38].

Magnetic ac-susceptibility measurements of $(Au)_x$/CuTl-1223 ($x = 0$, 0.5, 1.0 and 1.5 wt.%) composites are shown in Fig. 6. The ac-susceptibility measurements of these samples were carried out in field cooled (FC) conditions by the mutual inductance method using an SR530 Lock-in Amplifier working at a frequency of 270 Hz with $H_{AC} = 0.07$ Oe of primary coil. Single peak above the transition temperature in the ac-susceptibility measurements is observed for all the samples. There are two components of magnetic ac-susceptibility, in-phase component (χ') and out of phase component (χ''). The magnitude of diamagnetism of the superconducting materials is represented by the real part (χ') of the ac-susceptibility and the ac-losses corresponding to the flux penetration into superconductor sample is represented by imaginary part (χ''). The imaginary part of the ac-susceptibility provides the inter-granular contribution and therefore, gives information about the nature of inter-grains weak links and pinning strength [39–41]. The suppression of superconductivity within the grains decreases the magnitude of χ'. It is observed that the onset temperature as well as magnitude of diamagnetism initially increases and then decreases beyond certain optimum limit of Au nanoparticles addition. Similarly, the peak position in χ'' initially shifts to higher temperature values and then shifts to lower temperature values beyond certain optimum limit of Au nanoparticles addition. The value of onset of diamagnetism (T_c^{onset} (K)) increases up to $x = 1.0$ wt.% and then decreases, which predicts the optimum inclusion level of Au nanoparticles in CuTl-1223 matrix for maximum improvement of superconductivity. The initial increase in T_c^{onset} (K) is possibly due to improved superconducting volume fraction and carriers density with the increase of Au nanoparticles. The suppression of T_c^{onset} (K) and diamagnetic signal beyond a certain level of Au nanoparticles inclusion can be due to reduction of superconducting volume fraction and carriers density. The relatively higher density of voids and pores in pure un-added Au nanoparticles samples can be the cause of reduction of superconducting volume fraction and superconductivity. The other defects in the form of oxygen deficiencies can cause the reduction of carriers' density from the optimum level. By the incorporation of

Au nanoparticles at the grain-boundaries, the voids and pores can be filled and can improve the inter-grains weak-links. In this way, we can reduce the defects in the material and can improve the superconducting properties. The enhancement of T_c^{onset} (K) can be the indication of enhanced carriers' density towards optimization after Au nanoparticles addition. This can be due to the reduction of defects in the form of voids and oxygen deficiencies by filling the pores with these nanoparticles. But the non-superconducting metallic Au nanoparticles reduces the superconducting volume fraction in the superconducting state of CuTl-1223 matrix beyond the certain optimum level of Au nanoparticles inclusion i.e. $x = 1.5$ wt.% in this case.

The overall superconducting properties of CuTl-1223 matrix have been improved up to certain optimum level of Au nanoparticles addition that can be attributed to an increase in the inter-grains connectivity and enhanced superconducting volume fraction. The increase in superconducting properties can also be associated with the optimization of carriers' density in the CuO_2 planes supplied by the charge reservoir layer, which depends upon the optimum oxygen contents in the charge reservoir layer. Therefore, we can relate the oxygen contents with Au nanoparticles contents in the CuTl-1223 matrix. We have planned to carry out the infield measurement (i.e. J_c, ρ etc.) to investigate the role of Au nanoparticles as additional flux pining centers. The uniform distribution and controlled size of nanostructures added in the HTSCs matrices are still unresolved problems in this area of research. We are trying to address these issues in our future research work.

4. Conclusion

The effects of gold nanoparticles addition on superconducting properties as well as phase formation of CuTl-1223 matrix were thoroughly studied. We synthesized $(Au)_x$/CuTl-1223 composites successfully by solid-state reaction method. The tetragonal structure of CuTl-1223 matrix remained unaltered after nano-Au particles addition. It provides an evidence of the presence of nano-Au particles at inter-granular spaces (inter-grain boundaries). The SEM micrographs have shown the granular structure with enhanced grain sizes after nano-Au particles addition. The superconducting properties have been overall increased after the nano-Au particles addition but still the control of homogeneous distribution of Au nanoparticles is an unresolved problem. The systematic decrease in normal state resistivity and monotonic increase in T_c (0) with gradual increase of these nanoparticles contents up to certain optimum level is most probably due to somehow homogeneous and uniform distribution of these nanoparticles at the grain-boundaries of the bulk CuTl-1223 material. The improvement in the superconducting properties can be attributed to an increase in the inter-grains connectivity by healing up the inter-grains voids and pores by the addition of Au nanoparticles. The improved inter-grains connections can facilitate the carriers transport across the inter-crystallite sites. But the superconducting volume fraction starts to be reduced after certain optimum inclusion level of Au-nanoparticles, which causes the suppression of superconductivity parameters. The non-superconducting metallic Au nanoparticles reduce the superconducting volume fraction beyond certain optimum level of Au nanoparticles inclusion in superconducting state of CuTl-1223 phase.

Acknowledgements

We are thankful to Higher Education Commission (HEC) of Pakistan for continuous financial support. We are also highly thankful to Dr. Nawazish A. Khan and Prof. Qiu Xiang-Gang for providing the characterization facilities at Material Science Laboratory, Department of Physics (QAU), Islamabad Pakistan and Beijing National Laboratory of Condensed Matter Physics, Institute of Physics (IOP), Chinese Academy of Sciences (CAS) Beijing, China.

References

[1] H. Ihara, K. Tanaka, Y. Tanaka, A. Iyo, N. Terada, M. Tokumoto, M. Ariyama, I. Hase, A. Sundaresan, N. Hamada, S. Miyashita, K. Tokiwa, T. Watanabe, Physica C 341–348 (2000) 487.
[2] S. Acharya, A.K. Biswal, J. Ray, P.N. Vishwakarma, J. Appl. Phys. 112 (2012) 053916.
[3] A. Snezhko, T. Prozorov, R. Prozorov, Phys. Rev. B 71 (2005) 024527.
[4] L.N. Bulaevskii, E.M. Chudnovsky, M.P. Maley, Appl. Phys. Lett. 76 (2000) 2594.
[5] M.H. Pu, W.H. Song, B. Zhao, X.C. Wu, T. Hu, Y.P. Sun, J.J. Du, Supercond. Sci. Technol. 14 (2001) 305–310.
[6] K.T. Lau, S.Y. Yahya, R. Abd-Shukor, J. Appl. Phys. 99 (2006) 123904.
[7] J. Gutiérrez, A. Llordés, J. Gazquez, M. Gibert, N. Romá, S. Ricart, A. Pomar, F. Sandiumenge, N. Mestres, T. Puig, X. Obradors, Nat. Mater. 6 (2007) 367.
[8] T.G. Holesinger, L. Civale, B. Maiorov, D.M. Feldmann, J.Y. Coulter, J. Miller, V.A. Maroni, Z.J. Chen, D.C. Larbalestier, R. Feenstra, X.P. Li, M.B. Huang, T. Kodenkandath, W. Zhang, M.W. Rupich, A.P. Malozemoff, Adv. Mater. 20 (2008) 391.
[9] M. Miura, T. Kato, M. Yoshizumi, Y. Yamada, T. Izumi, Y. Shiohara, T. Hirayama, Appl. Phys. Exp. 1 (2004) 051701.
[10] S. Engel, T. Thersleff, R. Huhne, L. Schultz, B. Holzapfel, Appl. Phys. Lett. 90 (2007) 102505.
[11] T. Puig, J. Gutierrez, A. Pomar, A. Llordes, J. Gazquez, S. Ricart, F. Sandiumenge, X. Obradors, Supercond. Sci. Technol. 21 (2008) 034008.
[12] N.M. Strickland, N.J. Long, E.F. Talantsev, P. Hoefakker, J. Xia, M.W. Rupich, T. Kodenkandath, W. Zhang, X. Li, Y. Huang, Physica C 468 (2008) 183.
[13] M. Miura, M. Yoshizumi, T. Izumi, Y. Shiohara, Supercond. Sci. Technol. 23 (2010) 014013.
[14] R. Prozorov, T. Prozorov, A. Snezhko, IEEE Tran. Appl. Supercond. 15 (2005) 3277.
[15] W.D. Huang, W.H. Song, Z. Cui, B. Zhao, M.H. Pu, X.C. Wu, Y.P. Sun, J.J. Du, Phys. Status Solidi A 179 (2000) 189.
[16] Z.Y. Jia, H. Tang, Z.Q. Yang, Y.T. Xing, Y.Z. Wang, G.W. Qiao, Physica C 337 (2000) 130.
[17] M. Annabi, A. M'chirgui, F. Ben Azzouz, M. Zouaoui, F. Ben Salem, Physica C 405 (2004) 25.
[18] K. Christova, A. Manov, J. Nyhus, U. Thisted, O. Herstad, S.E. Foss, K.N. Haugen, K. Fossheim, J. Alloys Comp. 340 (2002) 1.
[19] Y. Xu, A. Hu, C. Xu, N. Sakai, I. Hirabayashi, M. Izumi, Physica C 468 (2008) 1363.
[20] N.H. Mohammed, A.I. Abou-Aly, I.H. Ibrahim, R. Awad, M. Rekaby, J. Alloys Comp. 486 (2009) 733.
[21] M.M. Elokret, R. Awad, A.A. El-Ghany, A.A. Shama, A. El-wanis, J. Supercond. Nov. Magn. 24 (2011) 1345.
[22] Nawazish A. Khan, A. Saleem, S.T. Hussain, J. Supercond. Nov. Magn. 25 (2012) 1725.
[23] M. Mumtaz, Asif I. Bhatti, K. Nadeem, Nawazish A. Khan, Abida Saleem, S. Tajammul Hussain, J. Low Temp. Phys. 170 (2013) 185.
[24] M. Annabi, A.M. Chirgui, F.B. Azzuoz, M.B. Salem, Physica C 25 (2004) 405.
[25] M. Annabi, A. Ghattas, M. Zouaoui, F. Ben Azzouz, M. Ben Salem, Physica C 468 (2008) 31.
[26] N.H. Mohammad, A.I. Abou-Aly, R. Awad, I.H. Ibrahim, M. Roumie, M. Rekaby, J. Physica C 172 (2012) 234–255.
[27] T.D. Dzhafarov, M. Altunbas, T. Kucukomeroglu, Mater. Lett. 25 (1995) 81–86.
[28] B. Zeimetz, S.X. Dou, H.K. Liu, J. Supercond. Sci. Technol. 9 (1996) 888.
[29] T.D. Dzhafarov, M. Altunbas, T. Kucukomeroglu, Solid. Stat. Commun. 99 (1996) 839–843.
[30] F.M. Julian, S. Ricart, A. Pomer, L.M. Marzan, J. Nanosci. Technol. 11 (2011) 3245–3255.
[31] M.N. Khan, M. Khizar, B.N. Mukeshev, J. Physica B 321 (2002) 257.
[32] H. Najafpour, S.H.R. Shojaei, S.M. Shojaeiu, J. Supercond. Non. Magn. 23 (2010) 487.
[33] M. Mumtaz, Nawazish A. Khan, E.U. Khan, Physica C 470 (2010) 428–434.
[34] M. Mumtaz, M. Kamran, K. Nadeem, Abdul Jabbar, Nawazish A. Khan, Abida Saleem, S. Tajammul Hussain, M. Kamran, Low Temp. Phys. Fiz. Nizk. Temp. 39 (2013) 806–813.
[35] M. Mumtaz, Nawazish A. Khan, Fiz. Nizk. Temp. 36 (2010) 196–201.
[36] Nawazish Ali Khan, Muhammad Mumtaz, Phys. Rev. B 77 (2008) 054507.
[37] M. Mumtaz, Nawazish A. Khan, Sajid Khan, J. Appl. Phys. 107 (2010) 103905.
[38] M. Mumtaz, Asif I. Bhatti, K. Nadeem, Nawazish A. Khan, Abida Saleem, S. Tajammul Hussain, J. Low Temp. Phys. 170 (2013) 185–204.
[39] F. Gomory, Supercond. Sci. Technol. 10 (1997) 523.
[40] R.V. Sarmago, K.L.C. Molina, L.J.D. Guerra, Physica C 364 (2001) 239.
[41] Nawazish.A. Khan, M. Mumtaz, A.A. Khurram, P. Kameli, Physica C 468 (2008) 233–236.

Eur. Phys. J. Appl. Phys. (2015) 69: 30601
DOI: 10.1051/epjap/2015140356

THE EUROPEAN PHYSICAL JOURNAL
APPLIED PHYSICS

Regular Article

Noble metals (Ag, Au) nanoparticles addition effects on superconducting properties of CuTl-1223 phase

Abdul Jabbar, Muhammad Mumtaz[a], and Kashif Nadeem

Materials Research Laboratory, Department of Physics, FBAS, International Islamic University (IIU), 44000 Islamabad, Pakistan

Received: 7 September 2014 / Received in final form: 11 December 2014 / Accepted: 2 February 2015
Published online: 18 March 2015 – © EDP Sciences 2015

Abstract. Low anisotropic $(Cu_{0.5}Tl_{0.5})Ba_2Ca_2Cu_3O_{10-\delta}$ (CuTl-1223) high temperature superconducting phase was synthesized by solid-state reaction, silver (Ag) nanoparticles were prepared by sol-gel method and gold (Au) nanoparticles were extracted from colloidal solution. We added Ag and Au nanoparticles in CuTl-1223 matrix separately with same concentration during the final sintering process to get $(M)_x$/CuTl-1223; M = Ag nanoparticles or Au nanoparticles ($x = 0$ and 1.0 wt.%) nano-superconductor composites. We investigated and compared the effects of these noble metals nanoparticles addition on structural, morphological and superconducting transport properties of CuTl-1223 phase. The crystal structure of the host CuTl-1223 superconducting phase was not affected significantly after the addition of these nanoparticles. The enhancement of superconducting properties was observed after the addition of both Ag and Au nanoparticles, which is most probably due to improved inter-grains weak-links and reduction of defects such as oxygen deficiencies, etc. The reduction of normal state room temperature resistivity is the finger prints of the reduction of barriers and facilitation to the carriers transport across the inter-crystallite sites due to improved inter-grains weak-links. The greater improvement of superconducting properties in Ag nanoparticles added samples is attributed to the higher conductivity of silver as compared to gold, which also suits for practical applications due to lower cost and easy synthesis of Ag nanoparticles as compared to Au nanoparticles.

1 Introduction

Different phases of $Cu_{0.5}Tl_{0.5}Ba_2Ca_{n-1}Cu_nO_{2n+4-\delta}$ (CuTl-12$(n-1)n$); $n = 2, 3, 4, \ldots$, high temperature superconducting (HTSCs) family can be synthesized at high (~5 GPa) as well as at ambient pressure [1]. At high pressure synthesis, the good quality samples of this HTSCs family can have relatively higher $T_c(0)$ because at such high pressure the porosity is low and superconducting volume fraction is high. The number of defects in the form of disorder or oxygen deficiencies, etc. can be reduced at such high pressure synthesis, which ultimately plays an important role in optimization of carriers and improvement of superconductivity. But for the large scale production of this material for application point of view, the synthesis at such high pressure can be a big hurdle; therefore, we have synthesized these samples at ambient pressure. At ambient pressure synthesis, the density of voids and pores are relatively high, which reduces the superconducting volume fraction. There are also some other defects in the form of oxygen deficiencies, which can cause the reduction of carriers from optimum level. Due to these reasons $T_c(0)$ of our samples is relatively low, which can be improved by some simple and easy ways other than high pressure synthesis and we are trying to resolve this issue by different techniques such as addition of nanoparticles of different materials, sizes and nature in the bulk CuTl-1223 matrix. There have been consistent efforts to overcome this problem and to enhance the superconducting properties of different compounds of HTSCs families by different techniques [2–4]. One of the most effective and easiest ways to address this issue is the inclusion of nanostructures at the grain-boundaries to heal up the inter-grains voids and pores to improve the inter-grains weal-links and superconducting properties of granular bulk superconductors. But the real challenge is to control the size, concentration and homogenous distribution of nanostructures at the grain-boundaries of the bulk HTSCs [5–8]. The improved inter-grains connections can facilitate the carriers transport across the inter-crystallite sites, but after certain optimum inclusion level of nanostructures, the superconducting volume fraction start to be decreased, which causes the suppression of superconductivity parameters. The nature of the material of nanostructure is also very crucial in this regards because the effects of nanostructure of different materials have different effects on the superconducting properties.

[a] e-mail: mmumtaz75@yahoo.com

The inclusion of MgO, Al_2O_3 and ZrO_2 nanoparticles in Bi-based HTSC has improved the superconducting properties such as critical current density (J_c), etc. [9–11]. The inclusion of MgO nanoparticles in Bi-2212 matrix has increased the superconducting transition sharpness and the superconductor volume fraction [12]. The volume pinning force density, onset temperature of dissipation, activation energy and J_c in applied magnetic field were found to be improved after the addition of nano-alumina in the polycrystalline (Bi, Pb)-2223 samples [13]. The addition of different nanoparticles of different materials with different sizes like $NiFe_2O_4$, Al_2O_3, ZrO_2, etc. in suitable amount helps in generating the effective flux pinning centers, which can enhance the critical superconductivity parameters [11,14,15]. The addition of Ag nanoparticles in Y123 superconducting thin films improved crystal structure and J_c values [16]. Superconducting and mechanical properties of Bi(Pb)-Sr-Ca-Cu-O superconducting matrix were improved by the addition of Ag nanoparticles which may be the cementing effects of these nanoparticles among the superconducting grains [17]. The improvement of superconducting volume fraction, T_c and J_c after the addition of Ag nanoparticles up to $x = 1.5$ wt.% in CuTl-1223 matrix has been observed [18]. The addition of nanostructures of Ag and Au has shown significantly improved superconducting properties in many superconducting systems [19–22]. Increased nano-Ag particles content in Bi-2223 matrix improved the inter-grains connectivity and enhanced J_c [23,24].

We have investigated and compared the effects of noble metals (Ag, Au) nanoparticles addition on structural, morphological and superconducting properties of CuTl-1223 phase in detail. As the electronic configuration, electronegativity, electrical conductivity of these metals are different, therefore, we were expecting their different effects on structural, morphological and superconducting properties of the host matrix. The addition of these nanoparticles in appropriate concentration can heal up the voids, pores and can improve the inter-grains weak-links, which can facilitate the carriers to translate through the bulk materials. In this way we can reduce the defects such as oxygen deficiencies, etc., and can improve the superconducting volume fraction and superconducting properties.

2 Experimental details for sample preparation and characterizations

$Cu_{0.5}Ba_2Ca_2Cu_3O_{10-\delta}$ precursor material was synthesized by using $Ba(NO_3)_2$ (99.50%, UNI-Chem), $Ca(NO_3)_2 \cdot 4H_2O$ (99%, AppliChem), $Cu_2(CN)_2 + H_2O$ (99%, BDH). These compounds were mixed in appropriate ratios and were ground in mortar and pestle for about 2 h. The mixture after grinding was put into quartz boat and placed in preheated chamber furnace for calcinations at 860 °C for 24 h. The furnace was switched off and the precursor material was cooled down to room temperature after 24 h. The fired material was again ground for about 1hour and again placed into the furnace for second time calcination under the same conditions. Then the precursor material was mixed with thallium oxide (Tl_2O_3) (99%, BDH) and nanoparticles in appropriate ratio and ground again for about 1 h. The ground material was pressed under 3.8 tons/cm^2 to obtain the desired pellets. The pellets were wrapped in gold capsules and sintered at 860 °C for nearly 10 min in preheated chamber furnace followed by quenching to room temperature to obtain the final product $(M)_x/(Cu_{0.5}Tl_{0.5})Ba_2Ca_2Cu_3O_{10-\delta}$ (M = Ag or Au, while $x = 0$, and $x = 1.0$ wt.%). Ag nanoparticles were synthesized by sol-gel technique and Au nanoparticles were extracted from the colloidal gold solution separately. The structure and phase purity of the $(M)_x$/CuTl-1223 composites were determined by XRD (D/Max IIIC Rigaku with a CuKα source of wavelength 1.54056 Å). The diffraction peaks were indexed and cell parameters were determined by cell refinement computer program (check cell). The morphology of the material was examined through scanning electron microscopy (SEM) by JOEL Jed-2300. The Fourier transform infrared (FTIR) absorption measurements of these samples were carried out using by Nicolet 5700 Fourier transform infrared (FTIR) spectrometer in the 400–700 cm^{-1} wave number range. The FTIR absorption spectroscopy was carried out using KBr as a background material. The dc-resistivity versus temperature measurements were carried out by four point probe technique with help of physical properties measurement system (PPMS, quantum design). The value of current during the dc-resistivity measurements was kept 1 mA. The dc-resistivity measurements were carried out during the heating cycle from 35 K to room temperature i.e., nearly 300 K. The rate of heating was kept 1 K/min to 3 K/min during these measurements. The dimensions of slab shaped samples were 1.2 × 1.0 × 4.0 mm^3 and low resistive four contacts were made on the samples with silver paint. The ac-susceptibility measurements were carried out by the mutual inductance method using an SR530 lock-in amplifier at a frequency of 270 Hz with $H_{AC} = 0.07$ Oe of primary coil. IV measurements were carried out at 70 K below the zero resistivity critical temperature and the criterion of J_c for these IV measurements was kept 1 μV/cm at 70 K in zero external applied magnetic field for all the samples.

3 Results and discussions

XRD patterns of Ag and Au nanoparticles are shown in Figures 1a and 1b. The prominent diffraction peaks are indexed with face-centered cubic (FCC) structure and the average size of Ag and Au nanoparticles calculated by Scherrer's formula is found to be 35 nm and 39 nm respectively. XRD analysis shows well indexed diffraction peaks (1 1 1), (2 0 0), (2 2 0) and (3 1 1) of FCC structures, which shows that silver and gold nanoparticles are better crystallized. No peak related to any impurity crystalline phase has been detected. These fine structures and metallic nature of Ag and Au nanoparticles can be useful in

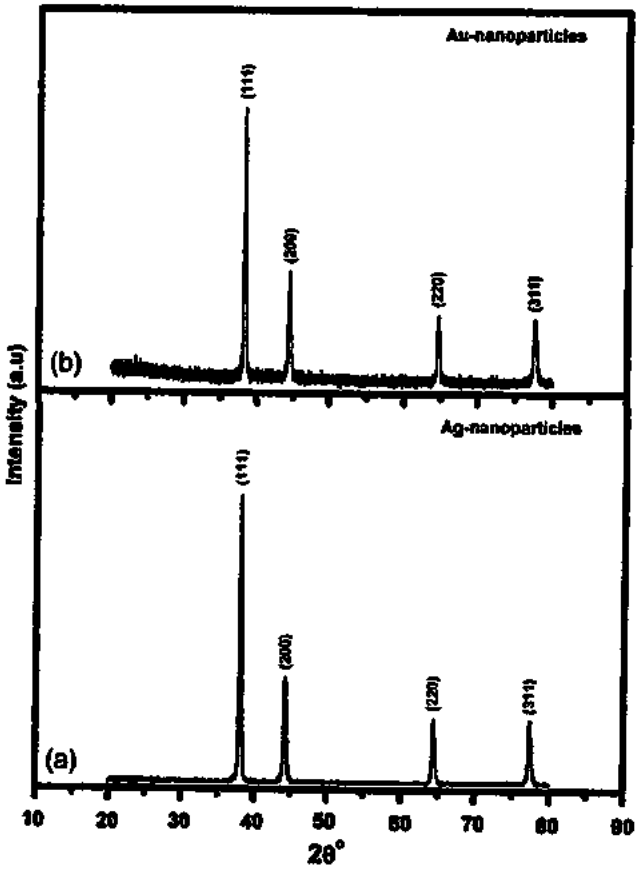

Fig. 1. (a) XRD pattern of Ag nanoparticles (b) XRD pattern of Au nanoparticles.

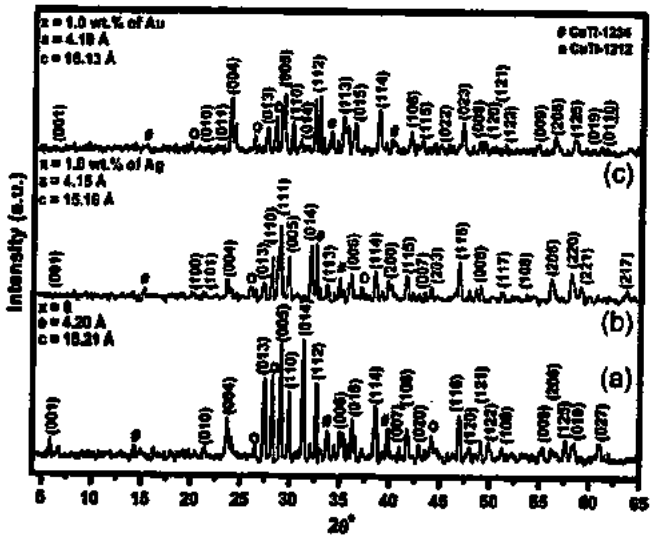

Fig. 2. XRD patterns of $(M)_x$/CuTl-1223 composites; M = Ag nanoparticles or Au nanoparticles (a) $x = 0$, (b) $x = 1.0$ wt.% of Ag nanoparticles and (c) $x = 1.0$ wt.% of Au nanoparticles.

many applications [25,26]. XRD patterns of $(M)_x$/CuTl-1223; M = Ag or Au, and $x = 0$, 1.0 wt.%, composites are shown in Figure 2. The diffraction patterns indicate the dominance of CuTl-1223 phase as most of the diffraction peaks are well indexed according to the tetragonal structure of this phase following the P4/mmm space group. The tetragonal structure and stoichiometry of the host CuTl-1223 compound remains unchanged after the addition of these nanoparticles, which clearly indicate that these nanoparticles have occupied the positions at the inter-crystallite sites (i.e., at grain-boundaries). The very few un-indexed diffraction peaks of relatively low intensity show the presence of other superconducting phases mentioned in the inset of Figure 2. The effect of some other phases on superconducting properties depends upon their wt.% present in the major parent phase. One of the most commonly observed effect of other superconducting phases in little amount is broadening of the superconducting transition width due to different values of $T_c(0)$ of different superconducting phases. The slight variation in lattice parameters may possibly be due to variation of oxygen contents and due to some stress and strains produced by the addition of these nanoparticles.

The surface morphology was examined by SEM micrographs of $(M)_x$/CuTl-1223 composites as shown in Figure 3. Few of the nanoparticles are encircled and reduction of inter-grain voids and improvement in the inter-grain weak-links can be visualized from inter-comparison of these micrographs of nanoparticles added and un-added samples. The main problem is to control the size of nanoparticles and to make the homogeneous mixing and distribution of these nanoparticles in the matrix.

The FTIR is very sensitive technique used to detect a trace amount of impurities and functional groups in the organic chemistry but here we used FTIR absorption spectroscopy to observe the different oxygen vibrational phonon modes, which play a vital role in superconductivity phenomenon. The FTIR absorption spectra of $(M)_x$/CuTl-1223 nano-superconductor composites in the wave number range from 400 to 700 cm^{-1} are shown in Figure 4a and 4b. The nomenclature (or symbols) of different atoms in the unit cell of CuTl-1223 superconductor has been demonstrated in Figure 4b. The bands in the range from 400 to 540 cm^{-1} are associated with the apical oxygen atoms and in the range around from 541 to 600 cm^{-1} are associated with CuO_2 planar oxygen atoms. The bands in the range from 670 to 700 cm^{-1} are associated with O_δ atoms in the charge reservoir layer. The apical oxygen modes of type Tl–O_A–Cu(2), Cu(1)–O_A–Cu(2) and planner oxygen modes Cu(2)–O_p–Cu(2) are observed around 418 cm^{-1}, 483 cm^{-1} and is around 532 cm^{-1} respectively for un-doped $Cu_{0.5}Tl_{0.5}Ba_2Ca_2Cu_3O_{10-\delta}$ samples. Almost all the oxygen modes remain unchanged in nano-Ag particles added samples and slight shift of apical and planner oxygen modes towards lower wave number (i.e., 473 cm^{-1} and 523 cm^{-1}) were observed in nano-Au particles added samples, Figure 4a. The softening of these modes is most likely associated with relaxation of apical and planner bond lengths due to stresses-strains produced after Au nanoparticles addition. Almost the fixed positions of these oxygen vibration modes confirm the preserved crystal structure and stoichiometry of the host CuTl-1223 matrix after the inclusion of these nanoparticles. This FTIR absorption spectroscopy shows the occupancy of these nanoparticles at the inter-granular sites.

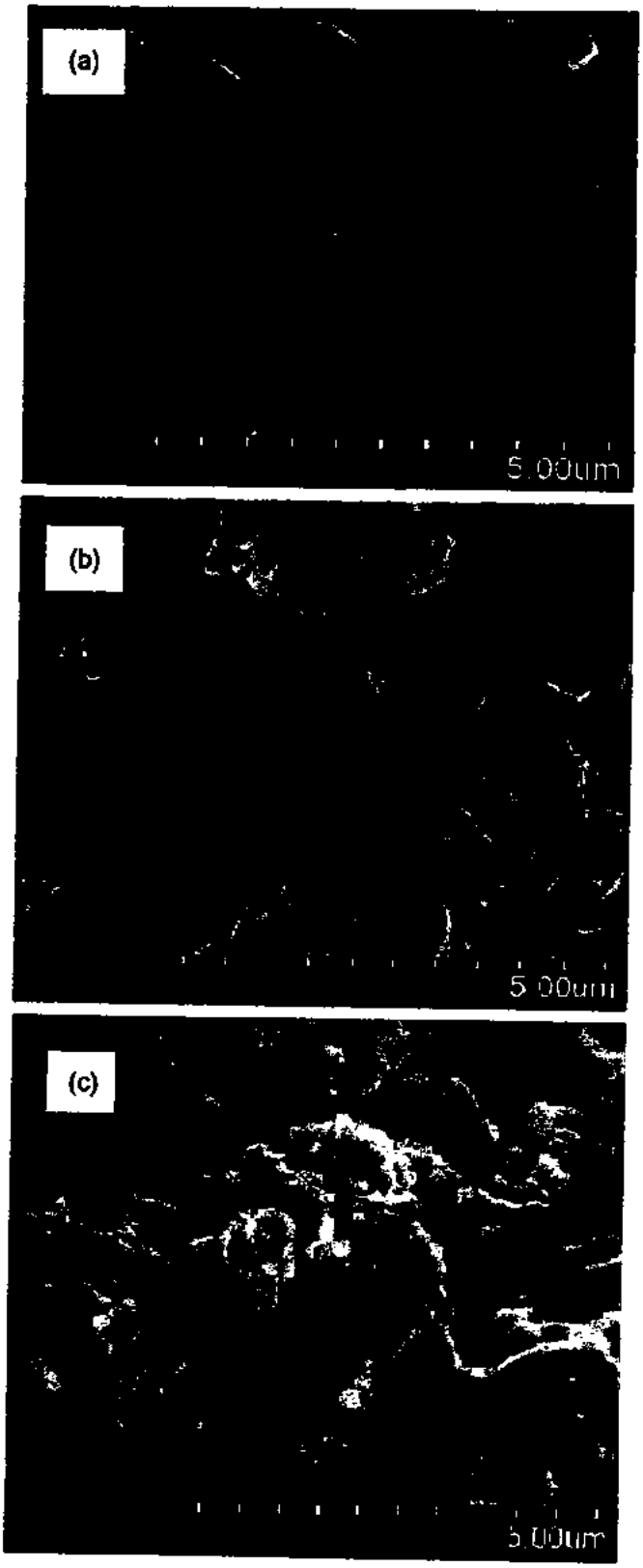

Fig. 3. SEM images of $(M)_x$/CuTl-1223 composites, where M = Ag nanoparticles or Au nanoparticles with (a) $x = 0$, (b) $x = 1.0$ wt.% of Ag nanoparticles and (c) 1.0 wt.% of Au nanoparticles.

The resistivity versus temperature measurements of $(M)_x$/CuTl-1223; M = Ag or Au ($x = 0$ and 1.0 wt.%) composites are shown in Figure 5. All these samples have shown a metallic variation in resistivity from room temperature down to onset of superconductivity with zero resistivity critical temperature $\{T_c(0)\}$ around 87, 101 and 98 K for $x = 0$, 1.0 wt.% of Ag nanoparticles and 1.0 wt.% of Au nanoparticles respectively. The variation of $T_c(0)$ with different contents of Ag and Au nanoparticles in CuTl-1223 matrix is given in the inset of Figure 5. The value of $T_c(0)$ increases initially up to certain contents in case of both Ag and Au nanoparticles added samples, which predicts their optimum inclusion level in CuTl-1223 matrix. The initial increase in $T_c(0)$ can be possibly due to improved weak-links among the superconducting grains by healing up the voids and pores with these nanoparticles. But after certain optimum inclusion level of these nanoparticles, the superconducting volume fraction start to be decreased, which causes the suppression of superconductivity parameters. Normally the zero resistivity critical temperature $T_c(0)$ of cuprates depends upon the carriers' density in their CuO_2 planes [27]. The carriers supplied by the charge reservoir layer to CuO_2 planes depend upon oxygen contents in the charge reservoir layer [28]. As $T_c(0)$ increases with the addition of these nanoparticles, which may due to optimization of carriers' density in the CuO_2 planes supplied by the charge reservoir layer. Therefore, it is obvious that the oxygen contents in the charge reservoir layer depends upon these nanoparticles contents in the CuTl-1223 matrix. The superconducting volume fraction can also be improved by the optimization of oxygen, which can occupy the oxygen vacancies in the bulk CuTl-1223 matrix. The decreasing trend in $T_c(0)$ beyond certain optimum limit of these nanoparticles addition may be due to agglomeration and segregation of these nanoparticles at the grain-boundaries in the bulk CuTl-1223 matrix, which can cause the degradation of the quality of the samples and reduce the superconducting bulk volume fraction in these samples. The improved inter-grain weak-links facilitate the charge carriers transport processes and reduce the energy losses across the grains boundaries. But after a certain optimum level of these nanoparticles addition, the agglomeration and segregation of nanoparticles result in the reduction of T_c by various mechanisms like scattering, pair-breaking, etc. [29,30]. Normal state resistivity $\{\rho_{(300\ K)}(\Omega\text{-cm})\}$ at room temperature (~300 K) decreases after the addition of these nanoparticles. The decrease in $\rho_{(300\ K)}(\Omega\text{-cm})$ and increase in T_c ($R = 0$) are relatively higher for Ag nanoparticles added samples as compared to those of Au nanoparticles added samples, which may be due to higher electricity conductivity of silver (i.e., 6.30×10^7 S/m at 20 °C) as compared to that of gold (i.e., 4.10×10^7 S/m at 20 °C) [31,32]. These nanoparticles can fill up the inter-grain voids and improve the inter-grain weak-links, which can facilitate the charge carriers' transport across the grains at inter-crystallite sites in the bulk CuTl-1223 matrix [29,30]. The normal state

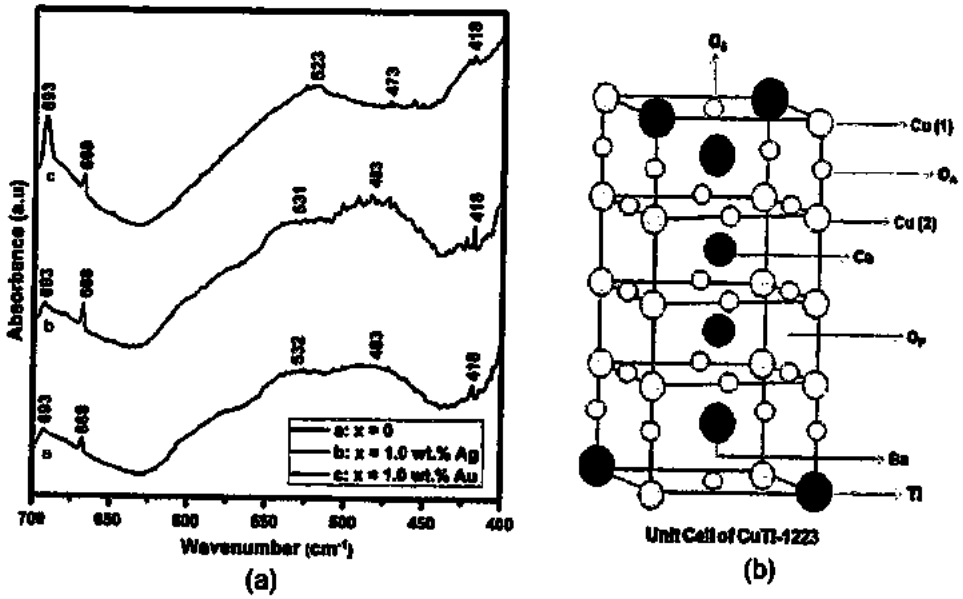

Fig. 4. FTIR spectra of $(M)_x$/CuTl-1223 composites, where M = Ag nanoparticles or Au nanoparticles with (a) $x = 0$, (b) $x = 1.0$ wt.% of Ag nanoparticles and (c) $x = 1.0$ wt.% Au nanoparticles.

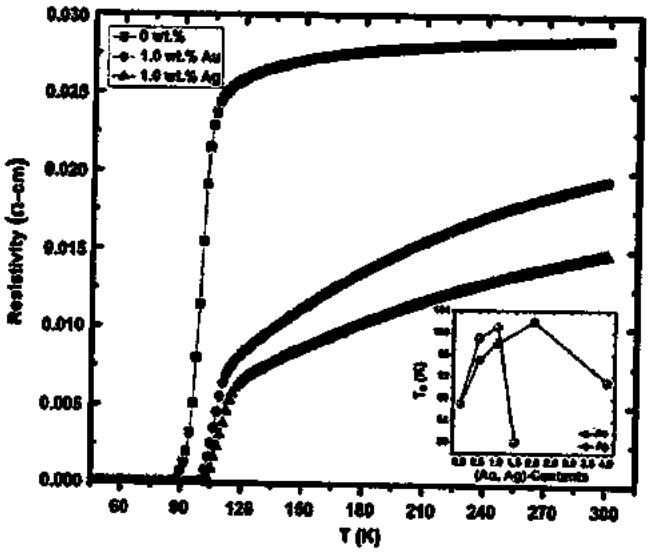

Fig. 5. Resistivity versus temperature measurements of $(M)_x$/CuTl-1223 composites, where M = Ag nanoparticles or Au nanoparticles with (a) $x = 0$, (b) $x = 1.0$ wt.% of Ag nanoparticles and (c) $x = 1.0$ wt.% Au nanoparticles. In the inset the variation of $T_c(R = 0)$ versus (Ag, Au)- nanoparticles contents is shown.

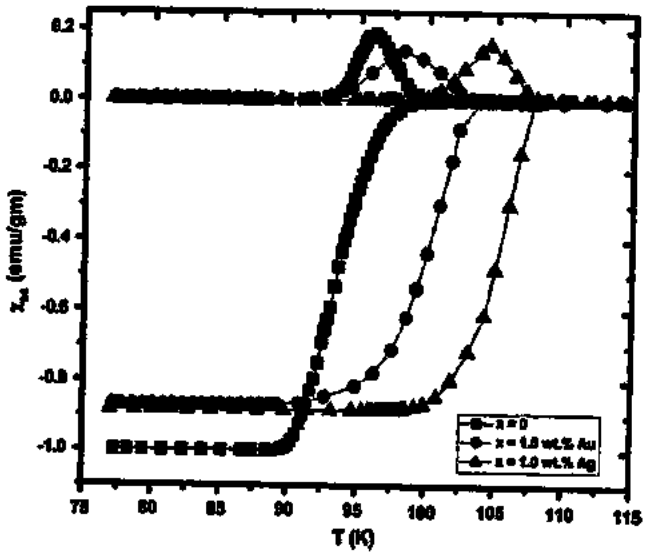

Fig. 6. AC-susceptibility measurements of $(M)_x$/CuTl-1223 composites, where M = Ag nanoparticles or Au nanoparticles with $x = 0$, 1.0 wt.% of Ag nanoparticles, and 1.0 wt.% Au nanoparticles.

resistivity of Ag nanoparticles added sample is lower as compared to Au nanoparticles added sample, which verifies the addition of these nanoparticles. The inclusion of these nanoparticles at the interstitial spaces among the superconducting grains reduces the barriers of insulating/semi-insulating grains-boundaries to the flow of carriers.

Ac-susceptibility measurements of $(M)_x$/CuTl-1223; M = Ag or Au ($x = 0$ and 1.0 wt.%) composites are shown in Figure 6. These ac-susceptibility measurements were carried out in field cooled (FC) conditions by the mutual inductance method using an SR530 lock-in amplifier working at frequency of 270 Hz with $H_{AC} = 0.07$ Oe of primary coil. There are two components of ac-susceptibility, in-phase component (χ') and out of phase component (χ''). The magnitude of diamagnetic signal of the superconducting materials is represented by the real part (χ') and the ac-losses corresponding to the flux penetration into superconductor samples is represented by the imaginary part (χ'') of the ac-susceptibility. The imaginary part of ac-susceptibility gives the information about the nature of inter-grains weak-links and pinning strength [33–38]. It is observed that onset temperature of diamagnetism $\{T_c^{\text{onset}}(K)\}$ has been increased

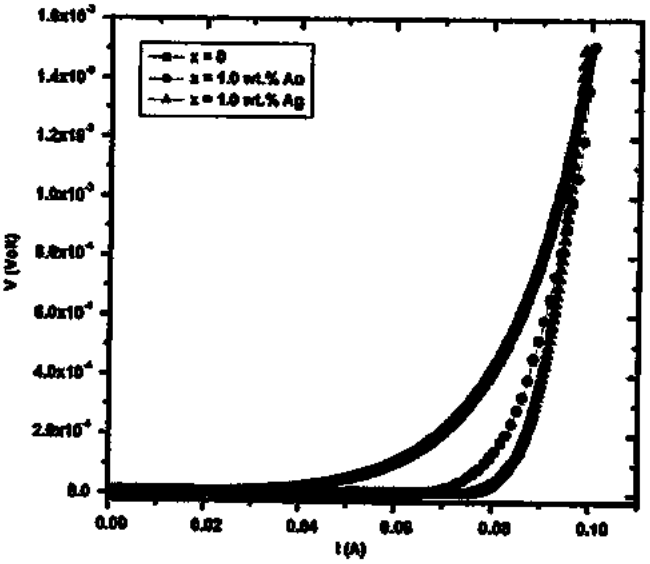

Fig. 7. Current versus voltage (IV) measurements of $(M)_x$/CuTl-1223 composites, where M = Ag nanoparticles or Au nanoparticles with x = 0, 1.0 wt.% of Ag nanoparticles, and 1.0 wt.% Au nanoparticles.

for both the Ag and Au nanoparticles added samples as compared to parent CuTl-1223 matrix. The increase in $T_c^{onset}(K)$ is possibly due to improved superconducting volume fraction and carriers density with the increase of these nanoparticles. The relatively higher density of voids and pores in pure host CuTl-1223 sample can be the cause of suppression of superconducting volume fraction and superconductivity. The other defects in the form of oxygen deficiencies can cause the reduction of carriers' density from the optimum level. By the incorporation of these metallic nanoparticles at the grain-boundaries, the voids and pores can be filled and can improve the inter-grains weak-links. In this way, we can reduce the defects in the material and can improve the superconducting properties. The enhancement of $T_c^{onset}(K)$ can be the indication of enhanced carriers' density towards optimization after addition of these nanoparticles. Due to higher electrical conductivity of Ag as compared to Au, the improvement in bulk superconductivity is relatively greater in case of Ag nanoparticles added samples as compared to Au nanoparticles added samples [31,32].

The current versus voltage (IV) measurements of $(M)_x$/CuTl-1223; M = Ag or Au (x = 0 and 1.0 wt.%) composites are shown in Figure 7. These IV measurements were carried out at 70 K below $T_c(0)$ for the samples. The criterion of J_c for the IV measurements was kept 1 μV/cm at 70 K in zero external applied magnetic field for all these samples. The IV characteristics curves show the improvement of critical current (I_c) with the addition of these nanoparticles particles in CuTl-1223 superconducting matrix. This increasing trend of I_c with addition of these nanoparticles is possibly due to the formation of superconductor-metal-superconductor junctions in the composites. The improvement of I_c is greater in case of Ag added samples than Au nanoparticles added samples due to higher electrical conductivity of silver as compared to gold [31,32].

The overall improvement of superconducting properties of CuTl-1223 matrix after the addition of Ag or Au nanoparticles can be attributed to an increase in the inter-grain connectivity by filling up the voids with these metallic nanoparticles of high conductivity. The improvement of superconducting properties in Ag nanoparticles added samples is greater due to higher conductivity of silver as compared to gold [31,32], which also suits for practical applications due to lower cost and easy synthesis of Ag nanoparticles as compared to Au nanoparticles.

4 Conclusion

We have synthesized the composites of Ag and Au nanoparticles and CuTl-1223 superconducting phase successfully. We have investigated, compared and summarized the effects of noble metals (Ag and Au) nanoparticles addition on structural, morphological and superconducting transport properties of CuTl-1223 superconducting phase. The crystal structure and stoichiometry of the host CuTl-1223 phase remain same despite of presence of the nanoparticles in the matrix. The enhancement in superconductivity was observed with the addition of these nanoparticles due to reduction in inter-grains voids, facilitation in carrier transport across inter-crystallite sites and improvement in weak-links. The decrease in normal state resistivity is the figure prints of healing up the pores and improved inter-grains connectivity with addition of these nanoparticles. The larger improvement of superconducting properties in Ag nanoparticles added samples is attributed to the higher conductivity of silver as compared to gold, which also suits for practical applications due to lower cost and easy synthesis of Ag nanoparticles as compared to Au nanoparticles.

We are also highly thankful to Dr. Nawazish A. Khan and Prof. Qiu Xiang-Gang for providing the characterization facilities at Material Science Laboratory, Department of Physics QAU Islamabad and Beijing National Laboratory of Condensed Matter Physics, Institute of Physics (IOP), Chinese Academy of Sciences (CAS) Beijing, China.

References

1. H. Ihara, K. Tanaka, Y. Tanaka, A. Iyo, N. Terada, M. Tokumoto, M. Ariyama, I. Hase, A. Sundaresan, N. Hamada, S. Miyashita, K. Tokiwa, T. Watanabe, Physica C **341–348**, 487 (2000)
2. S. Acharya, A.K. Biswal, J. Ray, P.N. Vishwakarma, J. Appl. Phys. **112**, 053916 (2012)
3. M.H. Pu, W.H. Song, B. Zhao, X.C. Wu, T. Hu, Y.P. Sun, J.J. Du, Supercond. Sci. Technol. **14**, 305 (2001)
4. M. Miura, T. Kato, M. Yoshizumi, Y. Yamada, T. Izumi, Y. Shiohara, T. Hirayama, Appl. Phys. Express **1**, 051701 (2008)

5. S. Engel, T. Thersleff, R. Huhne, L. Schultz, B. Holzapfel, Appl. Phys. Lett. **90**, 102505 (2007)
6. T. Puig, J. Gutierrez, A. Pomar, A. Llordes, J. Gazquez, S. Ricart, F. Sandiumenge, X. Obradors, Supercond. Sci. Technol. **21**, 034008 (2008)
7. N.M. Strickland, N.J. Long, E.F. Talantsev, P. Hoefakker, J. Xia, M.W. Rupich, T. Kodenkandath, W. Zhang, X. Li, Y. Huang, Physica C **468**, 183 (2008)
8. M. Miura, M. Yoshizumi, T. Izumi, Y. Shiohara, Supercond. Sci. Technol. **23**, 014013 (2010)
9. W.D. Huang, W.H. Song, Z. Cui, B. Zhao, M.H. Pu, X.C. Wu, Y.P. Sun, J.J. Du, Phys. Status Solidi A **179**, 189 (2000)
10. Z.Y. Jia, H. Tang, Z.Q. Yang, Y.T. Xing, Y.Z. Wang, G.W. Qiao, Physica C **337**, 130 (2000)
11. M. Annabi, A. M'chirgui, F.B. Azzouz, M. Zouaoui, M.B. Salem, Physica C **405**, 25 (2004)
12. K. Christova, A. Manov, J. Nyhus, U. Thisted, O. Herstad, S.E. Foss, K.N. Haugen, K. Fossheim, J. Alloys Compd. **340**, 1 (2002)
13. A. Ghattas, F.B. Azzouz, M. Annabi, M. Zouaoui, M.B. Salem, J. Phys.: Conf. Ser. **97**, 012175 (2008)
14. A. Ghattas, M. Annabi, M. Zouaoui, F.B. Azzouz, M.B. Salem, Physica C **468**, 31 (2008)
15. N.H. Mohammad, A.I. Abou-Aly, R. Awad, I.H. Ibrahim, M. Roumie, M. Rekaby, J. Low Temp. Phys. **172**, 234 (2013)
16. A.H. Li, M. Ionescu, H.K. Liu, T. Silver, X.L. Wang, S.X. Dou, IEEE Trans. Appl. Supercond. **15**, 2 (2005)
17. V. Bartunek, O. Smrckova, J. Supercond. Nov. Magn. **24**, 1241 (2011)
18. W. Abdeen, N.H. Mohammed, R. Awad, S.A. Mahmoud, M. Hasebbo, J. Supercond. Nov. Magn. **26**, 3235 (2013)
19. T.D. Dzhafarov, M. Altunbas, T. Kucukomeroglu, Mater. Lett. **25**, 81 (1995)
20. B. Zeimetz, S.X. Dou, H.K. Liu, Supercond. Sci. Technol. **9**, 888 (1996)
21. T.D. Dzhafarov, M. Altunbas, A. Varilci, T. Kucukomeroglu, S. Nezir, Solid State Commun. **99**, 839 (1996)
22. F.M. Julian, S. Ricart, A. Pomar, M. Col, P. Abellan, F. Sandiumenge, M.J. Casanove, X. Obradors, T. Puig, I.P. Santos, L.M.L. Marzan, J. Nanosci. Nanotechnol. **11**, 3245 (2011)
23. M.N. Khan, M. Khizar, B.N. Mukashev, Physica B **321**, 257 (2002)
24. H. Najafpour, S.H.R. Shojaei, S.M. Shojaei, J. Supercond. Nov. Magn. **23**, 487 (2010)
25. S.L.C. Hsu, R.T. Wu, Int. Proc. Chem. Biol. Environ. Eng. **2**, 55 (2011)
26. M.A.M. Khan, S. Kumar, M. Ahamed, S.A. Alrokayan, M.S. AlSalhi, Nano. Res. Lett. **6**, 434 (2011)
27. N.A. Khan, M. Mumtaz, Phys. Rev. B **77**, 054507 (2008)
28. M. Mumtaz, N.A. Khan, S. Khan, J. Appl. Phys. **107**, 103905 (2010)
29. J.C. Zhang, F.Q. Liu, G.S. Cheng, J.X. Shang, J.Z. Liu, S.X. Cao, Z.X. Liu, Phys. Lett. A **201**, 70 (1995)
30. P.F. Miceli, J.M. Tarascon, L.H. Greene, P. Barboux, F.J. Rotella, J.D. Jorgensen, Phys. Rev. B **37**, 5932 (1988)
31. R.A. Serway, *Principles of Physics*, 2nd edn. (Saunders College Pub., Fort Worth, Texas, London, 1998)
32. S. Reif-Acherman, Int. J. Heat Mass Transfer **77**, 542 (2014)
33. F. Gomory, Supercond. Sci. Technol. **10**, 523 (1997)
34. R.V. Sarmago, K.L.C. Molina, L.J.D. Guerra, Physica C **364–365**, 239 (2001)
35. N.A. Khan, M. Mumtaz, A.A. Khurram, P. Kameli, Physica C **468**, 233 (2008)
36. K.T. Lau, S.Y. Yahya, R. Abd-Shukor, J. Appl. Phys. **99**, 123904 (2006)
37. J. Gutiérrez, A. Llordés, J. Gazquez, M. Gibert, N. Romá, S. Ricart, A. Pomar, F. Sandiumenge, N. Mestres, T. Puig, X. Obradors, Nat. Mater. **6**, 367 (2007)
38. T.G. Holesinger, L. Civale, B. Maiorov, D.M. Feldmann, J.Y. Coulter, D.J. Miller, V.A. Maroni, Z. Chen, D.C. Larbales-tier, R. Feenstra, X. Li, Y. Huang, T. Kodenkandath, W. Zhang, M.W. Rupich, A.P. Malozemoff, Adv. Mater. **20**, 391 (2008)

Journal of Magnetism and Magnetic Materials 377 (2015) 6–11

Contents lists available at ScienceDirect

Journal of Magnetism and Magnetic Materials

journal homepage: www.elsevier.com/locate/jmmm

Highly coercive cobalt ferrite nanoparticles-CuTl-1223 superconductor composites

Abdul Jabbar, Irfan Qasim, Shahid A. Khan, K. Nadeem, M. Waqee-ur-Rehman, M. Mumtaz*, F. Zeb

Materials Research Laboratory, Department of Physics, FBAS, International Islamic University (IIU), Islamabad 44000, Pakistan

ARTICLE INFO

Article history:
Received 31 May 2014
Received in revised form
22 September 2014
Accepted 3 October 2014
Available online 8 October 2014

Keywords:
$(CoFe_2O_4)_x$/CuTl-1223 composites
Cobalt ferrite nanoparticles
Superconducting properties

ABSTRACT

We explored the effects of highly coercive cobalt ferrite ($CoFe_2O_4$) nanoparticles addition on structural, morphological, and superconducting properties of $Cu_{0.5}Tl_{0.5}Ba_2Ca_2Cu_3O_{10-\delta}$ (CuTl-1223) matrix. Series of $(CoFe_2O_4)_x$/CuTl-1223 ($x=0$ ~2.0 wt%) composites samples were synthesized and were characterized by x-ray diffraction (XRD), scanning electron microscopy (SEM), Fourier transform infrared (FTIR) absorption spectroscopy, and dc-resistivity versus temperature measurements. The magnetic behavior of $CoFe_2O_4$ nanoparticles was determined by MH-loops with the help of superconducting quantum interference device (SQUID). MH-loops analysis showed that these nanoparticles exhibit high saturation magnetization (86 emu/g) and high coercivity (3350 Oe) at 50 K. The tetragonal structure of host CuTl-1223 superconducting matrix was not altered after the addition of $CoFe_2O_4$ nanoparticles, which gave us a clue that these nanoparticles had occupied the inter-granular sites (grain-boundaries) and had filled the pores. The increase of mass density with increasing content of these nanoparticles in composites can also be an evidence of filling up the voids in the matrix. The resistivity versus temperature measurements showed an increase in zero resistivity critical ($T_c(0)$), which could be most probably due to improvement of weak-links by the addition of these nanoparticles. But the addition of these nanoparticles beyond an optimum level caused the agglomeration and produced additional stresses in material and suppressed the superconductivity.

1. Introduction

Normally, cuprate high temperature superconductors (HTSCs) are synthesized at very high pressure (3~5 GPa) but the compounds of $Cu_{0.5}Tl_{0.5}Ba_2Ca_{n-1}Cu_nO_{2n+4-\delta}$ (CuTl-12(n-1)n); n=2, 3, 4, ..., high temperature superconducting family can be easily synthesized at ambient pressure [1]. The superconducting parameters of this HTSCs family have the second highest values after Hg-based superconductors. Also $Cu_{0.5}Tl_{0.5}Ba_2Ca_2Cu_3O_{10-\delta}$ (CuTl-1223) phase with three CuO_2 planes has highest values of almost all superconducting parameters as compared to other phases of this HTSCs family [2,3]. Therefore, this class of superconductors is one of the most promising candidates for further investigation and technological applications. The overall structure is granular and porous in nature for large scale production in bulk form [2,3]. In order to enhance the superconducting properties, many attempts have been made by the different research groups working in this area. Post-annealing and creation of artificial defects by different techniques of the order of nanometer scale acting as extra effective pinning centers under the applied external field have been exercised [4,5]. Main objective of creation of additional effective pinning centers by different techniques is to enhance the critical current density (J_c) under the applied external magnetic field. These pinning centers are more effective when their sizes are of the order of coherence length [6]. The easy and very useful technique for the creation of artificial pinning centers is the addition of magnetic nanoparticles in the bulk superconducting materials [7].

The enhancement of critical current density (J_c) in many HTSCs families have been observed by the inclusion of nano-oxides of different nature, sizes and concentrations, which act as flux pinning centers in the applied external field [8–11]. The addition of Al_2O_3 and ZrO_2 nanoparticles acted as effective flux pinning centers in (Bi, Pb)-2223 superconductor and improved the infield J_c [12–14]. The lower addition of ZnO nanoparticles in $(Cu_{0.5}Tl_{0.25}Pb_{0.25})$-1223 matrix improved the superconducting transition temperature, J_c and superconducting volume fraction [15]. Also the addition of In_2O_3 and SnO_2 in CuTl-1223 matrix improved the superconducting volume fraction and reduced the porosity [16,17]. The improvement of J_c and suppression of T_c were

* Corresponding author. Fax: +92 51 9210256.
E-mail address: mmumtaz75@yahoo.com (M. Mumtaz).

http://dx.doi.org/10.1016/j.jmmm.2014.10.008
0304-8853/

also observed by the addition of ZrO_2 and ZnO in Gd-123 superconductor [18]. The superconducting properties (i.e. T_c, J_c etc.) of CuTl-1223 were improved by the addition of CuO, CaO_2 and BaO nanoparticles [19,20].

Recently, it was shown that magnetic nanoparticles play an important role as efficient pinning centers at lower densities [21,22]. $BiFeO_3$ (BFO) nanoparticles are the promising candidate for the various applications in recent years due to their large magneto-electric coupling [23]. Nano-BFO exhibits super-paramagnetism, which is very suitable for flux pinning centers in superconductors [24,25]. Enhancement in T_c was observed by the doping of paramagnetic Cr impurities in Pd films up to certain level in applied external magnetic fields [26]. The electrical resistivity versus temperature measurements showed that T_c has been increased up to 0.2 wt% addition of nano-Fe_2O_3 in CuTl-1223 matrix. The suppression in T_c on further increase of Fe_2O_3 nanoparticles concentration was due to Cooper pair-breaking mechanism or due to decrease in the volume fraction [27]. In recent years, the interest in creating the artificial pinning centers by the inclusion of magnetic nanoparticles in MgB_2 superconductor was also observed in literature [28]. Several models have been proposed to investigate the effects of the inclusion of magnetic nanoparticles within the bulk superconductors transport properties [29]. However, magnetic flux pinning depends on the magnitude and orientation of magnetization vector, which is a challenging problem for both theoretical and experimental investigations. The effects of magnetic nanoparticles addition on superconductivity in MgB_2 was investigated experimentally as well as theoretically but reported results were contradictory, which provide no evidence of magnetic pinning [30–36]. We have already reported the effect of addition of $ZnFe_2O_4$ nanoparticles in CuTl-1223 superconducting matrix. We have observed the improvement of the grain size with the addition of $ZnFe_2O_4$ nanoparticles. But after the addition of $ZnFe_2O_4$ nanoparticles, $T_c(0)$ and magnitude of diamagnetism were suppressed. The suppression of superconductivity was most likely due to trapping or localization of mobile free carriers and reflection of spin charge due to paramagnetic nature of $ZnFe_2O_4$ nanoparticles. Also, the reduction of $T_c(0)$ may be due to the possibility of Fe and Zn incorporation in lattice sites [37].

In this article, we have investigated the effects of $CoFe_2O_4$ nanoparticles addition on structural, morphological and superconducting transport properties of CuTl-1223 matrix. The main objective of this work was to improve the inter-grainweak-links by filling the pores and voids present in bulk form of the host CuTl-1223 matrix by the inclusion of these nanoparticles. The second objective was to increase the number of flux pinning centers to the optimum level by the addition of these magnetic nanoparticles. The suppression of superconducting properties in zero field with increasing $CoFe_2O_4$ nanoparticles contents is most probably due to localization and pair-breaking mechanisms of carriers across these highly coercive magnetic $CoFe_2O_4$ nanoparticles having net magnetic moments. The flux pinning measurements are our future plan. We have not done those measurements yet. In the present article our focus was to see the effects of magnetic $CoFe_2O_4$ nanoparticles on the superconducting transport properties of CuTl-1223 matrix.

2. Experimental details and characterization techniques

$CoFe_2O_4$ nanoparticles added bulk ceramic CuTl-1223 superconductor composites were synthesized by solid-state reaction. Initially, $Ba(NO_3)_2$, $Ca(NO_3)_2$ and Cu(CN) compounds were mixed in appropriate ratios and ground in an agate mortar and pestle for about two hours. The mixed material was loaded in quartz boats and fired in chamber furnace at 860 °C for 24 h followed by furnace cooling to room temperature. The firing step was repeated two times following one hour intermediate grinding to get $Cu_{0.5}Ba_2Ca_2Cu_3O_{10-\delta}$ precursor material. $CoFe_2O_4$ nanoparticles of 36 nm average size were synthesized separately by the sol-gel method. Later on, appropriate amount of thallium oxide (Tl_2O_3) and different wt% of $CoFe_2O_4$ nanoparticles were mixed in this precursor material at second stage and then ground again for about one hour. This ground material was then pelletized under 3.8 t/cm^2 pressure and pellets were enclosed in gold capsules for sintering at 860 °C for 10 min followed by quenching to room temperature to get $(CoFe_2O_4)_x$/CuTl-1223 (x=0, 0.5, 1.0, 1.5, and 2.0 wt%) composites samples.

Structure and phase purity of material was determined by XRD (D/Max IIIC Rigaku with a CuKα source of wavelength 1.54056 Å).

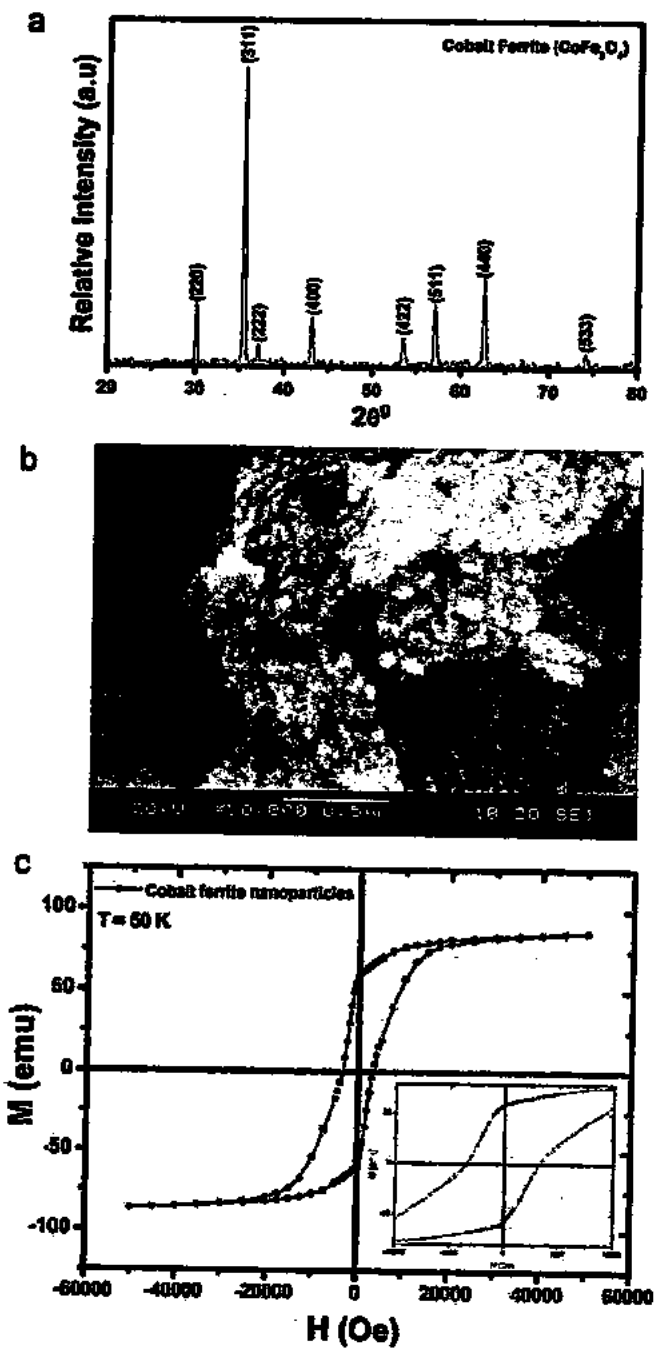

Fig. 1. (a–c). (a) XRD patterns of $CoFe_2O_4$ nanoparticles, (b) SEM image of $CoFe_2O_4$ nanoparticles at 500 nm scale, and (c) MH-loop of $CoFe_2O_4$ nanoparticles at T=50 K. (In the inset of (c) shows the coercivity region).

Morphology of material was examined by Scanning Electron Microscopy (SEM) (JOEL Jed-2300). MH-loop of magnetic nanoparticles was done by using a Superconducting Quantum Interference Device (SQUID) magnetometer (Quantum Design, MPMS-XL-7). Fourier transform infrared (FTIR) absorption measurements were carried out in 400–700 cm^{-1} wave number range by using Nicolet 5700 FTIR spectrometer. Potassium bromide (KBr) was used as a background for FTIR absorption measurements of these samples. Physical Properties Measurement System (PPMS, Quantum Design) was used for electrical dc-resistivity measurements. Four low resistance contacts with silver paint were made on the surface of the slab shaped samples with dimensions of $1.2 \times 1.0 \times 4.0\ mm^3$. The conventional four-probe technique was used and the value of current during the dc-resistivity measurements was kept 10 μA. We measured dc-resistivity with large applied currents and selected the appropriate current for our measurements at which response of the system was linear i.e. 10 μA. These dc-resistivity measurements were carried out during the heating cycle from 35 K to room temperature i.e. nearly 300 K. Heating rate was kept 1–3 K/min during these measurements. An electric field criterion of 1 μV/cm was chosen for the zero-resistance critical temperature $T_c(0)$. When the resistivity becomes of the order of 10^{-6} (Ω-m) then that temperature is considered as $T_c(0)$. Mass densities of samples were measured very carefully. Mass of each sample was measured by weighing balance (UW620H, Shimadzu) with 0.001 g accuracy and volume was determined by dipping the sample into water in calibrated test tube and a micro-pipit. Finally, we measured the mass density (mass/volume) from the measured mass and volume of the samples. We repeated these measurements four to five times and observe almost the same trend.

3. Results and discussion

XRD pattern of cobalt ferrite (CoFe2O4) nanoparticles is shown in Fig. 1(a). The characteristic peaks in XRD pattern of $CoFe_2O_4$ nanoparticles are in accordance with standard data values given in International Center for Diffraction Data (ICDD) record. The prominent peaks are indexed with cubic spinel structure and average size of $CoFe_2O_4$ nanoparticles calculated by using Debye-Scherrer's formula is 36 nm. XRD analysis shows exquisitely indexed (2 2 0), (3 1 1), (2 2 2), (4 0 0), (4 2 2), (5 1 1), (4 4 0), and (5 3 3) planes and sharpness of these peaks confirms that $CoFe_2O_4$ nanoparticles are better crystallized. Major phase has been observed at (h k l) value of (3 1 1). No peak of other impurity crystalline phases has been detected. The lattice parameter calculated to be $a=0.8392$ nm. SEM image of $CoFe_2O_4$ nanoparticles at 500 nm scale is shown in Fig. 1(b). It shows that nanoparticles are nearly spherical in shape and agglomerated due to magnetic interparticle interactions. We have measured MH-loop of $CoFe_2O_4$ nanoparticles at $T=50$ K by using SQUID magnetometer to confirm their magnetic behavior as shown in Fig. 1(c). These nanoparticles exhibit high saturation magnetization (86 emu/g) and high coercivity (3350 Oe) as evident in the inset of Fig. 1(c). Ammar et al. [38] reported a high saturation magnetization (85.1 emu/g) for chemically prepared $CoFe_2O_4$ nanoparticles. Liu et al. [39] reported the high saturation magnetization (83.6 emu/g) of nano-sized $CoFe_2O_4$ particles prepared by co-precipitation method and annealed at 1300 °C.

Typical XRD patterns of $(CoFe_2O_4)_x$/CuTl-1223 composites with $x=0$, 1.0 and 2.0 wt%, are shown in Fig. 2. The diffraction patterns indicate the dominance of CuTl-1223 phase as most of the peaks are well indexed according to tetragonal structure of this phase following the P4/mmm space group. The characteristic (001) peak of this CuTl-1223 phase appeared at $2\theta=5.84°$ and the stoichiometry remains unchanged after the addition of these nanoparticles, which may be an evidence that there is no variation in structural chemistry of the host CuTl-1223 compound. Structure of CuTl-1223 phase remains preserved even with the existence of $CoFe_2O_4$ nanoparticles, which clearly indicates that these nanoparticles occupy the positions at the inter-crystallite boundaries of CuTl-1223 matrix and help in improving the inter-grain weak-links. Beside the dominant CuTl-1223 phase, few un-indexed peaks appeared which are possibly due to presence of some impurities and some other superconducting phases. Extremely small variation in c-axis length was observed, which may possibly be due to some strains and change in oxygen (O_δ) contents after nanoparticles addition. The slight shift in the diffraction peaks to lower angles, which is due to uniform strain produced in the materials after the addition of $CoFe_2O_4$ nanoparticles. Also the slight decrease in the c-axis length and an increase in a-axis length

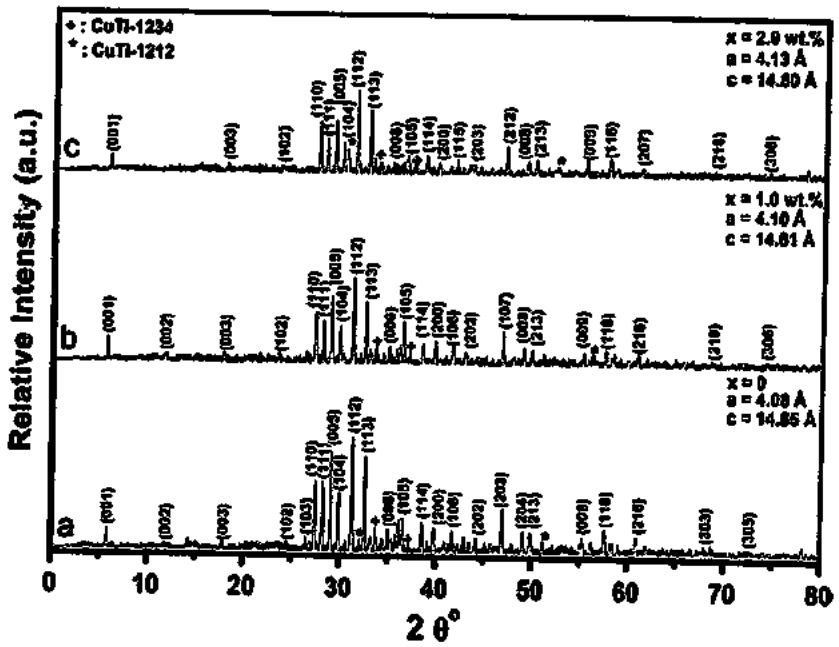

Fig. 2. XRD patterns of $(CoFe_2O_4)_x$/CuTl-1223 composites with (a) $x=0$, (b) $x=1.0$ wt%, and (c) $x=2.0$ wt%.

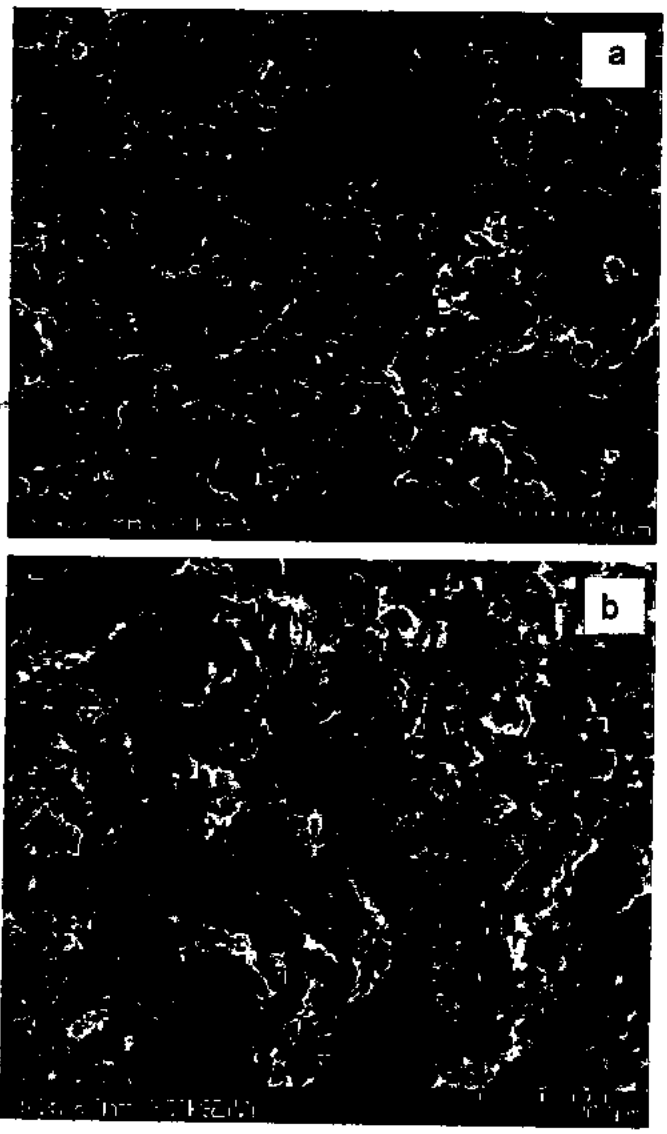

Fig. 3. SEM images of $(CoFe_2O_4)_x$/CuTl-1223 composites with (a) $x=0$ and (b) $x=2.0$ wt%.

are due to the slight compression in apical bond length and relaxation in CuO_2 planner bond lengths.

SEM images of $(CoFe_2O_4)_x$/CuTl-1223 composite samples are shown in Fig. 3. Some impression of agglomeration of magnetic nanoparticles have been observed in the composite sample with $x=2.0$ wt%. Similar results were already observed by Hafiz and Abd-Shukor [40] for nano-sized NiF_2 addition in $Bi_{1.4}Pb_{0.6}Sr_2Ca_2Cu_3O_{10+\delta}$ superconductor samples and Mohammad et al. [27] in studying the effect of nano-SnO_2 inclusion into the CuTl-1223 superconducting phase on superconducting properties.

FTIR is very sensitive technique used to detect a trace amount of impurities along with functional groups in the material. The FTIR absorption spectra of $(CoFe_2O_4)_x$/CuTl-1223 composites with $x=0$, 0.5, 1.0, 1.5 and 2.0 wt%, in the far infrared range from 400–700 cm^{-1} are shown in Fig. 4. The bands in the range from 400 to 540 cm^{-1} are associated with the apical oxygen atoms and in the range from 541 to 600 cm^{-1} are associated with CuO_2 planar oxygen atoms. The bands in the range from 670 to 700 cm^{-1} are associated with O_5 atoms in the charge reservoir layer [41–43]. Apical oxygen modes of type Tl–O_A–Cu(2) and Cu(1)–O_A–Cu(2) are observed around 418 cm^{-1} and 483 cm^{-1} and CuO_2 planner modes are observed around 533 cm^{-1} in pure $Cu_{0.5}Tl_{0.5}Ba_2Ca_2Cu_3O_{10-\delta}$ samples. The positions of both the apical oxygen modes were not altered significantly with the addition

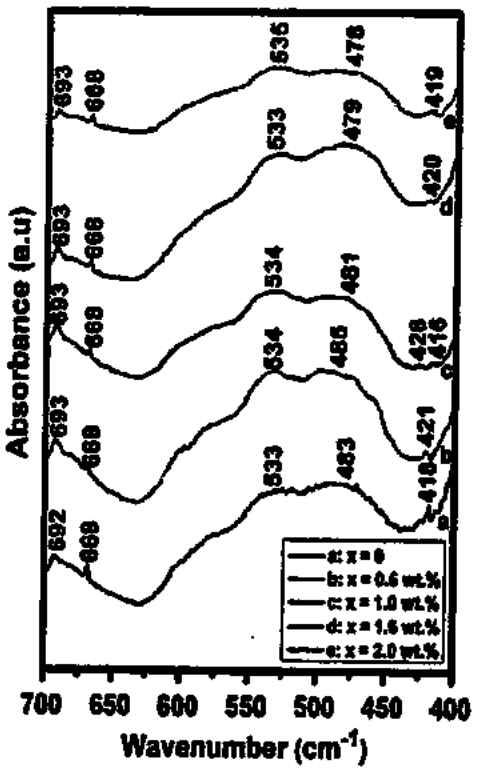

Fig. 4. FTIR absorption spectra of $(CoFe_2O_4)_x$/CuTl-1223 composites with (a) $x=0$, (b) $x=0.5$ wt%, (c) $x=1.0$ wt%, (d) $x=1.5$ wt%, and (e) $x=2.0$ wt%.

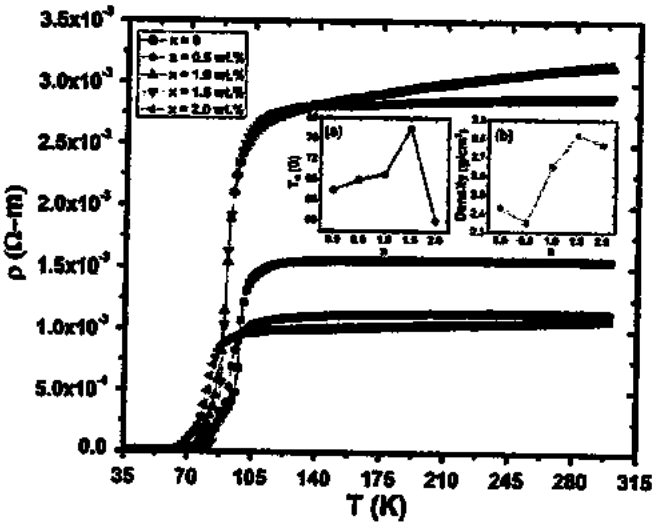

Fig. 5. Resistivity versus temperature measurements of $(CoFe_2O_4)_x$/CuTl-1223 composites; $x=0$, 0.5 wt%, 1.0 wt%, 1.5 wt%, and 2.0 wt%. In the inset (a) the variation of $T_c(0)$ versus x and in the inset (b) the variation of massive density versus x (i.e. $CoFe_2O_4$ nanoparticles).

of $CoFe_2O_4$ nanoparticles. The CuO_2 planner oxygen modes also did not change their positions with the addition of $CoFe_2O_4$ nanoparticles. The slight variation in these modes can be possibly due to stresses and strains produced in material after addition of these nanoparticles. The almost unchanged position of various oxygen modes with the addition of these nanoparticles showed that the unit cell structure of the host CuTl-1223 matrix remained unaltered. This is another indirect evidence of the occupancy of $CoFe_2O_4$ nanoparticles at the grain-boundaries. Therefore, these nanoparticles healed up the voids and improved the inter-grain coupling.

Resistivity versus temperature measurements of $(CoFe_2O_4)_x$/CuTl-1223 ($x=0$, 0.5, 1.0, 1.5 and 2.0 wt%) composites samples with various amounts of $CoFe_2O_4$ nanoparticles are shown in Fig. 5. The variation of T_c (0) versus $CoFe_2O_4$ nanoparticles content is shown in the inset (a) of Fig. 5. The values of T_c (0) for the samples with $x=0$, 0.5, 1.0, 1.5 and 2.0 wt% are around 66 K, 68 K, 69 K, 78 K and 60 K respectively. These measurements show that the value of $T_c(0)$ is increased after the addition of $CoFe_2O_4$ nanoparticles into CuTl-1223 superconducting matrix till $x=1.5$ wt% concentration and then suppressed on further increase in the amount of nanoparticles. The increase in T_c (0) after the inclusion of $CoFe_2O_4$ nanoparticles up to $x=1.5$ wt% is due improvement in the inter-grains connectivity and after certain optimum level of $CoFe_2O_4$ nanoparticles addition, the agglomeration starts which deteriorates the samples quality and produces stresses and strains in the materials [44,45]. In ceramic high T_c superconductors, there is always a resistive broadening due to two critical temperatures, one is the T_c^{onset} (K) at which Cooper pair formation starts and the second is the T_c (0) at which the materials goes into bulk superconducting state. The T_c^{onset} (K) depends on the electronic properties of the material, whereas $T_c(0)$ depends on the microstructure of the material and carriers density in the CuO_2 planes. The material with weak inter-grain connectivity and voids tends to have lower $T_c(0)$, as compared to that of a material with well connected and packed grains in spite of their equal T_c^{onset} (K). In the present article the T_c^{onset} (K) is monotonically decreasing with the increase of magnetic $CoFe_2O_4$ nanoparticles content, which is not surprising because magnetic nanoparticles have the ability to suppress the superconductivity. The reason behind the increase in $T_c(0)$ might be the improvement of the inter-grain connectivity, which is essential to get higher $T_c(0)$. The main problem is to make the distribution of $CoFe_2O_4$ nanoparticles uniform and homogeneous across the grain-boundaries of CuTl-1223 superconducting matrix. The non-monotonic variation of the normal state resistivities with magnetic $CoFe_2O_4$ nanoparticles content is most probably due to the inhomogeneous distribution of these nanoparticles at the grain-boundaries of the bulk material. The variation of mass density of $(CoFe_2O_4)_x$/CuTl-1223 composites with different content of $CoFe_2O_4$ nanoparticles is shown in the inset (b) of the Fig. 5. The overall slightly increasing trend in mass density is observed with increasing content of these nanoparticles in the matrix, which is an evidence of filling the voids in the bulk samples. Slightly non-monotonic variation in mass density can be most probably due to inhomogeneous distribution of these nanoparticles at the grain-boundaries of the samples.

4. Conclusion

The effects of highly coercive $CoFe_2O_4$ nanoparticles addition on the superconducting properties as well as on structure of the host CuTl-1223 matrix were investigated. We have synthesized $(CoFe_2O_4)_x$/CuTl-1223 composites samples successfully by two cycles solid-state reaction. The stoichiometry and crystal structure of the host CuTl-1223 matrix remained unchanged after the addition of $CoFe_2O_4$ nanoparticles. The enhancement in T_c (0) was observed with increasing contents of $CoFe_2O_4$ nanoparticles due to improvement of weak-links by filling the pores and crakes present in the bulk material. The increase in mass density of these samples after addition of these nanoparticles can also be due to filling of pores. The addition of these nanoparticles beyond a certain optimum concentration level causes agglomeration and produces additional stresses and strains in the bulk material and suppresses the superconducting properties. The suppression of $T_c(0)$ may due to pair-breaking mechanism caused by reflection/scattering of carriers and trapping or localization of mobile free carriers across the agglomerated $CoFe_2O_4$ nanoparticles present at grain-boundaries of the host CuTl-1223 superconducting matrix.

Acknowledgement

Authors would like to thank Higher Education Commission (HEC) of Pakistan for financial support through project no: PM-IPFP/HRD/HEC/2012/3511. We highly acknowledged the Material Science Laboratory, Department of Physics (QAU) Islamabad, Pakistan and Beijing National Laboratory of Condensed Matter Physics, Institute of Physics (IOP), Chinese Academy of Sciences (CAS) Beijing, China, for providing the characterization facilities.

References

[1] H. Ihara, K. Tanaka, Y. Tanaka, A. Iyo, N. Terada, M. Tokumoto, M. Ariyama, I. Hase, A. Sundaresan, N. Hamada, S. Miyashita, K. Tokiwa, T. Watanabe, Physica C 341–348 (2000) 487.
[2] M. Mumtaz, S.M. Hasnain, A.A. Khurram, Nawazish A. Khan, J. Appl. Phys. 109 (2011) 023906.
[3] H. Ihara, K. Tokiwa, K. Tanaka, T. Tsukamoto, T. Watanabe, H. Yamamoto, A. Iyo, M. Tokumoto, M. Umeda, Physica C 282–287 (1997) 957.
[4] M.H. Pu, W.H. Song, B. Zhao, X.C. Wu, T. Hu, Y.P. Sun, J.J. Du., Supercond. Sci. Tech. 14 (2001) 305–310.
[5] K.T. Lau, S.Y. Yahya, R. Abd-Shukor, J. Appl. Phys. 99 (2006) 123904.
[6] T. Haugan, P.N. Barnes, R. Wheeler, F. Meisenkothen, M. Sumption, Nature 430 (2004) 867.
[7] K. Togano, H. Kumakura, H. Maeda, E. Yanagisawa, K. Takahashi, Appl. Phys. Lett. 53 (1988) 1329–1331.
[8] Y.C. Guo, Y. Tanaka, T. Kuroda, S.X. Dou, Z.Q. Yang, Physica C 311 (1999) 65.
[9] E. Guilmeau, B. Andrzejewski, J.G. Noudem, Physica C 387 (2003) 382.
[10] T. Haugan, W. Wong-Ng, L.P. Cook, H.J. Brown, L. Swartzendruber, D.T. Shaw, Physica C 335 (2000) 129.
[11] S. Sengupta, V.R. Todt, P. Kostic, Y.L. Chen, M.T. Lanagan, K.C. Goretta, Physica C 264 (1996) 34.
[12] M. Annabi, F. A. M'chirgui, M. Ben Azzouz, Zouaoui, M. Ben Salem, Physica C 405 (2004) 25.
[13] A. Chattas, M. Annabi, M. Zouaoui, F. Ben Azzouz, M. Ben Salem, Physica C 468 (2008) 31.
[14] Z.Y. Jia, H. Tang, Z.Q. Yang, Y.T. Xing, Y.Z. Wang, G.W. Qiao, Physica C 337 (2000) 130.
[15] M.M. Elokret, R. Awad, A.A. El-Ghany, A.A. Shama, A. El-wanis, J. Supercond. Nov. Magn. 24 (2011) 1345.
[16] N.H. Mohammed, A.I. Abou-Aly, I.H. Ibrahim, R. Awad, M. Rekaby, J. Supercond. Nov. Magn. 24 (2011) 1463.
[17] N.H. Mohammed, A.I. Abou-Aly, I.H. Ibrahim, R. Awad, M. Rekaby, J. Alloy. Compound. 486 (2009) 733.
[18] Y. Xu, A. Hu, C. Xu, N. Sakai, I. Hirabayashi, M. Izumi, Physica C 468 (2008) 1363.
[19] Nawazish. A. Khan, A. Saleem, S.T. Hussain, J. Supercond. Nov. Magn. 25 (2012) 1725.
[20] M. Mumtaz, Asif I. Bhatti, K. Nadeem, Nawazish A. Khan, Abida Saleem, S. Tajammul Hussain, J. Low Temp. Phys. 170 (2013) 185.
[21] A. Snezhko, T. Prozorov, R. Prozorov, Phys. Rev. B 71 (2005) 024527.
[22] L.N. Bulaevskii, E.M. Chundnovsky, M.P. Maley, Appl. Phys. Lett. 76 (2000) 2594.
[23] T. Zhao, A. Scholl, F. Zavaliche, K. Lee, M. Barry, A. Doran, M.P. Cruz, Y.H. Chu, C. Ederer, N.A. Spaldin, R.R. Das, D.M. Kim, S.H. Baek, C.B. Eom, R. Ramesh, Nat. Mater 5 (2006) 823.
[24] T.J. Park, G.C. Papaefthymiou, A.J. Viescas, A.R. Moodenbaugh, S.S. Wong, Nano Lett. 7 (2007) 766.
[25] S. Acharya, A.K. Biswal, J. Ray, P.N. Vishwakarma, J. Appl. Phys. 112 (2012) 053916.
[26] H.J. Gardner, A. Kumar, L. Yu, P. Xiong, M.P. Warusawithana, L. wang, O. Vafek, D.G. Schlom, , Nat. Phys. 7 (2011) 895.
[27] N.H. Mohammad, A.I. Abou-Aly, R. Awad, I.H. Ibrahim, M. Roumie, M. Rekaby, J. Low Temp. Phys. 172 (2013) 234–255.
[28] N. Novosel, S. Galic, D. Pajic, Z. Skoko, I. Loncarek, M. Mustapic, K. Zadro, E. Babic, Supercond. Sci. Technol. 25 (2012) 095018.
[29] M.G. Blamire, R.B. Dinner, S.C. Wimbush, J.L. MacManus-Driscoll, Supercond. Sci. Technol. 22 (2009) 025017.
[30] B. Qu, X.D. Sun, J.-G. Li, Z.M. Xiu, S.H. Liu, C.P. Xue, Supercond. Sci.Technol. 22 (2009) 015027.
[31] C. Cheng, Y. Zhao, Physica C 463–465 (2007) 220.
[32] V.P.S. Awana, M. Isobe, K.P. Singh, E. Takayama-Muromachi, H. Kishan, Supercond. Sci. Technol. 19 (2006) S51, 19 (2006) 551.
[33] S.X. Dou, S. Soltanian, Y. Zhao, E. Getin, Z. Chen, O. Shcherbakova, J. Horvat, Supercond. Sci. Technol. 18 (2005) 710.

[34] T. Kuroda, T. Nakane, H. Uematsu, K. Kumakura, Supercond. Sci. Technol. 19 (2006) 1152.
[35] O.F. de Lima, K.B. Vieira, E. Moschim, V.P.S. Awana, H. Kishan, J. Mater. Sci. 45 (2010) 4929.
[36] N. Novosel, E. Babic, Physica C 493 (2013) 119.
[37] M. Mumtaz, S. Naeem, K. Nadeem, F. Naeem, Y.R. Abdul Jabbar, Zheng, Nawazish A. Khan, M. Imran, Solid Stat. Sci. 22 (2013) 21.
[38] S. Ammar, A. Helfen, N. Jouini, F. Fievet, I. Rosenman, F. Villain, P. Molinie, M. Danot, J. Mater. Chem. 11 (2001) 186–192.
[39] B.H. Liu, J. Ding, Z.L. Dong, C.B. Boothroyd, J.H. Yin, J.B. Yi, Phys. Rev. B 74 (2006) 184427.
[40] M. Hafiz, R. Abd-Shukor, Adv. Mater. Res. 895 (2014) 87–90.
[41] Nawazish A. Khan, M. Mumtaz, K. Sabeeh, M.I.A. Khan, Mushtaq Ahmad, Physica C 407 (2004) 103–114.
[42] Nawazish A. Khan, M. Mumtaz, Eur. Phys. J. Appl. Phys. 38 (2007) 47–51.
[43] M. Mumtaz, Nawazish A. Khan, Supercond. Sci. Technol. 21 (2008) 065015.
[44] J.C. Zhang, F.Q. Liu, G.S. Cheng, J.X. Shang, J.Z. Liu, S.X. Cao, Z.X. Liu, Phys. Lett. A 201 (1995) 70.
[45] P.F. Miceli, J.M. Tarascon, L.H. Greene, H.P. Barbou, F.J. Rotella, J.D. Jorgensen, Phys. Rev. B 37 (1988) 5932.

Journal of ELECTRONIC MATERIALS, Vol. 44, No. 1, 2015
DOI: 10.1007/s11664-014-3405-x

Structural and Superconducting Properties of $(Al_2O_3)_y$/CuTl-1223 Composites

ABDUL JABBAR,[1] IRFAN QASIM,[1] M. WAQEE-UR-REHMAN,[1] MUNAWAR ZAMAN,[1] K. NADEEM,[1] and M. MUMTAZ[1,2]

1.—Materials Research Laboratory, Department of Physics, Faculty of Basic and Applied Sciences (FBAS), International Islamic University (IIU), Islamabad 44000, Pakistan. 2.—e-mail: mmumtaz75@yahoo.com

The effects of nano-Alumina (Al_2O_3) particles inclusion on the structural and superconducting transport properties of $(Cu_{0.5}Tl_{0.5})Ba_2Ca_2Cu_3O_{10-\delta}$ (CuTl-1223) matrix were explored in detail. Different concentrations (i.e. y = 0–1.5 wt.%) of Al_2O_3 nanoparticles were added to a CuTl-1223 matrix to obtain the desired $(Al_2O_3)_y$/CuTl-1223 nano-superconducting composites. No significant change was observed in the crystal structure and stoichiometry of the host CuTl-1223 superconducting phase after the addition of Al_2O_3 nanoparticles. This indicates the occupancy of these nanoparticles at the intergranular spaces. The superconductivity was suppressed with increasing Al_2O_3 nanoparticles contents in the CuTl-1223 matrix. The suppression of superconducting properties is most probably due to a pair-breaking mechanism caused by the reflection/scattering of carriers across the insulating nano-Al_2O_3 particles present at the grain boundaries. The non-monotonic variation of the superconducting properties may be due to inhomogeneous distribution of Al_2O_3 nanoparticles at the grain boundaries.

Key words: CuTl-1223 superconductor, Al_2O_3 nanoparticles, superconducting properties, grain boundaries

INTRODUCTION

The $(Cu_{0.5}Tl_{0.5})Ba_2Ca_2Cu_3O_{10-\delta}$ (CuTl-1223) phase of $(Cu_{0.5}Tl_{0.5})Ba_2Ca_nCu_{n+1}O_{2n+4-\delta}$ high T_c superconducting family is most attractive due to its relatively larger critical current density (J_c), high superconducting transition temperature (T_c) and low superconducting anisotropy ($\gamma = \frac{\xi_{ab}}{\xi_c}$).[1–3] Two main constituents of the unit cell of this phase are the $Cu_{0.5}Tl_{0.5}Ba_2O_{4-\delta}$ charge reservoir layer (CRL) and the $nCuO_2$ conducting planes.[4,5] The effects of the substitution of impurities within the unit cell and the addition of suitable nanostructures (nanoparticles, nanorods, etc.) on the physical and structural properties of different superconducting families were investigated.[6–10] The addition of nanoparticles affects the superconducting properties by creating surface defects in the materials and varying the number of charge carriers in the CuO_2 planes. It has been observed in many superconducting families that superconductivity parameters vary by varying the oxygen contents.[11–15] The addition of elemental and oxides nanoparticles into high temperature superconductor (HTSC) matrices plays a vital role in increasing the critical current density (J_c) by the different mechanisms (i.e. flux pinning, inter-grain connectivity, etc.) occurring in the materials.[16–20] It has been reported that low concentrations of nano-ZnO addition in $(Cu_{0.5}Tl_{0.25}Pb_{0.25})$-1223 enhanced the superconducting transition temperature (T_c), critical current density (J_c) and melting point, while high concentrations of nano-ZnO enhanced the secondary phases and grain boundary resistance. This was possibly due to large agglomerations of nano-ZnO particles.[21] The microhardness of the CuTl-1223 superconducting phase was significantly improved by nano-SnO_2 particles addition.[22] It has also been observed that superconducting properties were improved by nano-Fe_2O_3 particles addition up

(Received May 20, 2014; accepted August 30, 2014; published online September 20, 2014)

to a certain concentration level and then started to decrease with a higher concentration of nano-Fe_2O_3 particles in the CuTl-1223 superconductor.[23] The suppression of superconducting properties was explained in terms of an enhanced pair-breaking mechanism due to scattering phenomenon at a higher concentration of nano-Fe_2O_3 particles in the CuTl-1223 superconductor. The nano-MgO particles addition up to 0.6 wt.% in the CuTl-1234 superconducting phase improved the phase formation, grain connectivity, and electrical transport properties, and reduced the thermal expansion co-efficient.[24] The improvement in J_c was believed to be due to the enhanced pinning effects of nano-MgO particles in the superconducting matrix.[25] No change observed in the tetragonal structure of the CuTl-1234 superconducting phase with the addition of nano-MgO particles. The study of the effects of Al_2O_3 nanoparticles addition on the superconducting properties of $YBa_2Cu_3O_y$ showed that there was no change in the structural symmetry, while the orthorhombicity slightly decreased with the increase of nano-Al_2O_3 particles content in the matrix. In an applied magnetic field, J_c of the superconducting material was observed to be enhanced significantly by nano-Al_2O_3 particles addition, which can be caused by the existence of the flux pinning centers.[26] The substitution of nano-Al_2O_3 particles did not affect the structural symmetry of the parent $YBa_2Cu_3O_y$ system, but the oxygen content was affected and therefore the superconductivity altered, as it is sensitive to oxygen content especially in this system. The effects of nano-Al_2O_3 particles addition in the polycrystalline (Bi, Pb)-2223 superconductors also illustrated the improvement of transport properties. The volume pinning force density, onset temperature of dissipation, activation energy and J_c in applied magnetic field were found to be improved.[27] The fluctuation-induced conductivity (FIC) analysis demonstrated that the three-dimensional (3D) conductivity region has been reduced, which is possibly due to scattering of mobile carriers across the nano-Al_2O_3 particles at the grain boundaries of the (Bi, Pb)-2223 superconducting matrix.[28] A small amount of nano-Al_2O_3 addition in $YBa_2Cu_3O_{7-\delta}$ (Y123) textured bulk superconductor has increased the J_c values that may be due to improved flux pinning after the inclusion of these insulating nanoparticles.[29] The structural symmetry of the Y123 superconducting matrix was also not affected after the inclusion of Al_2O_3 nanoparticles.[30] The improvement of J_c was most likely due to enhanced pinning effects by the insulating nano-Al_2O_3 particles acting as effective pinning centers in the Y123 superconducting matrix. The value of J_c depends upon the size, density of pinning centers and flux pinning strength. The values of J_c and H_{irr} were enhanced due to the presence of nano-Al_2O_3 particles at the grain boundaries of MgB_2 acting as strong pinning centers.[31] Some amount of aluminum (Al) was doped into the lattice and more Al_2O_3 nanoparticles were present at grain boundaries in the bulk at higher levels of nano-Al_2O_3 particles addition in the MgB_2 matrix.

We studied the effects of nano-Al_2O_3 particles addition on the superconductivity as well as on the crystal structure of the CuTl-1223 phase. The main motivation and objectives of the addition of Al_2O_3 nanoparticles were to improve the inter-grain connectivity by filling the pores present in the bulk form of the CuTl-1223 matrix and hence to enhance the superconducting properties. We were expecting the improvement of inter-grain weak links and grain size by the cementing effects of Al_2O_3 nanoparticles-added at the grain boundaries. The main issue is the uniform and homogeneous distribution of Al_2O_3 nanoparticles at the grain boundaries in the CuTl-1223 superconducting matrix. Still, this is an open question as to how can we make the distribution of Al_2O_3 nanoparticles uniform and homogeneous across the grain boundaries? The agglomeration of Al_2O_3 nanoparticles at interstitial spaces degrades the quality of the samples, resulting in the suppression of the superconducting properties. The non-monotonic variation in the superconductivity may be due to non-uniform and inhomogeneous distribution of Al_2O_3 nanoparticles at the grain boundaries. But the effects of Al_2O_3 nanoparticles addition in the CuTl-1223 superconducting matrix can be easily assessed from the inter-comparison of the variation of the superconducting properties of the nanoparticles-added and the non-added samples. The presence of nano-Al_2O_3 particles embedded in the superconductor matrix was investigated by x-ray diffraction (XRD), scanning electron microscopy (SEM), and energy dispersive x-rays (EDX) spectroscopy. The resistivity versus temperature, current versus voltage (IV), and Fourier transform infrared (FTIR) absorption measurements were carried out on the samples.

SAMPLES SYNTHESIS AND EXPERIMENTAL DETAILS

The nano-Al_2O_3 particles-added to bulk ceramic CuTl-1223 superconductor composites were synthesized by the two-cycle solid-state reaction method. Initially, $Ba(NO_3)_2$, $Ca(NO_3)_2$ and Cu(CN) compounds were used as starting compounds to prepare the $Cu_{0.5}Ba_2Ca_2Cu_3O_{10-\delta}$ precursor. These starting compounds were mixed in appropriate ratios and ground in an agate mortar and pestle for 2 h continuously. The mixed material was loaded into quartz boats and fired in a chamber furnace at 860°C for 24 h followed by furnace cooling to room temperature. The firing was completed in two steps each with 1 h intermediate grinding. Later on, this precursor material was mixed with Tl_2O_3 and different wt.% of Al_2O_3 nanoparticles of size 5 nm at the second stage and then ground again for 1 h to get $(Al_2O_3)_y$/CuTl-1223 (y = 0 wt.%, 0.5 wt.%, 1.0 wt.% and 1.5 wt.%) superconductor composites. The pellets of the final material were made under

3.8 tons/cm^2 pressure with the help of a hydraulic press. The pellets, enclosed in gold capsules, were sintered at 860°C for 10 min in a preheated chamber furnace followed by quenching to room temperature. Al_2O_3 nanoparticles were prepared separately by the co-precipitation method.

XRD (D/Max IIIC Rigaku with a CuK_α source of wavelength 1.54056 Å) was used for determination of phase purity and crystal structure of the material. With the help of a cell refinement computer program, cell parameters were determined. The conventional four-probe method was used for dc-resistivity and IV-measurements with the help of a commercial Physical Properties Measurement System (PPMS) manufactured by Quantum Design. The dimensions of the slab-shaped samples were $1.2 \times 1.0 \times 4.0$ mm^3 and four low-resistivity contacts were made on the samples with silver paint. The temperature stability was kept at 2 mK during these transport measurements. IV measurements were carried out at 50 K below the zero resistivity critical temperature, and the criterion of J_c for these IV measurements was kept at 1 μV/cm at 50 K in a zero external applied magnetic field for all the samples. The composition and morphology of the materials were examined by EDX spectroscopy and SEM with a JOEL Jed-2300. The phonon modes related to the vibrations of various oxygen atoms in the unit cell of the CuTl-1223 superconductor matrix were observed by FTIR absorption spectroscopy in the wave number range of 400–700 cm^{-1} with a Nicolet 5700 FTIR spectrometer. The FTIR absorption spectroscopy was carried out using potassium bromide (KBr) as a background material.

RESULTS AND DISCUSSION

The XRD pattern of the nano-Al_2O_3 particles is shown in Fig. 1. The various crystal features of Al_2O_3 nanoparticles, like crystal structure, crystallite size and diffraction pattern, are determined from the XRD spectrum. The random orientation of the crystals, smaller crystallite size, strains and structural faults lead to the peak broadening. The peaks are indexed with the cubic structure, and the average size of Al_2O_3 nanoparticles calculated by Sherrer's formula is found to be 5 nm. XRD analysis shows cubic structure and crystallinity with exquisitely indexed planes (3 1 1), (2 2 2), (4 0 0), (5 1 1) and (4 1 1), which are completely in accordance with International Center for Diffraction Data (ICDD). The typical XRD patterns of the $(Al_2O_3)_y$/CuTl-1223 superconductor matrix with $y = 0$ wt.%, 0.5 wt.%, and 1.0 wt.%, are shown in Fig. 2. The diffraction patterns indicate the dominance of the CuTl-1223 phase as most of the peaks are well indexed according to the tetragonal structure of this phase following the P4/mmm space group. The characteristic peak (001) of this CuTl-1223 phase appeared at $2\theta = 5.75°$ and there is no change in the overall XRD patterns for nano-Al_2O_3 particles-added samples,

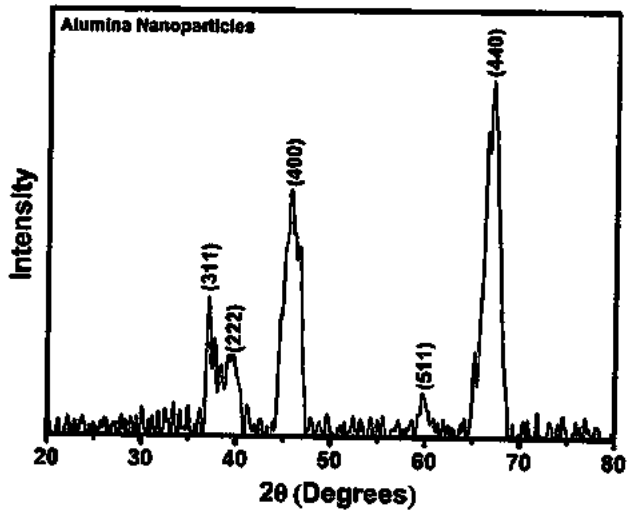

Fig. 1. XRD pattern of alumina (Al_2O_3) nanoparticles.

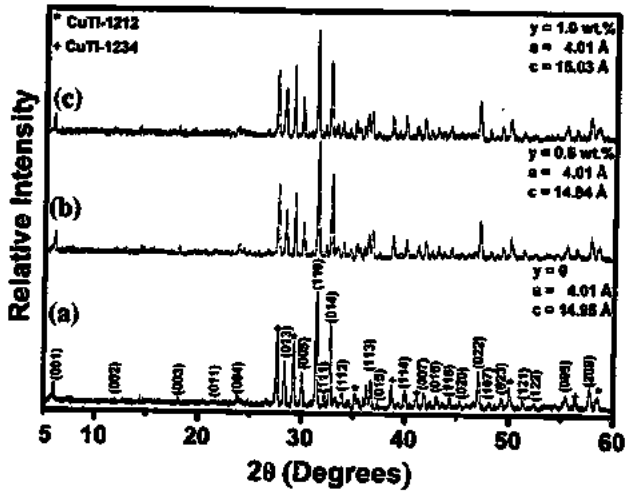

Fig. 2. XRD patterns of $(Al_2O_3)_y$/CuTl-1223 composites (a) $y = 0$, (b) $y = 0.5$ wt.%, and (c) $y = 1.0$ wt.%.

which may be evidence that there is no variation in the structural chemistry and stoichiometry after adding nano-Al_2O_3 particles. The structure of the CuTl-1223 phase remains preserved even with the existence of the Al_2O_3 nanoparticles, which clearly indicates that the nanoparticles occupy positions at the inter-crystallite boundaries of the CuTl-1223 superconductor matrix and help in improving the inter-grain weak links. Besides the dominant CuTl-1223 phase, a few non-indexed peaks appear which are possibly due to the presence of other superconducting phases and impurities. Therefore, the stoichiometry of the host CuTl-1223 compound remains unchanged after the addition of these nanoparticles. However, there is a slight variation of c-axis length, which may be due to oxygen (O_δ) variation or due to some stresses and strains, which can cause compression and relaxation in the apical bond length.

SEM images of $(Al_2O_3)_y$/CuTl-1223 samples show the presence of spherical and irregular nano-shapes among the plate-like grains of the host CuTl-1223 phase, which have reduced the inter-grain voids in the bulk samples, as shown Fig. 3. These nanoparticles remain at the inter-grain boundaries of the CuTl-1223 superconductor matrix and heal the inter-grain voids. Some of the nanoparticles present at the inter-grain boundaries are circled in the SEM images shown in Fig. 3b–d. In the SEM image, Fig. 3d, the agglomerations of nanoparticles can be visualized in large circles at some places. EDX spectrum shows the mass percentage of different elements in the composition (Fig. 4). SEM and EDX indicate that the nano-Al_2O_3 particles just occupy the interstitial spaces amongst the grains and do not enter into the crystal structure (i.e. unit cell) of the CuTl-1223 phase. Similar results were observed by Mellekh et al. [26] for Al_2O_3 nanoparticles-added to $YBa_2Cu_3O_y$ phase, and by Mohammad et al. [22] when studying the effect of nano-SnO_2 particles inclusion into the CuTl-1223 superconducting phase. The mass% of different elements present in the composition determined by the EDX analysis are listed in Table I for $y = 0$ wt.%, 0.5 wt.%, 1.0 wt.% and 1.5 wt.% in the CuTl-1223 matrix.

FTIR is a very sensitive technique used to detect a trace amount of impurities along with functional groups in the material. FTIR absorption spectra of $(Al_2O_3)_y$/CuTl-1223 composites with $y = 0$ wt.%, 0.5 wt.%, 1.0 wt.% and 1.5 wt.%, in the infrared range from 400 cm^{-1} to 700 cm^{-1}, are shown in Fig. 5. The bands in the range from 400 cm^{-1} to 540 cm^{-1} are associated with the apical oxygen atoms, and in the range from 541 cm^{-1} to 600 cm^{-1} are associated with CuO_2 planar oxygen atoms.[32,33] The bands in the range from 670 cm^{-1} to 700 cm^{-1} are associated with O_δ atoms in the charge reservoir layer.[34] In the pure $Cu_{0.5}Tl_{0.5}Ba_2Ca_2Cu_3O_{10-\delta}$ samples, the apical oxygen modes of type Tl–O_A–Cu(2) and Cu(1)–O_A–Cu(2) are observed around 418 cm^{-1} and 537 cm^{-1}, and the CuO_2 planner mode is around 580 cm^{-1}. The apical oxygen modes remain unchanged in the nano-Al_2O_3 particles-added samples. The CuO_2 planner mode is hardened to 591 cm^{-1} for $y = 1.0$ wt.% and slightly softened to 575 cm^{-1} and 576 cm^{-1} for $y = 0.5$ wt.% and 1.5 wt.%, respectively. The softening and hardening of these modes

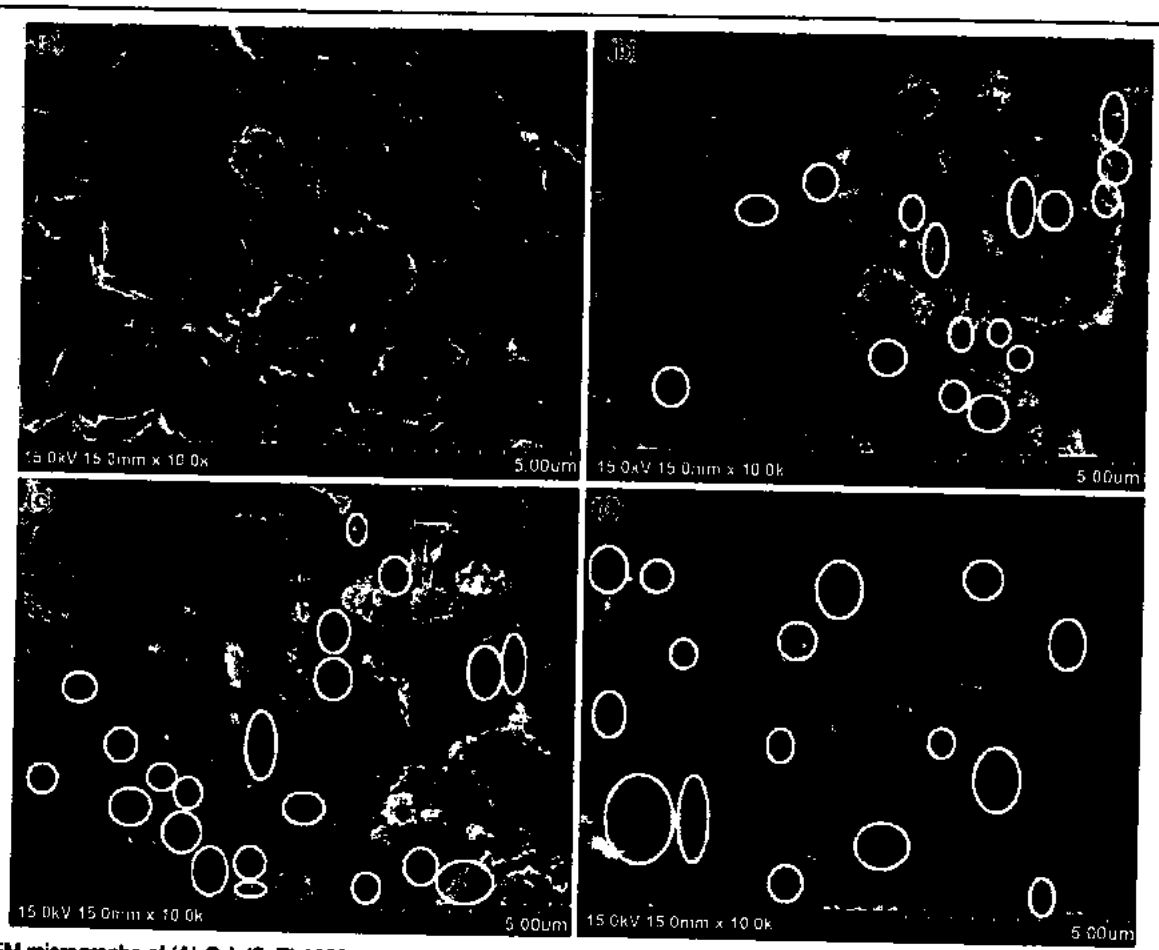

Fig. 3. SEM micrographs of $(Al_2O_3)_y$/CuTl-1223 composites with (a) $y = 0$, (b) $y = 0.5$ wt.%, (c) $y = 1.0$ wt.% and (d) $y = 1.5$ wt.%. (Some of the nanoparticles present at the inter-grain boundaries are circled in the SEM images of Al_2O_3 nanoparticles-added samples and agglomerations of nanoparticles can be visualized in large circles at some places).

is most likely associated with the stresses and strains produced in the materials after the addition of Al_2O_3 nanoparticles, which may affect the different bond length in the unit cell. There was no significant change in peak positions of oxygen modes after nanoparticles addition, but the shapes of the FTIR spectra are slightly different from one another with respect to the relative intensity for different samples. Different bond lengths in the unit cell can be affected due to stresses and strains produced in the materials by the inclusion of these nanoparticles as well as due to small variation in the O_δ in the CRL of the unit cell. This gives evidence that no decomposition of Al_2O_3 nanoparticles and no diffusion of Al in the unit cell of the host CuTl-1223 matrix have taken place. Therefore, the most suitable place of these nanoparticles in the CuTl-1223 matrix is the grain boundaries.

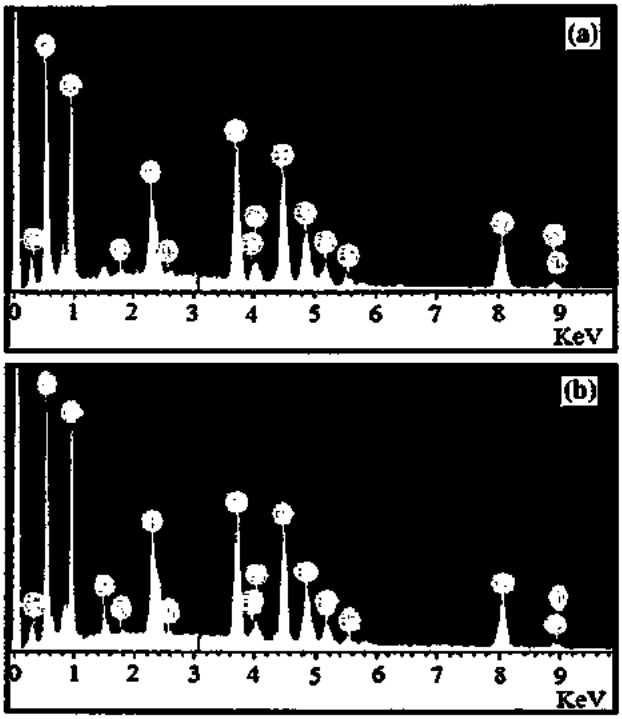

Fig. 4. Typical EDX spectra of $(Al2O3)_y$/CuTl-1223 composites (a) $y = 0$, (b) $y = 1.0\%$.

The measurements of resistivity versus temperature of $(Al_2O_3)_y$/CuTl-1223 (y = 0 wt.%, 0.5 wt.%, 1.0 wt.% and 1.5 wt.%) composites are shown in Fig. 6. All these samples have shown a metallic variation in resistivity from room temperature down to the onset of superconductivity with zero resistivity critical temperature [T_c (0)] around 86 K, 74 K, 72 K and 65 K. These measurements show that the value of T_c (0) is suppressed after the addition of nano-Al_2O_3 particles into the CuTl-1223 superconducting matrix. The absolute resistivity in normal state may strongly depend on porosity and grain boundary scattering. It is assumed that non-monotonic variation in T_c (0) is mainly because of non-uniform distribution of Al_2O_3 nanoparticles at the grain-boundaries of the host CuTl-1223 superconducting matrix. This decreasing behavior of T_c(0) with Al_2O_3 nanoparticles addition is either due to mechanisms related with oxygen vacancy disorder, or due to mobile holes trapping,[35–38] or due to lesser oxygen content in the material.[39] The possibility of the Al_2O_3 material dissolved into the matrix of the CuTl-1223 superconductor cannot be eliminated as it was synthesized at a higher temperature (860°C) for an elongated time (24 h).

The current versus voltage (*IV*) measurements of $(Al_2O_3)_y$/CuTl-1223 (y = 0 wt.%, 0.5 wt.%, 1.0 wt.% and 1.5 wt.%) composites are shown in Fig. 7. These *IV* measurements were carried out at 50 K below the zero resistivity critical temperature for the samples. The criterion of J_c for the *IV* measurements was kept at 1 μV/cm at 50 K in the zero external applied magnetic field for all the samples. The *IV* characteristics curves show the suppression of the critical current (I_c) with the addition of nano-Al_2O_3 particles in the CuTl-1223 superconducting matrix. The variation of J_c with different concentrations of nano-Al_2O_3 particles is shown in the inset of Fig. 7. This decreasing trend of J_c with increasing Al_2O_3 nanoparticles concentration is possibly due to the formation of superconductor–insulator–superconductor junctions in the composites. The insulating Al_2O_3 nanoparticles present at

Table I. Elemental analysis by EDX of $(Al_2O_3)_y$/CuTl-1223 composites with y = 0 wt.%, 0.5 wt.%, 1.0 wt.%, and 1.5 wt.%

	y = 0 wt.%			y = 0.5 wt.%			y = 1.0 wt.%			y = 1.5 wt.%		
Elements	**KeV**	**Mass%**	**At.%**	**KeV**	**Mass%**	**At.%**	**KeV**	**Mass%**	**At.%**	**KeV**	**Mass%**	**At.%**
O-K	0.535	20.68	58.05	0.536	18.78	54.65	0.538	20.40	57.08	0.540	20.22	55.96
Ca-K	3.695	8.87	9.94	3.696	9.16	10.64	3.698	7.67	8.57	3.702	8.78	9.70
Cu-L	0.952	26.93	19.03	0.955	26.00	19.05	0.958	27.85	19.62	0.960	27.48	19.15
Ba-L	4.484	31.83	10.41	4.486	33.55	11.37	4.488	30.16	9.83	4.492	30.63	9.88
Tl-M	2.325	11.70	2.57	3.321	11.54	2.63	2.318	12.64	2.77	2.315	11.12	2.41
Al-K	–	–	–	1.495	0.96	1.66	1.510	1.28	2.13	1.525	1.77	2.90
Total		100	100		100	100		100	100		100	100

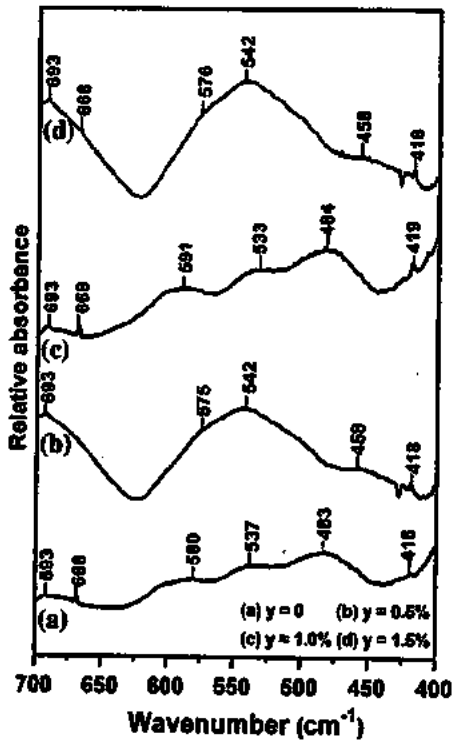

Fig. 5. FTIR absorption spectra of $(Al_2O_3)_y$/CuTl-1223 composites with (a) $y = 0$, (b) $y = 0.5$ wt. %, (c) $y = 1.0$ wt.%, and (d) $y = 1.5$ wt.%.

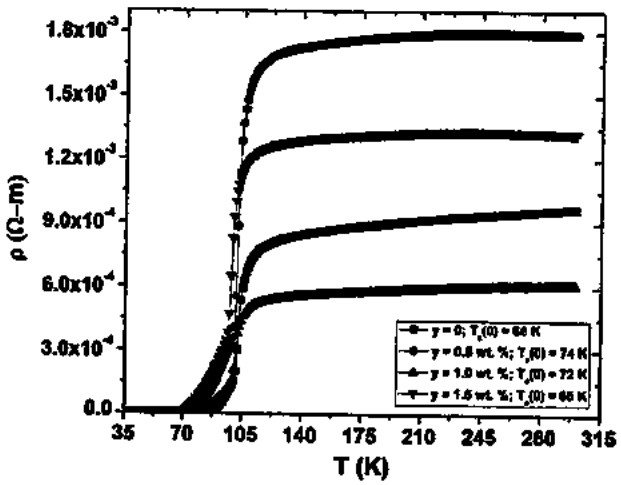

Fig. 6. Resistivity versus temperature measurements of $(Al_2O_3)_y$/CuTl-1223 composites with $y = 0.0$ wt.%, 0.5 wt.%, 1.0 wt.%, and 1.5 wt.%.

the grain boundaries reduce the activation energy of the carriers due to which pair-breaking occurs and superconducting parameters are suppressed.[40] But, we expect that Al_2O_3 nanoparticles will act as active pinning centers in the external applied magnetic field measurements.[26–31] The pinning effects of these nanoparticles will be explored by infield measurements of these composites, which are under way. In this paper, we have only reported the effects of Al_2O_3 nanoparticles addition on the structural

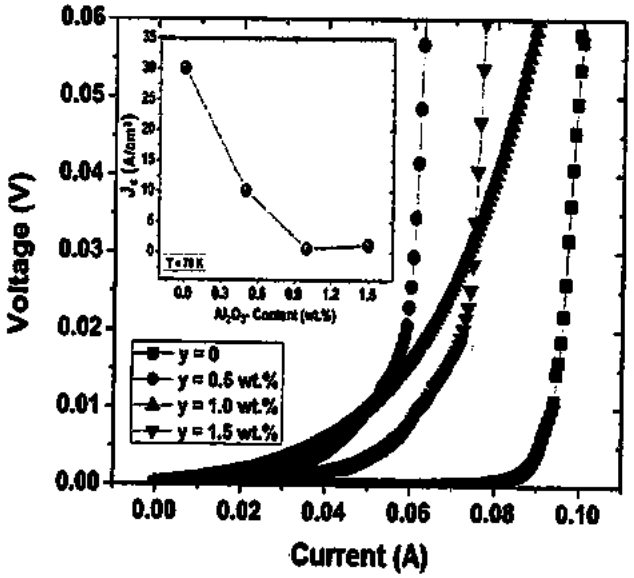

Fig. 7. Current versus voltage (IV) measurements of $(Al_2O_3)_y$/CuTl-1223 composites with $y = 0$ wt.%, 0.5 wt.%, 1.0 wt.%, and 1.5 wt.%. (In the inset J_c(A/cm^2) versus nano-Al_2O_3 particles content is shown).

and superconducting transport properties of the CuTl-1223 matrix without the external applied magnetic field. All the experimental results are very consistent and support each other.

CONCLUSION

The effects of nano-Al_2O_3 particles addition on superconducting parameters as well as on the phase formation of CuTl-1223 were investigated. The tetragonal structure of the CuTl-1223 matrix was not affected by the inclusion of Al_2O_3 nanoparticles, which provided a clue about the occupancy of these nanoparticles at the grain boundaries. The mass% of Al and O elements calculated from the EDX spectrum confirmed the presence of Al_2O_3 nanoparticles in the CuTl-1223 matrix. The suppression of T_c (0) and J_c was observed with increasing contents of Al_2O_3 nanoparticles. The suppression of these superconducting properties is most probably due to the pair-breaking mechanism caused by the reflection/scattering of the carriers during their transport across the insulating nano-Al_2O_3 particles present at the grain boundaries. The insulating nano-Al_2O_3 particles forming the superconductor–insulator–superconductor junctions in the $(Al_2O_3)_y$/CuTl-1223 composites has suppressed the superconductivity parameters. The quality of the $(Al_2O_3)_y$/CuTl-1223 composites samples were gradually deteriorated with increasing contents of Al_2O_3 nanoparticles in the CuTl-1223 matrix. The agglomeration of Al_2O_3 nanoparticles at the grain boundaries severely suppresses the superconductivity due to the reduction of the superconducting volume fraction and increased insulating nature of the grain boundaries.

ACKNOWLEDGEMENTS

We are grateful to the Higher Education Commission (HEC) of Pakistan for continuous financial support. We are also highly grateful to Dr. Nawazish A. Khan and Prof. Qiu Xiang-Gang for providing the characterization facilities at Material Science Laboratory, Department of Physics (QAU) Islamabad, Pakistan and Beijing National Laboratory of Condensed Matter Physics, Institute of Physics (IOP), Chinese Academy of Sciences (CAS) Beijing, China.

REFERENCES

1. H. Ihara, K. Tokiwa, H. Ozawa, M. Hirabayashi, A. Negishi, H. Matuhata, and Y.S. Song, *Jpn. J. Appl. Phys.* 33, L503 (1994).
2. H. Ihara, *Physica C* 364–365, 289 (2001).
3. Z.Z. Sheng and A.M. Hermann, *Nature* 332, 55 (1988).
4. Z.Z. Sheng, A.M. Hermann, A.E. Ali, C. Almasan, J. Estrada, T. Datta, and R.J. Matson, *Phys. Rev. Lett.* 60, 937 (1988).
5. Z.Z. Sheng and A.M. Hermann, *Nature* 332, 138 (1988).
6. G. Malandrino, D.S. Richeson, T.J. Marks, D.C. De Groot, J.L. Schindler, and C.R. Kannewurf, *Appl. Phys. Lett.* 58, 182 (1991).
7. M.L. Chu, H.L. Chang, C. Wang, J.Y. Juang, T.M. Uen, and Y.S. Gou, *Appl. Phys. Lett.* 59, 1123 (1991).
8. W.L. Oslon, M.M. Eddy, T.W. James, R.B. Hammond, G. Gruner, and L. Drabeck, *Appl. Phys. Lett.* 55, 188 (1989).
9. S.H. Yun and J.Z. Wu, *Appl. Phys. Lett.* 68, 862 (1996).
10. M. Annabi, A.M. Chirgui, F.B. Azzuoz, and M.B. Salem, *Physica C* 25, 405 (2004).
11. N.A. Khan, M. Mumtaz, K. Sabeeh, M.I.A. Khan, and M. Ahmed, *Physica C* 407, 103 (2004).
12. K. Semba, A. Matsuda, and T. Ishii, *Phys. Rev. B* 49, 10043 (1996).
13. M.K. Wu, J.R. Ashburn, C.J. Torng, P.H. Hor, R.L. Meng, L. Gao, Z.J. Huang, Y.Q. Wang, and C.W. Chu, *Phys. Rev. Lett.* 58, 908 (1987).
14. K. Heine, J. Tenbrink, and M. Thoner, *Appl. Phys. Lett.* 55, 2441 (1989).
15. J.Y. Yuang, J.H. Horng, S.P. Chen, C.M. Fu, K.H. Wu, T.M. Uen, and Y.S. Gou, *Appl. Phys. Lett.* 66, 885 (1995).
16. M. Mumtaz, N.A. Khan, and S. Khan, *J. Appl. Phys.* 107, 103905 (2010).
17. M. Mumtaz, N.A. Khan, and E.U. Khan, *Physica C* 470, 428 (2010).
18. N.A. Khan and M. Mumtaz, *J. Low Temp. Phys.* 151, 1221 (2008).
19. C. Wang, Z. Gao, L. Wang, Y. Qi, D. Wang, C. Yao, Z. Zhang, and Y. Ma, *Supercond. Sci. Technol.* 23, 055002 (2010).
20. B.P. Mikhailov, G.S. Burkhanov, G.M. Leitus, G.N. Mikhailova, A.M. Prokhorov, A.S. Seferov, A.V. Troitskii, and I.E. Lapshina, *Inorganic Mater.* 32, 1073 (1996).
21. M.M. Elokr, R. Awad, A.A. El-Ghany, A. Shams, and A.A. El-wanis, *J. Supercond. Nov. Magn.* 24, 1345 (2011).
22. N.H. Mohammad, A.I. Abou-Aly, I.H. Ibrahim, R. Awad, and M. Rek-aby, *J. Alloys Compd.* 486, 733 (2009).
23. N.H. Mohammad, A.I. Abou-Aly, R. Awad, I.H. Ibrahim, M. Roumie, and M. Rekaby, *J. Low Temp. Phys.* 172, 234 (2013).
24. S.G. Elsharkawy and R. Awad, *J. Alloys Compd.* 478, 642 (2009).
25. R. Awad, *J. Supercond. Nov. Magn.* 21, 461 (2013).
26. A. Mellekh, M. Zouaoui, F.B. Azzouz, M. Annabi, and M.B. Salem, *Solid Stat. Commun.* 140, 318 (2006).
27. A. Ghattas, F.B. Azzouz, M. Annabi, M. Zouaoui, and M.B. Salem, *J. Phys.* 97, 012175 (2008).
28. M. Annabi, A. Ghattas, M. Zouaoui, F.B. Azzouz, and M.B. Salem, *J. Phys.* 150, 052008 (2009).
29. N. Moutalibi, A. M'chirgui, and J. Noudem, *Physica C* 470, 568 (2010).
30. A. Mellekh, M. Zouaoui, F.B. Azzouz, M. Annabi, and M.B. Salem, *Physica C* 460–462, 426 (2007).
31. X.F. Rui, J. Chen, X. Chen, W. Guo, and H. Zhang, *Physica C* 412–414, 312 (2004).
32. K. Nadeem, F. Naeem, M. Mumtaz, S. Naeem, A. Jabbar, I. Qasim, and N.A. Khan, *Ceram. Int.* 40, 13819 (2014).
33. M. Mumtaz, M. Zubair, N.A. Khan, and S. Abbas, *Low Temp. Phys.* 40, 259 (2014).
34. M. Mumtaz, S. Naeem, K. Nadeem, F. Naeem, A. Jabbar, Y.R. Zheng, N.A. Khan, and M. Imran, *Solid Stat. Sci.* 22, 21 (2013).
35. J.C. Zhang, F.Q. Liu, G.S. Cheng, J.X. Shang, J.Z. Liu, S.X. Cao, and Z.X. Liu, *Phys. Lett. A* 201, 70 (1995).
36. P.F. Miceli, J.M. Tarascon, L.H. Greene, H.P. Barbou, F.J. Rotella, and J.D. Jorgensen, *Phys. Rev. B* 37, 5932 (1988).
37. S. Cao, L. Li, F. Liu, W. Li, C. Chi, C. Jing, and J. Zhang, *Supercond. Sci. Technol.* 18, 606 (2005).
38. V.P.S. Awana, S.K. Malik, W.B. Yelon, C.A. Cardoso, O.F. de Lima, A. Gupta, A. Sedky, and A.V. Narlikar, *Physica C* 338, 197 (2000).
39. E. Brecht, W.W. Schmahl, G. Miehe, M. Rodewald, H. Fuess, N.H. Andersen, J. Hanßmann, and Th. Wolf, *Physica C* 265, 53 (1996).
40. A. Jabbar, I. Qasim, M. Mumtaz, M. Zubair, K. Nadeem, and A.A. Khurram, *J. Appl. Phys.* 115, 203904 (2014).

JOURNAL OF APPLIED PHYSICS 115, 203904 (2014)

Suppression of activation energy and superconductivity by the addition of Al_2O_3 nanoparticles in CuTl-1223 matrix

Abdul Jabbar,[1] Irfan Qasim,[1] M. Mumtaz,[1,a)] M. Zubair,[1] K. Nadeem,[1] and A. A. Khurram[2]
[1]*Materials Research Laboratory, Department of Physics, FBAS, International Islamic University (IIU) Islamabad, Islamabad 44000, Pakistan*
[2]*Experimental Physics Labs, National Centre for Physics, Islamabad, Pakistan*

(Received 25 February 2014; accepted 10 May 2014; published online 23 May 2014)

Low anisotropic $(Cu_{0.5}Tl_{0.5})Ba_2Ca_2Cu_3O_{10-\delta}$ (CuTl-1223) high T_c superconducting matrix was synthesized by solid-state reaction and Al_2O_3 nanoparticles were prepared separately by co-precipitation method. Al_2O_3 nanoparticles were added with different concentrations during the final sintering cycle of CuTl-1223 superconducting matrix to get the required $(Al_2O_3)_y$/CuTl-1223, y = 0.0, 0.5, 0.7, 1.0, and 1.5 wt. %, composites. The samples were characterized by X-ray diffraction (XRD), scanning electron microscopy, energy dispersive X-ray, and dc-resistivity (ρ) measurements. The activation energy and superconductivity were suppressed with increasing concentration of Al_2O_3 nanoparticles in (CuTl-1223) matrix. The XRD analysis showed that the addition of Al_2O_3 nanoparticles did not affect the crystal structure of the parent CuTl-1223 superconducting phase. The suppression of activation energy and superconducting properties is most probably due to weak flux pinning in the samples. The possible reason of weak flux pinning is reduction of weak links and enhanced inter-grain coupling due to the presence of Al_2O_3 nanoparticles at the grain boundaries. The presence of Al_2O_3 nanoparticles at the grain boundaries possibly reduced the number of flux pinning centers, which were present in the form of weak links in the pure CuTl-1223 superconducting matrix. The increase in the values of inter-grain coupling (α) deduced from the fluctuation induced conductivity analysis with the increased concentration of Al_2O_3 nanoparticles is a theoretical evidence of improved inter-grain coupling. © *2014 AIP Publishing LLC.* [http://dx.doi.org/10.1063/1.4879197]

I. INTRODUCTION

The selection of the superconducting material for their applications depends upon the values of superconducting critical parameters (i.e., critical temperature T_c, critical current density J_c, critical magnetic field H_c). CuTl-based superconducting family has the second highest values of above mentioned critical parameters after Hg-based superconductor.[1,2] We have selected CuTl-1223 superconducting matrix due to its ambient synthesis conditions especially pressure and highest values of critical parameters.[3–6] The presence of inter-grain voids, impurity phases, oxygen vacancies, inhomogeneous micro-defects, etc., affects the performance of these compounds in bulk form due to their granular nature. One of the most important issues addressed in the literature is magnetic flux that cannot be completely expelled but is contained within magnetic fluxions, whose motion prevents the larger supercurrent. In polycrystalline bulk samples, the inter-granular critical current density is limited by the weak links caused by grain-boundaries and the intra-granular critical current is impeded principally by the thermally activated flux flow at high temperatures and in applied magnetic fields. To avoid the vortex motions and to enhance the flux pinning strength, it is necessary to introduce artificial pinning centers in the superconductor apart from those that occur naturally.[3–14] Various techniques such as high energy ion irradiation,[15] chemical doping and additives[16–18] were reported in the literature to act as artificial pinning centers. Various kinds of nano-additives including metallic and non-metallic nano-particles[10,11,19,20] and carbon nano-tubes[18] have shown positive effects on superconducting properties of various high temperature superconductor families. These additives improve the pinning ability by forming composites or acting as column defects comprised of nano-structures such as nanodots and nanorods.[21–23] The effect of nano sized SiC addition on polycrystalline Bi-2223 was reported[24] and was found that a small amount of SiC (0.15 wt. %) improved the critical current I_c and its behavior in magnetic field as a result of the enhancement in density, grain alignment, grain connectivity, and flux pinning in the samples. However, larger Si-based nano-additive concentrations inhibit the formation of the high T_c phase and decrease J_c. Nano-sized SiO_2 addition shows a negative effect on T_c and J_c of $SmBa_2Cu_3O_7$ materials due to the reaction between SiO_2 and matrix.[25] Structural analysis shows that SiO_2 addition leaves the Y-123 structure practically intact but influences the inter-grain regions of the $(YBa_2Cu_3O_{7-d})_{1-x}/(SiO_2)_x$ composite samples.[26] The effects of Al_2O_3 nanoparticles addition on the superconducting properties of $YBa_2Cu_3O_y$ showed that there was no change in the structural symmetry. Oxygen contents were changed in $YBa_2Cu_3O_y$ after nano-Al_2O_3 addition and, therefore, the superconductivity altered as it is sensitive to oxygen contents especially in this system.

a)E-mail: mmumtaz75@yahoo.com. Telephone: +92-51-9019715. Fax: +92-51-9210256.

A significant increase of J_c was observed in applied magnetic field, after nano-Al_2O_3 addition in $YBa_2Cu_3O_y$, which can be rendered to the existence of the flux pinning centers.[27] The addition of nano-Al_2O_3 in polycrystalline (Bi, Pb)-2223 also showed the improvement in transport properties. The volume pinning force density, onset temperature of dissipation, activation energy, and J_c in applied magnetic field were also improved.[28] The excess conductivity analysis showed that the width of three dimensional (3D) region has been reduced in nano-Al_2O_3 added polycrystalline (Bi, Pb)-2223 superconductors samples.[29] This effect was explained on the basis of the mobile carriers scattering source caused by nano-Al_2O_3 inclusion in (Bi, Pb)-2223 superconducting matrix. The J_c values were increased with a slight addition of alumina nano-particles in $YBa_2Cu_3O_{7-\delta}$ (Y123) textured bulk superconductor that may be due to stabilization of the flux lines lattice by the inclusion of insulating alumina nano-particles.[30] No change in the structural symmetry was observed in Y123 superconducting matrix by the inclusion of Al_2O_3 nano-particles.[31] The improvement of J_c with nano-alumina particles inclusion was likely rendered to the insulating nano-pinning centers embedded into Y123 superconducting matrix. It was also observed that the size of pinning centers can affect the J_c as well as the pinning mechanism. The experimental results showed that nano-alumina present at the grain boundaries of MgB_2 enhanced J_c and H_{irr} through strong pinning centers.[32] It was also observed that at higher level of nano-alumina addition, some amount of Al was doped into the lattice of MgB_2 and more Al_2O_3 nano-particles were present in the bulk of material.

To provide more evidence concerning the effect of Al_2O_3 nano-particles inclusion on the superconducting properties of CuTl-1223 bulk ceramics, a series of samples added with different amounts of Al_2O_3 (0–1.5 wt. %) were prepared by two steps solid-state reaction. We present our experimental results on the superconducting properties and the changes in microstructure correlated with nano-sized Al_2O_3 addition and the pinning mechanisms. The superconductivity dependence has been studied with a central objective to determine the dominant source and mechanism of vortex pinning.

II. EXPERIMENTAL DETAILS AND ANALYSIS

$(Al_2O_3)_y$/CuTl-1223 (y = 0.0%, 0.5%, 0.7%, 1.0%, and 1.5%) composites were synthesized by two cycles solid-state reaction. $Ba(NO_3)_2$, $Ca(NO_3)_2$, and Cu(CN) compounds were mixed in appropriate ratios and ground in an agate mortar and pestle for 2 h. The mixed material was loaded in quartz boats and fired in chamber furnace at 860 °C for 24 h followed by furnace cooling to room temperature. The firing step was repeated twice following 1 h intermediate grinding each time to get $Cu_{0.5}Ba_2Ca_2Cu_3O_{10-\delta}$ precursor material. The nano-particles of Al_2O_3 were separately prepared by co-precipitation method. The precursor material was mixed with Tl_2O_3 and different wt. % of Al_2O_3 nano-particles of 5 nm in size at second stage and then ground again for 1 h to get $(Al_2O_3)_y$/CuTl-1223 nano-superconductor composites. The material was then pelletized under 3.8 tons/cm^2 pressure and the pellets were enclosed in gold capsules for sintering at 860 °C for 10 min followed by quenching to room temperature.

The structure and phase purity of the samples were determined by X-ray diffraction (XRD) (D/Max IIIC Rigaku with a CuKα source of wavelength 1.54056 Å) specifying the CuTl-1223 dominant phase. The cell parameters were determined by cell refinement computer program. The composition and morphology of the materials were determined by energy dispersive X-ray (EDX) and scanning electron microscopy (SEM). Resistivity of the samples was measured by a commercial Physical Properties Measurement System (PPMS) manufactured by Quantum Design. The samples were cut in slab form with dimensions of $1.2 \times 1.0 \times 4.0$ mm^3 and low resistance contacts were made on the samples with silver paint. The temperature stability was kept 2 mK during these measurements. The dc-resistivity measured data were analyzed with the help of Aslamasov-Larkin (AL) Model. Fluctuation induced conductivity (FIC) analysis gives information about the scattering and superconducting pairing in cuprates as T approaches T_c^{onset} (K). The excess conductivity is

$$\Delta\sigma(T) = \left[\frac{\rho_n(T) - \rho(T)}{\rho_n(T)\rho(T)}\right], \quad (1)$$

where ρ(T) is the actually measured resistivity, and $\rho_n(T) = \alpha T + b$ is the normal-state resistivity of the sample extrapolated to resistivity at 0 K. The fluctuation conductivity according to AL theory is given as

$$\Delta\sigma(T) = A\varepsilon^{-\lambda}, \quad (2)$$

where A is the fluctuation amplitude, λ is dimensional exponent, and $\varepsilon = [T/T_c^{mf} - 1]$ is the reduced temperature and T_c^{mf} is usually referred to as the mean field critical temperature.[33,34] The exponent λ determines the dimensionality of the superconducting fluctuations and is given as $\lambda = 2 - D/2$; $\lambda = 1/2$, 1, 3/2 for three, two, and one dimensional fluctuations, respectively. A cross-over from two dimensional (2D) to three dimensional (3D) conductivity occurs at a cross-over temperature

$$T_o = T_c\left[1 + \left(\frac{2\xi_c(0)}{d}\right)^2\right]. \quad (3)$$

The second term is the inter-layer coupling strength, which is related to the reduced temperature ε by $J = \varepsilon/4$. In layered superconductors at very low temperature close to zero resistivity temperature $\xi_c > d$, where d is the distance between the conducting layers of adjacent unit cells (d is approximately equal to the c-axis lattice parameter of the unit cell).

III. RESULTS AND DISCUSSION

The typical XRD patterns of $(Al_2O_3)_y$/CuTl-1223 composites with y = 0 and 1.5 wt. % are shown in Fig. 1. The XRD patterns indicate the dominance of CuTl-1223 phase as most of the diffraction peaks are well indexed according to

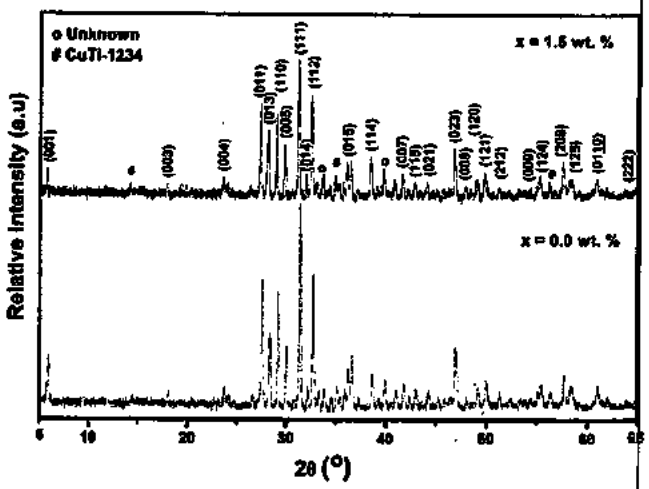

FIG. 1. XRD patterns of $(Al_2O_3)_y$/CuTl-1223 composites (a) y = 0.0% and (b) y = 1.5%.

tetragonal structure following the P4/mmm space group. The characteristic (001) peak of CuTl-1223 phase appeared at $2\theta = 5.75°$ and also there is no change in the overall XRD patterns of nano-Al_2O_3 added samples. The unit cell parameters calculated by computer software (crystal) are a = 4.01 Å, c = 14.95 Å for y = 0, and a = 4.13 Å, c = 15.16 Å for y = 1.5%, respectively. The structure of CuTl-1223 phase remains preserved even with the presence of Al_2O_3 nano-particles in the matrix. Therefore, the nano-particles can occupy the positions at the inter-crystallite boundaries of CuTl-1223 superconducting matrix and help in improving the inter-grain weak links. Beside the dominant CuTl-1223 phase, few nonindexed peaks may possibly be due to the presence of impurities as well as some other superconducting phases. Therefore, the stoichiometry of the host CuTl-1223 compound remains unchanged after the addition of these nanoparticles. The slight shift in the diffraction peaks to lower angles is due to the uniform strain produced in the materials after the addition of Al_2O_3 nanoparticles. Also, the slight variation in the c-axis length may be due to variation of oxygen (O_5), which can change the apical bond length.

TABLE I. Elemental quantitative analysis of CuTl-1223 superconductor with (a) 0.0 wt. % and (b) 1.50 wt. % Al_2O_3 added sample as presented in EDX graph.

	(a) 0.0 wt. % Al_2O_3 nanoparticles			(b) 1.5 wt. % Al_2O_3 nanoparticles		
Elements	KeV	Mass%	Atom%	KeV	Mass%	Atom%
O K	0.535	20.68	58.05	0.540	20.22	55.96
Ca K	3.695	8.87	9.94	3.702	8.78	9.70
Cu L	0.952	26.93	19.03	0.960	27.48	19.15
Ba L	4.484	31.83	10.41	4.492	30.63	9.88
Tl M	2.325	11.70	2.57	2.315	11.12	2.41
Al K	...	...	...	1.525	1.77	2.90
Total		100.00	100.00		100.00	100.00

The SEM images and EDX spectra of $(Al_2O_3)_y$/CuTl-1223 samples with y = 0 and 1.5 wt. % are shown in Fig. 2. The improvement in the grains size after the addition of nano-Al_2O_3 is possibly due to the presence of these nano-particles at the inter-grain boundaries that can heal up the inter-grain voids in CuTl-1223 superconductor matrix. The EDX spectra show the mass percentage of different elements in the composition. The SEM, EDX, and XRD indicate that the nano-Al_2O_3 particles just occupy the interstitial spaces amongst the grains and do not enter into the structure of CuTl-1223 phase. Similar results were observed by Mellekh *et al.*[27] for Al_2O_3 nanoparticles added $YBa_2Cu_3O_y$ phase and Mohammad *et al.*[35] in studying the effect of nano-SnO_2 inclusion into the CuTl-1223 superconducting phase. The mass percentages of different elements present in $(Al_2O_3)_y$/CuTl-1223 composition determined by the EDX analysis are listed in Table I.

Resistivity versus temperature measurements of $(Al_2O_3)_y$/CuTl-1223 composites with various amounts of nano-Al_2O_3 particles are shown in Fig. 3 and in the inset,

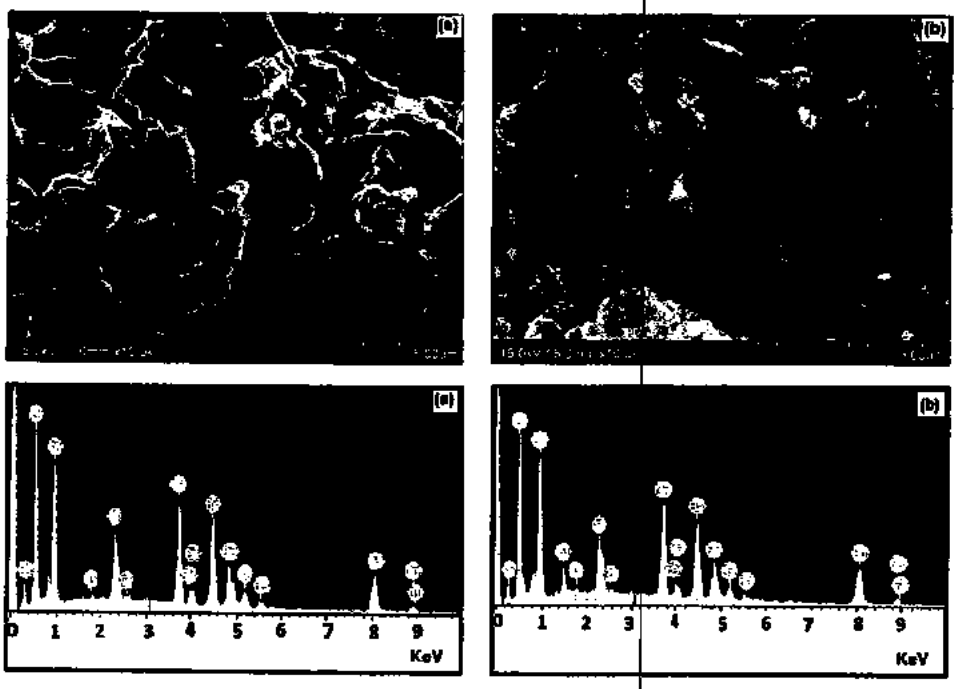

FIG. 2. Typical SEM micrographs and EDX spectra of $(Al_2O_3)_x$/CuTl-1223 composites (a) x = 0.0% and (b) x = 1.5%.

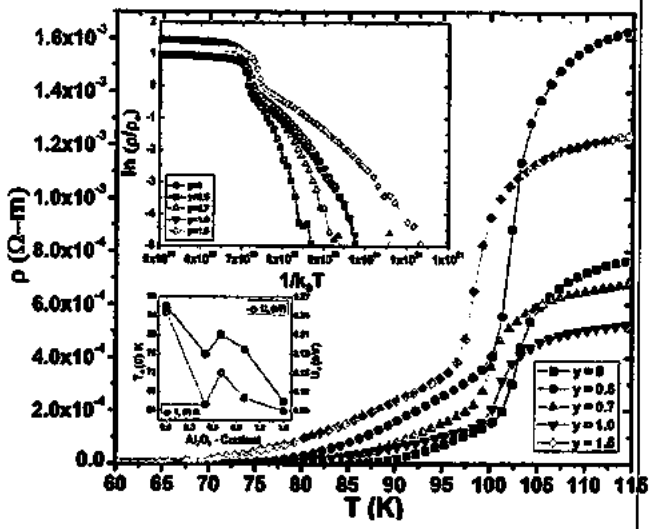

FIG. 3. Resistivity versus temperature measurements of $(Al_2O_3)_y$/CuTl-1223 composites with y = 0.0, 0.5, 0.7, 1.0, and 1.5 wt. %. In the inset are given the Arrhenius plots of $(Al_2O_3)_y$/CuTl-1223 composites with y = 0.0, 0.5, 0.7, 1.0, and 1.5 wt. %, activation energy, and T_c versus nano-Al_2O_3 contents.

there are shown the Arrhenius plots, activation energy, and T_c versus Al_2O_3 contents. There is a metallic variation in resistivity from room temperature down to onset of superconductivity for all these samples with zero resistivity critical temperature {T_c (R = 0)} around 86 K, 74 K, 79 K, 75 K, and 64 K for y = 0.0%, 0.5%, 0.7%, 1.0%, and 1.5%, respectively. These measurements show that the value of T_c (R = 0) is suppressed after nano-Al_2O_3 addition in CuTl-1223 superconducting matrix. The variation of T_c (R = 0) with different concentrations of nano-Al_2O_3 particles is shown in the inset of Fig. 3. There is non-monotonic variation in T_c (R = 0) with the increase of nano-Al_2O_3 particles concentration in the composites. It is assumed that this non-monotonic variation in T_c (R = 0) is mainly because of non-uniform distribution of Al_2O_3 nanoparticles at the grain boundaries of the host CuTl-1223 superconducting matrix. The overall suppression of T_c (R = 0) with Al_2O_3 nanoparticles addition is either due to oxygen vacancy disorder or due to mobile holes trapping[36–39] or due to lesser oxygen content in CuO_2 planes.[40] The main problem is to make the distribution of Al_2O_3 nanoparticles uniform and homogeneous across the grain-boundaries of CuTl-1223 superconducting matrix. It can be seen from the resistivity measurements that there is no clear relationship between the Al_2O_3 content and normal state resistivity at 300 K, which is most probably due to the inhomogeneous distribution of these nanoparticles at the grain-boundaries of the bulk material. At lower content of Al_2O_3 (0.5%), there is a chance that nanoparticles are relatively uniformly distributed across the grain-boundaries in the material, which act as scattering centres for carriers due to their insulating nature, whereas at higher content the inhomogeneous distribution might have favoured the formation of clusters of Al_2O_3 nanoparticles and most of the material is then free of such scattering centres. The possibility of the Al_2O_3 material dissolved into the matrix of CuTl-1223 superconductor cannot be eliminated as it was synthesized at higher temperature for elongated time (860 °C, 24 h). Since the vortex motion in high T_c superconductors is thermally assisted phenomena, therefore, we can use the Arrhenius Law to calculate the activation energy required to overcome the pinning barrier.[41–44] The Arrhenius Law for superconductors is $\rho = \rho_o \exp(-U/k_BT)$, where U is the activation energy and k_B is the Boltzmann constant. The Arrhenius plots of $(Al_2O_3)_y$/CuTl-1223 composites are shown in the inset of Fig. 3. We used the region close to T_c (R = 0) to calculate the activation energy. The plot of activation energy versus nano-Al_2O_3 contents is also shown in the inset of Fig. 3. It can be seen from this figure that activation energy has been decreased with the increase of nano-Al_2O_3 contents in the composites. The decrease of the activation energy with the increase of nano-Al_2O_3 contents is possibly due to enhanced insulating nature of inter-granular regions. These insulating weak links between the superconducting grains cause resistive broadening as the energy dissipation takes place during the transport of carriers. The lower values of the activation energies also show the weak flux pinning in these samples.

The FIC analysis on the resistivity versus temperature data of $(Al_2O_3)_y$/CuTl-1223 composites are carried out by using AL model in the mean field regime. The values of critical exponent (λ_{2D} and λ_{3D}), cross-over temperature (T_o), mean field critical temperature (T_c^{mf}), zero temperature coherence length along c-axis {$\xi_c(0)$}, inter-layer coupling (J) are given in Table II. The increased values of "α" after nano-Al_2O_3 particles addition are a theoretical evidence of insulating inter-grain boundaries in the composites samples. Moreover, it is also witnessed that $\xi_c(0)$ has been improved with the increase of "J" values with the nano-Al_2O_3 particles addition in CuTl-1223 superconducting matrix. The plots of $\ln(\Delta\sigma_{AL})$ versus $\ln(\varepsilon)$ of $(Al_2O_3)_y$/CuTl-1223 composite samples for (a) y = 0% and (b) y = 1.5% are shown in Figs. 4(a) and 4(b) and in the insets are shown the experimentally measured dc-resistivity ρ(Ω-cm) along with a straight line extrapolated from the room temperature (300 K) normal state resistivity to 0 K and derivative (dρ/dT) of

TABLE II. The superconductivity parameters observed from the FIC analysis of $(Al_2O_3)_y$/CuTl-1223 composites with y = 0.0, 0.5, 0.7, 1.0, and 1.5 wt. %.

Samples	ρ_n (300 K) (Ω cm) × 10^{-4}	T_c (K)	T_o (K)	T_c^{mf} (K)	$\alpha = \rho_n$ (0 K) (Ω cm) × 10^{-4}	$\lambda_{3D\ slope}$	$\lambda_{2D\ slope}$	ξ_c (0) (Å)	$J = [2\xi_c(0)]^2/d^2$
y = 0.0	9.650	86	104.34	102.31	7.79	0.52	1.05	3.664	0.238
y = 0.5	17.9	74	104.38	102.31	17.21	0.48	1.07	4.741	0.399
y = 0.7	6.105	79	103.34	101.31	5.316	0.5	1.02	4.91	0.429
y = 1.0	13.33	75	101.33	98.34	12.83	0.47	1.97	5.857	0.609
y = 1.5	13.33	64	101.33	98.34	12.752	0.48	1.99	6.181	0.679

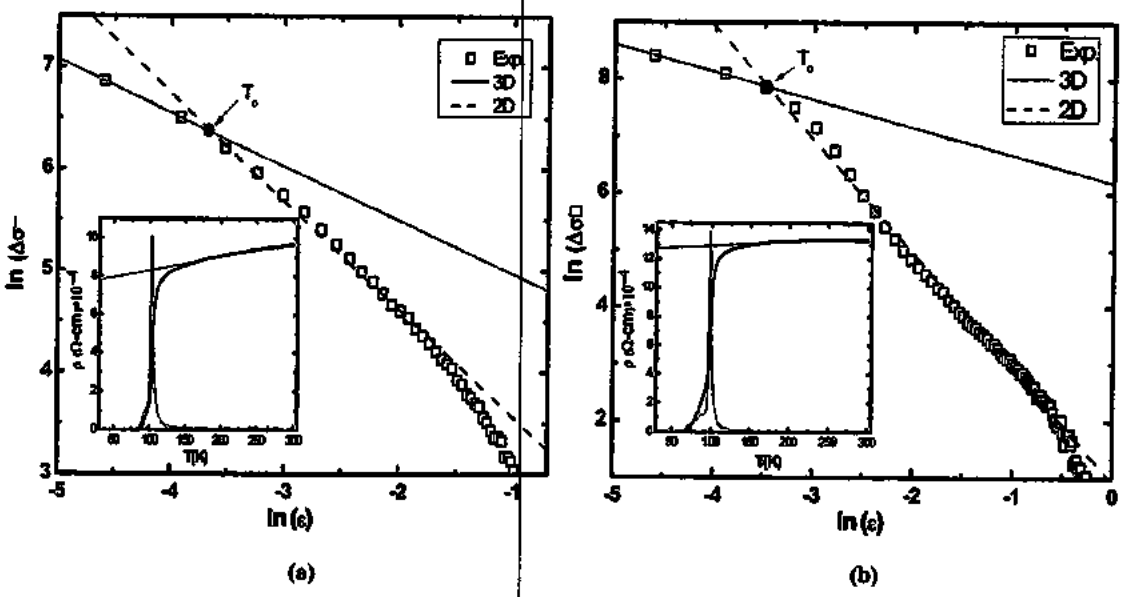

FIG. 4. (a) and (b) ln ($\Delta\sigma$) versus ln(ε) plot of $(Al_2O_3)_y$/CuTl-1223 composites; (a) y = 0, (b) y = 1.5 wt. %. (In the insets are shown the experimentally measured dc resistivity ρ(Ω-cm), derivative ($d\rho/dT$) of dc resistivity versus temperature, and the straight line extrapolated from the room temperature "300 K" normal state resistivity to 0 K.)

TABLE III. Widths of critical 3D and 2D fluctuation regions observed from fitting of the experimental data of $(Al_2O_3)_y$/CuTl-1223 composites with y = 0.0, 0.5, 0.7, 1.0, and 1.5 wt. %.

Sample	λ_{3D} T (K)	ln ε (range in 3D)	λ_{2D} T (K)	ln ε (range in 2D)
y = 0.0	103.34–104.34	$-4.59 < \ln\varepsilon < -3.91$	104.34–121.40	$-3.91 < \ln\varepsilon < -1.67$
y = 0.5	103.37–105.38	$-4.56 < \ln\varepsilon < -3.50$	105.38–129.47	$-3.50 < \ln\varepsilon < -1.32$
y = 0.7	102.34–103.34	$-4.58 < \ln\varepsilon < -3.50$	103.34–131.43	$-3.50 < \ln\varepsilon < -1.21$
y = 1.0	99.39–101.33	$-4.59 < \ln\varepsilon < -3.49$	101.33–154.51	$-3.49 < \ln\varepsilon < -0.55$
y = 1.5	99.33–101.33	$-4.60 < \ln\varepsilon < -3.49$	101.33–159.53	$-3.49 < \ln\varepsilon < -0.47$

dc-resistivity versus temperature. The fitting of experimental curves shows the existence of two different fluctuation regions in these samples. The values of critical exponent (λ_D) derived from the slopes of sample with y = 0 are found to be 0.52 and 1.05, which correspond to 3D and 2D AL fluctuations, respectively. Also, the values of λ_D were found to be (0.48, 1.07), (0.5, 1.02), (0.47, 1.97), and (0.48, 1.99) with y = 0.5, y = 0.7, y = 1.0, and y = 1.5 wt. %, respectively, for 3D and 2D fluctuations. There is a cross-over temperature (T_o) at which fluctuations have been changed from 2D to 3D in low temperature region. The widths of these fluctuation regions are given in Table III. It can be seen from the data that T_o has been shifted toward lower temperature with nano-Al_2O_3 particles addition. On the other hand, the increased values of $\{\xi_c(0)\}$ and (J) show that samples become more isotropic after nano-Al_2O_3 particles addition. The shift of 3D regime to lower temperature indicates that inter-grain boundaries become more insulating due to which T_c and T_o have been decreased. The variation in microscopic parameters extracted from FIC analysis verifies the overall suppression of superconductivity after nano-Al_2O_3 particles addition in CuTl-1223 superconducting matrix.

IV. CONCLUSION

A series of $(Al_2O_3)_y$/CuTl-1223 composites samples were successfully synthesized by solid state reaction method and their reproducibility was confirmed. The XRD analysis showed that the addition of Al_2O_3 nanoparticles did not affect the crystal structure of the parent CuTl-1223 superconductor phase. The SEM images of the superconducting matrix showed its granular structure. The suppression of superconducting properties is most probably due to pair-breaking mechanism caused by the reflection/scattering of carriers across the insulating nano-Al_2O_3 particles present at the grain-boundaries of the host CuTl-1223 superconducting matrix. The decrease of T_c may also be due to oxygen vacancy disorder induced by the nano-Al_2O_3 particles addition. The decrease of the activation energy with the increase of nano-Al_2O_3 contents is possibly due to enhanced insulating nature of inter-granular regions. These insulating weak links between the superconducting grains cause resistive broadening as the energy dissipation takes place during the transport of carriers. The lower values of the activation energies also show the weak flux pinning in these samples. The dc-resistivity data seem to be fitted very well with 3D and 2D Aslamasov-Larkin equations. The cross-over temperature (T_o) is shifted towards lower temperature values with the enhanced nano-Al_2O_3 particles concentration. The increase in $\xi_c(0)$ and J indicates the reduction of anisotropic nature of the material after nano-Al_2O_3 particles addition. The increased value of α is an evidence of improved insulating nature of inter-grain boundaries after nano-Al_2O_3 particles addition.

ACKNOWLEDGMENTS

We are thankful to Higher Education Commission (HEC) of Pakistan for continuous financial support. We are also highly thankful for providing the characterization facilities at Material Science Laboratory, Department of Physics (QAU), Islamabad and Beijing National Laboratory of Condensed Matter Physics, Institute of Physics (IOP), Chinese Academy of Sciences (CAS) Beijing, China.

[1]N. A. Khan, Y. Sekita, H. Ihara, and A. Maqsood, Physica C **377**, 43–48 (2002).
[2]E. V. Antipov, A. M. Abakumov, and S. N. Putilin, Supercond. Sci. Technol. **15**, R31 (2002).
[3]N. A. Khan, Y. Sekita, F. Tatesi, T. Kojima, K. Ishida, N. Terada, and H. Ihara, Physica C **320**, 39 (1999).
[4]K. Tokiwa, H. Aota, C. Kunugi, K. Tanaka, Y. Tanaka, A. Iyo, H. Ihara, and T. Watanabe, Physica B **284**, 1077 (2000).
[5]K. Tanaka, A. Iyo, N. Terada, K. Tokiwa, S. Miyashita, Y. Tanaka, T. Tsukamoto, S. K. Agarwal, T. Watanabe, and H. Ihara, Phys. Rev. B **63**, 064508 (2001).
[6]N. A. Khan and M. Mumtaz, Phys. Rev. B **77**, 054507 (2008).
[7]T. Matsushita, Supercond. Sci. Technol. **13**, 730 (2000).
[8]D. Larbalestier, A. Gurevich, D. M. Feldmann, and A. Polyanski, Nature **414**, 368 (2001).
[9]R. Goswami, T. J. Haugan, P. N. Barnes, G. Spanos, and R. L. Holtz, Physica C **470**, 318 (2010).
[10]F. Ben Azzouz, M. Zouaoui, A. Mellekh, M. Annabi, G. Van Tendeloo, and M. Ben Salem, Physica C **455**, 19 (2007).
[11]Y. Zhao, C. H. Chen, and J. Wang, Supercond. Sci. Technol. **18**, S43 (2005).
[12]J. Plain, T. Puig, F. Sandiumenge, X. Obradors, and J. Rabier, Phys. Rev. B **65**, 104526 (2002).
[13]S.-Y. Chen and I.-G. Chen, Supercond. Sci. Technol. **17**, 71 (2004).
[14]N. Hari Babu, E. S. Reddy, D. A. Cardwell, A. M. Campbell, C. D. Tarrant, and K. R. Schneider, Appl. Phys. Lett. **83**, 4806 (2003).
[15]K. Nakashima, N. Chikumoto, A. Ibi, S. Miyata, Y. Yamada, T. Kubo, A. Suzuki, and T. Terai, Physica C **463–465**, 665 (2007).
[16]A. Hamrita, F. Ben Azzouz, W. Dachraoui, and M. Ben Salem, J. Supercond. Nov. Magn. **26**, 879 (2013).
[17]S. Patnaik, A. Gurevich, S. D. Bu, S. D. Kaushik, J. Choi, C. B. Eom, and D. C. Larbalestier, Phys. Rev. B **70**, 064503 (2004).
[18]S. Dadras, Y. Liu, Y. S. Chai, V. Daadmehr, and K. H. Kim, Physica C **469**, 55 (2009).
[19]M. Farbod and R. M. Batvandi, Physica C **471**, 112 (2011).
[20]I. E. Agranovski, Y. Ilyushechkin, I. S. Altman, T. E. Bostrom, and M. Choi, Physica C **434**, 115 (2006).
[21]A. Goyal, S. Kang, K. J. Leonard, P. M. Martin, A. A. Gapud, M. Varela, M. Paranthaman, A. O. Ijaduola, E. D. Specht, J. R. Thompson, D. K. Christen, S. J. Pennycook, and F. A. List, Supercond. Sci. Technol. **18**, 1533 (2005).
[22]P. Mele, K. Matsumoto, T. Horide, A. Ichinose, M. Mukaida, Y. Y. Oshida, S. Horii, and R. Kita, Supercond. Sci. Technol. **21**, 032002 (2008).
[23]K. Yamada, A. Ichinose, S. Horii, H. Kai, R. Teranishi, M. Mukaida, R. Kita, S. Kato, Y. Yoshida, K. Matsumoto, and S. Toh, Physica C **468**, 1638 (2008).
[24]Y. C. Guo, Y. Tanaka, T. Kuroda, S. X. Dou, and Z. Q. Yang, Physica C **311**, 65 (1999).
[25]S.-Y. Chen, P.-C. Hseih, I.-G. Chen, and M.-K. Wu, Chin. J. Phys. **43**, 666 (2005). Available at: http://PSROC.phys.ntu.edu.tw/cjp.
[26]A. Gupta, A. J. Deshpande, V. P. S. Awana, S. Balamurugan, K. N. Sood, R. Kishore, H. Kishan, E. Takayama-Muromachi, and A. V. Narlikar, Supercond. Sci. Technol. **20**, 1084 (2007).
[27]A. Mellekh, M. Zouaoui, F. Ben Azzouz, M. Annabi, and M. Ben Salem, Solid State Commun. **140**, 318 (2006).
[28]A. Ghattas, F. Ben Azzouz, M. Annabi, M. Zouaoui, and M. Ben Salem, J. Phys.: Conf. Ser. **97**, 012175 (2008).
[29]M. Annabi, A. Ghattas, M. Zouaoui, F. Ben Azzouz, and M. Ben Salem, J. Phys.: Conf. Ser. **150**, 052008 (2009).
[30]N. Moutalibi, A. M'chirgui, and J. Noudem, Physica C **470**, 568–574 (2010).
[31]A. Mellekh, M. Zouaoui, F. Ben Azzouz, M. Annabi, and M. Ben Salem, Physica C **460–462**, 426–427 (2007).
[32]X. F. Rui, J. Chen, X. Chen, W. Guo, and H. Zhang, Physica C **412–414**, 312–315 (2004).
[33]A. L. Solovjov, H.-U. Habermeier, and T. Haage, Low Temp. Phys. **28**, 17–24 (2002).
[34]C. A. C. Passos, M. T. D. Orlando, J. L. Passamai, Jr., E. V. L. de Mello, H. P. S. Correa, and L. G. Martinez, Phys. Rev. B **74**, 094514 (2006).
[35]N. H. Mohammad, A. I. Abou-Aly, R. Awad, I. H. Ibrahim, M. Rounie, and M. Rekaby, J. Low Temp. Phys. **172**, 234–255 (2013).
[36]J. C. Zhang, F. Q. Liu, G. S. Cheng, J. X. Shang, J. Z. Liu, S. X. Cao, and Z. X. Liu, Phys. Lett. A **201**, 70 (1995).
[37]P. F. Miceli, J. M. Tarascon, L. H. Greene, H. P. Barbou, F. J. Rotella, and J. D. Jorgensen, Phys. Rev. B **37**, 5932 (1988).
[38]S. Cao, L. Li, F. Liu, W. Li, C. Chi, C. Jing, and J. Zhang, Supercond. Sci. Technol. **18**, 606 (2005).
[39]V. P. S. Awana, S. K. Malik, W. B. Yelon, C. A. Cardoso, O. F. de Lima, A. Gupta, A. Sedky, and A. V. Narlikar, Physica C **338**, 197 (2000).
[40]E. Brecht, W. W. Schmahl, G. Miehe, M. Rodewald, H. Fuess, N. H. Andersen, J. Hanβmann, and Th. Wolf, Physica C **265**, 53 (1996).
[41]S. J. Feng, J. Ma, H. D. Zhou, G. Li, L. Shi, Y. Liu, J. Fang, and X. G. Li, Physica C **386**, 22 (2003).
[42]A. J. Batista-Leyva, M. T. D. Orlando, L. Rivero, R. Cobas, and E. Altshuler, Physica C **383**, 365 (2003).
[43]M. Tinkham, Phys. Rev. Lett. **61**, 1658 (1988).
[44]T. M. Palstra, B. Batlogg, L. F. Schneemeyer, and J. V. Waszczak, Phys. Rev. Lett. **61**, 1662 (1988).